Bond degradation between FRP bars and concrete under sustained loads

A Thesis Submitted to the College of
Graduate Studies and Research
in Partial Fulfillment of the Requirements
for the Degree of Doctor of Philosophy
in the Department of Civil Engineering
University of Saskatchewan
Saskatoon

By
Fazlollah Shahidi

PERMISSION TO USE

In presenting this thesis in partial fulfilment of the requirements for a Postgraduate degree from the University of Saskatchewan, I agree that the Libraries of this University may make it freely available for inspection. I further agree that permission for copying of this thesis in any manner, in whole or in part, for scholarly purposes may be granted by the professor or professors who supervised my thesis work or, in their absence, by the Head of the Department or the Dean of the College in which my thesis work was done. It is understood that any copying or publication or use of this thesis or parts thereof for financial gain shall not be allowed without my written permission. It is also understood that due recognition shall be given to me and to the University of Saskatchewan in any scholarly use which may be made of any material in my thesis.

Requests for permission to copy or to make other use of material in this thesis in whole or part should be addressed to:

Head of the Department of Civil Engineering
University of Saskatchewan
Saskatoon, Saskatchewan, S7N 5A9

ABSTRACT

In recent times, fibre reinforced polymer (FRP) bars have been used as a replacement for conventional steel reinforcing bars in reinforced concrete members where the corrosion of steel is a major problem as a result of severely aggressive environments. The application of FRP bars as reinforcement in concrete structures has thus been proposed as a potential solution to the problem of steel corrosion in aggressive environments; however, the use of FRP could introduce other durability problems such as alkali resistant resins/fibres, de-icing chemical resistance, creep rupture of fibres, ultra-violet resistance, and freeze-thaw performance. One of the problems is long-term bond behaviour between FRP bars and concrete. FRP bars are coated with a polymer which is known to experience time-dependant deformation (creep) under sustained loads. It is anticipated that creep of the bars' coating and/or the bars' surface features (lugs) could be a factor contributing to the total creep in the reinforced concrete system. Also, glass FRP (GFRP) bars may deteriorate in water and alkaline environments if the coating is damaged and the glass fibres are exposed to water and alkaline solutions which are harmful for the glass fibres.

An experimental program was conducted in two phases to study the long-term bond behaviour between FRP bars and concrete under sustained loads. Also, the effects of water and alkaline solutions on the bond between FRP bars and concrete under sustained loads were investigated. In Phase I, two types of carbon FRP bars (CFRP) and one type of glass FRP bar (GFRP), in addition to conventional steel rebar, were used to make pullout specimens which were tested under various levels of sustained loads at room temperature and exposed to air. In Phase II, three different types of GFRP bars were employed in pullout specimens that were tested under two different sustained load levels in three different environments at room temperature. In this phase, the specimens were either submerged in water or an alkaline solution, or were exposed to air. To help explain the test results, image analysis, scanning electron microscopy (SEM), and electron microprobe analysis (EMPA) techniques were used to examine the materials and the tested specimens.

It was concluded that one of the two CFRP bars and the GFRP bar used in Phase I exhibited poor bond performance under sustained loads when compared to companion steel specimens. Deterioration of the bars' surface features was observed in these FRP bars. The other type of CFRP bar tested performed well in terms of long-term bond behaviour under sustained loads. For the FRP bars used in Phase II, bond degradation between the bars and concrete was not a problem. All three bars showed good bond behaviour under sustained loads. Instead, shear failure at the fibre-matrix interface was found to be a problem, causing a decrease in tensile strength of the bars under sustained loads. SEM investigation revealed circumferential cracks at the fibre-matrix interface in the bars' cross-sections, especially in the specimens tested at higher load levels. X-ray maps, obtained using EMPA, indicated no sign of calcium ion ingress in any of the specimens tested in Phase II. However, some specimens tested in water and alkaline solutions failed sooner than the companion specimens tested in air. This may have been because of degradation of the matrix due to absorption of water, although no evidence of deterioration of the matrix could be found.

ACKNOWLEDGEMENTS

I would like to express my sincere thanks to Dr. T. Rezansoff, Dr. B. F. Sparling, and Dr. L. D. Wegner for their valuable guidance and support throughout this study. Also, I am grateful to the advisory committee members Dr. M. U. Hosain, Dr. S. Yannacopoulos, and Dr. M. Boulfiza for their advice and contributions during the research program.

Furthermore, I am thankful to the department of civil engineering, especially Dr. D. E. Pufahl, for awarding me University of Saskatchewan scholarship.

Special thanks go to Messrs E. Allen, C. D. Fisher, T. Bonli, B. Novakovski, P. Siminoff, and X. C. Wu, laboratory technicians, for their assistance in the experimental work of this thesis.

Finally, financial support from the Natural Sciences and Engineering Research Council of Canada (NSERC) is gratefully acknowledged.

DEDICATION

To my dear wife Atife,

and to my dear children Meysam and Saynaz

for their encouragement, patience, sacrifices, and full support

TABLE OF CONTENTS

LIST OF TABLES

LIST OF FIGURES

LIST OF ABBREVIATIONS

A	= cross sectional area of the bar, mm^2
d_b or d_b	= bar diameter, mm
E	= modulus of elasticity of the bar, MPa
f_{fu}	= design tensile strength of the bar, MPa
ℓ_{bf}	= basic development length of the bar, mm
μ_f	= average bond stress of the bar, MPa
V_f	= volume fraction of fibres, %

Chapter 1

Introduction

1.1. Background

Fibre reinforced polymer (FRP) composites have been known since the early 1940's when their development began for military and aerospace applications. The low density, high stiffness to weight ratio, high strength, design flexibility, and excellent durability of fibre reinforced polymers were the primary reasons for their use in aircraft, marine, automotive, and other industries (Ballinger 1992). They have been used in rockets, satellites, main rotor blades for helicopters, ladder rails, automobiles, oxygen tanks, printed circuit boards, and tennis racquets, to name just a few applications. Also, because of their electromagnetic neutrality, FRP composites have been employed in environments where electrical or magnetic neutrality are required such as magnetic resonance imaging (MRI) and telephone communication equipment.

The corrosion of steel reinforcement in concrete structures has been a problem for years, especially in bridges and marine structures. The use of deicing salts in highway bridges and exposure to marine salt in marine structures has caused extensive corrosion of steel in these types of structures. Galvanizing (zinc coatings), polymer-impregnated concrete, epoxy coatings and glass fibre-reinforced polymer (GFRP) reinforcing bars are among the various solutions that have been investigated (American Concrete Institute (ACI) 1996).

It was not until the late 1970's that the first pedestrian bridges reinforced with GFRP were built in North America and Europe (Mufti et al. 1991). In 1981/82, the first GFRP reinforced concrete highway bridge was constructed in Bulgaria. Since then, there has been a tremendous advancement in the science and technology of FRP

materials. They have been used in three main applications in the construction industry, namely, as structural elements, for repair and rehabilitation of existing infrastructure, and as FRP reinforcing bars for concrete elements (Kant et al. 1997). The first bridge to use FRP bars (equipped with fibre optic sensors) constructed in Calgary, opened to traffic in 1993, is a good example of development of FRP bars (Rizkalla and Tadros 1994). The bridge is prestressed by both carbon FRP and steel tendons and its performance is monitored by using fibre optic sensors.

The application of FRP bars as reinforcement in concrete structures could resolve the problem of steel corrosion in aggressive environments, but it could cause other durability problems. So far, the short-term performance of FRP bars in concrete has been shown to be generally satisfactory. However, the long-term performance of such systems requires more research. One of the areas of uncertainty that still has to be investigated is the durability of bond between the FRP bars and the concrete under sustained loads.

The behaviour of concrete elements reinforced with FRP bars largely depends on the bond behaviour between the composite bar and the concrete (Nanni et al. 1995a). To ensure composite action, internal forces must be transferred between the reinforcement and the surrounding concrete. Also, the bearing forces between the deformations (lugs) on the reinforcement and the concrete must be maintained over time at service load levels. Appreciable losses in load transfer due to creep-related deformations in the concrete and especially in the bar surface deformations (lugs) and/or in the polymer coating of the bars would cause failure of the reinforced concrete element. It is anticipated that creep of the FRP bar surface deformations would be a factor contributing to the total creep in the composite system.

FRP bars consist of unidirectional continuous fibres embedded in a polymer resin matrix, produced using a pultrusion process. Fibres have high tensile strength and carry most of the applied load while the resin matrix acts as a binder and holds the fibres together (Mallick 1988). Studies have shown that glass fibres, commonly used in FRP, are susceptible to degradation in water and alkaline solutions (Nagae and Otsuka

1994, Al Cheikh et al. 1988). The polymer coating of the bars seems to protect fibres against the aggressive environments. However, creep-related deformations of the polymer coating of the bars at service load levels could cause damage to the coating and expose the fibres to the aggressive environments. As a result, damage to the fibres could cause failure.

1.2. Scope and objectives

An experimental study was conducted to investigate the long-term bond behaviour between FRP bars and concrete. The primary objectives were to study the long-term bond between the FRP bars and the concrete under sustained loads in an ambient laboratory environment (Phase I), and to investigate the long-term bond between the glass FRP bars and the concrete under sustained loads in aggressive environments (Phase II). A secondary objective in Phase II was to examine the effects of sustained loads and aggressive environments on the glass FRP bars embedded in concrete.

In Phase I of the program, the scope of the research was to examine the effects of the sustained loads on the bond between the FRP bars and the concrete due to creep-related deformations of the bar lugs and/or of the polymer coating of the bars. This was achieved by applying different intensities of sustained loads to pullout specimens made with glass and carbon FRP bars. Also, companion steel pullout specimens were used for comparison purposes. All the tests were done in laboratory room conditions.

The scope of the research in Phase II was to study the effects of the sustained loads on the bond between the glass FRP (GFRP) bars and the concrete due to creep-related deformations of the polymer coating and/or of the bar surface deformations (lugs) when the bars embedded in concrete were exposed to aggressive environments. Three types of GFRP reinforcing bars were used in pullout specimens, which were tested under two different sustained load levels in potentially hostile solution environments (water and alkaline), as well in air. All the tests were performed at room temperature. Furthermore, the Phase II study included an investigation of the effects of

sustained loads and aggressive environments on the tensile strength of the bars embedded in concrete.

1.3. Methodology

Several steps were considered to achieve the objectives of the research program. First of all, the design of the pullout specimens was required such that a bond failure, rather than splitting of concrete, would occur so that an accurate measure of bond strength could be obtained. This was done by making and testing several specimens initially fabricated using steel rebars. Static tests of the designed pullout specimens were performed to obtain bond strengths of the bars, using a test set-up made specifically for this purpose.

The next step was to develop an apparatus for long-term tests such that sustained tensile loads could be applied to the pullout specimens and could be monitored and adjusted if necessary. To monitor bond behaviour, free end slip of the bars was measured periodically using a height gauge. The designed pullout specimens were used to perform long-term tests in air. However, modification of the specimens was required in order to carry out the long-term tests in different hostile solution environments. Following the long-term tests, failed specimens were inspected and analyzed, using scanning electron microscopy and electron microprobe analysis, to determine the causes of the failures.

All the tests were performed in ambient laboratory conditions. Temperature and humidity of the laboratory were monitored during the test period. However, temperature and humidity were two factors that were considered to be beyond the scope of this research and no attempt was made to perform tests at different temperatures or to control the humidity of the room.

1.4. Overview

The thesis is divided into six chapters. Chapter One introduces the problem and defines the objectives of the research. Studies done by other researchers regarding short-term properties of the fibre reinforced polymer materials and durability issues

associated with these materials are presented in Chapter Two. In Chapter Three, the experimental program, which was conducted in two phases, is explained in detail. Test results are given in Chapters Four (Phase I) and Five (Phase II) along with a discussion of the results and failure analysis. Finally, conclusions and recommendations appear in Chapter Six of the report.

Chapter 2

Literature Review

2.1. Introduction

A composite material is defined as any heterogeneous solid structural material consisting of two or more distinct constituents with significantly different physical properties (American Society for Metals or ASM 1986). In the case of fibre-reinforced polymers (FRP), the composite material consists of fibres that are embedded in a polymer matrix. Performance of the FRP material depends on the mechanical properties of the fibre, the matrix, and the interface between the fibre and the matrix.

FRP bars are produced using continuous high strength fibres embedded in a polymer resin matrix. Many experimental studies have demonstrated that the physical and mechanical properties of FRP bars are different from the well-known properties of steel reinforcing bars. Specifically, FRP bars show elastic behaviour up to failure whereas steel rebars yield after initial elastic behaviour. The lower modulus elasticity of FRP bars also creates larger deflections in FRP reinforced elements. In the case of bond pullout failure, steel rebar lugs crush the surrounding concrete while the outer surface of FRP bars tends to shear off without causing significant damage to the nearby concrete.

FRP bars have a higher corrosion resistance than conventional steel rebars and, therefore, are being used to replace steel in reinforced concrete members where corrosion of steel is a major problem due to severely aggressive environments. However, many other durability issues come into play with respect to the FRP materials. For example, the naturally alkaline environment within concrete that initially protects steel reinforcement from corrosion is harmful to the glass fibres commonly used in FRP bars. In addition, creep within the FRP bars' lugs and/or the FRP bars'

coating in contact with concrete could lead to progressive slip of the bars under service loads.

Many researchers have examined different types of FRP bars to obtain physical and mechanical properties of the bars and to address durability issues associated with the use of the bars in different environments. Published literature regarding bond properties and other relevant physical and mechanical properties of FRP bars are presented in this chapter. Also, studies relating to durability issues and the failure analysis of FRP bars are addressed.

2.2. Properties of fibres and resins used in FRP bars

2.2.1. Introduction

Fibre reinforced polymer (FRP) bars used in the construction industry are usually made of continuous glass, aramid, or carbon fibres embedded in polyester, vinylester, or epoxy resins. The fibres generally have a high tensile strength and modulus of elasticity relative to the resins (Table 2.1) and, consequently, carry most of the applied load. Fibres should be stable and hold their strength during fabrication and handling. Also, minimal variations in strength of individual fibres as well as a uniform diameter and surface are desirable (Hollaway 1993). Glass fibres exhibit low resistance to water and alkaline environments and lose their tensile strength when exposed to water or alkaline. Aramid and carbon fibres, on the other hand, show more resistance to water and alkaline environments.

The primary role of matrix (resin) is to bind the fibres together, to keep the fibres in place and at the desired orientation, and to provide lateral support against buckling of the fibres (Hollaway 1993). Also, resin protects the fibres against damage during handling and fabrication, and against the environment. Despite all of these functions, the main role of matrix is to transfer stresses to the fibres efficiently by adhesion and/or friction.

In general, resins exhibit substantial creep under sustained loads and are prone

Table 2.1. Properties of resins and fibres used to produce FRP rebars.*

Component	Material	Specific gravity	Modulus of elasticity (GPa)	Tensile strength (GPa)	Strain at failure (%)	Coefficient of thermal expansion (μm/m/°C)	Poisson's ratio	Cure shrinkage (%)
Resin	Cast polyester	1.1-1.4	2.1-4.1	0.0345-0.1035	1-5	100-200	0.37-0.39	5-12
	Cast vinylester	1.12-1.32	3-3.5	0.073-0.081	3.5-5.5	n/a	n/a	5.4-10.3
	Cast epoxy	1.2-1.3	2.75-4.1	0.055-0.13	1-6	50-80	0.2-0.33	1-5
Fibre	E-glass	2.58	72.5	3.45	4.8	5	0.2	
	Aramid	1.44	131	3.6-4.1	2.8	-2 (longitudinal) 59 (radial)	0.35	
	Carbon	1.78-2.15	228-724	1.5-4.8	0.5-1.4	-0.1 to -1.6	~0.2	

*After Mallick 1988, Callister 2000.

to attack from water and chemical substances such as solvents, acids, and bases. Polymers can develop large creep strains at low stress levels and at room temperature (Mallick 1988). Some resins, like polyester, display a low creep and chemical resistance, whereas other resins, like epoxy, exhibit more resistance to creep and chemicals. As shown in Table 2.1, resins possess a large coefficient of thermal expansion and high degree of shrinkage during curing. In selecting a resin (matrix) for a structural FRP, important factors such as strength and stiffness, coefficient of thermal expansion, processing temperature, chemical shrinkage during processing, ability to bond to fibres, sensitivity to environmental factors, and cost should be considered (Bakis 1993). A specific matrix is chosen based on these factors, depending on the specific application.

The interface between the fibre and the matrix is an important transition region that is required to provide sufficiently stable bonding, both chemically and physically (Hollaway 1993). Stress transfer from the matrix to the fibres takes place by shear at fibre-matrix interface (Gdoutos 2000). The strength of the interface dictates the process of load transfer between the fibres and matrix in the neighbourhood of a fibre break or matrix crack. Interface properties are most difficult to determine; however, both the fibre and matrix can be characterized by conducting simple tests. Interfacial shear strength is an important parameter that controls the fibre-matrix debonding process and,

therefore, the sequence and relative magnitude of the various failure mechanisms in the composite.

The properties of the common polymers and fibres used in FRP bars are given in the subsequent sections. Since epoxy, polyester, and vinylester resins, together with carbon and glass fibres were the constituents of the FRP bars used in this study, the focus has been given to the mentioned constituents.

2.2.2. Properties of polymer resins

2.2.2.1. Epoxy

Epoxy resins are the most versatile resins for FRPs, especially for carbon fibre reinforced polymer (CFRP) bars. These resins have a broad range of physical and mechanical properties and are made under a wide variety of processing conditions (Bakis 1993). Properties such as chemical and solvent resistance, fibre adhesion, toughness, and creep resistance could be changed by modifying reactants, the chemical structures of the curing agent and the resin, and conditions of cure.

Generally, epoxy resins are known for their excellent strength and creep resistance, strong adhesion to fibres, chemical and solvent resistance, good electrical properties, high glass transition temperature, and low shrinkage during curing (Bakis 1993). The disadvantages of epoxy resins include a higher viscosity, longer cure time, and higher cost as compared to polyester and vinylester resins.

Creep resistance of epoxy resins depends on type of the resins. Studies indicate that different types of epoxies exhibit different behaviours under sustained loads at room temperature (Sturgeon 1978 and Miklofsky et al. 1965). Table 2.2 shows creep strains of three types of epoxies under sustained loads at room temperature. As shown in the table, MY 753 epoxy had a strain of 0.0022 under stress of 13 MPa while the strain was 0.0006 for ERLA 4617 epoxy under stress of 17 MPa after 100 hours. Although stress had increased in ELRA 4617, the strain was lower than that of MY 753. On the other hand, creep values were insignificant in Formulation G epoxy under stresses up to 14.6 MPa after 1300 hours. However, a stress of 26.7 MPa caused

Table 2.2. Creep strains of different types of epoxies at room temprature.*

Trade name of epoxy	Application	Sustained tensile stress (MPa)	Loading duration (hours)	Strain	Comments
Ciba-Geigy MY 753	Thermosetting matrix resin	13	82	0.0022	
Union Carbide ERLA 4617	Thermosetting matrix resin	17	100	0.0006	
		60	30	0.0030	
Formulation G	Concrete bonding compound	14.6	1300	18×10^{-9}	
		26.7	0.25	12×10^{-9}	Specimen failed.

* After Sturgeon 1978 and Miklofsky et al. 1965.

breaking of the specimen (stress rupture) only 15 minutes after loading.

The term "epoxy" refers to a bridge consisting of an oxygen atom bonded to two other atoms (in this case, carbon) already united in some way. These three-member rings of one oxygen atom and two carbon atoms (epoxide groups) exist in starting materials for epoxy matrix (Mallick 1988). The starting materials are low-molecular-weight organic liquid resins. Diglycidyl ether of bisphenol A (DGEBA) is a common starting material containing two epoxide groups, one at each end of the molecule. Diluents and flexibilizers may be mixed with the starting liquid (DGEBA) to reduce the viscosity and to improve the impact strength of the cured epoxy resin. The curing of epoxy begins by adding small amounts of a reactive curing agent (catalyst) before incorporating fibres into the liquid mix.

As the reaction continues, a three-dimensional network structure is slowly formed as the DGEBA molecules form cross-links with each other. The resulting material is a solid epoxy resin. Cross-link density (spacing between successive cross-link sites) is a major factor affecting the properties of a cured epoxy resin. Properties such as tensile modulus, glass transition temperature, thermal stability, and chemical resistance could be improved by increasing the cross-link density. However, strain at failure and fracture toughness both decrease with an increase in cross-linking.

2.2.2.2. Polyester

Polyester and vinylester resins are the most common resins used in glass fibre reinforced polymer (GFRP) bars. The properties of polyester can vary widely. They can be formulated to have outstanding chemical resistance and a variety of properties ranging from hard and brittle to soft and flexible (Mallick 1988).

In general, the principal advantages of polyester for FRPs are low viscosity, fast cure time, low cost, and chemical resistance. High volumetric shrinkage and less fatigue resistance are main disadvantages.

The effects of exposure to water, salt solution, and simulated concrete pore solution on vinylester and isopolyester resins were investigated by Chin et al. (1997). No significant changes were observed in tensile strengths for vinylester and isopolyester resins following 1300-hour immersion at room temperature. Equilibrium in solution absorption was reached in both polymers in all three solutions and at both temperatures (ambient and 60 °C) well before 50 hours immersion. However, 60 °C uptake data for isopolyester resins appeared to indicate mass loss after 100 hours for the pore solution and after 200 hours for the salt solution. This was attributed to the possibility of polymer breakdown followed by the leaching of hydrolysis or soluble degradation products.

In a related study, Chin et al. (1998) indicated that an overall decrease in tensile strength occurred over the exposure period for isopolyester and vinylester specimens following exposure to water, salt water, and simulated concrete pore solution at ambient temperature, 60 °C, and 90 °C. The standard deviation of the data was estimated to be ±23%, which was in the range of changes in the tensile strengths of the specimens tested at ambient temperature. Specimens in 60 °C and 90 °C pore solution exhibited the most severe degradation. In the case of isopolyester in 90 °C pore solution, specimens were so severely degraded after 10 weeks that they could no longer be tested. Water, salt water, and alkaline environments had less effect on vinylester than on polyester. Spectroscopic analysis of the exposed resins revealed varying degrees of ester hydrolysis.

Also in the study, energy dispersive X-ray analysis showed no ionic penetration into the 25 mm diameter specimens and no visible surface damage, when specimens were immersed in salt and pore solutions at ambient temperature and 60 °C for 60 days. Only for isopolyester specimen exposed to 60 °C pore solution, appreciable amounts of sodium, potassium, or calcium were found in the interior of the specimen. However, this particular specimen was visibly degraded on the surface and ion transport most likely occurred through the damaged resin.

An unsaturated polyester resin containing a number of C=C double bonds is the starting material for a thermoset (long-chain molecules of polymers are joined together by chemical linking or cross-links) polyester matrix (Mallick 1988). The reaction of maleic anhydride and ethylene or propylene glycol results in an unsaturated polyester resin, which is a polymeric liquid. It is then dissolved in styrene, which reduces its viscosity and makes it easier to handle. The styrene also contains C=C double bonds. It acts as a cross-linking agent by bridging adjacent polyester molecules at their unsaturation points. The properties of polyester resins depend on the cross-link density. Increasing the amount of styrene reduces the elastic modulus since it increases the space between polymer molecules causing a reduction of cross-linking and therefore a reduction of the elastic modulus of the cured polyester resin.

2.2.2.3. Vinylester

Vinylester resins are more flexible, tougher, more fatigue resistant, and more chemically resistant than polyester resins. Like polyesters, vinylesters possess a high volumetric shrinkage, low viscosity, and fast curing time.

Vinylester resins are produced by the reaction of an epoxy resin and a monofunctional unsaturated acid, such as methacrylic or acrylic acid (Mallick 1988). The C=C double bonds occur only at the ends of a vinylester molecule. Since the cross-linking can take place only at the ends, fewer cross-links are produced, and a cured vinylester resin is more flexible and has higher fracture toughness than a cured polyester resin. As in polyesters, styrene monomers are used to decrease the viscosity and to crosslink unsaturated points in neighbouring vinylester molecules. A vinylester

molecule contains a number of OH (hydroxyl) side groups along its length. Hydroxyl groups are capable of forming hydrogen bonds with similar groups on a glass fibre surface. This results in excellent wet-out (wetting of the fibres with the resin) and good adhesion with glass fibres.

2.2.3. Properties of fibres

2.2.3.1. Carbon fibres

In general, carbon fibres have high tensile strength to weight and tensile modulus to weight ratios, high fatigue strength, low coefficient of thermal expansion, and excellent moisture and chemical resistance (Benmokrane et al. 1997). Carbon fibres are also extremely resistant to stress-rupture and stress corrosion. However, they are substantially more expensive than glass fibres. For example, standard modulus continuous PAN carbon fibres cost about 14 times more than E-glass continuous fibres (Callister 2000). High modulus PAN carbon fibres even are more expensive (about 77 times the price of glass fibres).

Carbon fibres also have excellent chemical resistance to water and sodium hydroxide solution (Uomoto and Nishimura 1999). However, it was shown in the study that, for immersion in hydrochloric acid at a temperature of 80 °C, the tensile strength was reduced by about 20% after 120 days. There was a small reduction (about 5% to 8%) in the tensile strength of the fibres when exposed to water and sodium hydroxide solution at 20, 40, and 80 °C for 120 days.

There are generally two types of carbon fibres: PAN-based and pitch-based (Mallick 1988). The first type is manufactured from polyacrylonitrile (PAN), which is the most common textile precursor (starting material). The second type is made from pitch, a by-product of petroleum refining or coal coking. Pitch-based fibres have a higher modulus of elasticity and a lower tensile strength whereas PAN-based fibres sustain a higher ultimate strain, have a lower modulus of elasticity, and a higher tensile strength. The former is more expensive than the latter.

PAN fibres are produced by wet spinning and stretching of the precursor whereas melt spinning and drawing of the starting material are used in producing pitch fibres (Mallick 1988). PAN and pitch fibres are then processed in three general steps (Bakis 1993): 1) they are heated in the air to stabilize the precursor, which prevents melting, or fusion, 2) the fibres are carbonized by heat treatment in an inert atmosphere to eliminate the non-carbon elements, resulting relatively low modulus, high strength carbon fibres, and 3) the fibres are graphitized at high temperatures up to 2000 °C (with or without stretching) to improve the microstructure for enhanced stiffness and strength. Relatively high modulus, low strength fibres are produced when stretching is not applied and improved strength is gained by stretching (Mallick 1988). Pitch-based carbon fibres are more expensive than PAN-based fibres because of the need to stretch the fibres during the high temperature graphitization procedure for optimal microstructure and mechanical properties (Bakis 1993).

2.2.3.2. Glass fibres

Glass fibres are the most common of all reinforcing fibres for FRP materials. Low cost and a high tensile strength are the main advantages of glass fibres. Disadvantages include a low tensile modulus, a high density, sensitivity to abrasion, low fatigue resistance, low resistance to alkaline environments and moisture, and susceptibility to both stress rupture and stress corrosion.

There are different types of glass fibres. S-glass (magnesium aluminosilicate) and E-glass (calcium aluminoborosilicate) are two types of fibres most commonly used in the composite industry (Mallick 1988). S-glass has higher strength, stiffness, and ultimate strain than E-glass, but costs more than E-glass and is more susceptible to degradation in alkaline environments. Alkali-resistant (AR) glass fibres have been developed specifically to minimize weight and stress loss in alkaline environments (Bakis 1993). C-glass is used for its chemical stability in acidic environments. So far, commercially available GFRP bars in North America are made of E-glass fibres, and polyester or vinylester resins (Pultrall Inc., Hughes Brothers Inc., and Marshall Industries Composites Inc.).

Glass fibres are prone to degradation when exposed to water and chemicals such as acids and alkaline. They lose their tensile strength when exposed to the harsh environments especially at high temperatures. In addition, glass tensile strength decreases if subjected to tensile load for prolonged periods of time. Creep rupture also occurs in glass fibres and their composites under sustained tensile loads although creep strains at failure are not significant.

A study of glass fibres indicated that glass rods exhibit little creep at room temperature (Sturgeon 1978), with observed creep strains being very small and insignificant. In addition, it was reported that glass fibres display failure by stress-rupture. Bulk glass and S-glass fibres in an epoxy matrix lost 50% and 40% of their tensile strengths, respectively, after being under sustained loading for 1000 hours.

Studies have shown that the reaction of water with glass depends on the composition of the glass (Doremus and Mehrotra 1983). More durable glasses, such as commercial soda-lime silicates and certain mixed alkali silicates, react slowly with water whereas some other alkali silicates react much more rapidly. Water reacts with the silicate network in the glass and breaks the network. An H_2O molecule generates two Si-OH units by chemically reacting with the silicate network (Shackelford 1996):

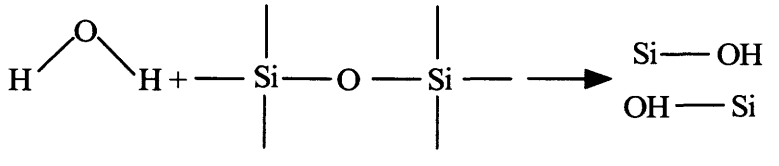

(2.1)

The hydroxyl units are not bonded to each other, leaving a break in the silicate network. When this reaction occurs at the tip of a surface crack, the crack is lengthened. This causes loss in tensile strength of the glass fibre over time.

Studies indicate that the tensile strength of a glass fibre decreases when immersed in water. A reduction of 10% in tensile strength was measured for E-glass after 200 hours in water at 25 °C (Nagae and Otsuka 1994) and about 25% at 60 °C. Uomoto and Nishimura (1999) indicated that S glass fibres retain only 90% and 55% of their tensile strength when exposed to water for 5000 hours at 20 °C and 80 °C,

respectively. Malvar (1998) has reported that glass fibres experience a loss of 10% in tensile strength after a few months of exposure to water.

When glass is under tension for prolonged periods of time, its strength decreases; the phenomenon is termed static fatigue and has been known for decades (McGarry 1994). It is similar to stress corrosion in metals. The net result is that the "infinite life" strength of glass under tension (the stress at which it will not break eventually) is a small fraction (5-10%) of its short time strength, as measured in a 2-3 minute tensile test.

Two key observations can be made about static fatigue phenomenon (Shackelford 1996): (1) it occurs in water containing environments, e.g. moist air, and (2) it occurs around room temperature. The mechanism is the reaction of water with silicate network, as described above. At relatively high temperatures (above about 150 °C), other factors such as viscous deformation can also contribute to static fatigue. At low temperatures (below about –100 °C) the rate of hydroxyl reaction is too low to produce a significant effect in practical time periods.

Harsh environments, especially alkaline, also have adverse effects on glass fibres and GFRP bars. The most damaging environment faced by glass fibres is the alkaline pore solution created during the hydration of the concrete (Porter et al. 1995). The hydration process may continue for months or years if water continues to be present. In that case, the glass will be subjected to chemical attack constantly throughout its lifetime to varying degrees.

The alkali attack of the glass is characterized by two separate mechanisms: 1) hydroxylation and dissolution, and 2) notching (Porter et al. 1995). In the first mechanism, the Si-O-Si bonds in the glass network are broken by the OH^- ions, which are highly concentrated in the alkaline pore solution (Bentur and Mindess 1990):

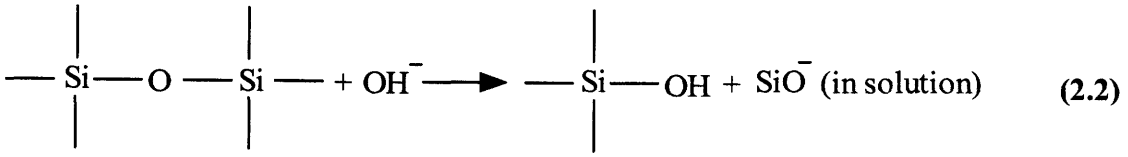

(2.2)

This causes leaching of calcium out of the bulk glass, resulting in the creation of calcium hydroxide, which adheres to the surface of the glass and slows the aging process (Porter et al. 1995). In the notching mechanism, notching of the glass occurs as the calcium crystals grow, aided by the glass itself. The glass along with the cement paste serves as a source of calcium. The notching of glass reduces the tensile strength of the glass fibres as a result of the reduction of the cross-section of the glass fibres in GFRP bar.

Uomoto and Nishimura (1999) have shown that S-glass fibres lose 96% of their tensile strength after 9 hours when they are exposed to sodium hydroxide solution at 80°C. The loss was 50% at 40 °C after about 1600 hours. The tensile strength of the glass fibres reduced rapidly with time when immersed in hydrochloric acid and water at a temperature of 80 °C.

2.3. Physical and mechanical properties of FRP bars

2.3.1. Introduction

Properties of fibre reinforced polymer (FRP) bars depend on the properties of the constituent materials (fibres and polymer matrix or resin), distribution of fibres, volume fraction of fibres (V_f), and interface properties. Fibres are elastic materials whereas resin displays a non-linear behaviour (Figure 2.1). The resin behaviour has minor effects on the tensile strength of FRP bar since the fibres are stronger and carry most of the applied load. Figure 2.1 illustrates the behaviour of fibres, resin, and FRP bars. As shown in the figure, fibres and FRP bars exhibit elastic behaviour up to failure.

FRP bars are anisotropic: their mechanical properties are different in the two principal transverse directions, with the longitudinal axis being the stronger orientation. Mechanical properties of FRP bars vary significantly from one product to another mainly because they are produced from different fibres and resins. In general, FRP bars

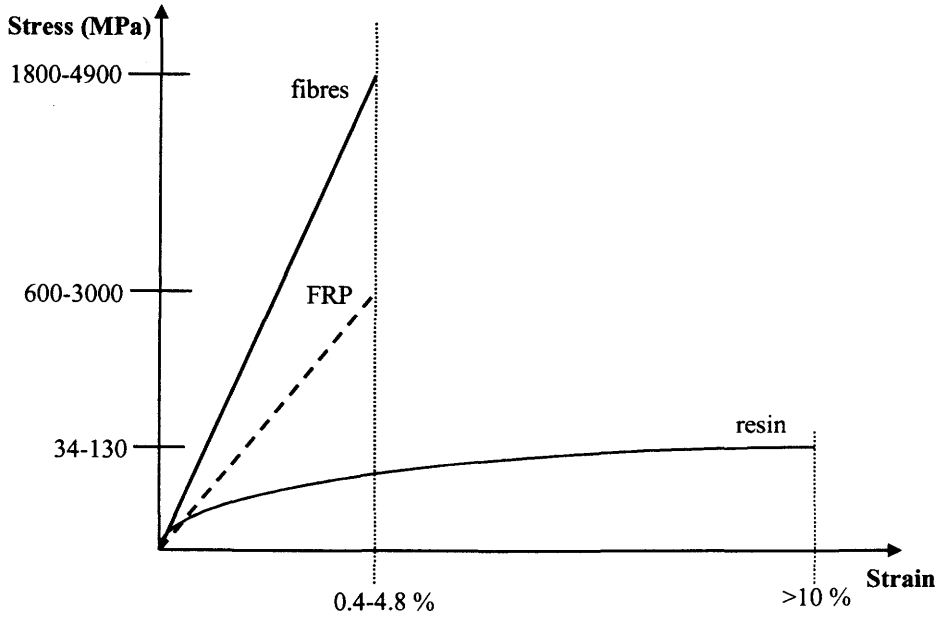

Figure 2.1. Stress-strain curves for fibres, resin, and FRP bars (after ISIS 2000).

have higher tensile strength than conventional steel (Figure 2.2). Carbon (CFRP) and aramid (AFRP) FRP bars can develop more than three times the tensile strength of reinforcing steel whereas glass (GFRP) FRP bars can develop more than twice that strength. The elastic modulus of FRP bars is lower than that of steel. This results in

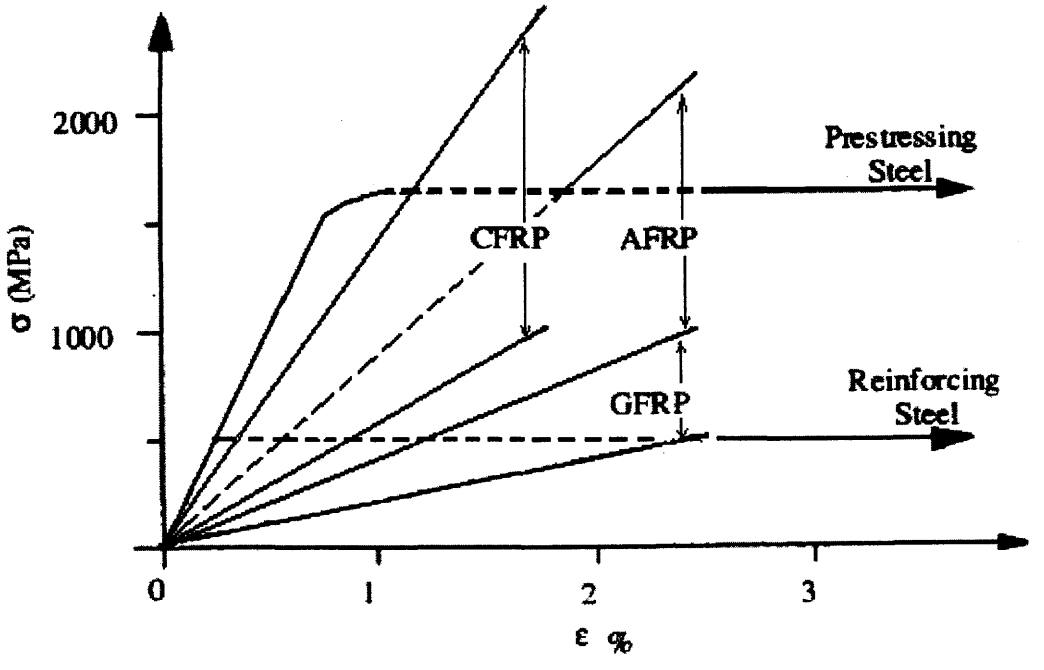

Figure 2.2. Stress-strain relationships for FRP and steel bars (after Gdoutos et al. 2000).

larger deflections in FRP reinforced concrete beams than that of in steel beams with similar reinforcement ratios. Therefore, design of FRP reinforced concrete beams is generally governed by serviceability limit states.

As shown in Figure 2.2, FRP bars remain practically elastic up to failure while steel rebars exhibit ductile behaviour. The FRP bars typically fail by tensile rupture of fibres, followed or accompanied by longitudinal splitting (debonding along the fibre/matrix interface) parallel to the fibres (Mallick 1988).

In addition, the compressive strength of FRP is not as great as the tensile strength due to buckling that occurs in the fibres (Gdoutos et al. 2000). In general, this is not considered a major problem in reinforced concrete because the bars are mainly used as tension reinforcement.

In the long term, FRP bars may demonstrate a decrease in tensile strength under tensile loads. This can lead to eventual failure of the bars under sustained loads, especially if the bars are exposed to aggressive environments. Also, a certain degree of creep is expected from FRP composites since the resin matrix of FRP is susceptible to creep (Gdoutos et al. 2000). Creep strain depends on the stress level and on temperature (Mallick 1988). Mechanical and physical properties of FRP bars especially CFRP and GFRP bars are presented in the following sections.

2.3.2. CFRP bars

In general, CFRP bars possess high tensile strength, show good resistance to creep and creep rupture, and exhibit good performance in aggressive environments. CFRP bars can also retain their tensile strength under tensile loads relatively well. The cost of CFRP bars is much higher (more than 30 times) than that of steel reinforcing bars (Mitsubishi Corporation).

Due to their high tensile strength, CFRP bars are mainly used in prestressed concrete. However, some manufacturers have tried to manufacture CFRP bars that could be used as reinforcement in non-prestressed concrete elements. Benmokrane et al. (2001b) obtained the tensile strength and modulus elasticity of two recently available

CFRP bars. The first of these (sand-coated bars) were made of a vinylester resin and carbon fibres. An average ultimate tensile strength of 1536 MPa was found for the 10 specimens tested. The modulus of elasticity was 128 GPa on average. The second type of the bars (ribbed bars) consisted of carbon fibres impregnated with a thermoset matrix. The average tensile strength for 10 specimens was 2138 MPa and the average modulus of elasticity was found to be 145 GPa. The two CFRP bars could be used as non-prestressed reinforcement for concrete structures since they satisfy the minimum requirements for CFRP bars as reinforcement for concrete structures, i.e. a minimum tensile strength of 1200 MPa, and a minimum modulus elasticity of 110 GPa, and a minimum of bond strength of 12 MPa (bond test results are presented in Section 2.4.2).

CFRP bars exhibit good creep behaviour under sustained loads, even when exposed to aggressive environments. Saadatmanesh and Tannous (1999) tested two types of carbon FRP bars (CFCC and Leadline) under 40% of the ultimate tensile loads at room temperature (25 °C) in air and in simulated aggressive environments (pH=3 and pH=12). Both Leadline and CFCC exhibited good creep behaviour with limited creep strains for the 3000-hour test duration. The creep strains for Leadline were 0.001% in air, 0.016% in solution with pH=12, and 0.017% in solution with pH=3. CFCC experienced higher creep strain (0.016%) than Leadline in air and slightly higher creep strains in alkaline and acidic solutions (0.019% and 0.023%, respectively).

In a related study, carbon FRP bars (CFCC) were exposed to sodium hydroxide (pH=13) and salt-water solutions for more than four years at a sustained stress of 60% of ultimate tensile strength (Santoh 1993 and Tokyo Rope 1993). The specimens showed no sign of deterioration. In addition, only minor tensile strength losses in the order of 1% to 7% were recorded.

Unlike GFRP bars, higher temperatures seem to have no major effects on CFRP bars exposed to harsh environments. Katsuki and Uomoto (1995) exposed aramid, glass, and carbon FRP rods to sodium hydroxide solution (1 mol/l for GFRP and 2 mol/l for AFRP and CFRP) at 40°C and zero load condition. Tension tests performed after 120 days exposure to the solutions showed that GFRP bars experienced a loss of 72% of

ultimate tensile strength, whereas there were no significant changes in the tensile strengths of AFRP and CFRP bars.

Glass and Kevlar 49 fibres and their composites exhibit failure by stress rupture at high stress levels at room temperature (Mallick 1988). On the other hand, carbon fibres are relatively less prone to stress rupture failure. Hundley and Dolan (1996) tested carbon/epoxy (volumetric fraction of fibres or $V_f = 0.650$), aramid/epoxy ($V_f = 0.557$), and glass/vinylester ($V_f = 0.483$) rods (3 mm diameter) in air at 20 °C and under a stress level of 85 to 95% of their tensile strengths. The creep tests showed that carbon had a lower creep-rate than glass or aramid. All ten GFRP and eight (out of 10) AFRP specimens failed by stress rupture, also known as creep rupture. Only three (out of 10) CFRP specimens failed by creep rupture and one specimen did not fail after 3915 minutes. The rest of the specimens experienced premature failures. The strains at failure ranged from 0.07% to 0.25% for AFRP specimens, and from 0.10% to 0.24% for GFRP specimens. The strain at failure for CFRP, which could be measured for only one specimen, was 0.06%. Variations in the time-to-rupture were observed for each type of bars under different stress levels. In general, bars with higher stress levels failed sooner. Time-to-rupture ranged from 2 to 2715 minutes (stress levels of 94.9% to 87.8%) for CFRP, from 2 to 898 minutes (stress levels of 93.3% to 86.1%) for AFRP, and from 2 to 59 minutes (stress level of 96.7%) for GFRP rods.

Experimental observations indicate that all fibre-reinforced polymers have long-term strengths that are only a fraction of the short-term strengths. Malvar (1998) proposed useable ratios of allowable to short-term ultimate stresses of 0.25, 0.40, and 0.64 for GFRP, AFRP, and CFRP, respectively based on data collected from experimental studies by numerous researchers. It was also noted that glass and aramid FRPs would degrade if in direct contact with concrete, in the presence of moisture, and when subjected to UV radiation.

In summary, CFRP bars appear to be good replacement for steel prestressing tendons where corrosion of steel due to aggressive environments is a major problem. Studies show that CFRP bars have insignificant creep strains under sustained loads and

could retain their tensile strength sufficiently. Also, they are less prone to water, salt, and alkaline solution, and exhibit good performance at higher temperatures.

2.3.3. GFRP bars

GFRP bars have a low modulus of elasticity and high tensile strength. Their tensile strength decreases as the temperature increases. The bars exhibit failure by creep rupture especially at high stress levels and at high temperatures. GFRP bars lose their tensile strengths under sustained loads, especially in harsh environments and at high temperatures.

Glass FRP bars exhibit a higher tensile strength than steel rebars. However, the modulus of elasticity of GFRP bars is much lower (about 20%) than that of steel. Chaallal and Benmokrane (1993) measured the mechanical properties of a GFRP rod (E-glass/polyester). A higher ultimate stress and much lower modulus of elasticity, compared to steel rebars, were found. An average ultimate tensile strength of 689 MPa and average modulus of elasticity of 42 GPa were reported. Also, it was shown that tensile strength of the GFRP rod decreased by increasing the temperature. The rod retained only 30% of its tensile strength at 400 °C whereas the deformed steel bars kept 85% of their tensile strength at the same temperature. In addition, the tensile strength of glass FRP bars decreases with an increase in bar diameter since the fibres near the outer surface of the bar cross-section carry more stress than the fibres near the centre (Faza and GangaRao 1993). This was attributed to the resin dependent shear lag phenomenon.

Glass fibres and their composites exhibit failure by creep rupture at high temperatures. Glass/polyester FRP plates (6 mm thick) exhibited creep rupture failures at 50 °C and 80 °C under 66% and 54% stress levels, respectively (Dutta and Hui 2000). The times to rupture were 30 minutes at 50 °C and 15 minutes at 80 °C. Strains at failure were 0.63% and 0.54% at 50 °C and 80 °C, correspondingly. The specimens with 73% stress level at 25 °C did not fail after 30 minutes.

Studies show that GFRP bars exhibit tensile strength reduction under sustained tensile loads especially when exposed to salt and alkaline solutions. Sen et al. (1993a)

studied the durability of S2 glass/Shell Epon 9310 epoxy bars used in pre-tensioned beam specimens (uncracked and precracked) exposed to simulated tidal cycles. The specimens, along with identical specimens with steel reinforcement, were placed in an inclined position in two tanks containing 15% sodium chloride solution at room temperature. Also, a set of control beams was kept inside the laboratory. The beams were tested at periodic intervals to obtain ultimate loads. Two-point loads were applied on each simply supported beam and mid-span deflection was measured at each load increment.

Nine of out of the 12 steel specimens, described above, experienced compression failure (crushing of concrete). Three others failed in shear. Test results indicated that the ductility of the exposed steel specimens was largely unaffected by different exposures. Only six out of 12 beams containing glass fibre/epoxy bars (including all unexposed control specimens) failed due to concrete crushing (compression failure). Of the remaining six, two failed in shear and four others failed in a corrosion mode. In this mode, failure occurred immediately after flexural cracking. This indicated that the bar or its bond with concrete had been totally destroyed at mid-span. It was concluded that the durability of glass fibre/epoxy reinforced specimens exposed to dry/wet cycles was much worse than that of identical steel reinforced specimens. There was no visual sign of deterioration in the glass fibre/epoxy pre-tensioned beams.

In another study on the effects of alkaline solution on FRP bars, an extensive research program studying one type of GFRP pre-stressing tendon, one type of CFRP pre-stressing tendon, and three types of #3 GFRP reinforcing bars was conducted at Iowa State University (Porter et al. 1995). Specimens made of the three types of GFRP reinforcing bars (designated A, B, and C) were exposed to an alkaline environment (pH=13) at 60 °C (aged specimens) with and without sustained loads (loaded and unloaded specimens). All three rebars had a diameter of 9.5 mm (#3 bars) with fibreglass wrapping giving the bars a deformed surface. Rebars A and B were made of E-glass fibres and polyester resins and were supplied by two different manufacturers.

Rebar A had a dark grey colour. Rebar C was made of E-glass fibres and vinylester resin.

The sustained load level for the above-mentioned specimens was 40% of the short-term ultimate tensile strengths of the bars. Some specimens (aged and loaded) remained under load for approximately 2-3 months while exposed to the alkaline environment whereas some others (preloaded and aged) were preloaded to the same stress level for 2-3 minutes and then unloaded before being submerged in the alkaline solution. Unaged and loaded specimens were kept at room conditions. All aged (loaded and unloaded) and unaged (loaded) specimens were tested in tension. Tension test results are summarized in Table 2.3.

As shown in Table 2.3, the aged and loaded specimens had the most loss of tensile strength (56% and 72%) and modulus of elasticity (7% and 9%). The aged and loaded Rebar C specimens could not be tested because they failed while still in the solution as a result of stress corrosion. Some of these specimens failed due to stress corrosion only after a few days of direct exposure to a highly alkaline environment rather than failing directly due to aging. The unaged and loaded Rebar C specimens showed some unexpected increase in the tensile strength and the stiffness. These increases were more likely due to large variations in the specimen properties and also possible random errors.

After the tension tests described above had been performed, surface images of unaged and aged GFRP specimens were collected using a camera mounted on an optical microscope. In samples taken from aged rebars A and B, corrosive attack on the surface was clearly visible. The unaged samples appeared glossy and resin rich on the surface. The surface of the aged samples exhibited severe notching and pitting and also appeared to be more fibrous and less rich in resin. The severe surface damage seen on the aged Rebar B specimens was only apparent on one side of the specimens. This was due to the uneven distribution of resin on the outer surface of these bars, as approximately half the surface was resin rich while the other side was relatively dry with significantly less resin. The alkaline surface attack on the aged Rebar C sample was less apparent than for

Table 2.3. Tension test results for three types of GFRP bars (after Porter et al. 1995).

Specimen	Condition*	Values	Stress, σ (ksi)	Max. strain, ε (in./in.)	Modulus of elasticity, E (ksi)
Rebar A (E-glass and polyester)	Unaged	Average	50.2	0.0146	5.28×10^3
	Aged (19 days)	Average	35.6	-	-
		Effect	-29.0%	-	-
	Aged (81 days)	Average	26.3	0.0069	5.21×10^3
		Effect	-47.6%	-52.7%	-1.3%
	Aged and preloaded	Average	26.3	0.0073	5.23×10^3
		Effect	-47.7%	-50.0%	-1.0%
	Unaged and loaded	Average	47.2	0.0116	4.90×10^3
		Effect	-5.9%	-20.5%	-7.2%
	Aged and loaded	Average	22.3	0.0051	4.91×10^3
		Effect	-55.6%	-65.1%	-7.0%
Rebar B (E-glass and polyester)	Unaged	Average	52.2	0.0217	3.78×10^3
	Aged (19 days)	Average	20.5	-	-
		Effect	-60.7%	-	-
	Aged (81 days)	Average	17.9	0.0070	3.88×10^3
		Effect	-65.8%	-67.7%	+2.5%
	Aged and preloaded	Average	17.3	0.0078	3.60×10^3
		Effect	-67.0%	-64.1%	-4.8%
	Unaged and loaded	Average	52.1	0.0179	3.65×10^3
		Effect	-0.4%	-17.5%	-3.4%
	Aged and loaded	Average	14.4	0.0046	3.45×10^3
		Effect	-72.4%	-78.6%	-8.7%
Rebar C (E-glass and vinylester)	Unaged	Average	53.3	0.0188	4.33×10^3
	Aged (19 days)	Average	28.9	-	-
		Effect	-45.8%	-	-
	Aged (81 days)	Average	18.6	0.0060	4.15×10^3
		Effect	-65.1%	-68.1%	-4.2%
	Aged and preloaded	Average	16.0	0.0054	4.18×10^3
		Effect	-70.1%	-70.7%	-3.5%
	Unaged and loaded	Average	58.3	0.0179	4.51×10^3
		Effect	+9.3%	-4.8%	+4.2%
	Aged and loaded	Specimens failed before tension tests while they were in solution and under load.			

* The "aged" condition refers to exposure in an alkaline solution maintained at 60 °C.

rebars A and B. A visual comparison of unaged and aged Rebar C specimens also showed that the colour of the rebars had changed from being light blue (unaged) to light yellow.

In a related study, Vijay and GangaRao (1999) investigated the effects of salt and alkaline solutions under freeze-thaw cycles and also at high temperature. Two types of GFRP bars (designated as IG1 and IG2, both sand coated and with helical wrappings on the surface) from one manufacturer and three types of GFRP (C-bars, ribbed and designated as M1, M2, and M3) bars from another manufacturer were used. The bars were conditioned in salt and alkaline solutions with or without stress (20% and 40% of the short-term tensile strengths of the bars) at room temperature and at varying temperatures between –11 °C and 49 °C. Also, the sand coated bars were conditioned in alkaline solution at 65 °C with stress whereas C-bars were conditioned in the same solution without stress. High temperature, particularly 65 °C, with stress and alkaline conditioning proved to be more detrimental than any other testing environment. The tensile strength reduction for the sand-coated bars was 84.7% on average within four months at 40% stress application. For C-bars, maximum strength reductions in salt and alkaline conditioning at room temperature were 24.5% and 30% respectively after 30 months of exposure. Similarly, 51.5% and 55% maximum strength reductions were measured under freeze-thaw conditions after 30 months exposure to salt and alkaline solutions, respectively.

In most of the tension tests on the sand coated bars, the helical wrappings on the bars started to fail between 50% and 60% of the ultimate stress in the middle third of the gripped zone (the bar length between the two end grips). Salt conditioned bars typically exhibited a failure of the helical wrappings of the bars followed by vertical splitting of the bars and fibre failure (like a blooming shape) in the middle third of the gripped zone. Alkaline conditioned bars typically had "necking" failures where the outer portion affected by alkalinity would stretch and fail earlier than the inner core. C-bars under salt conditioning usually failed with vertical splitting of the bars whereas the alkaline conditioned bars typically exhibited "necking" failures.

In another study, an experimental program was conducted by Benmokrane et al. (2001a) on different type of GFRP bars in various alkaline environments under sustained load levels of 25-68% of the tensile strengths of the bars. It was shown that under a 30% stress level in pore water solution, the 5/2-polyester/vinylester-glass bar lost 15% of its tensile strength after 90 days whereas the strength loss was 3% for glass/vinylester bar under the same conditions. The type of glass fibres (E-glass) was the same for both bars. To determine effect of fibre types, two types of GFRP bars with the same resin and different glass fibres (E-glass 366 Advantex and normal E-glass) were tested in simulated pore water solution under a stress level of 30% of their tensile strength for periods of 90 and 140 days. More fibre pullout and less fibre damage were observed in the E-glass 366 than in the normal E-glass.

In addition, the observed results showed clearly that penetration of alkaline ions into GFRP bars depends on concentration of alkaline solution. One bar type exhibited a tensile strength reduction of 22% in NaOH solution with a pH=13.1 after 60 days whereas the tensile strength for the same bar did not change in a pH=12.1 NaOH solution after 60 days. Furthermore, test results for GFRP bars exposed to different alkaline environments and different stress levels showed that specimens with a stress level up to 25% did not show any rupture. However, failure occurred due to stress corrosion at higher load levels.

Although the above studies showed degradation of GFRP bars in extremely aggressive environments, results reported by Sekijima et al. (1999) indicated no sign of degradation in GFRP bars that were tested. They made many prestressed concrete beams using a grid (mesh) glass fibre reinforced polymer (GFRP) reinforcements as prestressing tendons. The GFRP reinforcement was made of E-glass fibres (40% by volume) and vinylester resin and was moulded into a grid shape. The initial prestressing forces ranged from 0 to 52.5% of the tensile capacity of the GFRP reinforcement. The beams were left outdoors for seven to eight years. The annual average temperature was 15.7° C and the annual precipitation amounted to 1483 mm at the test field. After the aforementioned period, the beams were demolished and the grid reinforcement was taken out. The tensile capacities of the grid decreased only a little and tensile rigidities

did not change. The scanning electron microscope (SEM) observations showed that the glass fibres were not attacked by the alkalis of the concrete. This could be attributed to the fact that the beams were not under any loading and therefore, no flexural cracking existed in the beams and the concrete cover could have served as a protection to GFRP mesh under wet-dry cycles.

In summary, studies on GFRP bars indicate that tensile strength of GFRP bars decreases under constant loads. The tensile strength reduction is much higher at higher loads and at high temperatures. The bars show creep rupture especially at high stress levels. Also, salt and alkaline solutions are harmful to GFRP bars and cause higher tensile strength reduction and corrosion of the bars.

2.4. Bond properties of FRP bars

2.4.1. Introduction

The performance of FRP reinforced concrete elements depends to a large extent on the bond between the reinforcement and the concrete, making bond an important factor in arriving at design guidelines. As with steel rebars, the bond strength of FRP bars is affected by many factors including reinforcement size, configuration of the reinforcement, surface condition of the bars, and variations in loading conditions. However, a number of additional factors complicate the bond of FRP bars to concrete. The relative softness of FRP bars, when compared with steel reinforcement, may result in damage to the FRP bar surface deformations due to bond action, causing a pullout type of failure rather than the crushing and splitting of the concrete that occurs with steel reinforcement.

With steel rebar, chemical adhesion, friction, and mechanical interaction between concrete and steel define the bond mechanisms (Lutz and Gergely 1967). Bond in deformed bars depends primarily on mechanical interlocking between steel and concrete. Initially chemical adhesion combined with mechanical interaction resists the applied load. The ribs of the deformed bar restrain the slip of the bar by bearing against the concrete between the ribs after slip occurs and adhesion is lost. Forces produced by

the ribs bearing on the concrete cause transverse and longitudinal cracking. Slip of the bar occurs when the ribs either crush the concrete or push the concrete away from the bar (wedging action).

Flexural or primary cracking becomes apparent on the concrete surface when the longitudinal stresses in the concrete near the bar are more than the tensile strength of the concrete. Steel stress is at a local peak at each of the surface cracks and is lower between cracks since the concrete carries part of the tension force. Bond stress is zero at location of the crack. Small internal cracks (secondary cracks) are also formed shortly after formation of primary cracks (Goto 1971). These internal cracks cannot be seen at the surface of the concrete and are developed at bond stresses much less than the bond capacity. Several uncracked concrete rings are produced around the reinforcing bar by the internal cracks. As a result, inclined compressive bond force acting at the rib of the bar transfers the applied force to the surrounding uncracked concrete rings.

The longitudinal component of the resultant bond force acting at the rib of the bar balances out with the tensile force of the reinforcement while the radial component of the resultant bond force produces circumferential or hoop tensile stresses in the concrete rings. These stresses tend to split the concrete away from the bar resulting in loss of bond between the reinforcement and the concrete. If enough confinement exists around the bar to prevent splitting of the concrete then the bar pulls out of the concrete when the bond is lost.

Bond with FRP bars is controlled by several factors, including chemical bond, friction due to roughness of the surface, mechanical interlock against the concrete, hydrostatic pressure due to shrinkage of the hardened concrete, and swelling due to temperature change and moisture absorption (Cosenza et al. 1997). Adhesion (chemical bond) is the main resisting mechanism during initial pullout. Afterwards, friction and/or mechanical interlock replace adhesion in transferring the bond stress. Adhesion and friction are the most dominant mechanisms in transferring bond stress in straight bars, having smooth or sand coated surface. In deformed bars (ribbed, indented, or spiral shape), mechanical interlock is the major means of stress transfer. Bond characteristics

of FRP bars such as bond strength, the mechanics of stress transfer by bond, and durability issues with respect to bond have been investigated by many researchers. These studies are reviewed in the following sections.

2.4.2. CFRP bars

CFRP bars generally exhibit good bond performance when in contact with concrete in the short term. The bond strength, as well as bond mechanism, is dependent on the surface configuration of the bars. CFRP bars with a smooth surface show low bond strength whereas deformed bars possess much higher bond strength. In the case of prestressed concrete, CFRP bars can transfer the prestressing force to the concrete in a shorter length than prestressing steel tendons. Some of the studies related to aforementioned characteristics of CFRP bars are presented in this section.

CFRP bars are mostly used in prestressed concrete since they have a high modulus of elasticity and a high tensile strength. Experimental studies have been conducted to obtain the transfer length of CFRP bars. The transfer length is defined as the length of strands over which the prestressing force is totally transferred from the reinforcement to the concrete. In an experimental program conducted by Domenico et al. (1998), a total of 20 pre-stressed concrete beams pre-tensioned by carbon fibre composite cable (CFCC) strands were constructed and tested. The variables included the beam cross-section, strand diameter, concrete cover, concrete strength, pre-stress level, embedment length, and loading conditions. Transfer lengths were measured, using strain gauges and demec point readings.

Also in the same study, development length was determined as the length range at which the failure mode changed from bond slippage failure to rupture of cables. The development length is the sum of the transfer length and the flexural bond length (the length beyond the transfer length required to develop the full tensile strength of the prestressing strand). The test results showed that transfer length for CFCC was approximately half of that for steel strand. The flexural bond length for CFCC was 25 to 40 percent of that of steel strand. Equations for the transfer and flexural bond lengths were proposed based on the test results.

In a related study, an experimental program was conducted to examine the transfer lengths of two carbon and three aramid FRP pre-stressing tendons (Ehsani et al. 1997a). FRP pre-stressing tendons were found to have average transfer lengths shorter than those of steel tendons (60 to 94 percent for aramid FRP tendons and 78 to 80 percent for carbon FRP tendons).

Other studies have investigated the bond strength and development length of CFRP bars. Jerrett and Ahmad (1995) obtained the bond strength of 8 mm diameter CFRP bar (Leadline) by using concrete slabs to anchor the bars. A total of nine smooth and nine deformed CFRP rods were tested. The results of the smooth rod bond tests showed that the average bond strength was very low compared with its ultimate tensile strength, having a value of 417 kPa. As cited in the study, the average bond strength of a similar size deformed steel rebar was about 5510 kPa. The performance of the deformed CFRP rods was significantly better than that of the smooth rods. The average bond strength of the deformed rods at the onset of free end slip was 1630 kPa, whereas the maximum average bond stress at failure was 7440 kPa. Test results showed that the mechanical bond rather than adhesion and friction accounts for the higher bond strength in deformed CFRP rods.

In another study, Benmokrane et al. (2001b) did pullout tests to measure the bond strength of two recently available CFRP bars as non-prestressed reinforcement for concrete structures. Variables considered in the study were the type of bars and the embedment length. Both types of the bars exhibited almost the same bond strength as the steel bar studied. The experimental basic development length was 215 mm (20 times bar diameter or $20d_b$) for the sand-coated bars (carbon/vinylester) and 290 mm ($30d_b$) for the ribbed bars (thermoset matrix/carbon). These basic development lengths resulted in average bond strengths of 18.9 MPa and 15.7 MPa for the sand-coated and the ribbed bars, respectively. Pullout specimens with embedment lengths less than the basic development length experienced pullout bond failure while the other specimens failed by FRP bar tensile failure. No splitting bond failure was observed due to the large amount of confinement provided in the pullout specimens.

Some researchers have tried to classify the bond mechanisms of FRP bars. Kanakubo et al. (1993) proposed two types of bond mechanisms to study the bond splitting strength (the strength that splits the concrete away from the bar) of FRP bars. One was the bearing-resistant type while the other was the friction-resistant type. In bearing resistant type bars, stress transfer was mostly through mechanical interaction between the bar surface deformations and the concrete where bar surface deformations restrain the slip by bearing against the concrete between the bar surface deformations. The dominant mechanism was friction in friction resistant type bars. Pullout and cantilever type bond tests were performed using CFRP, AFRP, GFRP, and steel bars. The concrete cover was 25 mm. Six different shapes of bars, i.e. straight, deformed, braided, strand, spiral, and double spiral, were considered (Figure 2.3). It was concluded that the bond splitting strength of the bearing resistant type bar (deformed or spiral shape) was almost the same as the deformed steel bar. The friction resistant type (straight, braided, or strand shape) had a bond splitting strength of 80-95% of that of the bearing resistant type.

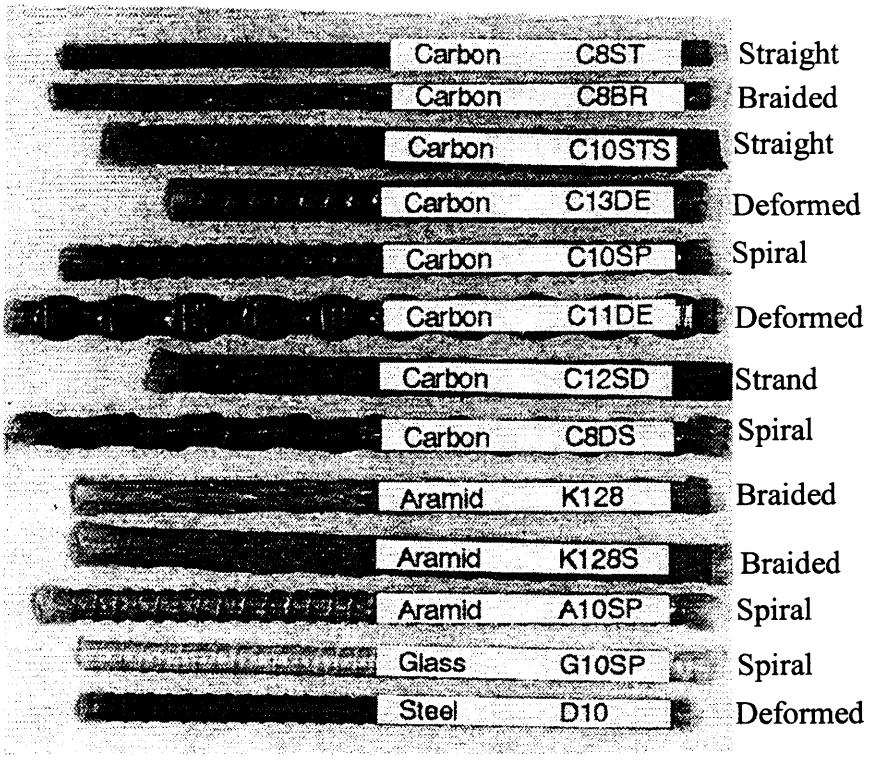

Figure 2.3. FRP bars used in the simple bond tests (after Kanakubo et al. 1993).

In a related study, Makitani et al. (1993) performed bond tests with 29 beam specimens (CFRP, AFRP, GFRP, vinylon FRP, and steel bars) and 8 truss specimens (CFRP bars). Vinylon was a synthetic fibre made by dry spinning of polyvinyl alcohol. The bars had a 10 mm diameter with straight (sand coated), straight with spiral or helical wrapping, spiral, and braided (with and without sand coating) shapes. The single FPR bars in the beam specimens had a concrete cover of 35 mm; in addition, No. 10 stirrups were used in the beams.

From the beam specimen tests, it was found that bond strength increased significantly if the surfaces of bars were processed in a spiral form and were sand coated. The sand coated bars (straight and braided shapes) had very small slip values at their peak bond strength relative to other rods. FRP bars with bond lengths of 40 times the bar diameter, except for spiral shaped carbon and braided aramid FRP bars, were broken due to tension. The spiral shaped carbon and braided aramid FRP bars experienced pullout failure. The glass FRP bar with spiral wrappings and steel rebar, both with bond lengths of 20 times the bar diameter, failed by tensile rupture of the bars, while the other bars with the same bond length were pulled out of concrete.

Also in another study, the load transfer behaviour between FRP reinforcement and concrete was investigated by Nanni et al. (1995a). They did direct pullout tests to determine critical parameters affecting bond performance and to obtain the bond strengths of the glass/vinylester, carbon/vinylester, and carbon/epoxy rods (smooth and machined). The machined rods were made by machining the surface of smooth rods to make ring shaped deformations on the bar surface. The specimens were concrete cubes with dimension of 150 mm per side. The embedment length of the rod was five or ten times the rod diameter. The machined bars had a much higher bond strength than the smooth bars. In all machined rods, the rings (lugs) on the bar surface sheared off, followed by sliding of the bar within the concrete. Carbon/epoxy rods exhibited higher bond strengths than carbon/vinylester rods (1.5 MPa versus 0.6 MPa for smooth rods and 23 MPa versus 13 MPa for machined rods). The bond strengths for glass/vinylester rods were 12 MPa and 1 MPa for machined and smooth bars, respectively. Smaller diameter rods had higher bond strengths at pullout failure than larger diameter rods with

the same embedment length. The bond of FRP rods tended to be controlled by the strength and mechanical action of deformations on the rod surface rather than by adhesion and friction. The strength of the concrete appeared to have an insignificant influence on the bond strength and failure mechanism of the FRP rods. Concrete failure was not experienced in any of the pullout tests.

Design guidelines for non-pre-stressed concrete structures reinforced with FRP bars were presented by Sonobe et al. al (1997). Guidelines for an appropriate design method, materials, loads and their combinations, stress and deformation, ultimate state design, serviceability limit-state design, structural details, and standard test methods for tensile and bond pullout strengths were given. The values for bond stress at bond splitting failure were given for FRP reinforcement based on the tests conducted on unsymmetrical pullout specimens with a concrete cover of 32.5 mm and without any transverse reinforcement. According to the conducted tests, the bond splitting strength varied for different types of FRP bars, hence it must be confirmed for each type of reinforcement through tests. In addition, equations to evaluate the bond splitting strength were given, which were based on the performed tests. Since the types of reinforcement used in the tests were limited, the equations were not applicable generally and were given only for reference.

In another study, Gilstrap et al. (1997) reviewed worldwide efforts for developing design codes and specifications for fibre-reinforced polymer (FRP) used in pre-stressed concrete structures. They reviewed and compared Canadian (Canadian Highway Bridge Design Code or CHBDC 1996), European (Eurocode reported by Clark et al. 1996 and by Federation International de la Précontrainte or FIP 1992), and Japanese (prestressed concrete code or JMC 1995, FRP reinforced concrete code or JSCE 1995) codes cited in the review. For bond and development length, CHBDC has given an equation for the development length of FRP bars in tension, but different parameters used in the equation were not discussed in details in the review. According to the Eurocode, the bond strength should be determined from tests, incorporating an appropriate safety factor to obtain design bond stress. Recommendations for such a safety factor were not given. The Eurocode has suggested a specified pull out test and

has stated that the safety factor must account for variations in the manufacturing process and changes with time with respect to the attack of the resin by the alkalinity of the concrete. A report by working commission of FIP states that knowing the bond strength and bond-slip behaviour is very important and bond characteristics can be determined from the test procedures they have developed for pre-stressing steel. The Japanese prestressed concrete code does not discuss the bond issue.

Also, the Japanese prestressed concrete code (JMC 1995) handles durability issues through a series of strength reduction factors. CHBDC limits the usage of FRP tendons and gives material requirements to address durability. It states that FRP tendons may only be used if they are made with thermosetting polymer matrices. In addition, the use of glass fibre in pretensioning tendon is not permitted due to alkali reactivity. FIP provides a statistical analysis method that may be used to determine the probable strength retention of FRP tendons, but specific strength retention requirements are not given.

American Concrete Institute (ACI 2001) gives the following equation for the development length of a straight FRP bar for a pullout-controlled failure if the concrete cover is more than twice the bar diameter:

$$\ell_{bf} = \frac{d_b f_{fu}}{18.5}, \tag{2.3}$$

where ℓ_{bf} is basic development length of the bar in mm, d_b is bar diameter in mm, and f_{fu} is design tensile strength of the bar in MPa. Also, an equation for the equilibrium of forces acting on the bar results in following equation:

$$\ell_{bf} = \frac{d_b f_{fu}}{4\mu_f}, \tag{2.4}$$

where μ_f is average bond stress acting on the surface of the bar. By substituting ℓ_{bf} from Equation 2.3 into equation 2.4 and solving for μ_f, it is found that $\mu_f = 4.63$ MPa. Therefore, 4.63 MPa is the maximum allowable bond stress used to calculate the

development length required to develop the tensile strength of the bar. ISIS Canada (2000) gives an equation identical to Equation 2.3 for development length.

Mashima and Iwamoto (1993) examined the effects of low temperature on bond strength of different FRP bars. Pullout specimens were tested after undergoing 200 or more freezing and thawing cycles. Each specimen consisted of a single FRP rod embedded at the centre of a 100x100x100 mm concrete cube. The bond length was four times bar diameter for all specimens. The test results showed that the bond pull out strength was not influenced significantly by freezing and thawing for glass, vinylon (a synthetic fibre made by dry spinning of polyvinyl alcohol), and carbon FRP bars. The bond strength of aramid FRP bars (both braided and coiled) reduced gradually with progressive freeze thaw cycling.

Since most of the resins show time dependent deformation under sustained loads, FRP bars covered with resins may possibly show time dependent slip (bond creep) subjected to pullout load (Hollaway et al. 1990). To study bond creep behaviour of two types of FRP bars embedded in concrete, Hattori et al. (1995) did pullout creep tests using concrete cube specimens (100 mm per side). Twisted carbon fibre cable (carbon/epoxy) consisting of 7 strands twisted together, and deformed aramid fibre bars (aramid/vinylester) with large lugs and ribs formed by fibre winding were used. The bond length was 64 mm for all bars. The applied bond stresses were 68% and 65% of bond strengths obtained from static tests for carbon and aramid FRP bars, respectively. Static test results indicated that the mechanical properties of the resins used in the bars and surface shape affect the bond slip behaviours of the FRP bars especially in the preliminary stage of pulling out, when the bond stress is rather small. The wound spiral fibre on the surface of the deformed aramid fibre was scraped, although not taken away completely. Also, the concrete surrounding the bar was damaged. For the twisted carbon fibre, the surface of the surrounding concrete remained intact and the average bond stress was nearly constant after it reached its maximum. Pullout creep test results indicated that the twisted carbon fibre cable showed less increase in the free end slip (0.2 mm) than the deformed steel (0.3 mm) with the same bond stress level after about

8000 hours. The deformed aramid fibre bar showed a larger increase in free end slip (0.6 mm) than the deformed steel rebar.

In summary, bond strength of CFRP bars depends on the type of the resin used in the bars as well as surface shape of the bars. CFRP bars generally show lower bond strength than steel rebars. Bond strength of smooth CFRP bars is much lower than that of deformed CFRP bars. Different surface shapes result in different mechanisms of bond stress transfer between the CFRP bars and the surrounding concrete. Adhesion is the main bond mechanism in smooth bars whereas friction or mechanical interaction is the dominant mechanism in deformed CFRP bars, depending on the surface configuration. CFRP bars embedded in concrete may show bond failure under constant bond stress since the bars are covered with resins which show creep behaviour under sustained loads.

2.4.3. GFRP bars

In general GFRP bars possess lower bond strength than that of steel rebars. The bond strength of a specified GFRP bar decreases with an increase in diameter; therefore, larger development lengths are required for larger diameter bars. Also, for a particular bar size, bond strength decreases with an increase of anchorage length. Like steel and CFRP bars, bond strength of GFRP bars depends on the shape of the surface of the bars. The bars with rough or deformed surface exhibit more bond strength than do the bars with a smooth surface. Characteristics of bond for GFRP bars investigated by some researchers are discussed in this section.

The bar diameter affects the bond strength of GFRP bars. Larger diameter bars have smaller bond strength (larger development length) for a particular bar type. Daniali (1992) experimentally investigated the development length of E-glass/vinylester bars. A glass fibre strand was wrapped around the bars in a 45° helical pattern, making surface deformations on the bars. A total of 30 concrete beams were tested. A concrete cover of 38 mm was used for 13 mm and 19 mm diameter bars whereas the concrete cover was 44.5 mm for 25 mm diameter bar. The beams were also reinforced with 9.5 mm (#3) stirrups along the shear spans. Based on the test results, it was concluded that a

development length of 200 mm was adequate to develop the full tensile strength of a 13 mm (#4) diameter bar, or 460 mm for a 19 mm (#6) diameter bar. By comparison, it could be seen that the ratio of development lengths for 19 mm and 13 mm bars (460/200) is higher than the ratio of the bars diameters (19/13), indicating a higher bond strength for 13 mm diameter bar. All specimens reinforced with 25 mm (#8) diameter bars failed due to inadequate bond or concrete cover splitting after developing 70% to 90% of their ultimate tensile strains (strengths). The development length for these specimens was 508, 636, or 762 mm.

Also, studies show that the bond strength of GFRP bars is lower than bond strength of steel rebars and decreases when anchorage length is increased for a bar with a specified diameter. Chaallal and Benmokrane (1993) obtained the bond strength of a GFRP rod (E-glass/polyester). Deformations on the bar surface were made by winding glass fibres around the bar in ±45° double helical pattern. Three different bar diameters (12.7, 15.9, and 19.1 mm) with two anchored lengths (5 times or 10 times bar diameter) were considered. The bars were embedded in 150 mm diameter by 300 mm long concrete cylinders. A total of 24 pullout specimens were tested. Pullout test results indicated that the bond pullout strength varied from 11.1 to 15.1 MPa with an overall average of 12.9 MPa. The bond strength decreased with an increase in anchorage length for a specified bar size. The results of pullout tests carried out on 19 mm diameter deformed steel rebar yielded an average bond strength of 18 MPa, which was higher than that of the GFRP rod (12.9 MPa).

In a similar study, Larralde and Silva-Rodriguez (1993) studied the bond properties of FRP rebars in concrete. The rebar was made of continuous glass fibres and vinylester resin with a single strand, spirally wrapped around the outside diameter, to produce a spiral shaped indentation (groove) on the bar. From pullout test results, it was concluded that the bond strength of FRP rebar was 0.73 to 0.96 times the steel bond strength. Also, the slip at failure was greater for FRP rebar, compared to steel reinforcing bar. The slip of FRP bars ranged from 1.75 mm to 7.92 mm while slip of the steel rebar varied between 0.69 mm and 1.78 mm.

In another study, the bond strength of GFRP reinforcing bars in concrete was investigated by Benmokrane et al. (1996). One type of reinforcing bar with four different diameters was used in 20 concrete beams. The bars were made of E-glass fibres and polyester resin. Deformations on the bar surface were made by winding glass fibres around the bar in ±45° double helical pattern. The results were compared to pullout tests results (Chaallal and Benmokrane 1993) that were done previously. It was found that the bond strength of beam specimens was 55 to 95 percent of typical values from pullout specimens. The bond strength of GFRP reinforcing bars was 60 to 90 percent of bond strength of steel rebars. The average bond strength of GFRP bars increased as the bar diameter decreased. The bond stress distribution was typically exponential along the embedment length. The maximum bond stress moved further and further down the free end due to progressive bond failure. The bond failure zone was theoretically located between the loaded end of the bar and the position of the maximum bond stress.

Bond strength of GFRP bars is affected by surface configuration of the bars and also by amount of confinement provided. Four different types of GFRP reinforcing bars with different deformation patterns were examined to study tensile and bond stresses (Malvar 1995). The surface of the bars were single helical wrapped, indented, double helical wrapped, or indented with coating. The bars composed of E-glass fibres with a volume fraction of 45% embedded in a vinylester or polyester resin matrix. The pullout specimens consisted of 76 mm (3") diameter by 102 mm (4") long concrete cylinders. Radial confinement pressure on the concrete cylinders was applied via a thin ring (102 mm long open end tube) surrounding the concrete cylinder. Ultimate tensile strengths varied from 448 to 710 MPa and modulus of elasticity ranged from 28 to 48 GPa for 19 mm (¾") diameter bars tested. For an equal amount of confinement pressure, the bond strengths of the GFRP rebars were 0.67 to 0.83 times the bond strength of steel rebar. For the bar with double helical wrapped surface, the concrete cylinder never split and the bond strength was almost unaffected by confinement. For this bar, the deformations, initially glued to the bar, broke and separated from the bar during the test. For the bar with surface indentations, a decrease in indentation (1.45 mm to 0.56 mm) resulted in a decrease of bond strength of about 18% under the same confinement pressure. Also, it

was concluded that increasing confinement pressure could usually increase bond strength.

In a related study, Ehsani et al. (1997b) investigated the bond behaviour of GFRP reinforcing bars in concrete. Forty eight beam specimens and 18 pullout specimens were constructed with GFRP bars. One bar type (E-glass/polyester) with an indented surface and with three different diameters was used in the study. The tensile load was applied to the bars gradually until failure was induced. The slip between the rebar and concrete was measured. It was concluded that the ultimate bond strength decreased with larger concrete cast depth, but increased with higher concrete compressive strength and clear concrete cover. The beam specimens with a concrete cover equal to the bar diameter experienced bond splitting failure. Pullout failure and rebar fracture modes were observed when the concrete cover was equal to or larger than twice the rebar diameter. The loaded end slip and ultimate bond strength of the beam specimens were lower (about 13% lower bond strength in average) than that found from the pullout specimens.

To investigate bond stress distribution, Larralde et al. (1993) conducted pullout tests using two types of FRP bars. The first type of the bars had relatively smooth surface with small indentations. The second type had deeper indentations. The constituents of the bars were not specified in the study. The bond stress distributions were inferred from the longitudinal bar strains and from the free-end and loaded-end slips. The bond stress at the concrete-reinforcement interface at the loaded end of the bar first increased under increasing pullout force, but then dropped to zero at higher load levels indicating loss of bond at the loaded end of the bar. Also, it was suggested that a bond failure might progress with time under sustained bond stresses that are lower than the static bond strength.

Also, studies show that bond stress is a maximum at the loaded end of pullout specimens while being a minimum at the free end (Nanni et al. 1995 and Benmokrane et al. 1996). Abrishami and Mitchell (1996) predicted a ratio of 1.37 for maximum bond

stress to average bond stress using differential equation for bond and assuming a linear relation between bond stress and average slip.

Concrete pore solution could cause degradation of the constituents of GFRP bars and affect the bond strength of the bars. In accelerated tests done by Bank et al. (1998), the effect of material degradation of GFRP bars on their bond strength and bond stiffness properties was reported. Four different types of GFRP bars were used to make embedded-rod test specimens which were placed in three environments: tap water for 14 days at 80° C, tap water for 84 days at 80° C, and air at room temperature and humidity for 84 days. Pullout tests were performed on the conditioned specimens. The specimens conditioned in water for 14 and 84 days at a temperature of 80° C showed appreciable material degradation and lower bond strength when compared to identical control bars held at room temperature.

In summary, bond characteristics of GFRP bars are similar to those of CFRP bars mentioned at the end of Section 2.4.2. However, GFRP bars tend to show lower bond strengths than CFRP bars. Unlike CFRP bars, pore alkaline solution in concrete may affect the long-term bond performance of GFRP bars due to material degradation of the bars. Like CFRP bars, GFRP bars embedded in concrete may show bond failure under sustained bond stress.

2.5. Failure analysis of FRP bars

Failure analysis is an important aspect of the application of materials in engineering design. It helps engineers to have a better understanding of the material behaviour and thereby avoid catastrophic failures in the future. A well-established, systematic methodology for failure analysis of metals has been developed (ASM 1986) which can be used as a guideline for studying other materials; however, the specific stages of analysis may vary with the particular material and the specific type of failure being considered. The general method for failure analysis of composites is therefore similar to that of other engineering materials, although the types of failures and the features that distinguish failure mechanisms can be quite different.

In general, an accumulation of different types of internal damage leads to failure of fibre reinforced composites (Gdoutos 2000). Fibre breaking, matrix cracking, and interface debonding define the failure mechanisms of these materials on the micro-mechanical scale. Also, fibre and matrix degradation (corrosion) due to exposure of the composite to harsh environments followed by aforementioned failure mechanisms could lead to the failure of the composite when the composite is under load (stress corrosion). The sequence and interaction of the failure mechanisms depend on the type of loading, type of the surrounding environment, and the properties of the constituents, i.e. fibre, matrix, and interface. For example, the polymer resins used in making FRP bars tend to creep under stress; therefore, bond degradation between the FRP bars and concrete under sustained loads could be a problem as a result of creep of the resin under existing bond stress. Macroscopic fracture shortly before catastrophic failure occurs following the growth of the internal damage. A study of the progressive degradation of the material, particularly the sequence of growth for the internal damage, is very important in understanding failure.

This section will cover the results reported in the literature related to the failure analysis of long fibre reinforced polymer bars under tensile loading in different environments. Scanning electron microscopy (SEM) was found to be a common method observing and analyzing failures at the micro-mechanical scale.

As previously discussed in Section 2.2.3.2, the tensile strength of glass fibre decreases, in part, due to the reduction of the cross-section of the fibre as a result of hydroxylation and dissolution, and notching of the glass in the cement paste. Figure 2.4 shows a SEM image of the surface of an E-glass fibre taken out of a glass fibre reinforced cement paste. Similar results were observed when the E-glass fibres were exposed to saturated calcium hydroxide solution (Figure 2.5).

Sen et al. (1993b) exposed prestressed concrete beams (uncracked and cracked) to water. Each beam was put in 15% sodium chloride solution at an angle such that it had dry and wet portions near the ends and a splash zone at the middle. One 9.5 mm diameter strand consisting of seven rods was used in each beam. Each rod had a

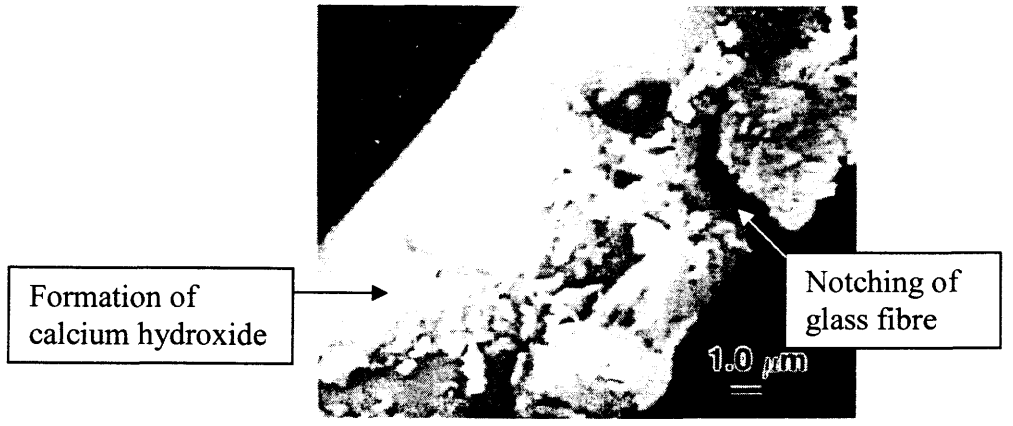

Figure 2.4. The surface of E-glass fibre removed from a cement paste matrix after aging for two months in water at 20 °C, showing severe corrosion (after Bentur and Mindess 1990).

diameter of 3 mm and was made of S-2 glass fibres and an epoxy matrix. The prestressing stress was 38% of the ultimate tensile strength of the strand. A SEM examination of the cross-section of the strand taken out of an uncracked beam was conducted after 18 months of exposure to wet/dry cycles. For the sample taken from the wet location, there was considerable evidence of deterioration and degradation, particularly in those fibres located close to the concrete interface (Figure 2.6c). The extent of degradation for this sample appeared to be greater in comparison to the sample taken from the splash zone (Figure 2.6b).

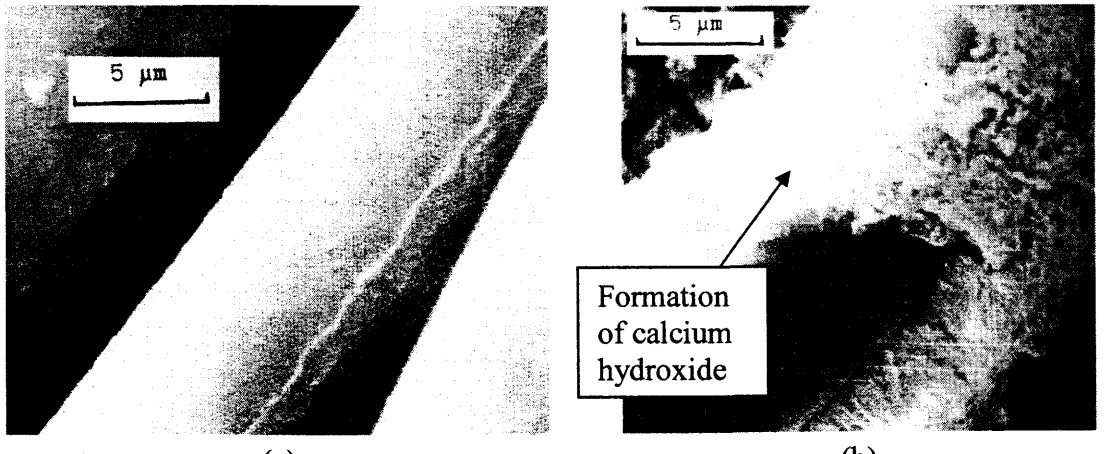

(a) (b)

Figure 2.5. SEM images of E-glass fibre filaments: (a) before dissolution and (b) after dissolution in saturated calcium hydroxide solution at 25°C for 150 days (after Al Cheikh and Murat 1988).

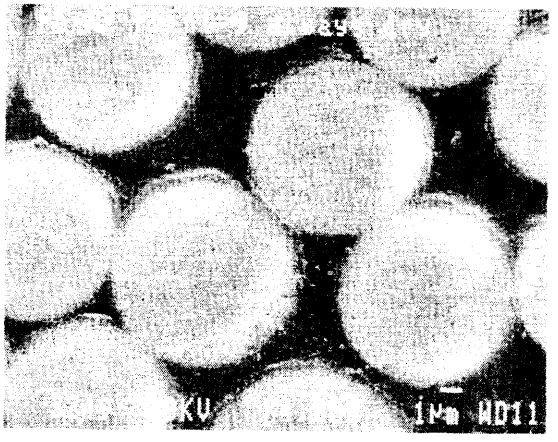

(a) Always dry specimen

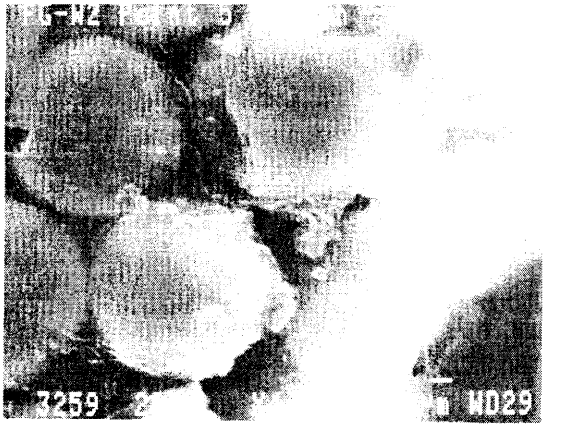

(b) Splash zone specimen near concrete interface

(c) Submerged specimen near concrete interface

Figure 2.6. SEM images of the cross-section of the strand taken out of uncracked beams after 18 months exposure to wet/dry cycles (after Sen et al. 1993b).

Using an electron microprobe analyzer, Katsuki and Uomoto (1995) showed that alkali could penetrate into a rod containing fibres with a poor alkali resistant. It was found that alkaline solution (1.0 mole/l aqueous NaOH) could penetrate through the GFRP rods with S-glass fibres and vinyl matrix. Although the AFRP and CFRP rods tested had the same matrix and were both immersed in 2.0 mole/l aqueous NaOH, alkali could not penetrate into these rods. Figure 2.7 shows the nature of fracturing in GFRP rod tested after being immersed in 1.0 mole/l aqueous NaOH at 40 °C for 90 days. It should be noted that the thickness of the resin, which protected the fibres, was very thin (less than several mm) and the alkaline solution penetrated to resin layer in all three FRP rods. However, the solution could not go through aramid and carbon fibres while it could penetrate to glass fibres. As a result, the tensile strength of GFRP rods was

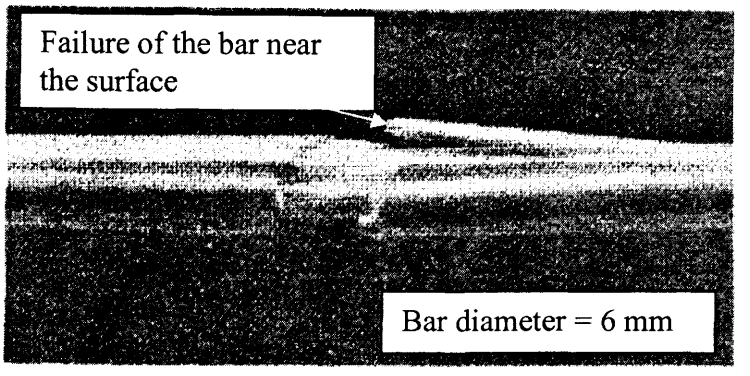

Figure 2.7. Failure mode ("necking" failure) of a tested GFRP rod exposed to alkaline solution (after Katsuki and Uomoto 1995).

decreased with time when immersed in aqueous NaOH, whereas that of AFRP and CFRP rods was not decreased. It was observed that the failure pattern near the surface differed from that near the inner part of the GFRP rod. Breaking near the surface occurred at a lower load, while breakage of the inner part occurred only at the failure.

Bank et al. (1998) also studied the degradation of two types of GFRP bars using SEM. The bars were embedded in concrete cylinders and immersed in a tank of tap water for 84 days at 80 °C. The SEM samples were obtained by cutting concrete cylinders (with the embedded rods) with a conventional diamond-blade concrete cut-off saw. Figure 2.8 shows the micrograph of the first bar that had a smooth surface. A portion of the surface of the bar at the location of a "blister" spot on the bar surface is shown in Figure 2.8a. There appears to be localized deterioration of the bar surface only in the blister area. The remainder of the bar, even at the surface, appears undamaged. The locations of the large blisters on the bar surface were found to coincide with the locations of micro cavities in the concrete at the bar interface. A magnified view of the bar close to a blister location (Figure 2.8b) shows the development of a radial crack into the interior of the bar. The glass fibres show some signs of erosion. The reason could be that the micro-cavities in the concrete were filled with highly alkaline solution during the submerged conditioning. The alkaline solution affects the nearby matrix and fibres, causing the formation of blisters and the degradation of the adjacent fibres and resin.

The second bar had a deformed surface, with helical roving strands wrapped around the bar. The bar showed a loss of surface sheen as well as whitening. As shown

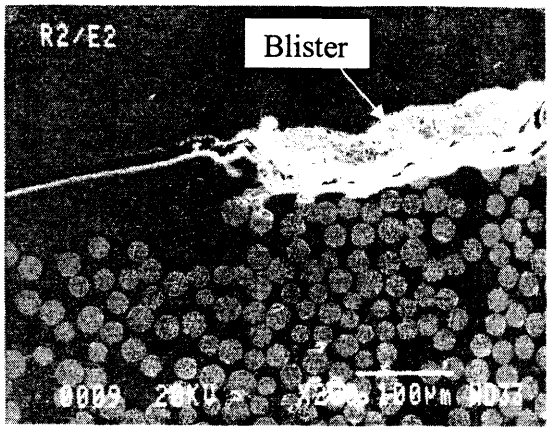

(a) Micrograph of the cross-section of the bar showing a deteriorated "blister" region on the circumference of the bar.

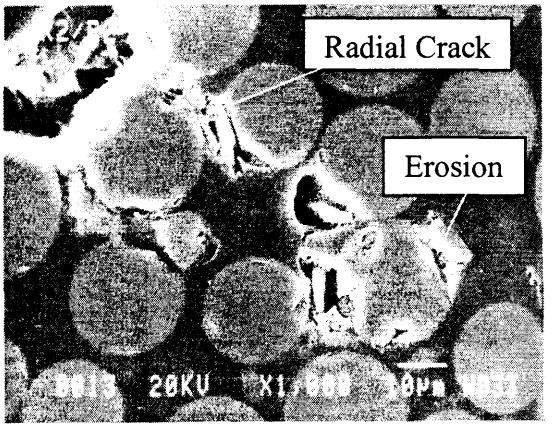

(b) Magnified view of the cross-section of the bar showing degradation of the polymer matrix and damage to the glass fibres.

Figure 2.8. SEM images of the GFRP smooth bar (after Bank et al. 1998).

in Figure 2.9a, the fibres in the helical wrapping can be seen in the outer layer, with the unidirectional fibres of the inner core visible alongside this layer. A circumferential crack between the helical fibres and the core fibres can be seen. While the large crevices appeared to be due to poor processing (as do the numerous voids in the interior of the bar), the cracking between the crevices was believed to be due to penetration of the pore alkaline solution into the bar (Figure 2.9b).

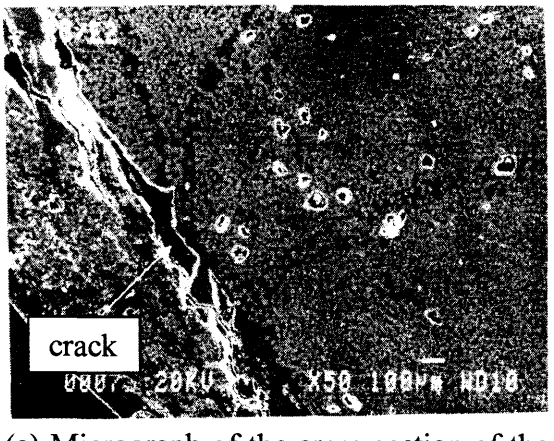

(a) Micrograph of the cross-section of the bar showing deterioration in the helical fibre layer and the interface between this layer and the interior core of the bar.

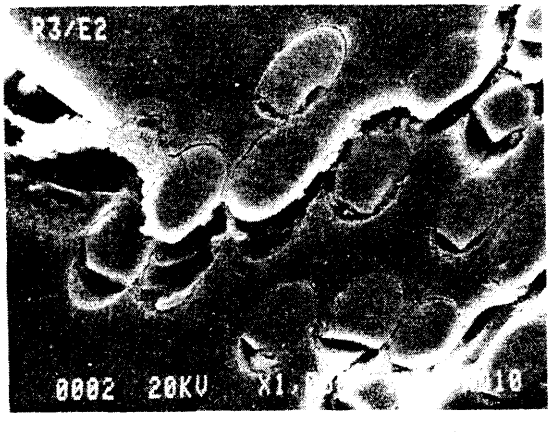

(b) Micrograph of the bar showing degradation of the polymer matrix and damage to the glass fibres.

Figure 2.9. SEM images of the GFRP deformed bar (after Bank et al. 1998).

In summary, accelerated tests on GFRP bars embedded in concrete showed degradation of the constituent materials and the interface between the fibres and matrix resin. Notching of glass fibres occurred if they were in direct contact with concrete. Sodium chloride solution had damaging effects on the glass fibres used in GFRP bars under sustained loads. Also, alkaline solutions were found to penetrate through GFRP bars with thin resin layers at the surface of the bars and cause tensile failure of the outer layer of the bars at much lower stresses than tensile strength of the bars due to deterioration of the interface between outer resin layer and the fibres. Degradation of fibre matrix interface also could result in significant bond strength reduction of GFRP bars embedded in concrete. Concrete alkaline pore solution damaged both the interface and fibres and caused bond degradation between the bars and the concrete when the pullout specimens were submerged in water at high temperature.

2.6. Summary

The studies on FRP bars and their constituents showed that polymers exhibit large creep strains at low stress levels and at room temperature. Glass fibres lose their tensile strength when exposed to water or alkaline and show low resistance to water and alkaline environments. Glass fibres are also susceptible to both stress rupture and stress corrosion.

CFRP bars exhibit good creep behaviour under sustained loads, even when exposed to aggressive environments. They are less prone to water, salt, and alkaline solution, and show good performance at higher temperatures. However, higher temperatures seem to have major effects on GFRP bars exposed to harsh environments. GFRP bars display failure by creep rupture especially at high stress levels and at high temperatures. The bars also exhibit tensile strength reduction when exposed to salt and alkaline solutions especially under sustained tensile loads.

Bond strength of CFRP and GFRP bars depends on configuration of the bars as well as type of the resin used in the bars. Depending on the surface configuration, friction or mechanical interaction is the dominant mechanism in deformed FRP bars

whereas adhesion is the main bond mechanism in smooth bars. GFRP bars tend to have lower bond strengths than CFRP bars.

Although short term bond properties of FRP bars are addressed in the literature to a large extent, more research is needed on long term bond properties of the bars. Since FRP bars are covered with resins, which show creep behaviour under sustained loads, the bars embedded in concrete may show bond failure under constant bond stress. In addition, pore alkaline solution in concrete may affect the long-term bond performance of GFRP bars due to material degradation of the bars.

Chapter 3

Experimental program

3.1. Introduction

An experimental program was undertaken to examine the long term bond behaviour between fibre reinforced polymer (FRP) bars and concrete. The program was conducted in two phases. In Phase I, two types of carbon FRP bars (CFRP), one type of glass FRP bar (GFRP), and conventional steel rebar were used to make pullout specimens. Sustained loads of different magnitudes were applied to the specimens at room temperature in air. In Phase II, three different types of GFRP bars were employed in pullout specimens that were tested under two different sustained load levels in three different environments at room temperature, where the specimens were either submerged in water or an alkaline solution, or were exposed to air.

Components of the experimental program included the design and manufacture of the pullout specimens, the static testing, the design and calibration of the loading apparatus, adaptation of instrumentation, and the long term pullout testing including load maintenance and measurement of bond slip. Image analysis, scanning electron microscopy, and electron microprobe analyzing techniques were applied to examine the materials and tested specimens. A detailed description of the pullout specimens, material properties, and test set-up as well as the testing procedure for each phase of the program is presented in this chapter.

3.2. Phase I

3.2.1. Introduction

Phase I of the experimental program was conducted to examine the bond behaviour of two types of CFRP bars and one type of GFRP bar (as well as conventional steel rebar) embedded in concrete under sustained loads in room conditions. The program began with preliminary static pullout tests to provide information for designing the pullout specimens to be used in the long term tests. Appropriate supports were made to hold the bars in place while casting the pullout specimens. Static pullout tests were performed to obtain the bond strength of the bars. A loading apparatus was designed, fabricated, and tested in order to perform the long term tests. Available instrumentation was evaluated for the static and the long term bond tests. Further detail is provided in the following sections.

3.2.2. Preliminary tests

As described in Section 2.4.1, splitting of the concrete cover often defines bond failure in structural concrete members where inadequate development length is provided for the reinforcement. However, since this study was focused on evaluating bond resistance between FRP bars and concrete, the test specimens were designed such that pullout failure, rather than concrete splitting, would govern in order to observe changes in bond characteristics over time. A bar pullout failure provides information on the highest bond strength that can be obtained.

In a review of the literature, the concentric pullout test was found to be the most popular test method adopted by FRP concrete researchers (Nanni et al. 1995b). The test has the advantage of simplicity, but presents two disadvantages: 1) the concrete is subjected to compression at the loaded end; and 2) the concrete surrounding the bar tends to split. The compression at the loaded end of pullout specimens prevents transverse cracking of concrete and results in a higher bond strength than that of beam specimens where transverse cracking of concrete could occur (Section 2.4.1). As mentioned before, the test specimens were designed such that concrete splitting would

not occur. In spite of the two disadvantages, it was decided to use pullout specimens for the present study since they were straightforward to fabricate and handle.

Preliminary static tests were performed to determine a suitable design for pullout specimens that would ensure a pullout failure, rather than splitting bond failure, based on the performance using a No. 10 conventional steel reinforcing bar. The FRP bars that were to be studied for long term performance also had diameters in this size range. Since studies by previous researchers had indicated that bond strength (stress) for FRP bars was similar to or lower than the bond strength found with conventional steel reinforcement (Jerrett and Ahmad 1995, Chaallal and Benmokrane 1993), using steel reinforcement was deemed appropriate for sizing the test specimens.

Initially, the steel bars were embedded into 100 mm diameter by either 150 or 200 mm long concrete cylinders. The specimens were then tested statically using a universal testing machine model 60HVL with a capacity of 250 kN manufactured by Baldwin corporation. All specimens failed by splitting of the concrete, indicating that the cover provided by the 100 mm diameter concrete cylinder did not confine the steel bar sufficiently to achieve a pullout failure even when a relatively strong concrete with a compressive strength of 35 MPa was used. Splitting failures were also obtained when the cover on the reinforcing bars was increased by using 150 mm diameter cylinders with lengths of 100, 150, and 200 millimetres for the pullout specimens. To prevent such splitting failures, steel spirals were then placed around the rebar in 150 mm diameter by 100 mm long specimens. Plain bar with a diameter of 6 mm diameter was used to make spirals with a 30 mm pitch and 90 mm outside diameter. Test pullout specimens with the spiral confinement exhibited pullout failures with a minimum ultimate load of 68 kN. Due to some surface cracking in the concrete, it was decided to increase confinement by using 8 mm diameter bars for spirals in subsequent specimens. Details of the pullout specimens used in Phase I of the program are given in Section 3.2.4.

3.2.3. Apparatus

3.2.3.1. Introduction

The loading unit was designed to test the pullout specimens under sustained loads over time. The unit could carry a design load of 50 kN, which was more than the yield load of No. 10 steel rebar (48 kN) used in the pullout specimens made for the preliminary tests. The unit had a kind of load cell to measure and to monitor the applied load on the pullout specimen over time. Also, it was necessary that the load could be adjusted easily if needed. Furthermore, the loading system of the unit had the advantage of holding most of the load if slip of reinforcing bar occurred in the pullout specimen. Based on these requirements, a demonstration loading frame was designed and built in order to evaluate its ability to apply relatively uniform sustained loads to the pullout specimens. Figure 3.1 shows a view of the test apparatus with pullout specimen in place.

An aluminum rod with a diameter of 16 mm was used to serve as a load cell. Six demec gauge points were impressed into the rod to allow measurement of the elongation that was, in turn, proportional to the load applied to the pullout specimen. Tightening the nut on the aluminum rod was used to induce a tensile load into the aluminum rod. The 2:1 ratio of lever arms on either side of the pinned support resulted in a load in the test specimen that was double the force in the aluminum rod. The steel compression spring was incorporated into the loading frame to help maintain a more uniform tension load in the aluminum rod over a range of slip deformations that could occur in the pullout specimen over time.

As shown in Figure 3.1, half of a 19 mm diameter plain bar was welded to the base plate just below the test (upper) end of the specimen. This allowed for the rotation of the top beam while applying a concentric load vertically to the specimen. The half bar could rotate inside the groove provided on the bottom of the bearing plate at the test end of the specimen. Details of the pullout specimen will be described later in Section 3.2.4.

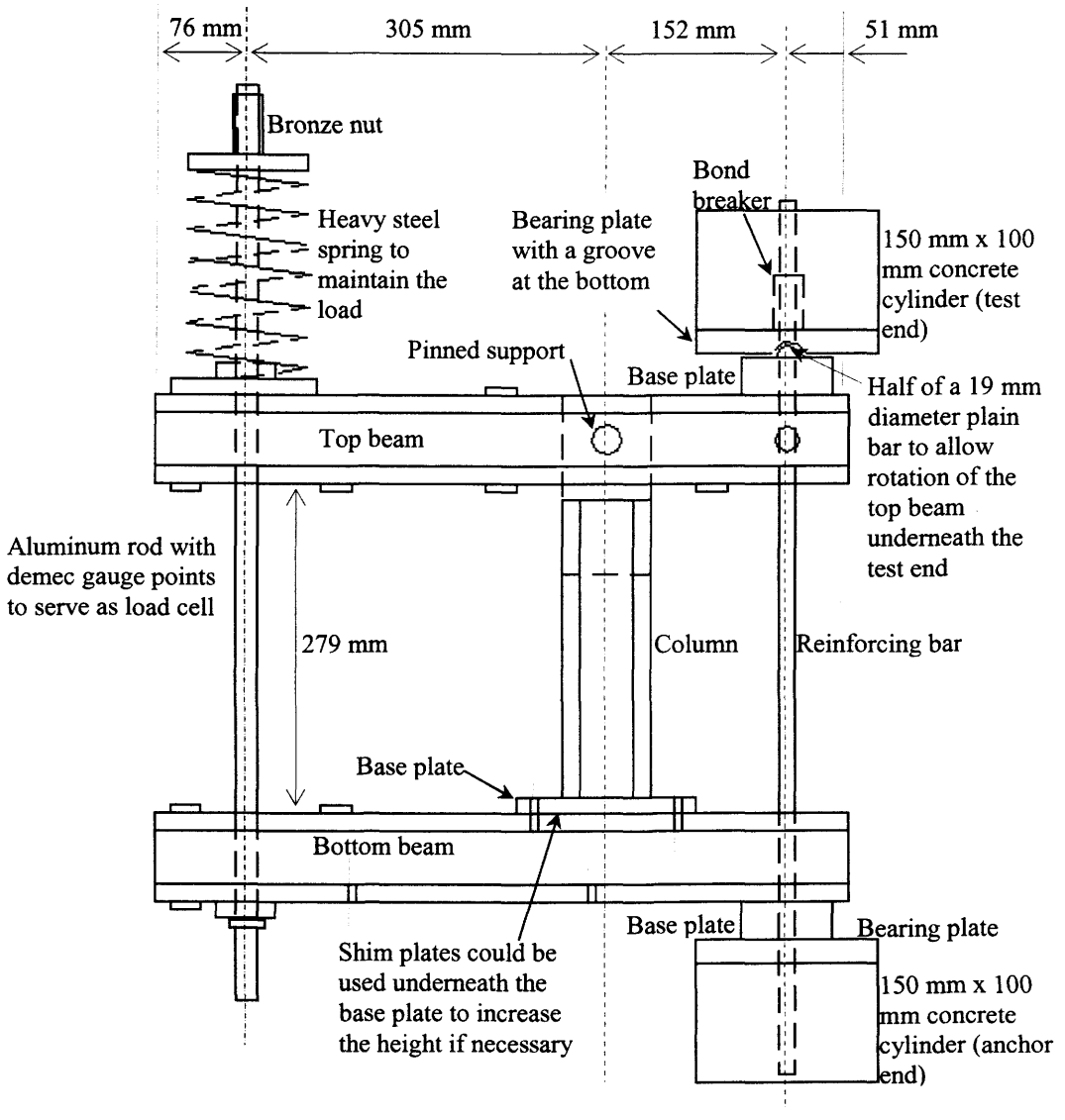

Figure 3.1. Details of loading frame with pullout specimen in place.

3.2.3.2. Aluminum rod

A tension test was performed on a sample of the aluminum rod to obtain the maximum elastic load that could be carried by the rod. A Type 60-T-E-897 testing machine with a capacity of 267 kN (60000 lbs) manufactured by Baldwin corporation was used. The aluminum rod was set in the testing machine using nuts and bearing plates at the threaded ends. The load was read off the load scale of the machine. At each load increment, the elongation of the rod was measured over three 200 mm gauge lengths marked by six demec gauge points on the rod using a 200 mm gauge with digital display (type IDB-112ME manufactured by Mitutoyo) with an accuracy of

±0.005 mm. Three pairs of demec points at each end of the 200 mm gauge length were distributed circumferentially at equal distances around the perimeter of rod surface. The average of the elongation values from the three pairs was then used to plot a load-elongation curve (Figure 3.2).

As shown, maximum elastic load was found to be approximately 56 kN. The design load for the loading frame was 50 kN in the specimen and a corresponding 25 kN in the aluminum rod to ensure that the aluminum rod would behave elastically over the range of sustained loads applied to the pullout specimens.

3.2.3.3. Steel spring

A steel spring was incorporated in the loading frame to help maintain a uniform tensile load, and to prevent total loss of the applied load when varying slip deformations occurred in the pullout specimen over time. Two types of steel compression springs were available in the laboratory to be used in the apparatus.

To compare the springs, compression tests were performed on the springs using type 112-TP-95-L testing machine with a capacity of 1334 kN (300 kips) manufactured by Baldwin Corporation. Two dial gauges were put between the loading plates of the testing machine at two opposite sides of the spring. The change in dial gauge readings

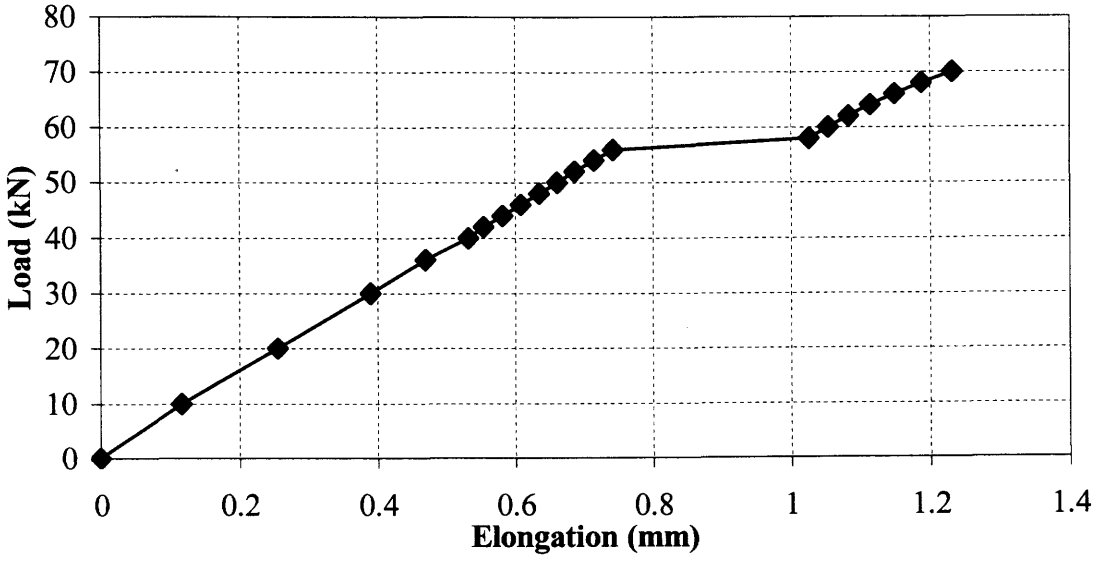

Figure 3.2. Load-elongation curve for aluminum rod used in apparatus.

would indicate the deformation of the spring at each load increment. The average value of the deformation obtained from the two dial gauges was used.

The test results are displayed in Figure 3.3. Both springs exhibited nearly elastic behaviour although the spring factors (load to deflection ratio) were slightly different. Different spring factors did not cause any problems since the load frame was calibrated later regardless of the type of spring used. Therefore, it was determined that either of the two types of steel springs could be used in the loading frame.

3.2.3.4. Calibration of tension link

The loading frame was calibrated in order to apply the desired load to the pullout specimen. A 42 kN (9500 lbs) capacity tension link (model STL-4.75 manufactured by Intertechnology Inc.) was used to calibrate the load frame. The tension link was calibrated itself before being used for calibration of the load frame. The tension link was calibrated in a testing machine (type 60-T-E-897 testing machine with a capacity of 267 kN (60000 lbs) manufactured by Baldwin corporation). Load versus tension link reading data (measured by strain indicator model P-3500 manufactured by Intertechnology Inc.) was plotted (Figure 3.4). Using best-fit line resulted in R^2 value of 1.00 indicating that the behaviour of tension link was linear. Therefore, the slope of the

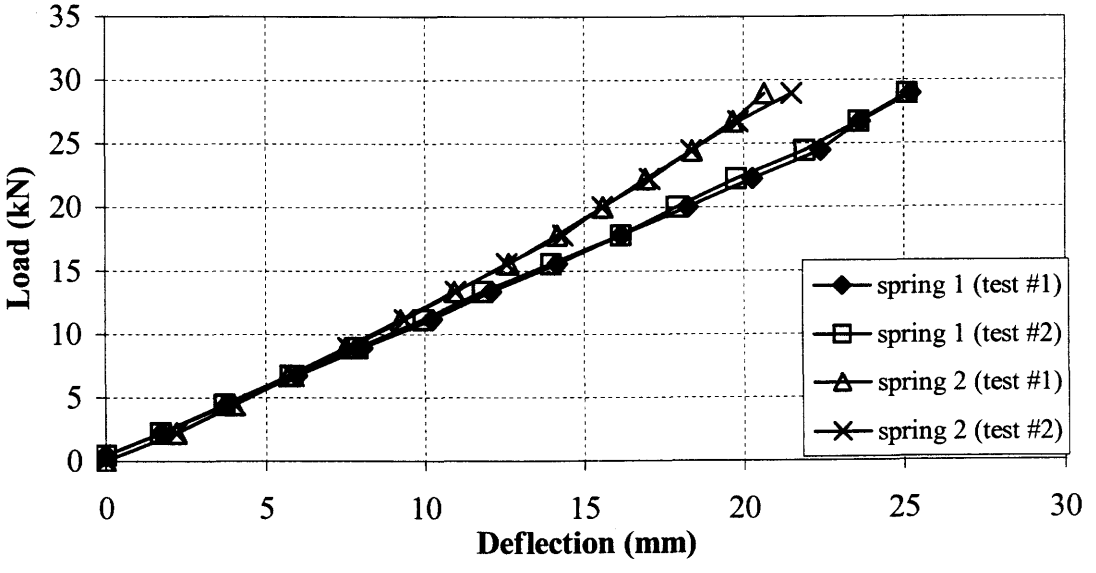

Figure 3.3. Load-deformation curves for steel springs.

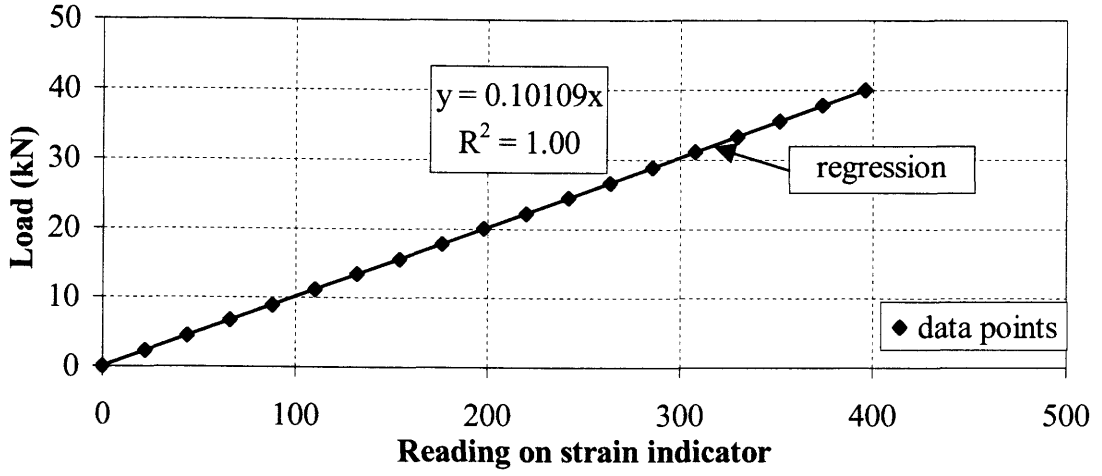

Figure 3.4. Calibration curve for the tension link.

best-fit line in the figure (0.10109 kN/reading of tension link) indicated the calibration factor for the tension link. This value was subsequently used in the calibration of the apparatus.

3.2.3.5. Calibration of apparatus

As mentioned before, the aluminum rod was used in the apparatus to serve as a load cell. The relationship between the load in the aluminum rod and the load in the specimen was required in order to apply the desired load to the pullout specimen. To have this relationship (calibration curve), the calibrated tension link was used in place of the specimen in the apparatus. Using a connector (Figure 3.5b) and two high strength pins, the tension link was connected to the top beam of the apparatus. It was then joined to the bottom beam using a high strength pin and another connector (Figure 3.5a). This connector was made such that it could be placed around the bottom beam in the apparatus and could be attached to the tension link by a high strength pin. The set-up for calibration of the apparatus is shown in Figure 3.6. Tensile load was applied to the aluminum rod and the tension link by tightening the nut on the rod. The elongation of the aluminum rod was measured over the three-200 mm gauge lengths at each load increment.

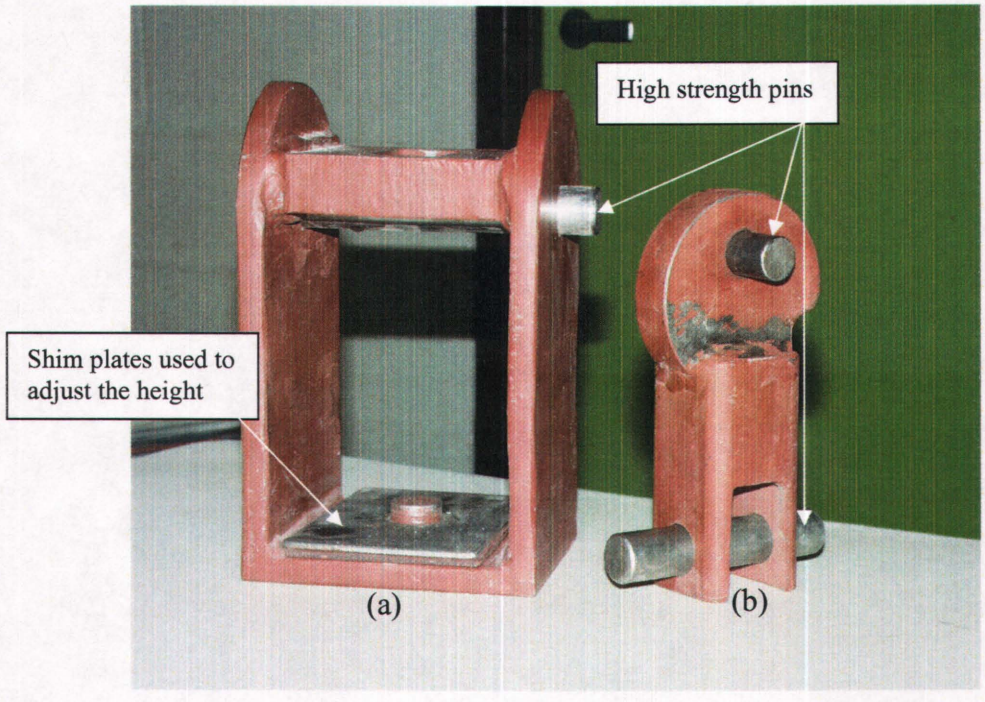

Figure 3.5. Photo of connectors made to attach tension link to the apparatus.

The average reading obtained from the aluminum rod (elongation) versus the reading from the tension link (load) is presented in Figure 3.7. It was apparent that the curve was not linear for data points with readings in the tension link of less than 50 (5

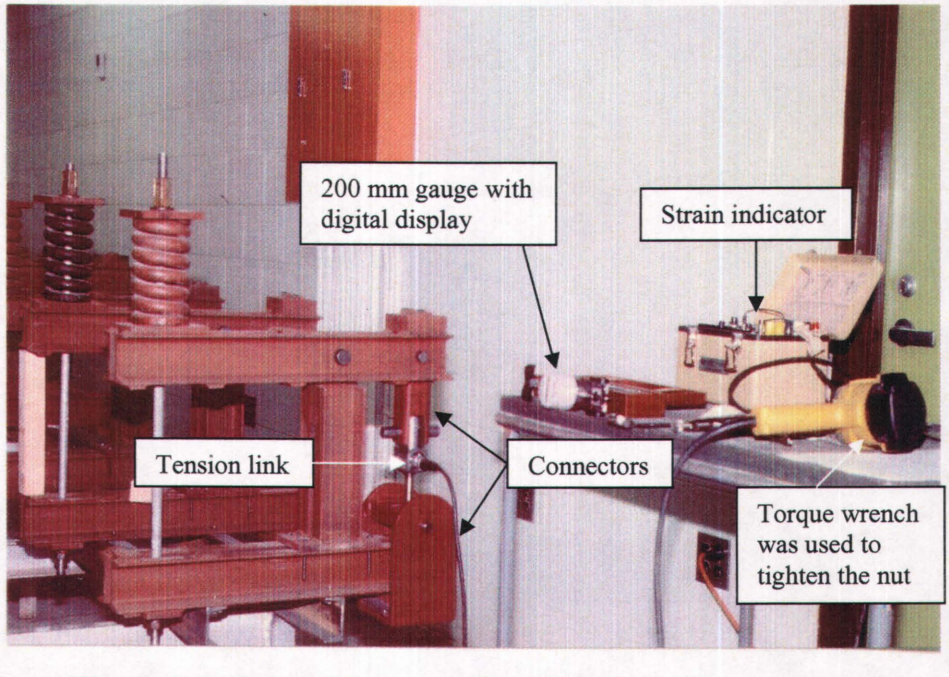

Figure 3.6. Photo of the set-up for calibration of the apparatus.

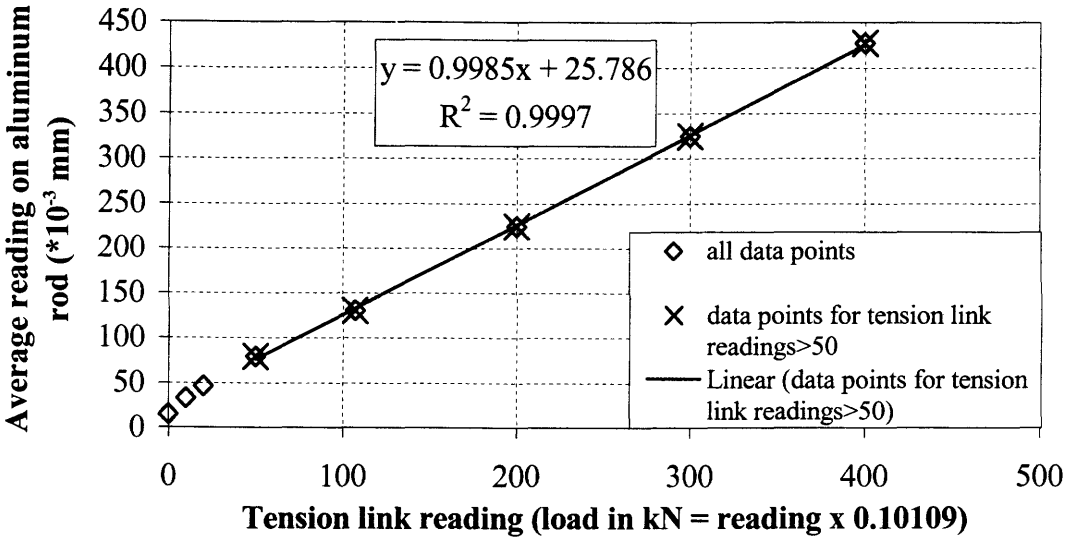

Figure 3.7. Calibration curve for the apparatus.

kN load). An investigation indicated that a small lateral force was applied to the 200 mm gauge to seat the gauge in demec points and to keep the gauge in place when taking readings on the rod. The small lateral force was thought to cause a slight bending of the rod when the applied tensile load in the rod was low. As shown in Figure 3.7, when the reading on tension link (load) was less than 50 (5 kN load), the slight bending of the rod affected the readings and caused the non-linearity in the curve. However at higher readings of tension link (loads), tensile force in the rod restrained bending, resulting in more accurate readings being obtained from the rod.

Also, further investigation revealed that if the aluminum rod was not seated in place properly before applying the load, bending of the rod occurred due to eccentric load on ends of the rod at the initial stages of loading. At higher loads, the rod was fully seated in an aligned position and exhibited less bending. In addition, the weight of the connector at the bottom end of the tension link did not cause any tension in the rod before loading. However, that weight induced an insignificant tension in the tension link.

To eliminate the errors mentioned above, the best-fit line for the data points with tension link readings greater than 50 (5 kN load) was found (Figure 3.7). The slope of the line (0.9985) defined the relation between the load in the aluminum rod and the load

in the tension link. Repeating the calibration procedure indicated that the slope of the best-fit line (for tension link readings greater than 50 or load greater than 5 kN) was almost the same (0.983≈0.9985). However, the y-intercept (37.013), obtained from the best-fit line in the second calibration, was different than the value (25.786) shown in the best-fit line equation in Figure 3.7. The y-intercept was corrected by using the measurements on the aluminum rod when it was sitting on a flat surface. An average value of 17 was obtained. It should be noted that the gauge, used for taking readings on the aluminum rod, was zeroed out on a reference steel bar with two demec gauge points made at a distance of 200 mm before taking readings on the aluminum rod every time. Therefore, the corrected equation for the line was taken to be y=0.9985x+17 and was used to apply the desired load (more than 5 kN) to the pullout specimens. However, if the desired load in the specimen was less than 5 kN, the obtained equation could not be used. Since the accuracy of the 200 mm gauge, used to measure the elongation of the aluminum rod, was ±0.005 mm, the accuracy of the applied loads to the specimens was estimated to be ±0.5 kN (0.005*1000*0.10109/0.9985=0.5).

3.2.3.6. Evaluation of the loading frame

Since a total of 36 loading frames were required to perform long term tests, the demonstration test apparatus and the instrumentation were evaluated before more load frames were fabricated. To evaluate the test apparatus and the instrumentation, three sample pullout specimens were made based on the information obtained from the initial preliminary tests.

A No. 10 steel rebar was embedded in a 150 mm diameter x 75 mm long cylinder at one end (test cylinder) and a 150 mm x 150 mm cylinder at the other end (anchor cylinder). Cylinders were reinforced with 8 mm diameter steel spirals that featured a 30 mm pitch and 90 mm outside diameter. As it was difficult to grip FRP bars for testing purposes, a longer embedment length (150 mm) in a concrete cylinder was used as an anchor at the grip end. This same detail was utilized for the sizing of the pullout specimens, as well as for the reinforcing steel bars used in control specimens in the first test series.

One of the sample pullout specimens was put in the loading frame and an arbitrary load of 40 kN was applied to the specimen. Using the calibration equations of the apparatus and the tension link, it was determined that the average reading on the aluminum rod should be 412 to induce a load of 40 kN in the specimen. It should be noted that load application to a desired level was a tedious incremental process. Three manually measured gauge readings over the 200 mm demec gauge lengths were required to estimate the load applied to the test specimen. Care had to be exercised to prevent exceeding the target load, so the load had to be gradually increased and measured at each stage.

Also, it was realized that applying the load lowered the top beam end on the aluminum rod side since the beam rotated around the pinned support. At some point during loading procedure, the rotation of the top beam caused bending of the aluminum rod as it was pushed against the central hole in the bottom plate below the spring. To prevent this, the centre hole in the base plate was modified to an oval shape, allowing movement of the rod inside the hole during loading. In addition, the modification allowed placing the top beam in an inclined position initially, with the beam end on the rod side initially placed higher (about 13 mm above horizontal position). This way, the top beam was close to a horizontal position after loading the specimen.

Other problems were also encountered when the test frame was being evaluated. Slip of the bar in the pullout specimen raised the end of the top beam on the specimen side and lowered the end of the beam on the aluminum rod side, causing a drop in the applied load. To adjust the load, the nut was retightened so that the initial applied load was maintained. After several adjustments of the load, the nut could not be tightened anymore since it had reached to the end of the available threads on the top end of the aluminum rod. Also, the aluminum rod was starting to bend, pushing against the base plate below the steel spring inside the oval shape hole.

To solve the problems mentioned above, the top beam and the column were lifted together to increase the column height. First, a jacking system was used between the two ends of the specimen to push the ends apart and to maintain the applied load in

the specimen while the nut on the aluminum rod was loosened. Also, a support was put under the specimen to carry the weight of the specimen and the jacking system. Then, the bolts on the column base plate were released and the top beam and the column were lifted together by using a jacking system under the top beam. Shim plates with an appropriate thickness were placed under the column base plate to adjust the column height such that the top beam was in an inclined position (higher at the rod end) before tightening the nut on the aluminum rod. After removing the jacking system used under the top beam, the bolts on the column base plate were tightened. The nut on the aluminum rod was also tightened to apply the desired load to the specimen before releasing the jacking system used between the two ends of the specimen. Care was taken to ensure that the aluminum rod was not bent. At this point, the nut on the aluminum rod could now be tightened further to adjust the load if necessary.

In addition, the shim plates with different thickness were used so that the height of the column could be adjusted to accommodate slightly different pullout specimen lengths before applying load initially. The shim plates with pre-fabricated grooves could be fit under the column base plate from both sides.

As mentioned previously, the calibrated demec gauge points on the aluminum rod were monitored over time for the required tension. The tension was maintained at the target load by retightening the nut on the aluminum rod whenever necessary.

The free end and loaded end slips were measured using a 600 mm height gauge with an accuracy of ±0.05 mm (model 192-618 manufactured by Mitutoyo). Figure 3.8 displays a photo of the height gauge in position for slip measurement. An aluminum plate was made such that it could be fitted around the top flange of the bottom beam in the loading frame. The height gauge was seated on the aluminum plate and held in position by a clamp.

To provide a smooth surface on top of the test end concrete cylinder, a small bronze plate was glued on top of the concrete and used as reference point to measure the free end slip (Figure 3.9a). The level of the top of the bar was then measured with respect to the reference point (Figure 3.9b). Free end slip was calculated by subtracting

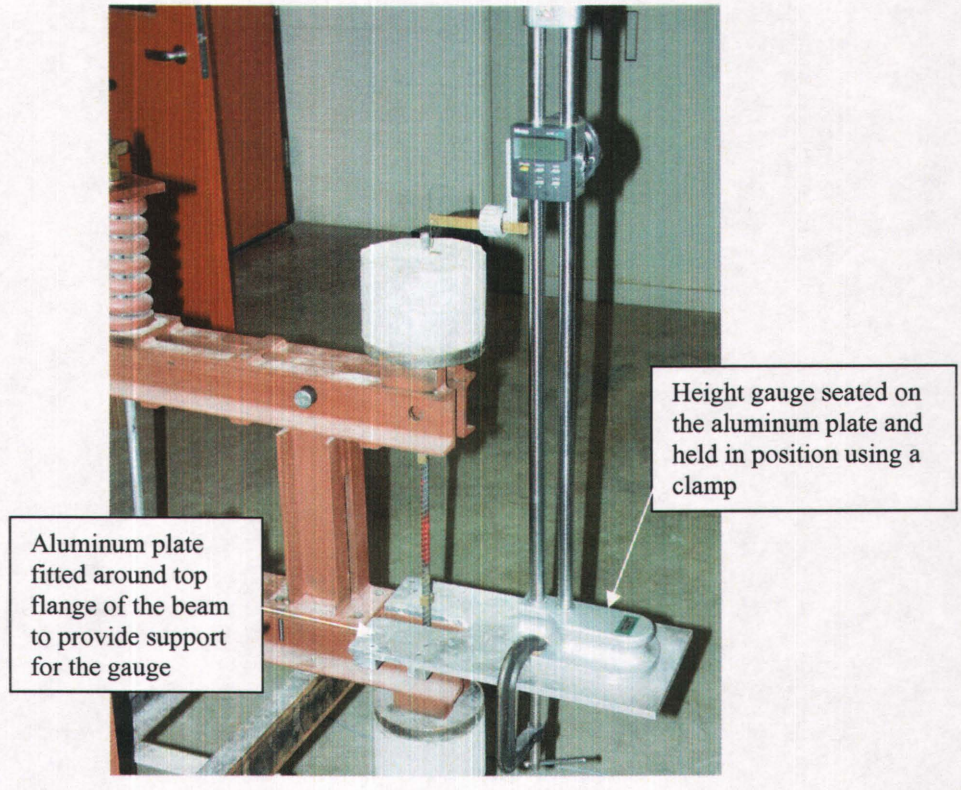

Figure 3.8. Photo of the 600 mm high height gauge.

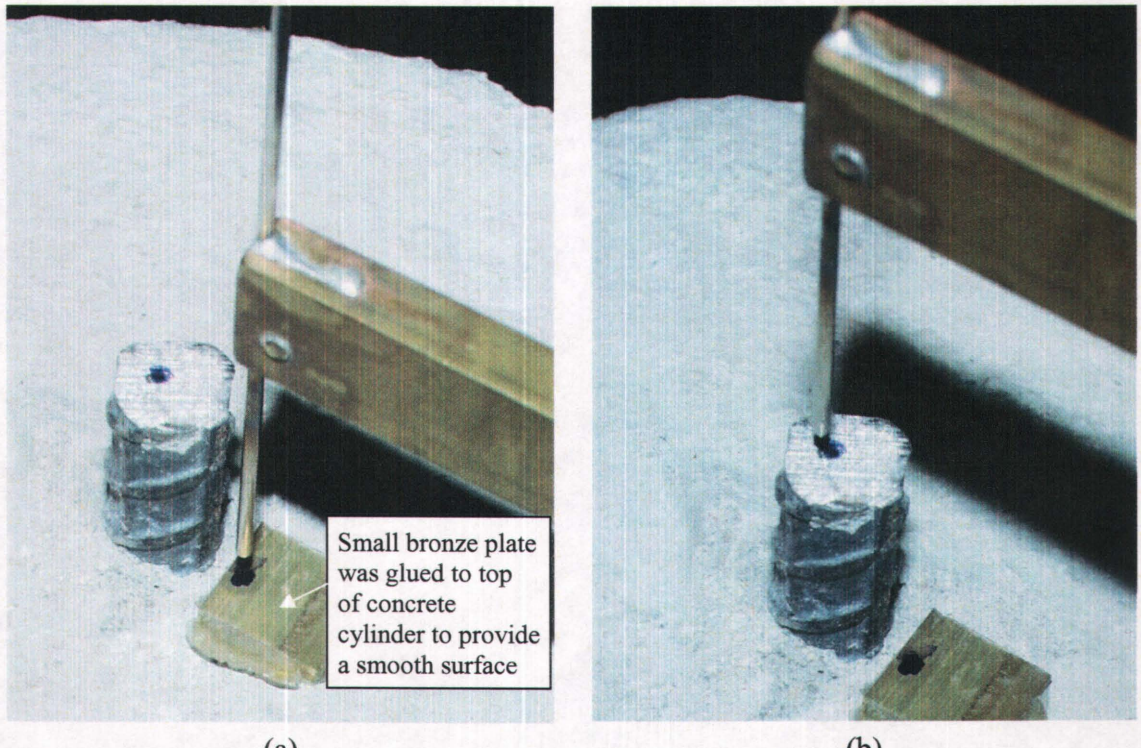

(a) (b)

Figure 3.9. Free end slip measurement: (a) gauge was set to zero at the reference point on the small plate, and (b) level of the top of the bar was measured.

readings at two consequent time intervals. The reference point for the measurement of the loaded end slip was the bottom of the bearing plate provided under the concrete cylinder (Figure 3.10a). The level of the bar at the loaded end was then measured to a short angle glued to the bar (Figure 3.10b). The difference between the readings at two consequent time intervals was the loaded end slip.

After verifying that the load frame and the instrumentation worked properly, 35 more loading frames were built (by Venables Machine Works Ltd., Saskatoon), assembled, and calibrated.

3.2.4. Pullout specimens

Pullout specimens used in static and long term tests were made based on information obtained from preliminary tests and also from static testing of two out of three sample pullout specimens mentioned in the previous section. The latter static tests resulted in pullout failures at an average ultimate load of 64 kN. As this load was much higher than the yield load of the steel rebar (48 kN), a reduced embedment length of 50

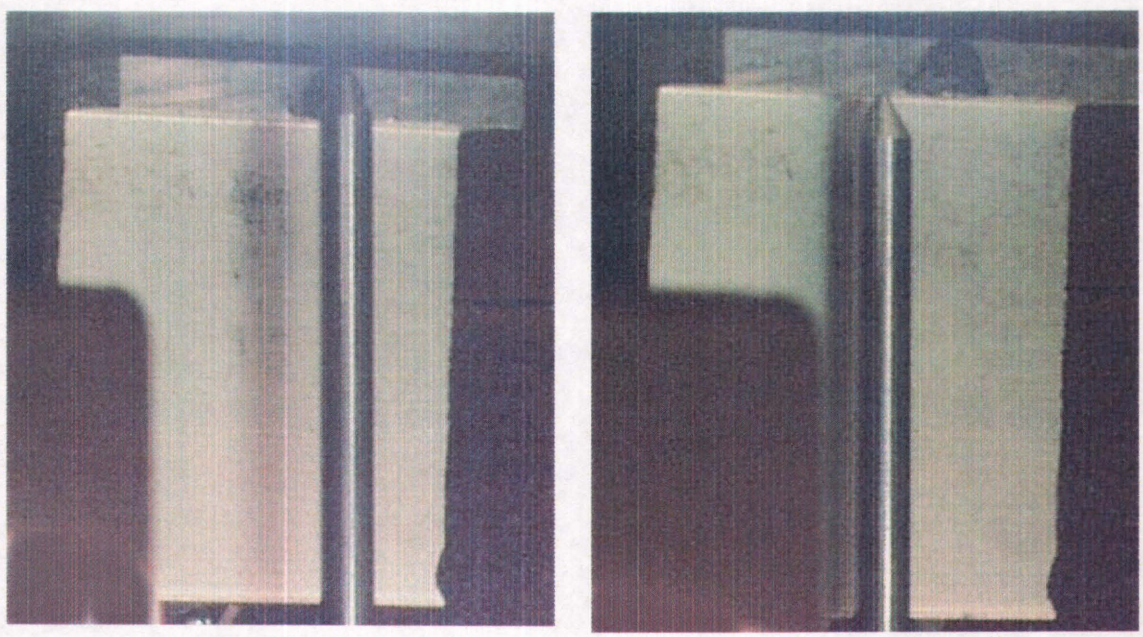

(a) (b)

Figure 3.10. Loaded end slip measurement: (a) gauge was set to zero at the bottom of the bearing plate, and (b) level of the bar at the loaded end was measured to the short angle glued to the bar.

splitting (see Section 3.2.2), the cylinders were reinforced with an 8 mm diameter smooth steel bar formed into a spiral with a pitch of 30 mm and an outside diameter of 90 mm (Figure 3.11). The gaps between the bar and the bearing plates and between the bearing plates and cylinders were sealed using multi-purpose sealant in order to keep cement paste from leaking out of the cylinder.

To put the 150 mm diameter by 120 mm long cylinders at each end of reinforcing bar, a 16 mm diameter hole was drilled at the centre of the base of cylinder moulds (Figure 3.12a). Another hole (with different diameters based on the test bar diameters) was made at the centre of the 150 mm diameter x 20 mm thick bearing plates (Figure 3.12b). Three holes (6 mm diameter) were drilled 10 mm deep into the bearing plate and equally spaced around the spiral to accommodate three 6 mm diameter bars used as supports for the spiral. A side view of bearing plate with the spiral and supports in place is shown in Figure 3.12a. Also, a 3 mm deep groove (Figure 3.12b) was made on the bottom of the test end bearing plate to fit the half of a 19 mm plain bar used in the top beam of apparatus (mentioned in Section 3.2.3.1). This groove was greased to allow free rotation of the top beam of the apparatus under the test end of the specimen when load was applied to the specimen.

The test end and anchorage end of the pullout specimens were cast at different times. This required the use of two sets of plywood frames in order to keep the bars

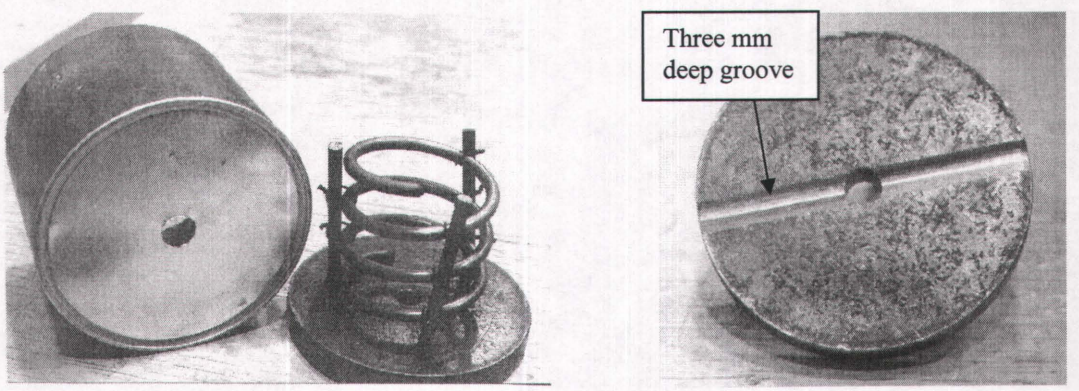

(a) Cylinder mould with a centre hole and spiral mounted on bearing plate.

(b) Groove provided on bottom of bearing plate used inside test end cylinder.

Figure 3.12. Photos showing cylinder, spiral, and bearing plate used in pullout specimens.

mm was used in the pullout specimens to ensure that a bond pullout failure would occur below the yield load of the steel bar. In addition, the pullout specimens were modified to reduce the bearing plate confinement, as the concrete cylinder would be subjected to compression at the loaded end. Details of these pullout specimens are described in this section.

A total of 48 pullout specimens were made using three different types of FRP reinforcing bars, as well as conventional reinforcing steel bars (12 for each bar type). Specifications of the bars are given in Section 3.2.5.1. For each pullout specimen, one 150 mm diameter by 120 mm long cylinder was constructed at each end of the reinforcing bar (Figure 3.11). The cylinder mould was cut to a length of 120 mm so that the resulting concrete cylinder was 100 mm high when the 20 mm thick bearing plate was placed inside the mould. Fifty millimetre long pipe insulation was used around the reinforcing bar at the loaded end of the test cylinder to serve as a bond breaker, to give a reduced embedment length of 50 mm, and to reduce the influence of bearing plate confinement on the bonded portion of the bar (Figure 3.11a). The anchor cylinder on the opposite end of the reinforcing bar did not contain a bond breaker (Figure 3.11b). As it was difficult to grip FRP bars for testing purposes, a longer embedment length (100 mm) in the lower concrete cylinder was used as an anchor at the grip end. To prevent

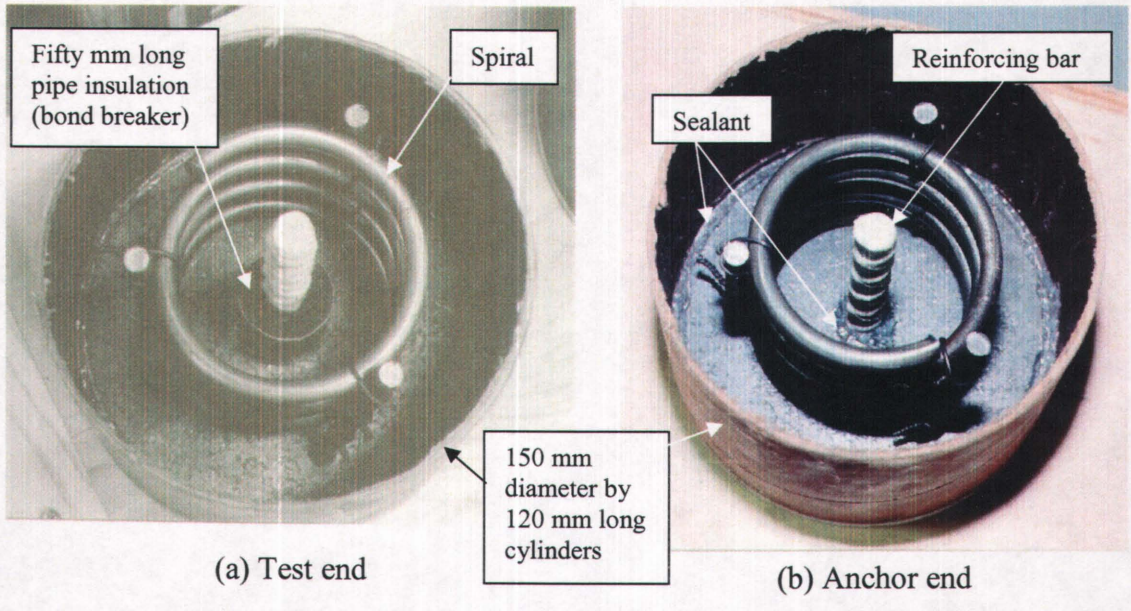

Figure 3.11. Photos of pullout specimen at both ends of reinforcing bar.

vertical and in place when pouring concrete into the cylinders. Figure 3.13 shows the set-up for pouring the concrete cylinders at the anchor ends of the pullout specimens. The holes made in top and bottom plywood plates were vertically aligned and were slightly larger than the size of the reinforcing bars. The height of the set-up was such that the top end of reinforcing bars were level with the top of the cylinders. Since CFRP bars with larger diameters were slightly bent initially, an additional plywood plate was used between the top and bottom plywood plates to keep these bars vertical (Figure 3.14).

The set-up for pouring concrete in the test end cylinders is displayed in Figure 3.15. The top plywood plate was cut in half longitudinally through the holes that allow passage of reinforcing bars and then was connected together using strips of plywood and wood screws. This way the specimens could be removed from the plywood frames after the concrete was cured. The centre of the 150 mm diameter holes on the bottom plywood plate for holding the previously cast anchor end cylinders were vertically aligned with centre of bar size holes on the top plywood plate. The height of the support frame was set to allow the bars to stick out of the top-end cylinders by about 25 mm so that the free end slip could be measured when specimens were tested.

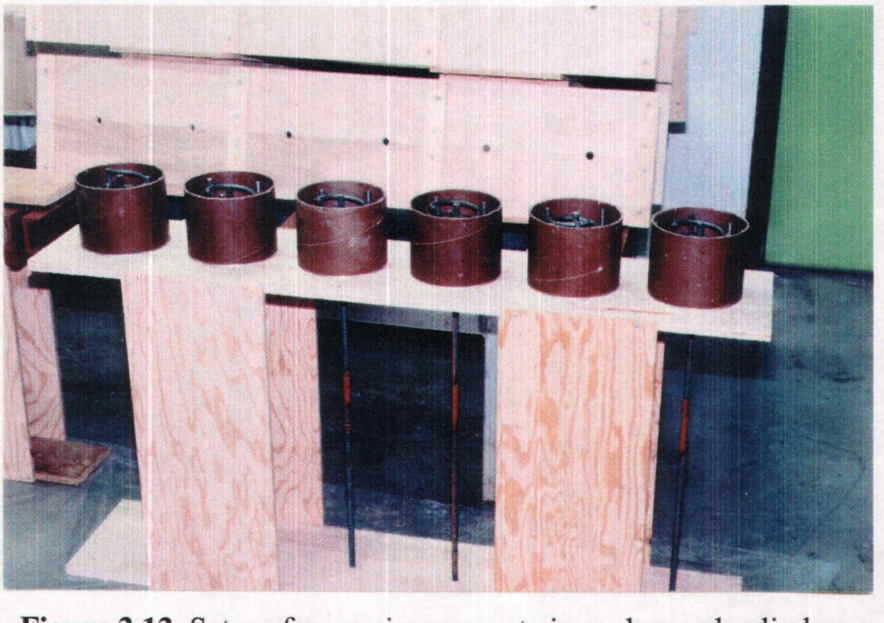

Figure 3.13. Set-up for pouring concrete in anchor end cylinders.

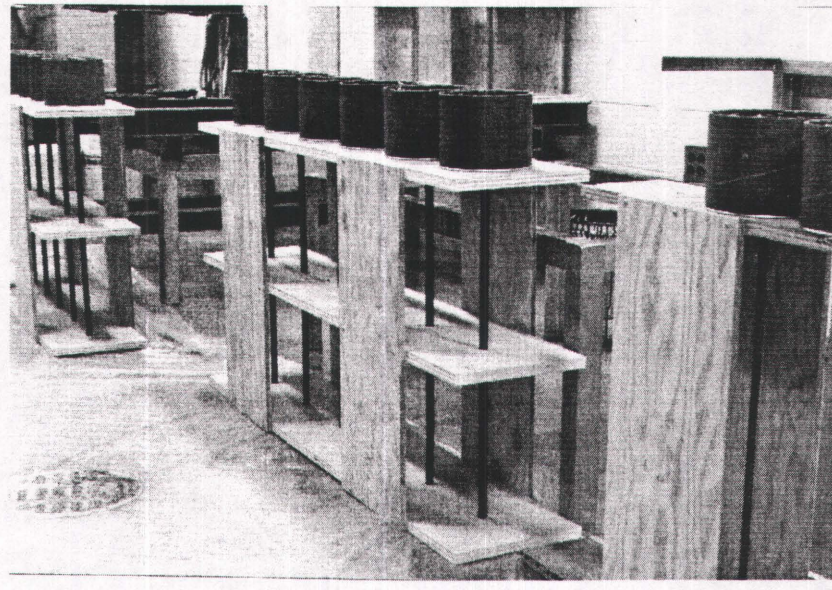

Figure 3.14. Set-up (with added middle plywood plate) for pouring concrete in anchor end cylinders.

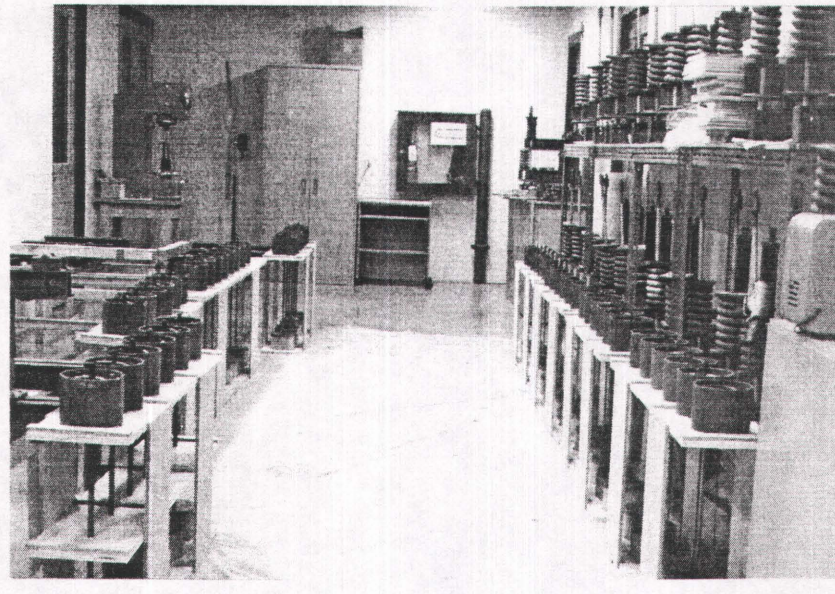

Figure 3.15. Set-up for pouring concrete in test end cylinders.

3.2.5. Material properties

3.2.5.1. Reinforcing bars

Four types of reinforcing bars were used to make the pullout specimens. Figure 3.16 shows the configuration of the bars used in Phase I of the experiment. From top to bottom in Figure 3.16, the bars were a glass fibre reinforced polymer rod (Isorod manufactured by Pultrall Inc., Thetford Mines, Canada); a carbon fibre reinforced polymer rod (Leadline manufactured by Mitsubishi Corporation, Tokyo, Japan), a carbon fibre composite cable (CFCC manufactured by Tokyo Rope Mfg. Co., Tokyo, Japan), and conventional deformed steel rebar. The specifications of the bars are presented in Table 3.1. It should be mentioned that the specifications of FRP bars were provided by the manufacturers, while the ultimate and yield strengths, and the modulus of elasticity for the steel rebars were measured in the Structures Laboratory as part of this program.

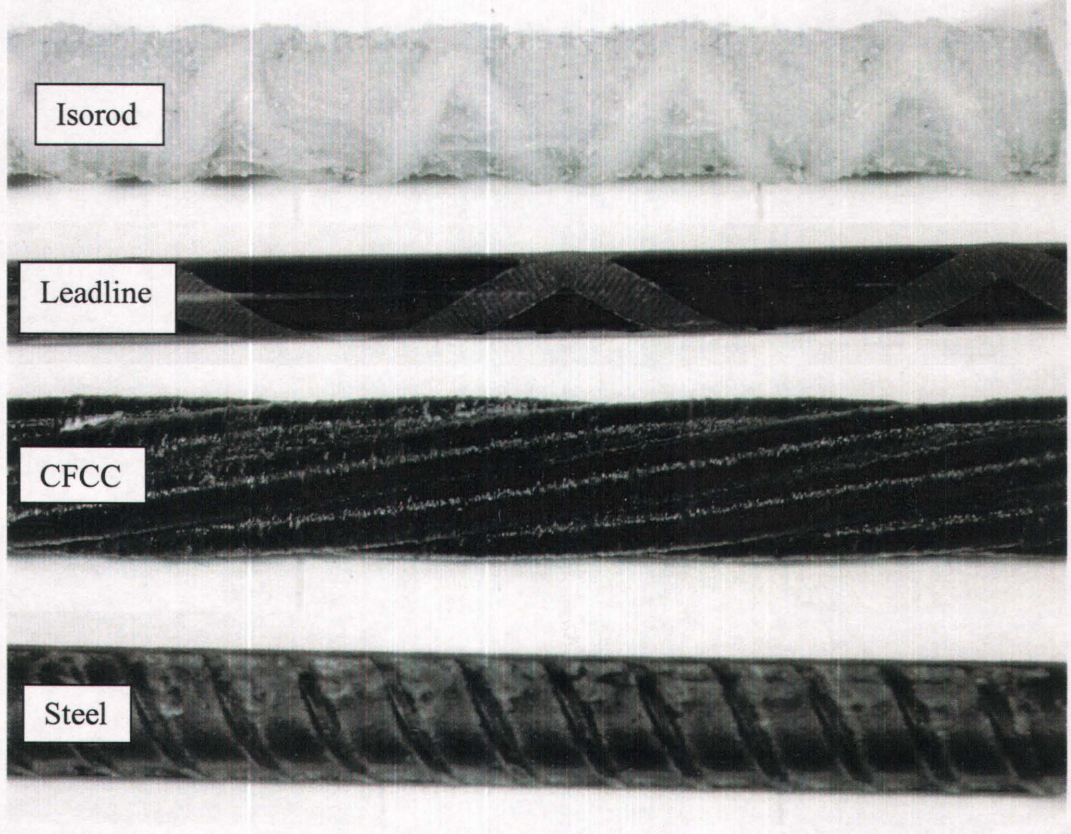

Figure 3.16. Reinforcing bars used in Phase I.

Table 3.1. Specifications of the reinforcing bars.

Type of bar	GFRP (Isorod)	CFRP (Leadline)	CFRP (CFCC)	Steel
No. of specimens	12	12	12	12
Diameter (mm)	12.7	8	15.2	11.3
Fibre (% of volume)	E-glass (73 to 78)	Pitch-based carbon (65)	PAN type carbon (64)	n/a
Resin (% of volume)	Polyester (22 to 27)	Epoxy (35)	Epoxy (36)	n/a
Ultimate tensile strength (MPa)	683	2550	2120	800
Yield strength (MPa)	n/a	n/a	n/a	485
Bond strength (MPa)	15.0*	n/a	7.22*	n/a
Modulus of elasticity (GPa)	40	147	137	200
Longitudinal coefficient of thermal expansion (/°C x 10^{-6})	9.10	0.7	0.6	12
Weight per unit length (kg/m)	0.25	0.08	0.17	0.78
Unit price ($/m)	2.42	16.50	n/a	0.47

* Bond strengths provided in manufacturers literature did not provide information on how obtained.

3.2.5.2. Fibre content

Fibres carry most of the load applied to FRP bars. Therefore, the fibre content of the reinforcing bars is an important factor in determining the tensile strength of the bars. To check the fibre content of the FRP bars, an image analysis technique was used. Cross sections of the as delivered bars were cut by a thin blade, low speed electric diamond saw (Isomet 11-1180 manufactured by Buehler Ltd. and located in materials lab, mechanical engineering department) at a speed of about 100 rpm. The cross-sections were then polished using 600-micron grit and successively finer pastes of 6, 1, and 0.25 microns. The images of the polished cross sections, obtained using an optical microscope (model M3Z manufactured by Wild Heerbrugg and located in Hardy Lab) attached image analyzer software (Matrox Inspector 2.0 designed by Matrox Electronics Systems Ltd.), were not usable since the colour of fibres and matrix were light and image analyzer could not distinguish between the fibres and matrix. The polished cross

sections were then coated with carbon and were viewed using an electron microprobe analyzer (JXA-8600 Super probe manufactured by Jeol and located in geology department). Backscattered images of the bar cross sections were obtained (Figure 3.17) and used to find the fibre content of FRP bars using another image analyzer software package (Digital Photo Image Collection Tool or dPict, designed by Geller MicroAnalytical Laboratory). The average fibre contents were 71%, 65%, and 64% for Isorod, Leadline, and CFCC, respectively compared to 73%, 65%, and 64% suggested by the manufacturers.

3.2.5.3. Concrete

The final mix design used to make the pullout specimens is given in Table 3.2. The concrete mix design used in the pullout specimens was obtained after testing a few different mixes. It was realized that the size of the coarse aggregate should be small so that concrete could fill in the space inside and outside the spiral used in 150 mm diameter cylinders. Coarse aggregate with a maximum size of 10 mm was therefore used. Also, the coarse aggregate to sand ratio of 1.0 was used so that the sand particles could fill in the voids between the coarse aggregate. For every 45.36 kg of cement used, 28.3 ml of air-entrainment agent was used to produce a more workable concrete.

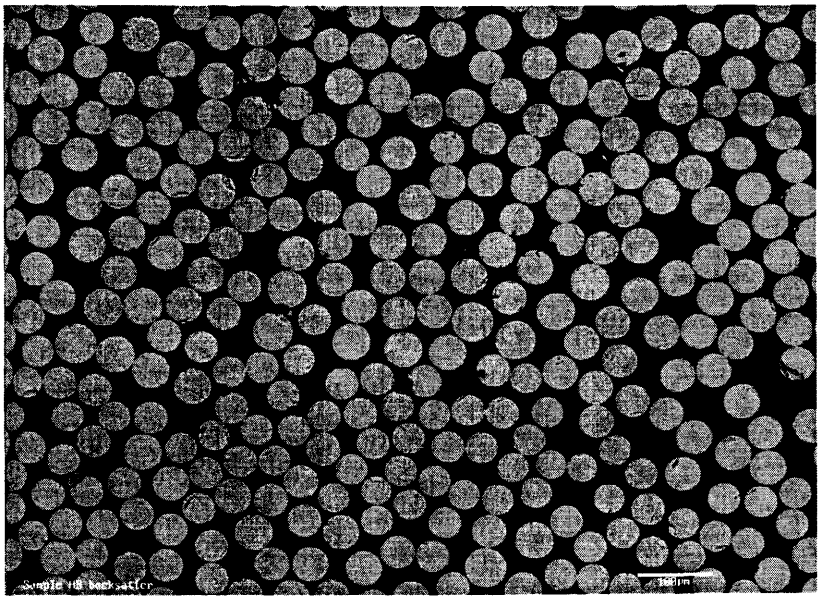

Figure 3.17. Backscattered image of Isorod.

Table 3.2. Mix design for making concrete.

Material	Cement	Water	Sand	Coarse aggregate
Weight (kg/m^3 of concrete)	372	175	841	841
Proportions by weight	1.00	0.47	2.26	2.26

Using an electric rotary mixer (model C9-CE manufactured by Monarch Industries), 0.14 m^3 concrete was made to fill each of the two ends of the pullout specimens, as well as 24-100 mm diameter by 200 mm long sample concrete cylinders. The slump was 120 mm for both batches of concrete, while the air content was found to be 7% for the first batch (anchor end of the specimens) and 6.6% for the second batch.

The concrete was poured in two layers in each of the end cylinders of the pullout specimens. For proper compaction, each layer was tamped 25 times using the standard 16 mm tamping rod. The end cylinders were covered with plastic bags to inhibit the evaporation of concrete water. Also, 100 x 200 mm cylinders used for compression tests were made. All concrete cylinders from each batch were covered with plastic and were kept beside the pullout specimens in room conditions to replicate the curing conditions of the test specimens. The concrete cylinders were completely dry three weeks after casting and were then taken out of the moulds.

Compression tests were performed on sample concrete cylinders 28 days after casting. The test results are shown in Table 3.3.

Table 3.3. Compression test results for 100 mm by 200 mm concrete cylinders.

Specimen no.	Load (kN)			Average load (kN)	C.O.V. (%)	Average strength (MPa)
	1	2	3			
Batch #1	285	267	285	279	3.0	34
Batch #2	276	271	258	268	2.8	33

3.2.6. Room conditions

The room temperature and relative humidity were monitored using a hygrometer/thermometer (model 35519-044 manufactured by VWR) featuring digital displays for the relative humidity (accuracy of ±2%) and temperature (accuracy of ±1°C). No attempt was made to control either. The temperature and relative humidity for a one-year period (from August 1998 to July 1999) are illustrated in Figure 3.18. During the one-year period, the minimum and maximum temperatures were 20.9 °C and 24.2 °C (a change of 3.3 °C) in July and January, respectively. The temperature range was from 20.9 °C to 23.6 °C in July, whereas it changed between 21.5 °C and 24.2 °C in January. The minimum and maximum relative humidity measured were 15% and 66% (a change of 51%) in January and August, respectively. The relative humidity changed between 15% and 19% in January and between 30% and 66% in August.

3.2.7. Static tests

Static tests were performed to obtain ultimate pullout loads and also to establish load levels for long term tests. Three specimens out of 12 specimens for each bar type were tested under static (short term monotonic) loads. Figure 3.19 shows the static test

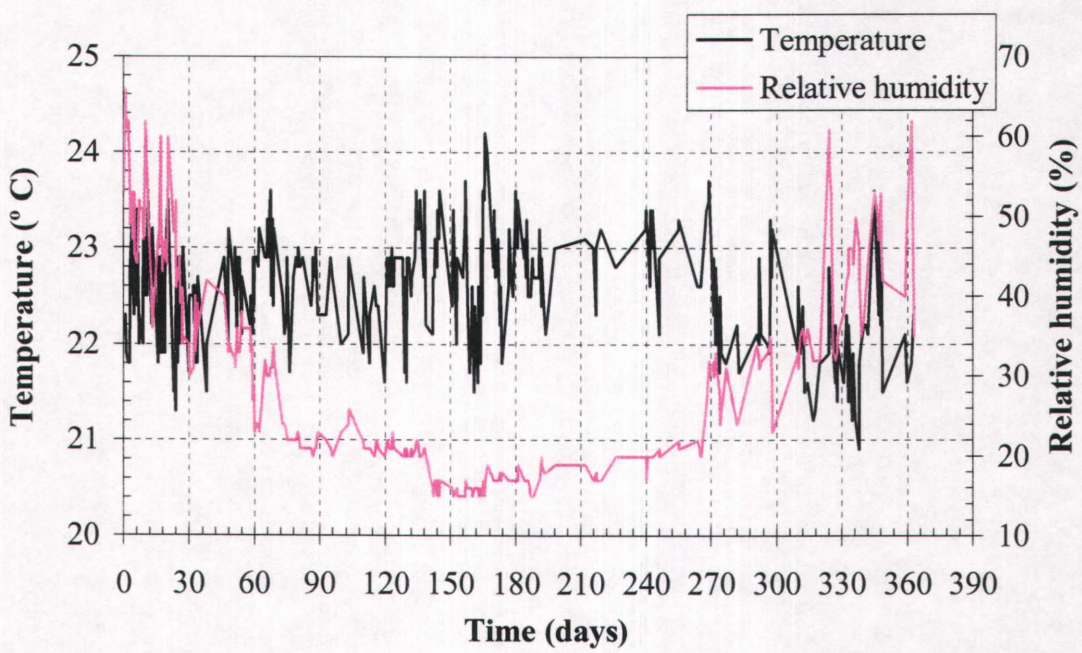

Figure 3.18. Room temperature and relative humidity vs. time.

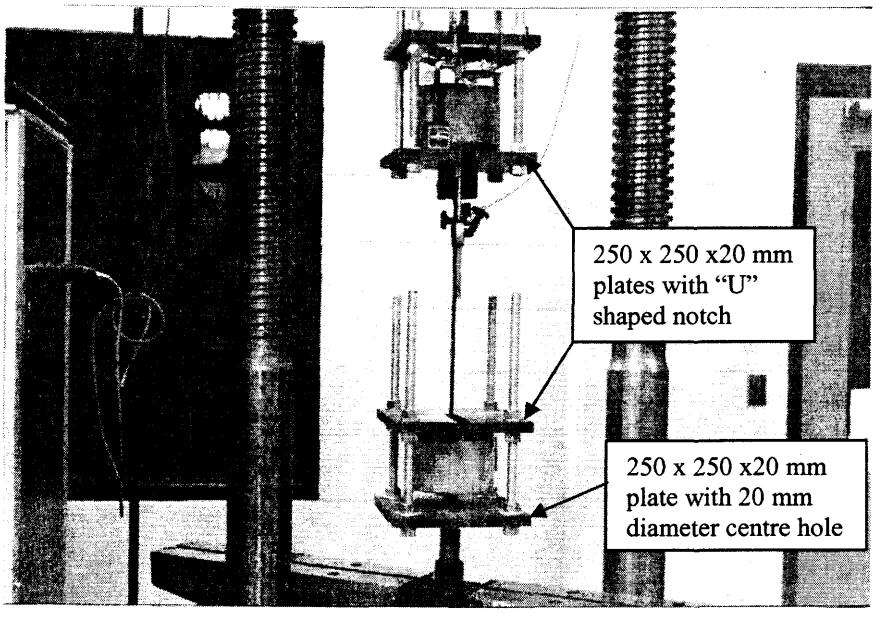

Figure 3.19. Static test set-up for pullout specimens.

set-up for the pullout specimens. In order to test the pullout specimens in the testing machine (type 30THZ724 manufactured by Wolpert-Amsler), a set of four 250 mm x 250 mm x 20 mm plates were used. Two of the plates had a "U" shaped notch machined to their central axis to permit placing the pullout specimen into the testing assembly. The other two plates had a 20 mm hole at the centre to attach the plates to the testing machine using a 19 mm diameter threaded rod and nuts. Each of the four plates had four 20 mm diameter holes close to the corners to permit connecting one plate with "U" shaped notch to another plate with centre hole using four 19 mm diameter threaded rods and nuts.

Mechanical dial gauges (one to each of the free and the loaded ends of the reinforcing bar) were attached in an attempt to monitor the occurrence of slip of the bar through the concrete cylinder while the load was increased to produce a pullout failure (Figure 3.20). Because of space limitations, the dial gauge reading at the free end was obtained using a pivotal arrangement so that readings on the gauge were 0.1 times of the actual slip at the free end. The gauge readings were taken with an accuracy of ±0.005 mm at each load increment (minimum of 1 kN).

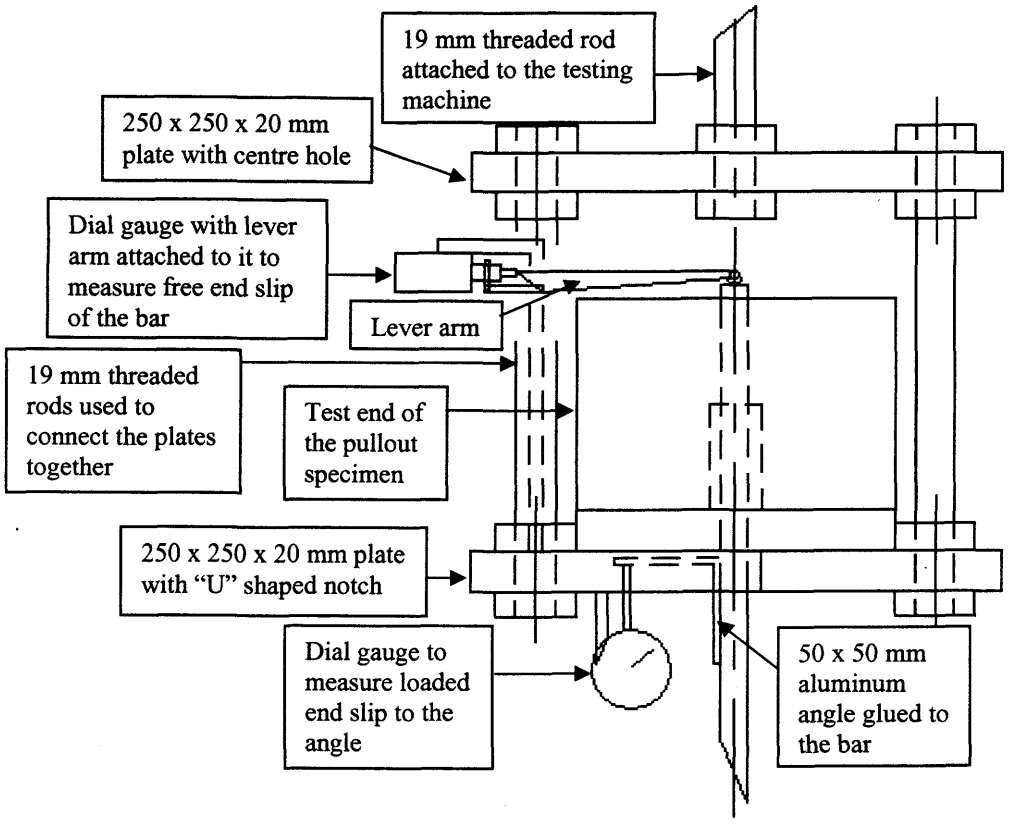

Figure 3.20. Details of set-up at the test end of the specimen.

To measure the loaded end slip, a short length of 50 mm x 50 mm aluminum angle was glued near the loaded end of the bar and the dial gauge reading was taken to the angle (Figure 3.20). Because of gauge size, the loaded end slip was measured about 50 mm from the bar longitudinal axis. This affected the dial readings in the specimens that featured bars with some initial curvature. Also, if some rotation occurred in the bearing plate to which the dial gauge was attached, the readings would be unreliable. In most specimens, the loaded end slips were deemed to be incorrect, providing only an indication of the load at which considerable slip began to occur. However, the measured loaded end slip values were adjusted for the elongation of the rod between the actual loaded end of the embedment length and the attachment point of the dial gauge (a length of 75 mm):

$$\text{Actual Slip} = \text{Measured Slip} - \frac{\text{load x length}}{\text{A x E}}, \qquad (3.1)$$

where A and E are the cross sectional area and the modulus of elasticity of the bar, respectively.

3.2.8. Long term tests

Tests were undertaken to examine the long term bond behaviour between fibre reinforced polymer (FRP) bars and concrete. The tests were performed using the loading frames previously described (Section 3.2.3). The test set-up for the long term tests on the pullout specimens is displayed in Figure 3.21. Nine pullout specimens from each bar category were loaded to selected load levels below the average ultimate loads obtained from static pullout tests. Load levels between 14% and 45% of the ultimate static pullout strength were selected to provide almost the same bond stresses induced in the FRP specimens. High load levels in the range of 60% to 90% of the ultimate pullout strength were chosen to generate high bond stresses and also to accelerate the tests. During the loading of the specimens, it was realized that appreciable initial free end slips occurred in Isorod and Leadline specimens under 75% load level. Therefore, load levels for the Isorod and Leadline specimens were limited to 60% and 75% of the ultimate static pullout loads. The CFCC specimens were loaded to 60, 75, and 90% of ultimate, while the steel specimens were under load levels ranging from 14 to 90%.

Figure 3.21. Test set-up for long term tests in Phase I.

The target sustained load for each specimen is presented in Table 3.4. The slope values were the slope of best-fit lines obtained from calibration curves for each loading frame as described in Section 3.2.3.5. These slope values were divided by slope of the calibration curve (0.10109) for the tension link (Section 3.2.3.4) to calculate the average reading on the aluminum rods as explained in Section 3.2.3.6. The zero readings on the aluminum rods were measured when the rods were sitting on a flat surface.

Loads were monitored, at least once a week for first month and at least once every two weeks after first month, using the demec points on the aluminum rod and the 200 mm gauge with digital display. The nut on aluminum rod was retightened if necessary to keep the load at specified value. Free and loaded ends slips were measured using a 600 mm height gauge (Section 3.2.3.6).

Table 3.4. Target sustained loads applied to the pullout specimens.

Load frame No.	Specimen	Load (kN)	Load/ Static pullout load (%)	Load/ Max. Tensile load* (%)	Slope from the calibration curve	Slope/ 0.10109	Zero Reading on Alum. Rod	Average Reading on Alum. Rod
4	CFCC 60% #1	15.2	60	6.3	1.125	11.129	24	193
8	CFCC 60% #2				1.127	11.148	33	202
26	CFCC 60% #3				0.984	9.731	-230	-82
10	CFCC 75% #1	19.1	75	7.9	1.004	9.934	-8	181
31	CFCC 75% #2				0.979	9.684	-42	143
35	CFCC 75% #3				1.142	11.301	81	297
3	CFCC 90% #1	22.9	90	9.5	1.146	11.331	203	463
13	CFCC 90% #2				0.987	9.766	-173	51
36	CFCC 90% #3				0.984	9.735	-112	111
5	Isorod 60% #1	6.9	60	8.0	1.136	11.236	-26	52
14	Isorod 60% #2				0.994	9.829	81	149
30	Isorod 60% #3				1.147	11.345	-11	67
34	Isorod 60% #4				0.995	9.842	32	100
7	Isorod 75% #1	8.7	75	10.1	0.997	9.860	171	257
11	Isorod 75% #2				0.998	9.873	26	112
19	Isorod 75% #3				1.139	11.266	76	174
23	Isorod 75% #4				1.005	9.946	-3	84
28	Isorod 75% #5				1.130	11.181	-196	-98
17	Leadline 60% #1	8.8	60	7.5	0.989	9.786	187	273
21	Leadline 60% #2				0.987	9.768	-118	-32
25	Leadline 60% #3				0.995	9.843	-68	19
27	Leadline 60% #4				1.077	10.654	24	117
16	Leadline 60% #5				1.153	11.403	8	109
15	Leadline 75% #1	11	75	9.4	1.020	10.087	114	225
18	Leadline 75% #2				1.009	9.978	-68	42
29	Leadline 75% #3				1.007	9.961	-1	109
33	Leadline 75% #4				1.137	11.247	-95	29
6	Steel 14% #1	6.1	14	13	1.111	10.986	8	75
32	Steel 20% #1	8.8	20	18	0.988	9.775	-88	-2
9	Steel 26% #1	11.5	26	24	1.111	10.994	12	138
24	Steel 33% #1	14.2	33	30	1.121	11.091	13	170
22	Steel 39% #1	16.9	39	35	1.030	10.189	-7	165
12	Steel 45% #1	19.5	45	40	0.982	9.715	-4	186
1	Steel 60% #1	26.1	60	54	0.999	9.877	17	275
2	Steel 75% #1	32.7	75	68	0.988	9.775	-25	295
20	Steel 90% #1	39.3	90	82	1.016	10.048	47	442

*Yield load for steel and manufacturers' ultimate tensile load values for FRP bars.

3.2.9. Scanning electron microscopy

A scanning electron microscope (SEM 515 manufactured by Philips and located in the materials lab, mechanical engineering department) was used to observe the surface of the FRP bars. Although only a small area of each bar surface could be observed, SEM observations provided good information about the surface damage. After both the static and the long term tests were completed, samples were cut from the bonded portions of selected FRP bars inside test end concrete cylinders. To take the FRP bars out of the concrete, the test end cylinders were cut (four longitudinal cuts for each cylinder) using a concrete diamond saw (model J-2 manufactured by Highland Park Manufacturing, Hawthorne, CA, located in structures and materials laboratory), such that the bar remained undisturbed. Surface samples were cut from near the middle of the bonded portions of the FRP bars. A thin blade electric diamond saw (Isomet 11-1180 manufactured by Buehler Ltd.) was used to cut the samples. This diamond saw was located in the materials lab, mechanical engineering department. Samples were then polished using 600-micron grit, and 6 and 1 micron pastes. The polished samples were glued with carbon glue to the 12 mm diameter steel stubs used with the SEM and were coated with gold or carbon using a machine called a sputter coater. A total of 15 samples were made and observed under a SEM.

3.3. Phase II

3.3.1. Introduction

Phase II of the experimental program was undertaken to evaluate the bond performance of three types of GFRP reinforcing bars embedded in concrete under long term loading in potentially hostile solution environments, as well in air. The program consisted of preliminary pullout tests, manufacturing of pullout specimens, static tests, long term tests in the three different environments, image analysis to find fibre contents of bars, scanning electron microscopy of bars, and the use of an electron microprobe analyzer to obtain x-ray maps of bar cross sections. Details of the experimental program in Phase II will be covered in subsequent sections.

3.3.2. Environmental conditions

Studies show that the glass fibres have a low resistance to alkaline environments and moisture (Section 2.2.3.2). They lose their tensile strengths when exposed to water and alkaline solution. This could cause a problem in GFRP bars if glass fibres in the bars are exposed to wet and alkaline environments due to cracking of the polymer coating of the bar, which initially, protects the glass fibres. Cracking could be induced in the coating at any stage in the service life of the bar, starting with manufacturing process.

The long term tests were performed in three different environments provided around the test ends of the pullout specimens (details of pullout specimens are provided in Section 3.3.4). Twelve specimens (four from each bar category) were tested in room conditions (air). Another twelve specimens were tested at room temperature while the test ends of the specimens were submerged in tap water. An alkaline solution was poured around the test ends of the last 12 pullout specimens.

The alkaline solution was made by dissolving calcium hydroxide in 100 litres distilled water until the solution was saturated. Then, two moles (80 g) of sodium hydroxide per litre of the solution was dissolved in the saturated calcium hydroxide solution to give a solution with a pH of more than 13. The pH was measured using a pH metre with an accuracy of ±0.1 pH (model 600 manufactured by Fisher Scientific Company). After pouring the alkaline solution around the 12 pullout specimens, the unused portion of the solution was kept in a container with a tight lid and was used to re-supply the fluid levels if necessary. The fluid levels changed slightly during the long term tests.

3.3.3. Preliminary pullout tests

Preliminary tests were performed in Phase II to modify the design of the pullout specimens used in Phase I, which was based on preliminary tests performed using deformed steel rebar (Section 3.2.2). Since steel rebar was not used in Phase II due to limited number of loading frames (36), preliminary tests were carried out to determine whether the spiral confinement used in the concrete cylinders of Phase I specimens

(Section 3.2.4) could be eliminated while still producing pullout failures. Also, the possibility of using a longer embedment length (75 mm instead of the 50 mm that was used in Phase I) was examined. A pullout failure rather than a concrete splitting failure was chosen as a testing requirement, for the reasons discussed previously in Section 3.2.2. The preliminary pullout specimens were made using two types of GFRP bars (HB and C-bar) that were available at the time. The specifications of the bars are provided in Section 3.3.5.1.

A 150 mm diameter x 100 mm high cylinder was constructed at each end of the reinforcing bar to be tested. A 25-millimetre length of pipe insulation was used as a bond breaker around the bar at the loaded end of the test end cylinder of the specimen, leaving an embedment length of 75 mm. The anchor end cylinder of the specimen did not contain a bond breaker. As it was difficult to grip FRP bars for testing purposes, a longer embedment length (100 mm) in the grip end concrete cylinder was used as an anchor. Four specimens were made from each bar type, with two of the specimens containing spirals in the end cylinders to inhibit splitting of the concrete while the other two had no spirals. Spirals were made from 8 mm diameter smooth bar formed into a spiral with a pitch of 30 mm and an outside diameter of 90 mm.

Static tests were performed on the specimens using the set of four 250 mm x 250 mm x 20 mm plates and the testing machine used in static tests in Phase I (Section 3.2.7). All eight specimens experienced pullout failure at the test ends. No cracks on the concrete cylinders were visible. As shown in Table 3.5, average ultimate loads of 42.5 kN and 46.3 kN were obtained for the two types of reinforcing bars (HB and C-bar), respectively. There was a small difference (about 2 kN) in the average ultimate loads between the confined and unconfined specimens for each bar type, indicating that confinement due to spiral had no significant effect on the ultimate loads. Therefore, an embedment length of 75 mm at the test end without spiral confinement was provided in subsequent pullout specimens used in the static and long term tests.

Table 3.5. Results of preliminary static tests in Phase II.

Reinforcing bar	Specimen no.	Ultimate load (kN)	Average ult. load (kN)	Total average ult. load (kN)	C.O.V.	Failure mode
Type 1 (HB*)	1S+	39.7	41.4	42.5	6.0	pullout
	2S+	43				pullout
	3	46.4	43.7			pullout
	4	40.9				pullout
Type 2 (C-bar*)	1S+	45.8	47.1	46.3	3.0	pullout
	2S+	48.4				pullout
	3	46.5	45.6			pullout
	4	44.6				pullout

* Specifications of the bars are given in Section 3.3.5.1.
+ The letter "S" represents the specimens confined with spiral.

3.3.4. Pullout specimens

A total of 45 pullout specimens (15 specimens for each bar category) were made using three different types of GFRP bars. Specifications of the GFRP bars are given in Section 3.3.5.1. Three specimens from each bar type (for a total of nine specimens) were used to perform static tests while the other 12 specimens were employed in performing long term tests in air, water, and alkaline solution environments. Two identical specimens were loaded at each of two load levels in each bar category and environment.

The same plywood frames used in Phase I were used to make the anchor end of the specimens. The details in anchor ends were similar to the ones made in Phase I of the experimental program (a) except that no spirals were used for confinement in the cylinders this time. Also, three specimens from each bar type that were used for static tests were made using shorter bars (140 mm shorter than other bars with 760 mm length) so that the free end slips could be measured directly (Section 3.3.6). The test ends of 21 specimens (nine static specimens and 12 long term test specimens exposed to air) were made using the same set-up used in Phase I. Pipe insulation, 25 mm in length, was wrapped around the bar at the loaded end to act as a bond breaker. As mentioned in the previous section, the test cylinder did not contain spiral confinement in Phase II.

Details for the test ends of the 24 specimens that were to be subjected to either water or alkaline solution environment required major modifications. To permit the

submerging of the test end cylinder, the bearing plate diameter had to be increased to accommodate a 200 mm diameter by 140 mm long plastic sewage pipe that would confine the liquid around the test end concrete cylinder. Unlike the carbon steel bearing plate used elsewhere, stainless steel plates were used to prevent corrosion in the wet environment. Figure 3.22 shows the details of the stainless steel bearing plate (240 mm diameter x 20 mm thick). A 3 mm deep groove was made at the bottom of the plate to fit on top of the 19 mm diameter half bar used in the top beam of the loading frame (Section 3.2.3.1). The centre hole size was chosen in accordance with the size of the bars. Two 150 mm and 200 mm circular grooves (2 mm deep) were made on top of the plate to place the 150 mm diameter hollow concrete cylinder mould and the 200 mm plastic sewage pipe. For this detail, the bearing plate formed the bottom of the cylinder mould as the metal bottom plate of the cylinder mould was removed when the mould was cut to the required length.

For the above-mentioned specimens with larger bearing plates at the test ends, new support and alignment frames with larger plywood plates at the top and bottom were made. The bars with their pre-cast anchor ends were aligned in the frame. Then, the larger bearing plates were lowered around the bars through the centre holes of the

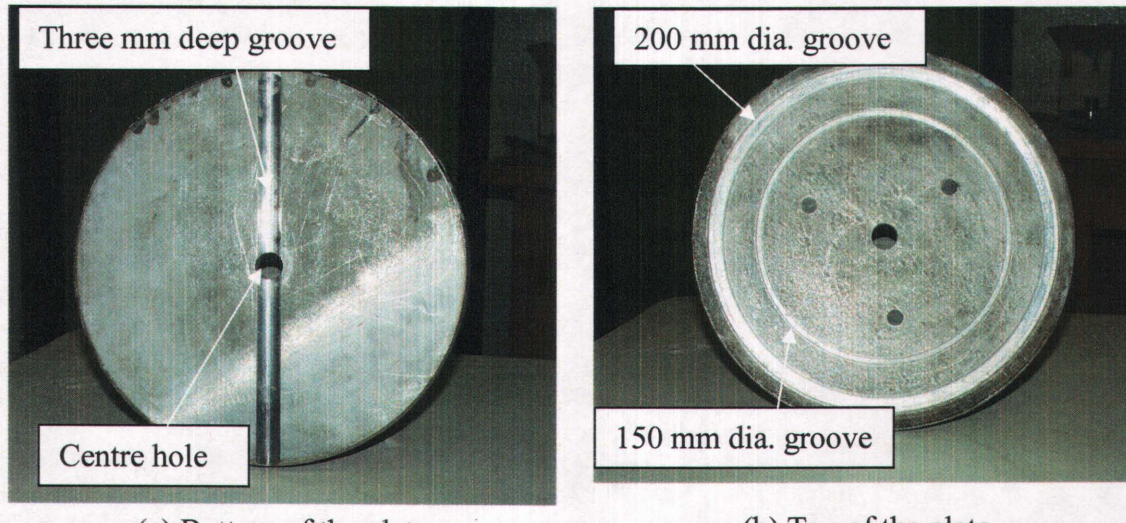

(a) Bottom of the plate (b) Top of the plate

Figure 3.22. Details of the 240 mm diameter x 20 mm thick stainless steel bearing plate.

plates. The gap between the bar and hole was sealed with multi-purpose sealant. The 25 mm long pipe insulation (bond breaker) was then wrapped around the bar at the loaded end. The 150 mm diameter circular groove was filled with sealant and then the hollow 150 mm diameter by 102 mm long cardboard cylinder mould was pushed down inside the groove to provide a seal between the mould and bearing plate. After the sealant was dry, the concrete was poured in the cardboard cylinders.

3.3.5. Material properties

3.3.5.1. Reinforcing bars

Three types of GFRP bars from three different manufacturers were employed in making the pullout specimens in Phase II (Figure 3.23). One bar had a ribbed surface

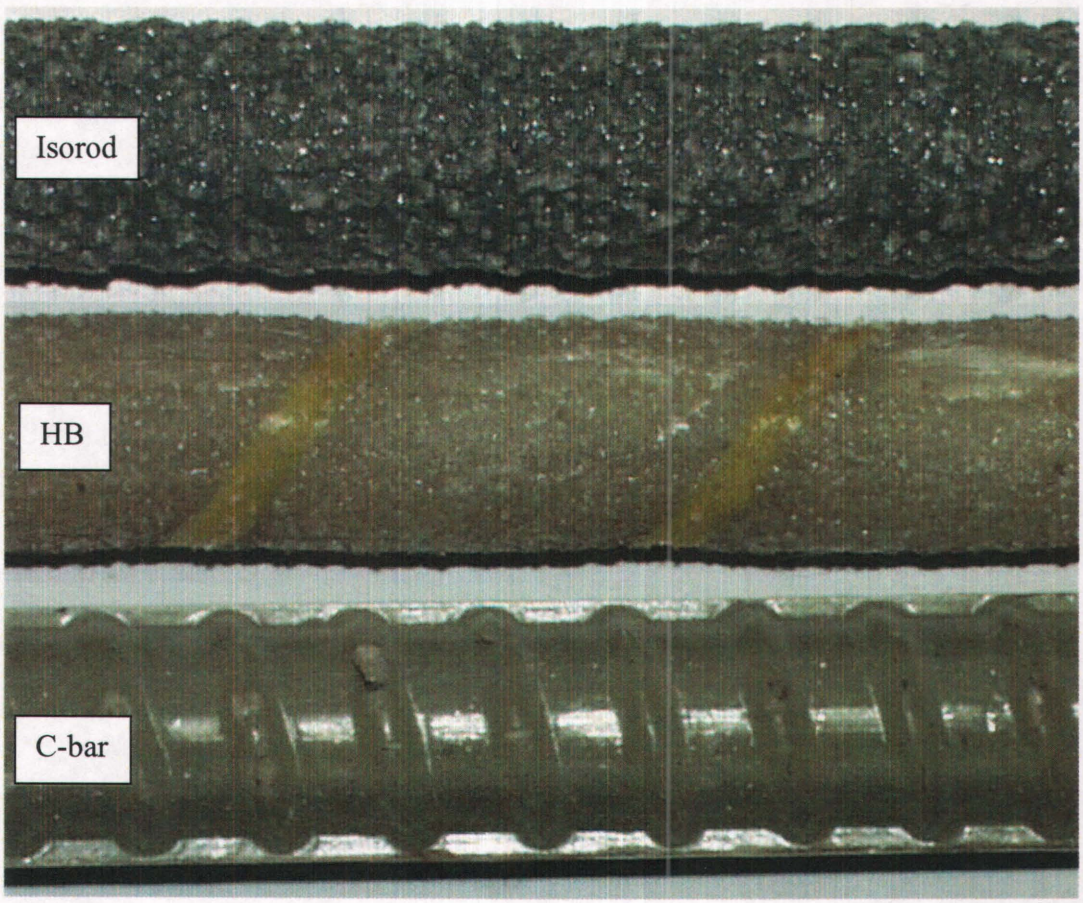

Figure 3.23. GFRP reinforcing bars used in Phase II.

(C-bar manufactured by Marshall Industries Composites Inc., Jacksonville, USA). The second bar had a rough sand-coated surface with spiral shaped indentations (HB manufactured by Hughes Brothers Inc., Seward, USA), and the third bar was an updated design of the GFRP bar used in Phase I (Isorod manufactured by Pultrall Inc., Thetford Mines, Canada). This bar had a very rough sand-coated surface, with no additional deformation or indentation detail, and a grey colour, instead of a helical wrapping and white colour (Figure 3.16) featured in the bar used in Phase I. Specifications of the bars are presented in Table 3.6. It should be mentioned that the specifications of GFRP bars were provided by the manufacturers.

Table 3.6. Specifications of the GFRP bars.

Type of GFRP bar	Isorod*	C-bar	HB
No. of specimens	15	15	15
Diameter (mm)	12.7	12.7	12.7
Fibre (% of volume)	E-glass (75%)	E-glass (n/a)	E-glass (>70%)
Resin (% of volume)	Vinyl ester (25%)	Vinyl ester (n/a)	n/a (<30%)
Ultimate tensile strength (MPa)	683	770	740
Bond strength (MPa)	n/a	17	11.6
Modulus of elasticity (GPa)	42	42	41
Longitudinal coefficient of thermal expansion (/°C x 10^{-6})	8.88	n/a	9.9
Weight per unit length (kg/m)	0.25	0.25	0.24
Unit price ($/m)	2.42	4.43	2.34

*This bar was different (resin type and configuration of the bar) from the Isorod bar used in Phase I.

3.3.5.2. Fibre volume fraction

To check the fibre content of the FRP bars, an image analysis technique was used. As in Phase I, backscattered images for cross sections of the bars were obtained using an electron microprobe analyzer (JXA-8600 Super probe manufactured by Jeol and located in geology department) and subsequently used to find the fibre content of FRP bars using image analyzer software (Digital Photo Image Collection Tool or dPict, designed by Geller MicroAnalytical Laboratory). A typical backscattered image is shown in Figure 3.24. The fibre content or fibre volume fraction (V_f) for C-bar was found to be 70%, on average. Average fibre contents of Isorod and HB bars were 73% and 70%, respectively, compared to 75% and (greater than) 70% given by the manufacturers.

3.3.5.3. Concrete

The same concrete mix design as was described in Phase I (Table 3.2) was used to make the pullout specimens in Phase II. Using an electric rotary mixer (model C9-CE manufactured by Monarch Industries), 0.14 m^3 of concrete was made to fill each end (i.e. the anchor or test ends) of the pullout specimens and to make 24 sample concrete cylinders.

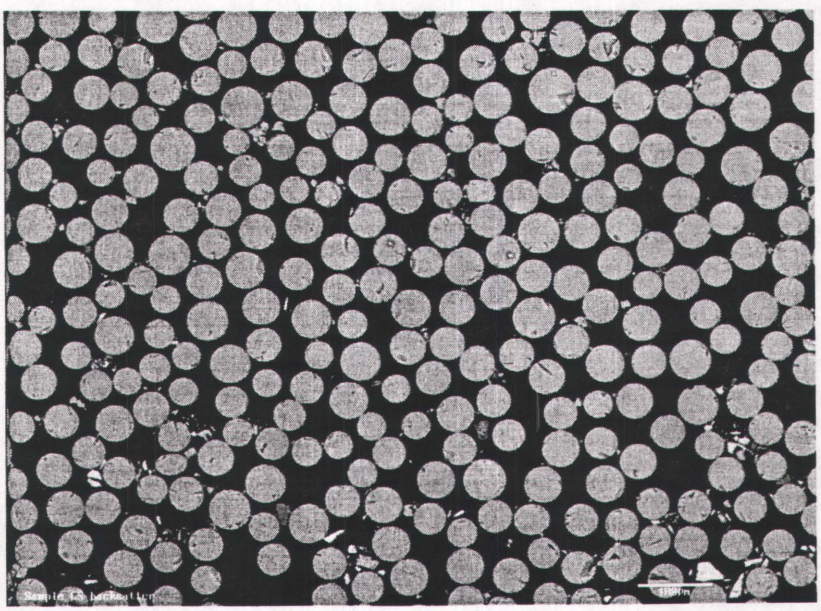

Figure 3.24. Backscattered EMPA image of C-bar.

The slump and air content for batch #3 (anchor end concrete) were 115 mm and 5%, respectively. The slump for batch # 4 (test end concrete) was 110 mm while an air content of 6.5% was measured. The compressive strengths of the sample cylinders for the phase are displayed in Table 3.7.

3.3.6. Static tests

Static tests were performed to obtain the ultimate pullout loads and to establish load levels for the long term tests. Three pullout specimens from each bar category were tested to failure under static loads. These specimens were made using bars with a shorter length (620 mm) than that of other 36 specimens (760 mm) so that the dial gauge readings could be obtained directly and more accurately for the free end slip of the bar. The dial gauge was attached directly to the free end of the bar and unlike Phase I, no pivotal arrangement (lever arm) was used. The same set-up, with four plates used in Phase I (Figure 3.19 and Figure 3.20), was employed in performing the static tests. The gauge readings were taken at 2 kN load increments with an accuracy of ±0.005 mm. As previously described in Section 3.2.7, loaded end slips were measured to provide an indication of the load at which considerable slip began to occur. As in Phase I, loaded end slips were thought to be incorrect in most of the specimens.

3.3.7. Long term tests

Long-term tests were carried out to evaluate the bond performance of three types of GFRP reinforcing bars embedded in concrete under long term loading in potentially hostile solution environments, as well in air. The tests were performed using the loading frames used in Phase I (see Section 3.2.3). The test set-up for the long term tests on the pullout specimens is displayed in Figure 3.25. Before placing the specimens in the

Table 3.7. Compression test results for 100 mm by 200 mm concrete cylinders.

Specimen no.	Load (kN)			Average load (kN)	C.O.V. (%)	Average strength (MPa)
	1	2	3			
Batch #3	276	268	284	276	2.4	34
Batch #4	280	276	296	284	3.1	35

Figure 3.25. Test set-up for long term tests in Phase II.

apparatus, the gaps between the bars and the holes at the bottom of the 240 mm diameter bearing plates (total of 24) were sealed by sealant. Then, they were set in the apparatus and sealant was applied around the bottom of the concrete cylinders to prevent leaking of solution through the path between the top of the plate and the bottom of the concrete cylinder. The 200 mm diameter circular groove at the top of the plate (Section 3.3.4) was filled with multi-purpose sealant. The 200 mm diameter plastic pipe was then pushed down in the groove and securely seated. After the sealant was dry, the specimen was loaded to the desired load. Tap water or alkaline solution was poured around the submerged test-end concrete cylinders inside the plastic pipes such that the free end of the bar was submerged in the solution. Test ends of four specimens from each bar type (a total of 12 specimens) were submerged in alkaline solution while test ends of the other 12 specimens (four for each bar category) were submerged in tap water. The pH in tap water solution was 11.1. The tops of the plastic pipes for the 24 submerged specimens were covered with disposable foam plates to prevent the evaporation of the solutions. Solutions were added as required if evaporation did occur. The pH of the alkaline solution was monitored during the long term tests; it was found that there was no significant change in pH value (13.2).

Table 3.8 shows the sustained loads selected for the specimens. Of the four specimens for each bar category and environment, two specimens were loaded to a value of 25% of average ultimate static load while the remaining two were loaded to 50% of the ultimate load. Zero readings of aluminum rods were measured and checked before placing the specimens in the apparatus. As in Phase I, the zero readings were measured when the rods were sitting on a flat surface. It was realized that the zero readings (Table 3.8) were less than the values obtained in Phase I (Table 3.4). Investigation of the demec gauge points on the rods revealed that the holes had an oval cross section rather than the circular shape that they had initially. The possible reason could be wearing of the gauge points due to contact between steel tips of the 200 mm gauge and the gauge points, and the large number of readings during the long term tests in Phase I. Also, the rods were re-threaded since some of the threads were damaged during Phase I. Furthermore, a few loading frames were chosen randomly and were calibrated. There were no significant changes in the slopes of the best-fit lines (Table 3.8) obtained from the calibration curves when compared to the values (Table 3.4) found in Phase I (Section 3.2.8).

Table 3.8. Selected sustained loads applied to the pullout specimens in Phase II.

Load frame No.	Specimen	Load (kN)	Load/ Static pullout load (%)	Load/ Max. Tensile load* (%)	Slope from the calibration curve	Slope/ 0.10109	Zero Reading on Alum. Rod	Average Reading on Alum. Rod
13	C-bar 25% Air #1	11.8	25	14	0.987	9.766	-183	-68
14	C-bar 25% Air #2				0.994	9.829	73	189
29	C-bar 25% Alkaline #1				1.007	9.961	-12	106
30	C-bar 25% Alkaline #2				1.147	11.345	-16	118
5	C-bar 25% Water #1				1.136	11.236	-51	82
6	C-bar 25% Water #2				1.111	10.986	-7	123
15	C-bar 50% Air #1	23.6	50	27	1.020	10.087	112	350
16	C-bar 50% Air #2				1.153	11.403	-3	266
31	C-bar 50% Alkaline #1				0.979	9.684	-48	181
32	C-bar 50% Alkaline #2				0.988	9.775	-111	120
7	C-bar 50% Water #1				0.997	9.860	152	385
8	C-bar 50% Water #2				1.127	11.148	21	284
9	HB 25% Air #1	10.5	25	11	1.111	10.994	-8	107
10	HB 25% Air #2				1.004	9.934	-21	83
25	HB 25% Alkaline #1				0.995	9.843	-79	24
26	HB 25% Alkaline #2				0.984	9.731	-236	-134
1	HB 25% Water #1				0.999	9.877	18	122
2	HB 25% Water #2				0.988	9.775	-33	70
11	HB 50% Air #1	20.9	50	22	0.998	9.873	5	211
12	HB 50% Air #2				0.982	9.715	-11	192
27	HB 50% Alkaline #1				1.077	10.654	18	241
28	HB 50% Alkaline #2				1.130	11.181	-209	25
3	HB 50% Water #1				1.146	11.331	192	429
4	HB 50% Water #2				1.125	11.129	17	250
17	Isorod 25% Air #1	14.5	25	16	0.989	9.786	188	330
18	Isorod 25% Air #2				1.009	9.978	-69	76
22	Isorod 25% Alkaline				1.030	10.189	-10	138
23	Isorod 25% Alkaline				1.005	9.946	-10	134
33	Isorod 25% Water #1				1.137	11.247	-107	56
34	Isorod 25% Water #2				0.995	9.842	25	168
19	Isorod 50% Air #1	29.1	50	33	1.139	11.266	65	393
20	Isorod 50% Air #2				1.016	10.048	46	338
21	Isorod 50% Alkaline				0.987	9.768	-131	153
24	Isorod 50% Alkaline				1.121	11.091	5	328
35	Isorod 50% Water #1				1.142	11.301	75	404
36	Isorod 50% Water #2				0.984	9.735	-117	166

*Based on manufacturers' data.

3.3.8. SEM samples

A scanning electron microscope (SEM) was used to observe longitudinal and transversal cross sections, and also the surface of the FRP bars. Although small areas of each bar could be observed, SEM observations provided good information about damage at a micro-mechanical scale. After the mechanical tests, samples were cut from both bonded and unbonded portions of some of the bars inside the test end concrete cylinders. To take the FRP bars out of the concrete, the cylinders were cut (four longitudinal cuts for each cylinder) using a concrete diamond saw (model J-2 manufactured by Highland Park Manufacturing), such that the bar remained undisturbed. The bars were taken out and cut by a thin blade low speed electric diamond saw (Isomet 11-1180 manufactured by Buehler Ltd.) at a speed of about 100 rpm. The low speed diamond saw was located in the materials lab, mechanical engineering department. A length of 13 mm on each side of the interface between the bonded and unbonded portions of the bar was used to make surface, cross-sectional, and longitudinal samples as shown in Figure 3.26. Longitudinal and cross sectional samples were polished using 600 micron grit, and 6 and 1 micron pastes. All samples (6 for each bar) were glued on 12 mm diameter stubs using carbon glue and were coated with gold

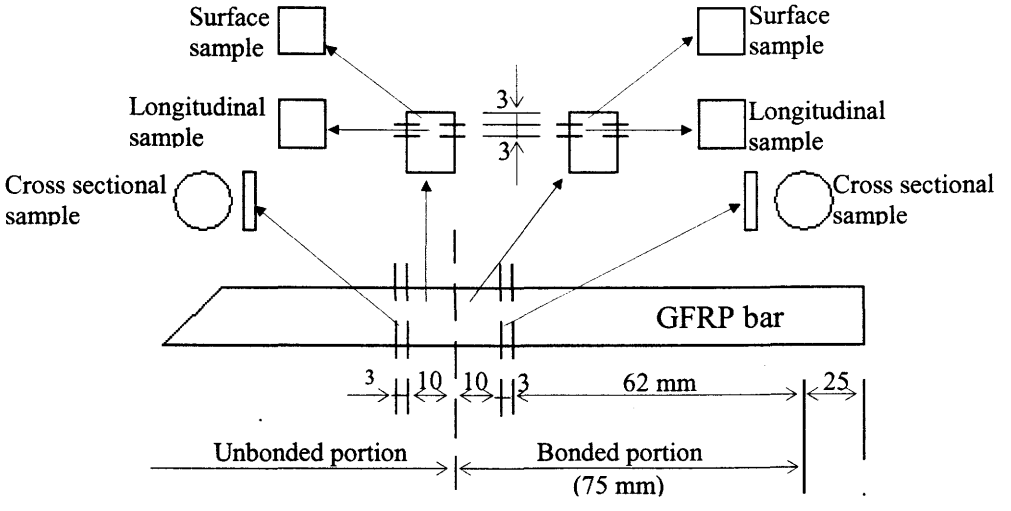

Dashed lines show the cut points.

Figure 3.26. Location of six SEM samples made from part of the bar inside the test end cylinder.

by means of a sputter coater. A total of 55 SEM samples were made and examined using SEM's models 505 and 515 manufactured by Philips. The SEM's were located in biology and mechanical engineering departments, respectively.

3.3.9. Electron microprobe analysis

An Electron Micro Probe Analyzer (EMPA), JXA-8600 Super probe manufactured by Jeol and located in geology department, was used to trace calcium and sodium ions (x-ray maps) in the cross sections of the bars embedded in concrete and exposed to water and alkaline environments. Also by using EMPA, backscattered images of the bar (as delivered) cross sections were obtained to find the fibre contents of the bars as mentioned in Section 3.3.5.2. After the SEM investigation (Section 3.3.8), some of the cross sectional samples made for the SEM were polished again to remove the gold coating and produce an undisturbed surface. These samples were moulded using Lecoset epoxy 7007 cold curing resin, polished using 0.25-micron paste, and then coated with carbon. The carbon-coated samples were put in EMPA (JXA-8600 Super probe manufactured by Jeol and located in geology department) to obtain the x-ray maps. These x-ray maps were compared with the x-ray maps obtained from cross sectional samples of the unloaded and unconditioned bars. These samples were also used to obtain backscattered images to find the fibre contents of the bars (Section 3.3.5.2). The basic information about electron microprobe analyzer is given in following paragraphs and is quoted directly from University of Oklahoma, electron microprobe laboratory, web site (January 2002):

> "The EMPA is based upon the electron optical column of a conventional scanning electron microscope (SEM), but incorporates a hardware addition specifically designed for the accurate, quantitative chemical analysis of solid materials. (Figure 3.27) illustrates different parts of an electron microprobe analyzer.
>
> Like the SEM, the EMPA uses a primary electron beam to stimulate signal emission. An important capability of the EMPA, however, is the ability to fix the beam into an immobile "spot" or probe of user-defined size and automatically monitored and regulated current. This permits the selection of single locations for irradiation at a constant electron flux over time.

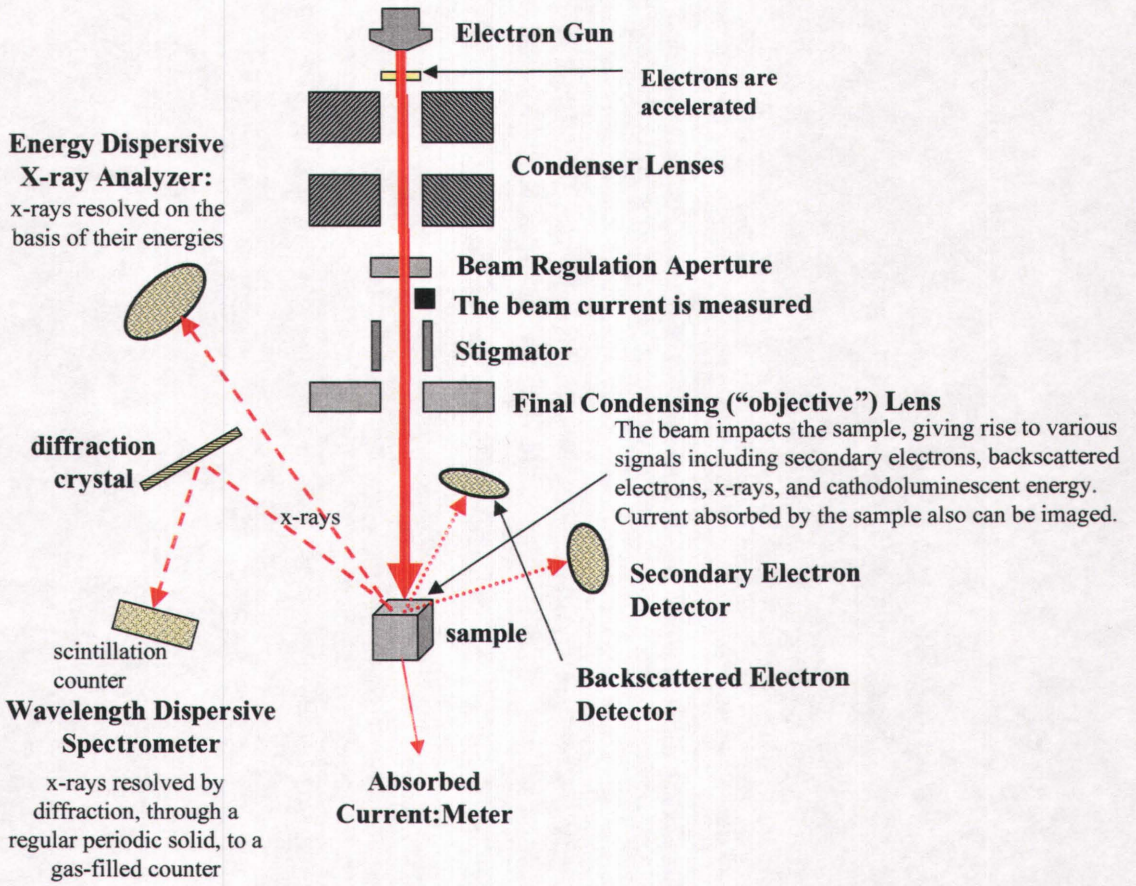

Figure 3.27. Different parts of an electron microprobe analyzer (after University of Oklahoma, electron microprobe laboratory (January 2002)).

Chemical analysis with the EMPA is performed by the detection and counting of fluorescent x-rays that are produced by electron transitions (from outer to inner orbitals) in atoms of the sample, the transitions being stimulated by electron bombardment (by the primary beam). Because the energy levels of electron orbitals for the atoms of a given element are intrinsic, the fluorescent x-rays also have characteristic energies. As a form of electromagnetic radiation, x-rays exhibit both particle- and wave-like properties, permitting two different methods of detection.

The particle-like properties allow separation on the basis of energies, using a solid-state detector in a device known as the energy-dispersive x-ray analyzer (EDXA). EDXA has the advantage of rapid analysis stemming from the simultaneous acquisition of the entire x-ray spectrum. The rapidity of this process makes it an invaluable qualitative tool for phase identification, and it can be used in a quantitative capacity as well.

The EMPA also can sort fluorescent x-rays on the basis of their wave-like properties utilizing one or more wavelength-dispersive

spectrometers (WDS): these are the "added hardware" mentioned above. The WDS resolve x-rays via diffraction through regular periodic solids in a manner very similar to the way a prism can separate component colours from white light. Hence by selecting the position and inter-planar spacing of the diffraction element, a single x-ray emission line can be resolved and sent to a gas-filled, "scintillation-type," detector for counting."

Chapter 4

Test results and discussions (Phase I)

4.1. Introduction

As mentioned in Chapter 3, a total of 48 pullout specimens were made and tested in Phase I of the experimental program (Sections 3.2.4, 3.2.7, and 3.2.8). The primary objective of these tests was to investigate long term bond slip behaviour of FRP reinforcement under sustained loads. Steel, GFRP, and two types of CFRP bars were used in the pullout specimens. Three specimens from each bar type were tested statically. Nine steel specimens were loaded from 14 to 90% of ultimate static pullout load (Table 3.4). GFRP bars and one type of CFRP bars (Leadline) were loaded to 60 and 75% of ultimate static pullout loads. Nine specimens made with another type of CFRP bars (CFCC) were tested under sustained loads of 60, 75, and 90% of ultimate static pullout load. The results of the tests are presented and discussed in this chapter. Also, the results obtained from scanning electron microscopy, which was used to investigate failure mechanisms, are given in this chapter.

4.2. Static tests

Pullout tests were performed on 12 specimens (3 for each bar type) to determine reference ultimate loads and capacities of the test specimens. For each specimen, tensile load was applied to the specimen at a steady rate using a universal testing machine. All specimens experienced a pullout failure, as expected.

A summary of static test results is presented in Table 4.1. As expected (see Section 3.2.2), steel rebar had the highest average bond strength of 24.5 MPa. Isorod had the lowest bond strength, with an average of 5.8 MPa (39% of bond strength

Table 4.1. Summary of static test results.

Material	Diam. (mm)	Free end slips at ultimate loads (mm)	Ultimate loads (kN)	Average ultimate load (kN)	Ave. bond strength (MPa)	C.O.V. (%)	Specified bond strength (MPa)	Ratio: Ave. bond/ Specified bond	Ratio: Ave. bond/ Steel bond
Steel	11.3	0.27, -, 0.27	43.6, 43.6, 43.4	43.5	24.5	0.2	-	-	1.00
Isorod	12.7	4.07, 1.63, 2.17	12.6, 10.6, 11.5	11.6	5.8	7.1	15	0.39	0.24
CFCC	15.2	0.00, 0.24, 0.05	24.6, 25.6, 26	25.4	10.6	2.3	7.2	1.47	0.43
Leadline	8	8.67, 8.00, 6.64	13.3, 15.2, 15.5	14.7	11.7	6.6	6.57*	1.78	0.48

* Maximum bond stress given for 12 mm nominal diameter Leadline rod (JSCE).

provided by the supplier, Pultrall Inc. 1992), which was 24% of steel bond strength. Leadline had the highest bond strength (11.7 MPa) among the FRP bars, although it had the highest free end slip at ultimate load (7.8 mm average). The average bond strength of Leadline bars was 48% that of steel. The CFCC performance was the best among FRP bars with respect to free end slip values. An average bond strength of 10.6 MPa was recorded for the CFCC specimens, which was 43% of steel average bond strength. Free end slips of CFCC specimens were lower than those of steel specimens, with an average value of 0.1 mm as compared to 0.27 mm for steel.

Figure 4.1 illustrates the load-slip curves for the steel specimens. Steel specimens achieved the highest ultimate loads. There was no slip at the free end of the specimens up to an applied load of at least 16 kN. The apparent slip at the loaded end was higher than slip at the free end at all load levels because some rotation occurred in the bearing plate to which the dial gauge was attached, as explained in Section 3.2.7. The slip values at ultimate load were higher than those at critical bond stress. For steel reinforcing bars at service load conditions, the critical bond stress is defined as the

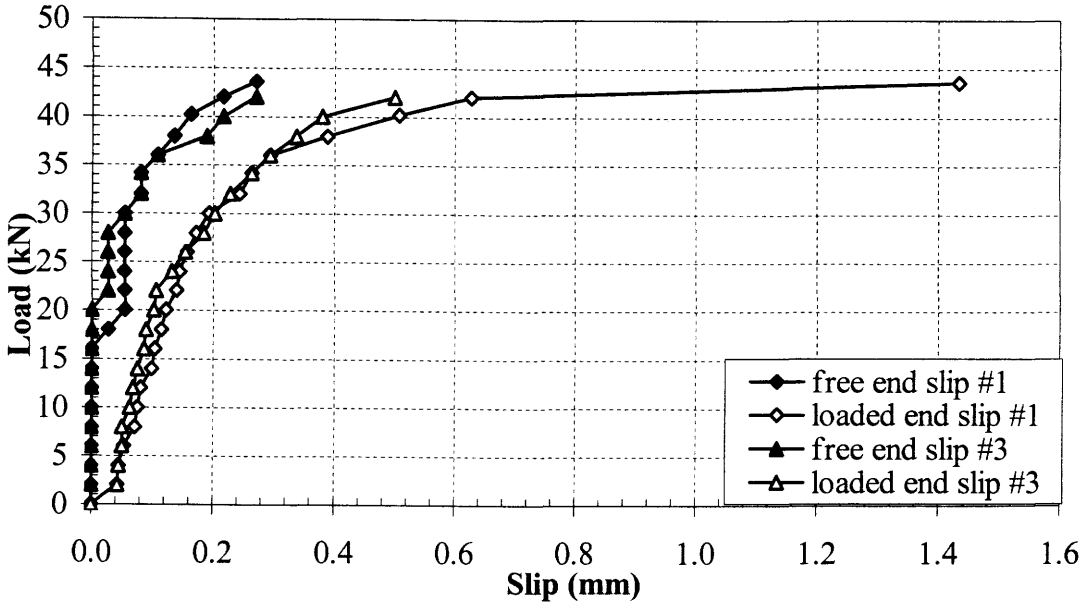

Figure 4.1. Load versus slip curves for steel specimens.

smaller of that associated with a free end slip of 0.05 mm or a loaded end slip of 0.25 mm (Mathey and Watstein 1961).

At the ultimate load, the bar pulled through the concrete as the bar lugs crushed and sheared the confining concrete. No damage was observed on the bar surface. An average ultimate load of 43.5 kN was obtained for the three specimens tested statically. The average slip at the free end was 0.27 mm for Specimens #1 and #3 at ultimate loads.

The curves are not shown for steel Specimen #2 since the load was not back to zero at the end of the test. This load reading was –9 kN. The cause of the load shift during the test could not be determined. Adding 9 kN to the obtained ultimate load (34.6 kN) resulted a load close to ultimate loads obtained from the tests of Specimens #1 and 3. Therefore, the value of 43.6 kN was used as ultimate load for Specimen #2 when calculating the average ultimate load. However, the slip values could not be used for this specimen since the point of load shift during the test could not be determined.

Three Isorod specimens in the static tests failed at lower loads than expected values, when compared to the value given by the manufacturer (Pultrall Inc. 1992). The

average ultimate load obtained from these three tests was 11.6 kN. This gives an average bond stress of 5.8 MPa, 61% less than the bond stress (15 MPa) specified by the manufacturer. The bond between the lugs and shaft of the bar was found to be weaker than the bond between the bar and concrete since the helical wrappings around the bar (lugs) sheared away from the main shaft of the bar and remained inside concrete cylinder while the bar shaft was pulled out of the concrete (Figure 4.2). There was little evidence of any damage to the concrete surrounding the lugs. Subsequent investigation revealed that the manufacturer has modified the design of this reinforcement to improve its bond resistance (Pultrall Inc.). This improved design bar was used in Phase II of this program.

As can be seen in Figure 4.3, there was a negligible free end slip in all specimens below an applied load of approximately 2 kN. This applied load can then be considered as the force that caused breaking of the adhesion in the entire embedment length of the bar. The loaded end slips were higher than, but close to, the free end slips, which was an indication of slipping of the entire bar inside concrete. The free end slip values at ultimate loads were much higher than those of steel specimens. An average value of 2.6 mm was obtained for three Isorod specimens at the free ends, compared to

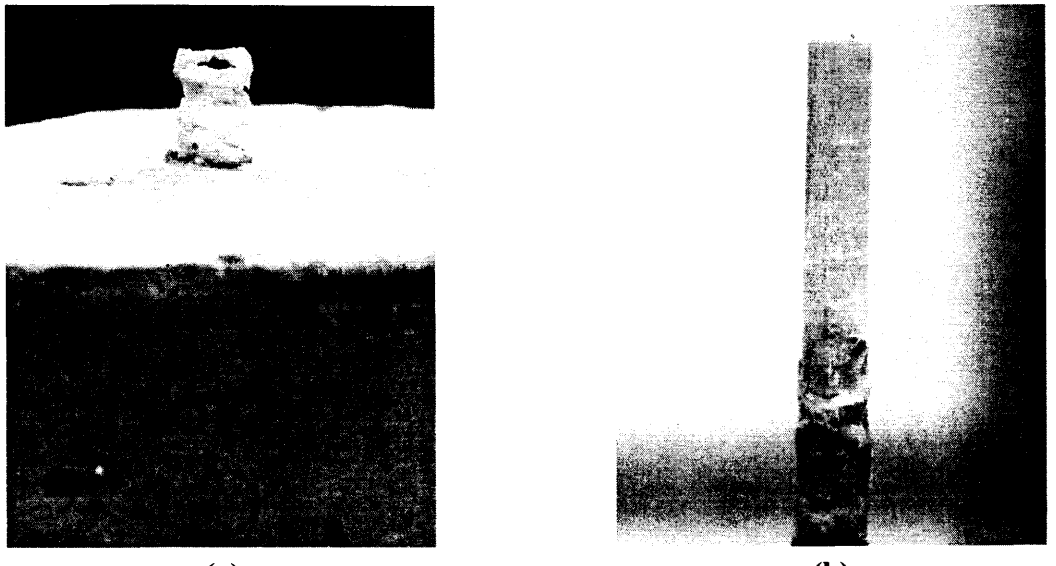

(a) **(b)**

Figure 4.2. Loaded end of the pullout specimen made with Isorod bar after the static test: **(a)** the lugs of the bar remaining in the concrete cylinder, and **(b)** the main shaft of the bar.

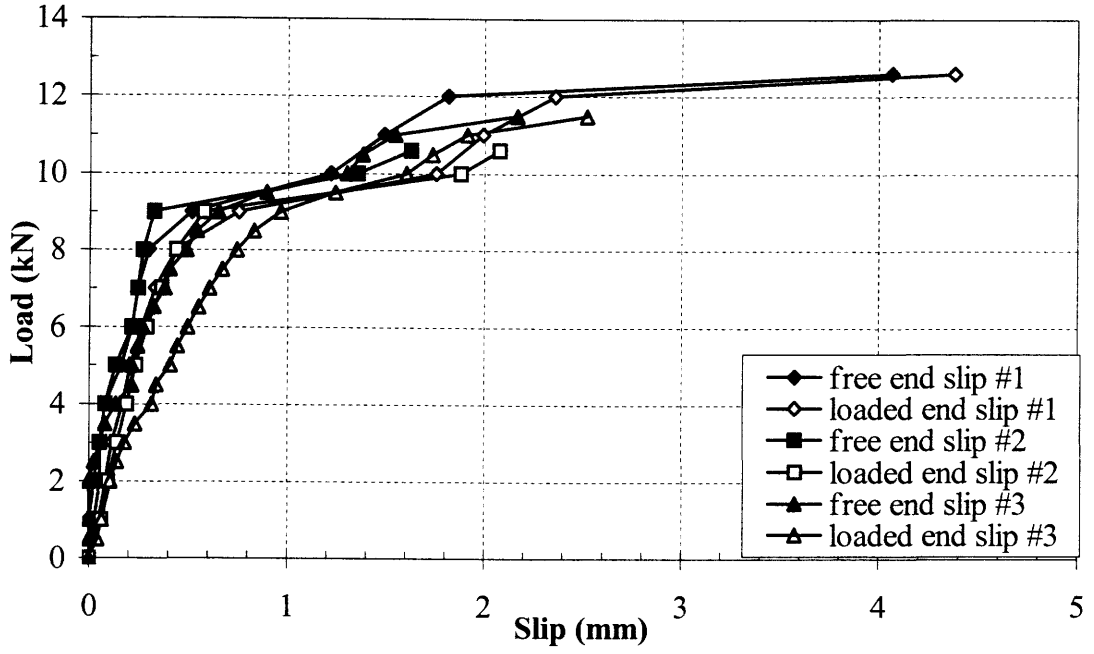

Figure 4.3. Static test load-slip curves for Isorod specimens.

0.27 mm for the steel specimens.

Scanning Electron Microscopy (SEM) was used to do more investigation on the surface of the bar. Figure 4.4 shows images of surface of the Isorod bar in the bonded region before and after the static test. Only the sand coating of the bar could be observed before the static test. During the test, however, the coating of the bar was damaged and the glass fibres were exposed. Fibres close to the surface of the bar were

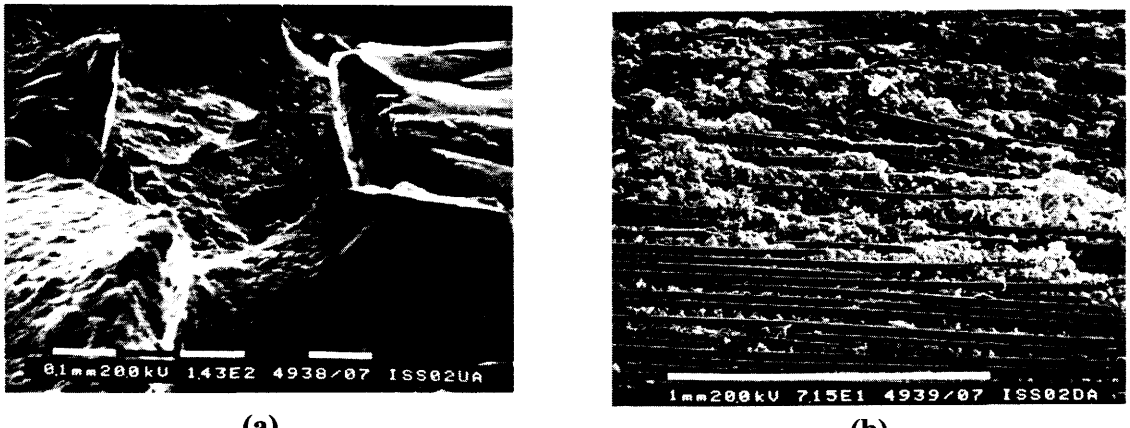

(a) **(b)**

Figure 4.4. SEM images of the surface of the Isorod bar: **(a)** showing sand coated surface before the test, **(b)** showing damaged surface with broken fibres after the pullout test.

seen to be broken and damaged.

The Leadline specimens had the highest free end slips among the FRP bars with an average free end slip of 7.8 mm at ultimate loads. During the tests, sudden slippage of the bars was observed due to local damage to the indentation of the bars accompanied by banging sounds. Since the bars had indentions on the surface, the mechanical interlock between the indentations and the concrete was the main bond mechanism contributing to total bond. Bond related damage to the Leadline bars was apparent, though higher loads achieved in these tests also produced some visible cracking to the surrounding concrete. Photos of the bar surface, before and after the static test, for one of the specimens are shown in Figure 4.5. Indentations of the bar after the test were either flattened in some areas or damaged partially in other areas of the bar indicating the loss of the mechanical interlock between the bar and the surrounding concrete.

Damage to the bar coating and indentations was observed using scanning electron microscopy. As shown in Figure 4.6b, carbon fibres close to the surface of the bar were broken, and the coating and indentations of the bar were totally removed in the area shown.

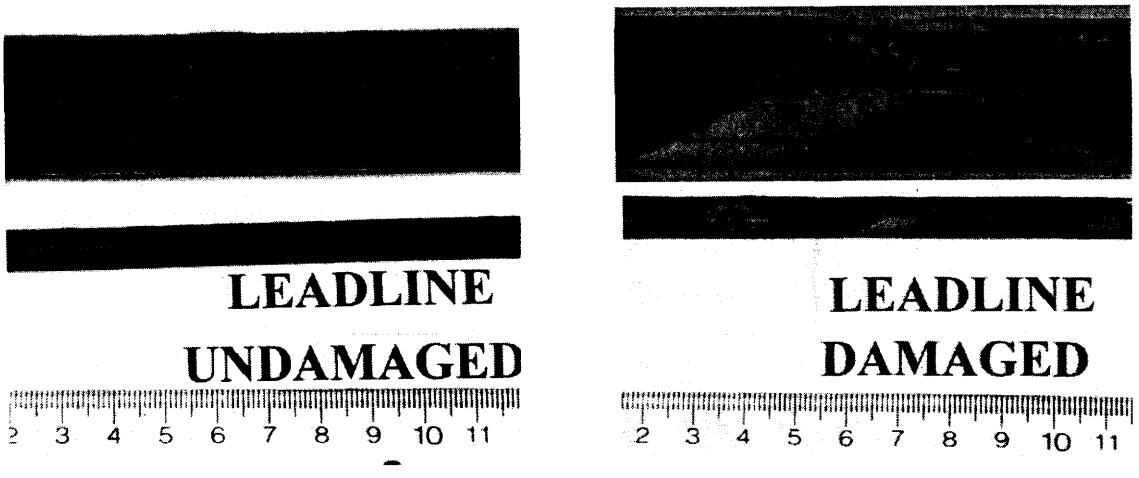

(a) **(b)**

Figure 4.5. Photos of the surface of the Leadline bar: **(a)** showing bar indentation before the static test, and **(b)** showing damage to the bar indentation after the test.

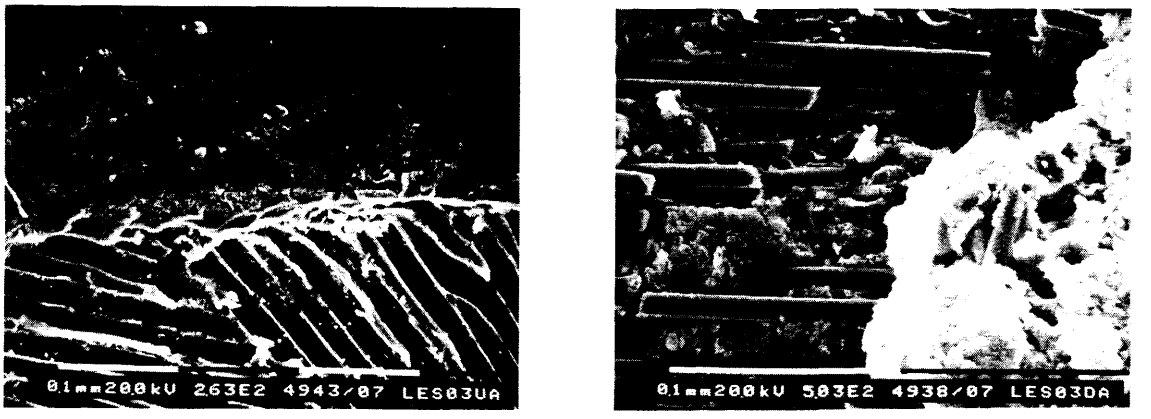

(a) **(b)**

Figure 4.6. SEM images of the Leadline bar: **(a)** coating and part of indentation on the bar surface before test, **(b)** damaged surface of the bar and broken fibres after static test.

Load-slip curves for Leadline specimens are presented in Figure 4.7. The loaded end slip curve for Specimen #1 could not be shown because the angle, which was attached to the bar at the loaded end, separated from the bar after three readings. As shown in Figure 4.7, the free end of the bars began to slip at a load of approximately 6 kN. Larger slips were apparent at higher loads with the loaded end slips observed to be a little higher than the free end slips. As mentioned before, sudden slips of the bars occurred during the tests. Sudden slips caused some drop in the load, but the load

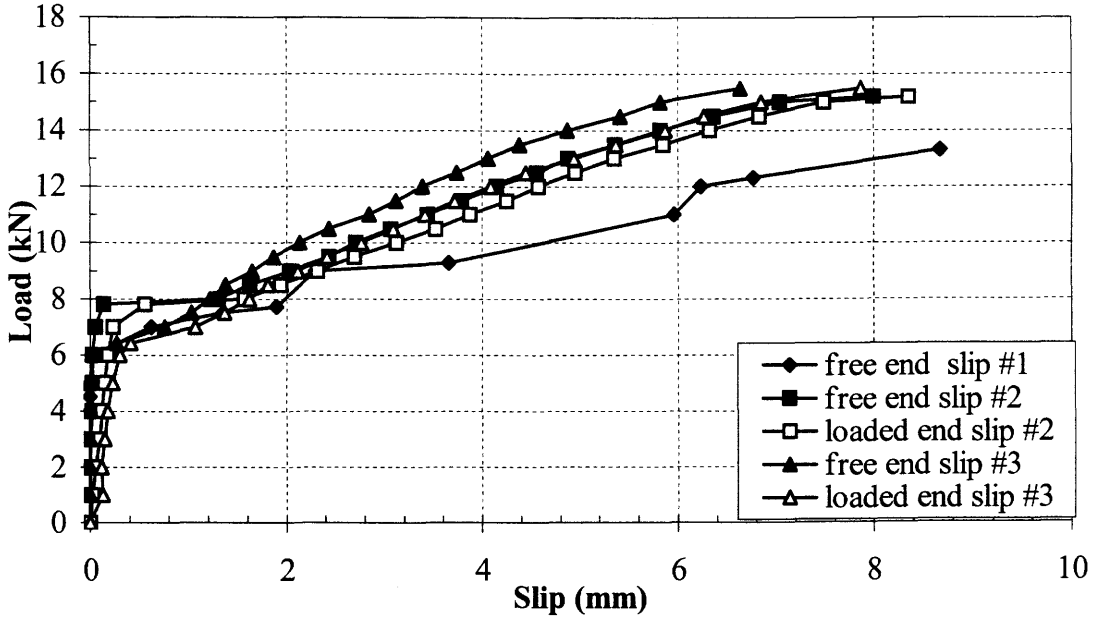

Figure 4.7. Load versus slip curves for Leadline specimens.

subsequently started to increase again.

An average ultimate load of 14.7 kN was found. The calculated bond stress (11.7 MPa) was 78% higher than the specified maximum bond stress of 6.57 MPa (JSCE). No bond stress was provided in the product specification for Leadline (Mitsubishi Corporation 1993).

CFCC specimens performed well in the static pullout tests. The CFCC bars were made of seven individual strands. Each strand had a diameter of 5 mm with six strands wrapped in a gradual helical pattern around a single strand at the centre of the bar (Figure 4.8(a)). During the static tests, damage to the surface of bar was observed (Figure 4.8(b)). More investigation, using SEM, revealed that the coating of each individual strand consisted of thicker fibres (about 40 μm in diameter) wrapped around longitudinal carbon fibres (Figure 4.9(a)). After the test, only this coating was damaged and no significant damage to the longitudinal carbon fibres was observed (Figure 4.9(b)).

As shown in Figure 4.10, free end slips at ultimate loads were 0.24 and 0.05 mm for Specimens #2 and #3, respectively. A zero slip was measured at the free end of Specimen #1 until just before the ultimate load was reached. The average free end slip for CFCC bars was lower than that of steel: 0.1 mm compared to 0.27 mm. An average bond strength of 10.6 MPa was obtained, which was 47% higher than the concrete adhesion strength (7.2 MPa) given in the manufacturer's specification (Tokyo Rope Mfg. Co. Ltd. 1993). However, the latter was based on a less efficient embedment

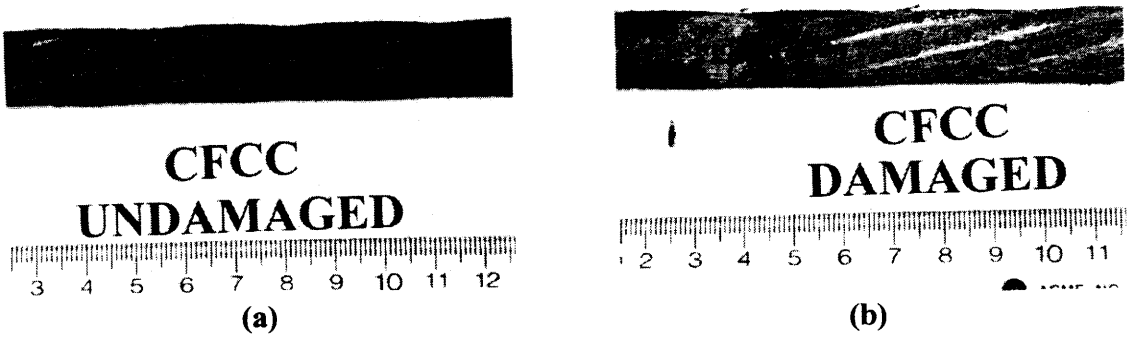

Figure 4.8. Photos of surface of CFCC: (a) before the test, (b) after the static test.

(a) (b)

Figure 4.9. SEM images of CFCC surface: **(a)** showing fibres wrapped around one of the strands (coating) of the bar before the test, **(b)** showing damaged wrapped fibres exposing longitudinal fibres after the static test.

length of 150 mm when compared with the 50 mm length used in this study.

Due to some initial curvature of the bars in the CFCC specimens, measured loaded end slip values were much higher than free end slips. As the bar was becoming straight due to applied tensile load, the angle (attached to the bar at the loaded end) experienced rotation as well as displacement, both of which contributed to the dial gauge readings. For this reason, the loaded end slips shown in Figure 4.10 should be

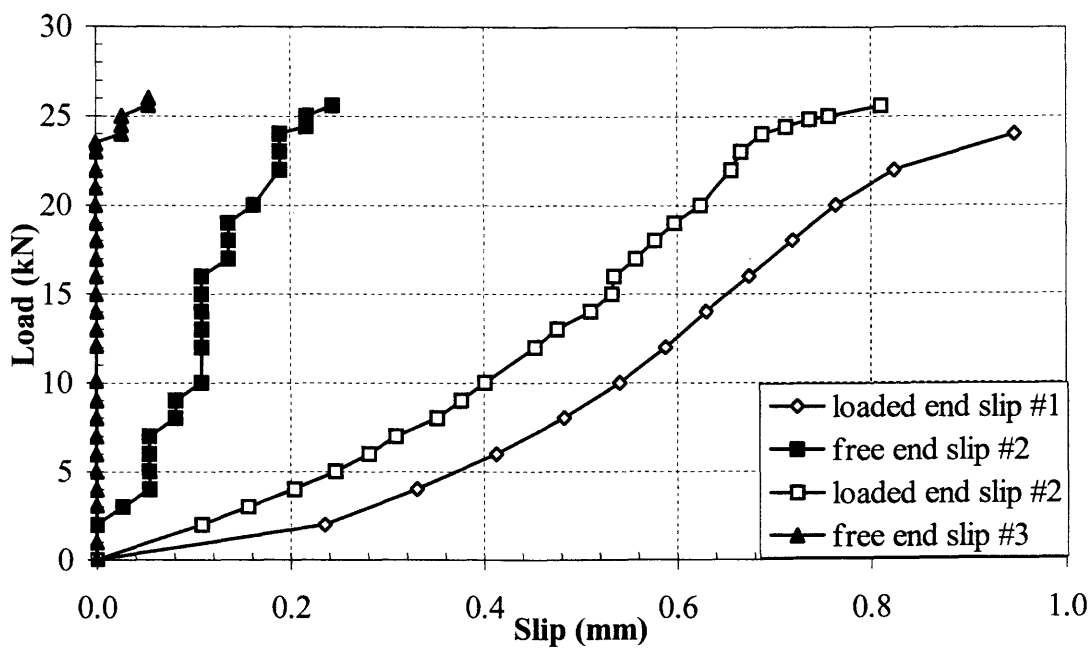

Figure 4.10. Load-slip curves for CFCC specimens.

viewed with considerable caution.

In summary, the FRP bars showed less bond strength than that of the steel rebar as the bond between the FRP bar surface deformations and the main shaft of the bars was weaker than the bond between the bars and the concrete. In steel rebars, mechanical interaction caused crushing of the surrounding concrete. For Isorod and Leadline bars, mechanical interlock between the bars surface deformations (lugs or indentations) and the concrete appeared to be the main mechanism in transferring the bond stress since the lugs or indentations were damaged in the pullout tests. For CFCC bars, the main resisting mechanism was friction. The helical wrapping pattern, however gradual, would produce some degree of mechanical interlock.

4.3. Long term tests

4.3.1. Overview

A total of 36 specimens (nine of each reinforcing bar category) were tested under sustained loads set at various levels lower than the ultimate static loads. Relatively uniform sustained loads were applied to the specimens. Loads were monitored and adjusted during the tests, if required. However, it was found to be difficult to maintain the loads in the Isorod and Leadline specimens with a load level of 75% of the ultimate load.

Free end and loaded end slips were measured. However, it was realized that loaded end slips were not being measured correctly due to the limited visibility and accessibility of the measurement points, which made taking consistent measurements very difficult. Loaded end slips were even found to be smaller than free end values in some cases, a result which is obviously erroneous. Therefore, loaded end slip values were discarded.

Table 4.2 summarizes long term test results. As discussed in Chapter 3, the reference load levels (60%, 75%, etc.) were based on the static strength of companion specimens, tested under short term loading (that were designed to fail in pullout). As

Table 4.2. Summary of long term test results.

Material	Specified bond stress (MPa)	Bond stress/ Static bond strength (%)	Tensile stress/ Tensile strength* (%)	Bond stress (MPa)	Specimen no.	Test period (days)	Initial slip (mm)	Final slip (mm)	Change in slip (mm)	Comments
Steel	-	14	13	3.4	1	431	0.03	0.12	0.09	
		20	18	4.8	1	430	0.10	0.25	0.15	
		26	24	6.3	1	366	0.03	0.14	0.11	
		33	30	7.9	1	366	0.09	0.19	0.10	
		39	35	9.4	1	366	0.04	0.18	0.14	
		45	40	10.8	1	347	0.13	0.19	0.06	
		60	54	14.5	1	434	0.12	0.35	0.23	
		75	68	18.1	1	431	0.29	0.50	0.21	
		90	82	21.7	1	350	0.51	0.88	0.37	
CFCC	7.2	60	6.3	6.3	1	289	0.10	0.17	0.07	
					2	277	0.13	0.23	0.10	
					3	366	0.28	0.48	0.20	
		75	7.9	7.9	1	273	0.17	0.37	0.20	
					2	272	0.00	0.16	0.16	
					3	350	0.21	0.30	0.09	
		90	9.5	9.4	1	Overloaded to 98% accidentally.				
					2	Premature pullout failure at 76% load.				
					3	345	0.16	0.27	0.09	
Leadline	6.57	60	7.5	7.0	1	242	1.52	2.86	1.34	
					2	328	1.05	3.70	2.65	
					3	329	0.95	3.17	2.22	
					4	309	2.46	5.54	3.08	
					5	Premature pullout failure at 57% load.				
		75	9.4	8.8	1	284	3.65	8.38	4.73	
					2	242	2.76	5.90	3.14	
					3	309	3.63	8.59	4.96	
					4	128	4.19	9.95	5.76	Pullout failure.
Isorod	15	60	8.0	3.4	1	320	1.23	1.99	0.76	
					2	329	0.53	1.41	0.88	
					3	330	0.03	0.24	0.21	
					4	330	0.49	0.77	0.28	
		75	10.1	4.3	1	Premature pullout failure at 37% load.				
					2	Premature pullout failure at 32% load.				
					3	94	1.00	14.84	13.84	
					4	Premature pullout failure at 66% load.				
					5	1	3.47	14.24	10.77	Pullout failure.

* Yield strength for steel and ultimate tensile strength for FRP bars as given by manufacturers.

another measure of load intensity, however, the load levels relative to the ultimate tensile strength of the bars are also provided. The CFCC bars performed well under sustained loads. Although the free end slips were higher than the companion steel specimens (with 26, 33, and 39% load levels), they were much smaller than those of the Isorod and Leadline bars. The Isorod specimen with a 75% load had the highest free end slip, although the bond stress was less than that of comparable CFCC and Leadlline specimens. The Isorod specimen with a 60% load performed better than corresponding Leadline specimens. Free end slips ranged from 1.34 to 5.76 mm in the Leadline specimens, which were much higher than the slips in the companion steel specimens.

Long term test results are presented and discussed in detail in the following sections. For the FRP bars, a typical load-slip curve and load history curve are shown and discussed for each load level (percentage of the applied load to ultimate load obtained from static pullout tests) followed by load-slip curves for all specimens with the same load level. Also, the surfaces of the tested bars were observed under scanning electron microscope (SEM) to investigate the damage to the bars under sustained loads. These results are also available in the following sections. SEM images are presented only for the specimens with highest load level for each bar category.

4.3.2. Steel rebar

Nine steel specimens were loaded in the range of 14 to 90 percent of the average ultimate load obtained from static tests (see Table 4.2). The free-end slips are provided in Figure 4.11. The initial free end slip (slip at time=0 or immediate slip after application of load) varied from 0.03 to 0.51 mm for the various load levels. For steel reinforcing bars at service load conditions, the critical bond stress is defined as the smaller of that associated with a free end slip of 0.05 mm or a loaded end slip of 0.25 mm (Mathey and Watstein 1961). However, bond strengths cited in this study are based on ultimate load conditions, where much larger slips were encountered.

As shown in Figure 4.11, free end slips reached maximum values and stabilized after approximately 100 to 150 days, except at high load levels. A significant free end slip of 0.9 mm was observed with the steel specimen loaded to 90 percent of ultimate

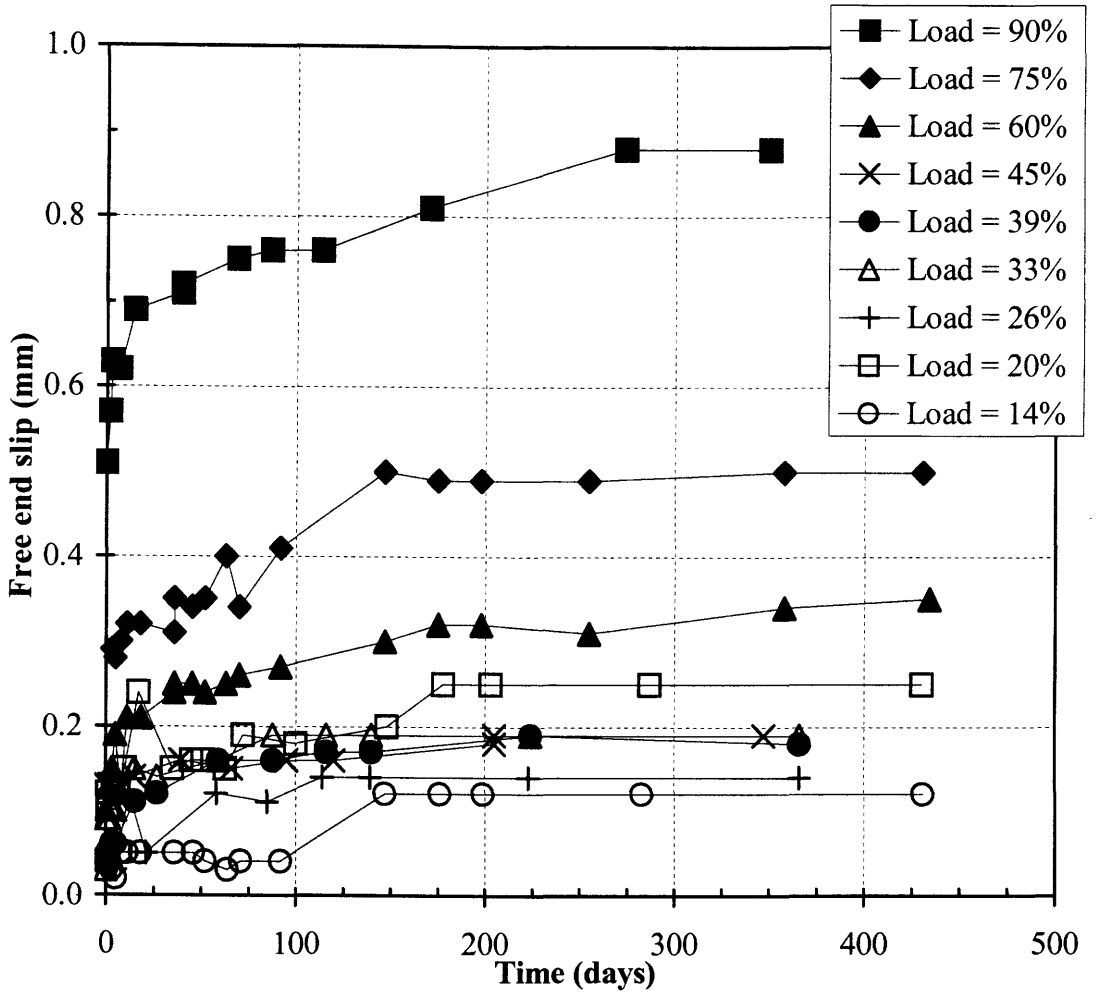

Figure 4.11. Slip-time curves for steel specimens.

load after 350 days, while the slip of the specimen with 14% load was 0.12 mm after 431 days. Although there is some discrepancy in the data for the specimens with 20 and 33% loads, Figure 4.11 shows bond degradation occurred much sooner in the specimens with higher loads when compared with the specimens with lower loads. Initial slips indicated that the adhesion between the bars and concrete were lost and stresses produced by the ribs bearing against concrete caused internal cracking of the concrete at the location of the ribs as shown by Goto (1971). As time increased, increased slip occurred, indicating the developing of the internal cracks. At lower loads up to 45% of the static bond strength, the stabilizing of the slip values verified that internal cracking did not develop after 100 to 150 days. However, internal cracks continued to develop at higher loads due to higher stress concentrations at the ribs. Since none of specimens

failed under the sustained loads and the total changes in slip values ranged from 0.09 mm to 0.37 mm over the entire test period it could be concluded that the overall long term bond performance of steel rebar was acceptable and not likely to lead to failure except perhaps at the 90% load level.

4.3.3. CFCC bars

A total of nine CFCC specimens were tested under sustained loads of 60 75 and 90% of the average ultimate load obtained from static tests (6.3-9.5% of the ultimate tensile strength of the bars). It was intended that three CFCC specimens be subjected to a sustained load of 90% of the average static bond strength. One specimen was accidentally overloaded to failure. The second specimen experienced pullout failure prematurely at 76% of static strength, most probably because of poor fabrication of the specimen. Therefore, only one specimen could be loaded to 90% of ultimate static load. This specimen, though, performed well under sustained load. Figure 4.12 shows the free end slip versus time for the specimen, as well as load level maintained during the test period. There was no significant change observed in the load and, therefore, no need to adjust the load significantly. As shown, the load level dropped about 2% after 112 days,

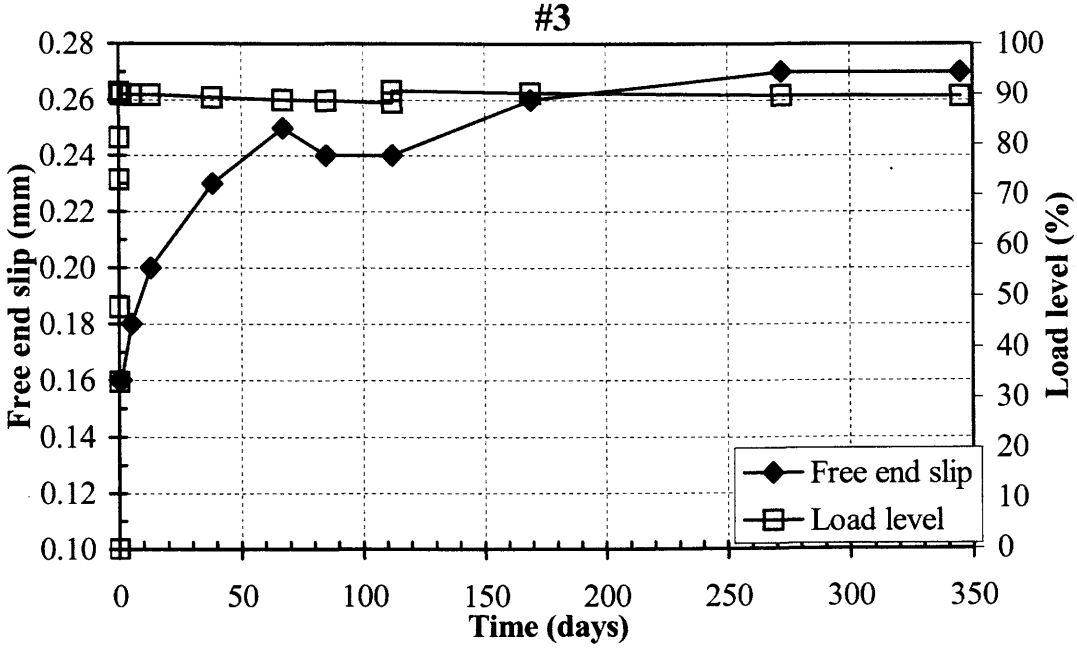

Figure 4.12. Slip-time curve for CFCC specimen (#3) with 90% load level.

at which time it was adjusted. An initial slip (immediate slip after application of load) of 0.16 mm was recorded. The free end slip increased to 0.25 mm after 67 days, with little change (0.02 mm) occurring after that. The total change in free end slip was 0.11 mm after 345 days.

The steel specimen loaded to 39% of its static strength had the same bond stress of 9.4 MPa as the CFCC specimen loaded to 90% of its static strength. The steel specimen (Figure 4.11) had a free end slip of 0.04 mm initially, increasing to 0.18 mm after 366 days. These values were smaller than the free end slips for the CFCC specimen with 90% load level. Since CFCC bar had softer surface compared to the steel rebar, a larger initial slip was seen for CFCC bar. After the initial slip and seating the CFCC bar into place, the change in slip was slightly lower than that of the companion steel rebar (0.09 mm vs. 0.14 mm in steel), indicating similar behaviours under the same level of bond stress. However, both the CFCC and steel can be said to have good bond performance at this level of sustained bond stress since the slip values were low and comparable.

The effect of sustained load on the CFCC bar surface is shown in Figure 4.13.

Figure 4.13. SEM image of the surface of the CFCC specimen (#3) with 90% load level after the test. Damage to coating (wrapped fibres) is evident.

Some of the wrapped fibres around the strand (bar coating) were damaged, but no broken longitudinal carbon fibres could be observed. This observation is consistent with the good bond performance of CFCC under high sustained load (90% of static strength) as discussed above.

Three CFCC specimens were loaded to the 75% load level (i.e. 75% of the static bond strength). A typical free end slip versus time curve for one of the specimens is displayed in Figure 4.14. It was noted that the load did not change, but remained at the desired level during the test. The initial slip at the free end was 0.21 mm. The free end slip increased to 0.3 mm after 350 days. The total change in slip was therefore 0.09 mm for the specimen after being under sustained load level of 75% for 350 days.

To compare the behaviour of the specimens, slip-time curves for all three specimens with 75% load level are provided in Figure 4.15. Initial slips ranged from 0 to 0.21 mm. Free end slips became stable within the first 57 days, after which there was little change (0.04 mm). The total change in free end slips over the entire loading period were 0.2, 0.16, and 0.09 mm for Specimens #1, #2, and #3, respectively.

For the steel specimen with the same bond stress of 7.9 MPa (at the 33% load level), free end slips were 0.09 mm initially and increased to 0.19 mm after 366 days

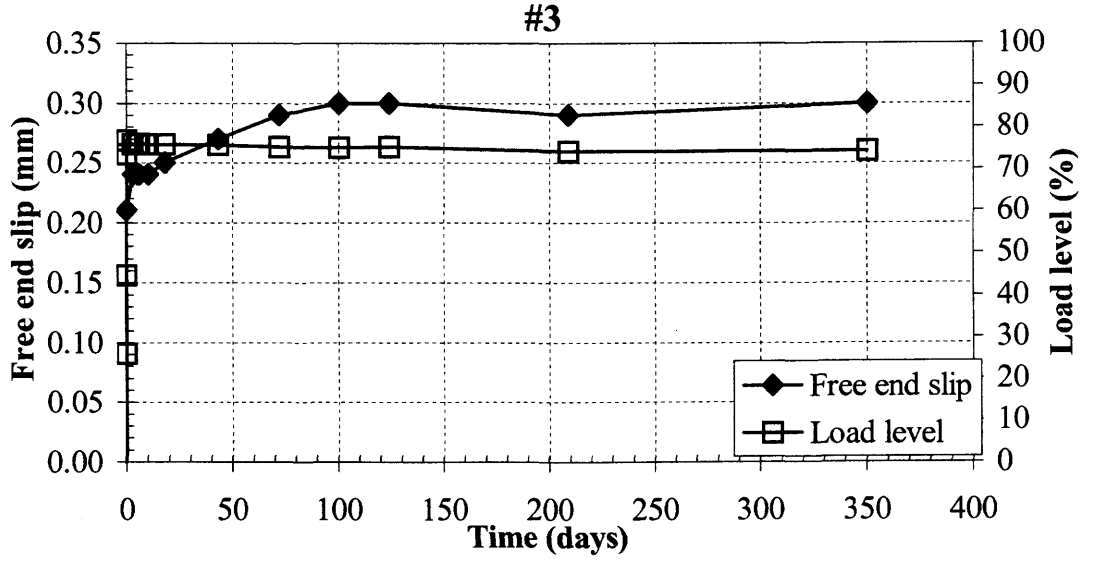

Figure 4.14. Slip-time curve for CFCC Specimen #3 with 75% load level (typical).

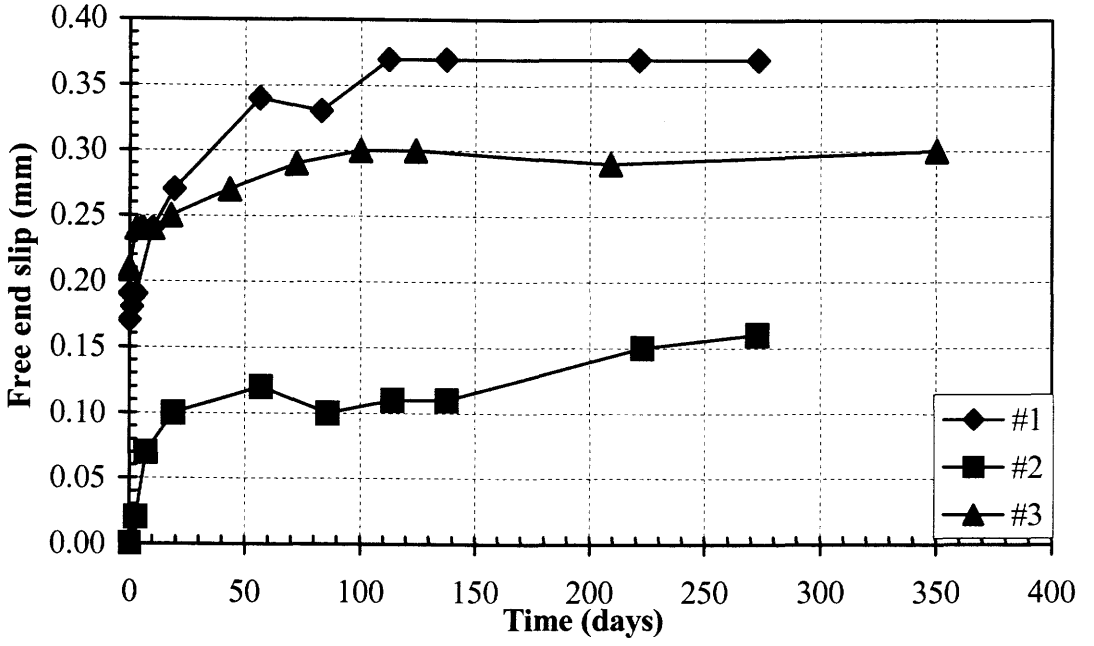

Figure 4.15. Slip-time curves for all CFCC specimens with 75% load level.

(Figure 4.11). The CFCC specimens with 75% load level therefore showed higher free end slips than their companion steel specimen; however, the CFCC slip values were not excessive and were considered to represent acceptable performance.

An example slip-time curve for one of the CFCC specimens at the 60% load level is shown in Figure 4.16. The initial applied load was easily maintained during the test period, with only a minor adjustment in load required after 20 days. As shown, the free end slip was 0.1 mm initially and increased to 0.17 mm after 289 days. A decrease of 0.01 mm in free end slip was measured after 147 days, which could not be correct and should be ignored (measurement error). Slip values stabilized after 100 days and there was no increase in slip after that, indicating good bond performance under the sustain load.

The long-term slip behaviour of the three CFCC specimens at the 60% load level are compared in Figure 4.17. Specimen #3 had larger free end slip values than those of the other two specimens. This could indicate a weaker bond due to faulty fabrication of the specimen. Specimens #1 and #2 exhibited similar behaviours, with the free end slips initially measured at 0.1 and 0.13 mm, and then increasing to 0.17 and

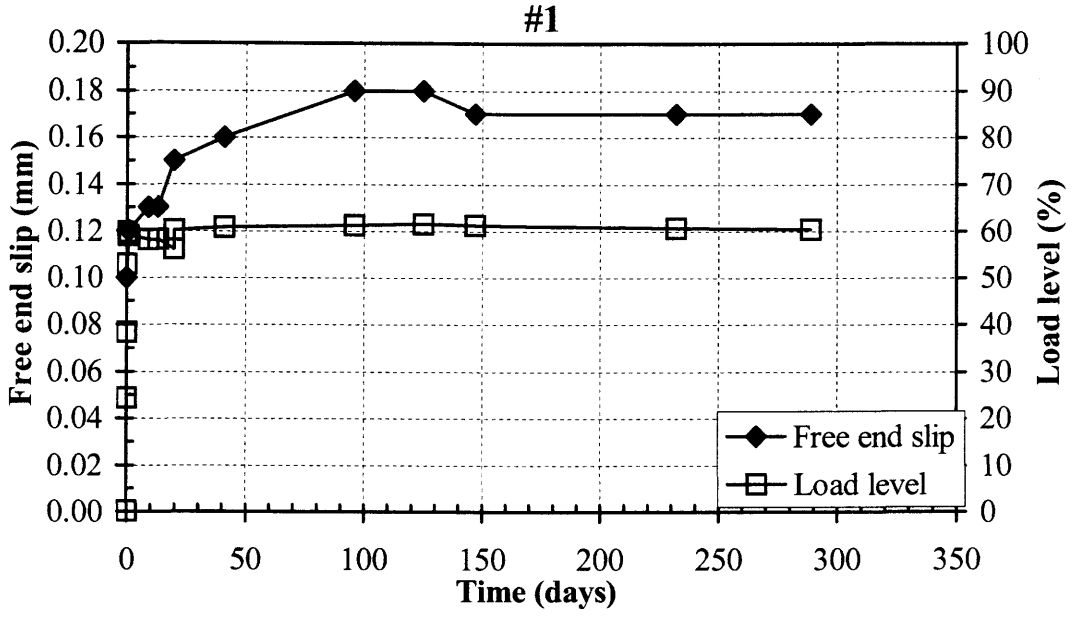

Figure 4.16. Load-slip curve for CFCC Specimen #1 with 60% load level (typical).

0.23 mm after 280 days. No change in free end slips could be seen after 96 days in the two specimens.

The steel specimen with a 26% load level had the same bond stress (6.3 MPa) as

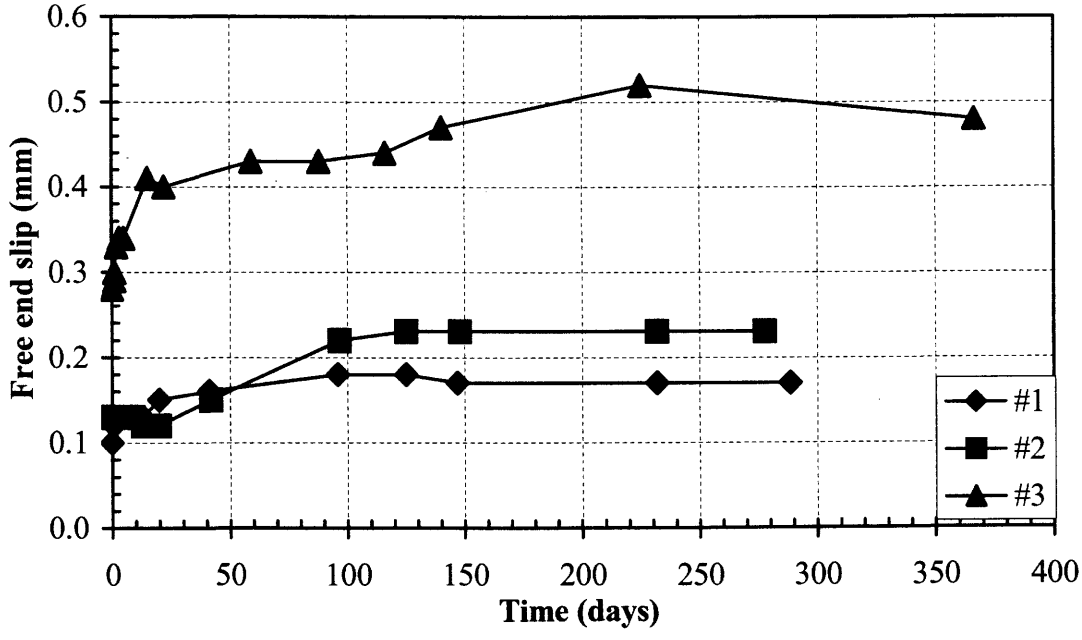

Figure 4.17. Slip-time curves for all CFCC specimens with 60% load level.

the CFCC specimens with a 60% load level. The steel specimen had a free end slip of 0.03 mm initially and 0.14 mm after 366 days (Figure 4.11). These values are less than the corresponding values for CFCC specimens with a 60% load level, but the change in slip for the two bars was comparable.

In general, CFCC specimens showed good bond performance under sustained loads. Initial slips were higher for CFCC bars than those in the companion steel rebars mostly because CFCC bars had softer surface relative to steel bars. The CFCC bars were made of spirally wrapped strands on the outer layers, which tended to twist and to become straight under sustained tensile load. The concrete surrounding the strands prevented the strands from twisting and becoming straight, causing the bars to bear against the concrete. After initial slip, the friction between the bars and the concrete resisted the applied stresses. This explains similar bond performance for CFCC and steel bars after initial slips occurred in both bars.

Also, in the CFCC specimens with 75 and 90% load levels, free end slips were not that high compared to other FRP bars tested although the applied bond stresses (7.9 and 9.4 MPa) were higher than allowable bond stresses specified by the manufacturer (Tokyo Rope Mfg. Co. Ltd. 1993) and American Concrete Institute (ACI 2001), 7.2 (concrete adhesion) and 4.63 MPa, respectively.

4.3.4. Leadline bars

A total of nine Leadline specimens were tested under sustained loads. Four specimens were loaded to 60% and four to 75% of ultimate bond strength obtained from static tests (corresponding to 7.5 and 9.4% of the ultimate tensile strength of the bars). The remaining specimen experienced premature pullout failure at a load level of 57% of the static bond strength. A sudden drop in load during loading of this specimen was accompanied by a measured increase in slip. It was not possible to subsequently increase the load. It was found to be difficult to apply the required loads because of sudden drops in the loads associated with large initial slips at free ends. Although it was possible to maintain the 60% and 75% loads with difficulty, large slips occurred every

time the loads were adjusted. It was therefore decided not to test a 90% load level for Leadline specimens.

The slip-time behaviour of Leadline Specimen #1 with 75% load level is shown in Figure 4.18. Large free end slips of 3.65 mm initially and 8.38 mm after 284 days occurred for this specimen. As shown, the load had to be adjusted several times, with some slip of the bar occurring at every load adjustment. A sudden release of load, signalled by a banging sound, occurred several times during the test period. This was found to be due to bond deterioration causing the slip of the bar and a decrease in the load.

Following the test, the bar used in Specimen #1 was taken out of the concrete cylinder at the test end (Section 3.2.9). A sample from the surface of the bar was cut and prepared for investigation under scanning electron microscope (SEM). The SEM image of the sample is displayed in Figure 4.19. Bond deterioration was evident. The coating with indentations on the bar surface was seen to be almost completely removed and some of the longitudinal carbon fibres were distorted and broken.

The slip-time curves for all Leadline specimens with 75% load level are provided in Figure 4.20. All specimens experienced large free end slips. Free end slips

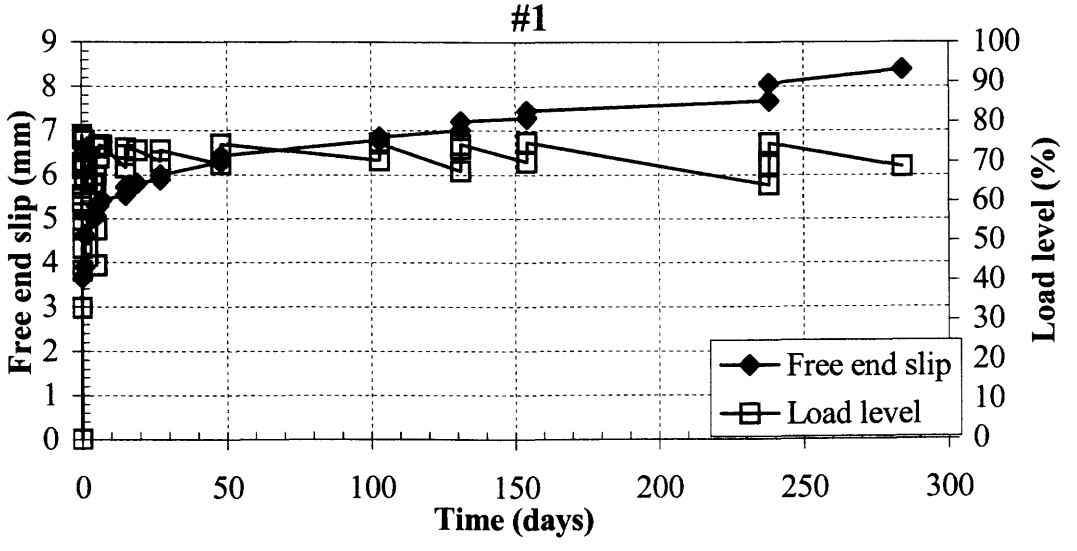

Figure 4.18. Slip-time curve for Leadline Specimen #1 with 75% load level (typical).

specimens experienced pull out failure due to separation of the lugs from the shaft of the bar (Figure 4.23).

The last specimen (designated as #3) was loaded successfully to 75% of the static bond strength. The slip-time curve for this specimen is shown in Figure 4.24. The free end slip was 1.22 mm at first and increased to 8.96 mm after 27 days at which time the load level dropped to 60%. During this 27-day period, load was adjusted several times. After 22 days, the load level was 41% with and free end slip was 4.05 mm. The free end slip increased to 7.79 mm when the load level was adjusted. After 27 days, the top part of the loading frame was lifted up to accommodate additional tightening of the nut on the aluminum rod. After releasing the jacking system, the load level was measured as 26% of the static bond strength, which can be seen in Figure 4.24. The free end slip was 9.95 mm after adjusting the load level. After 94 days, the free end slip was 14.84 mm. Due to the very large slip values, the test was not continued after 94 days.

The companion steel specimen with a 20% load level had a bond stress of 4.8 MPa, as compared to a bond stress of 4.3 MPa in the Isorod specimen (#3) loaded to 75% of the static bond strength. The slip values were much higher in the Isorod specimen than those of the companion steel specimen (0.1 mm and 0.25 mm at first and

Figure 4.23. Photo of failed Isorod specimen at test end. The specimen experienced premature pullout failure at 66% load.

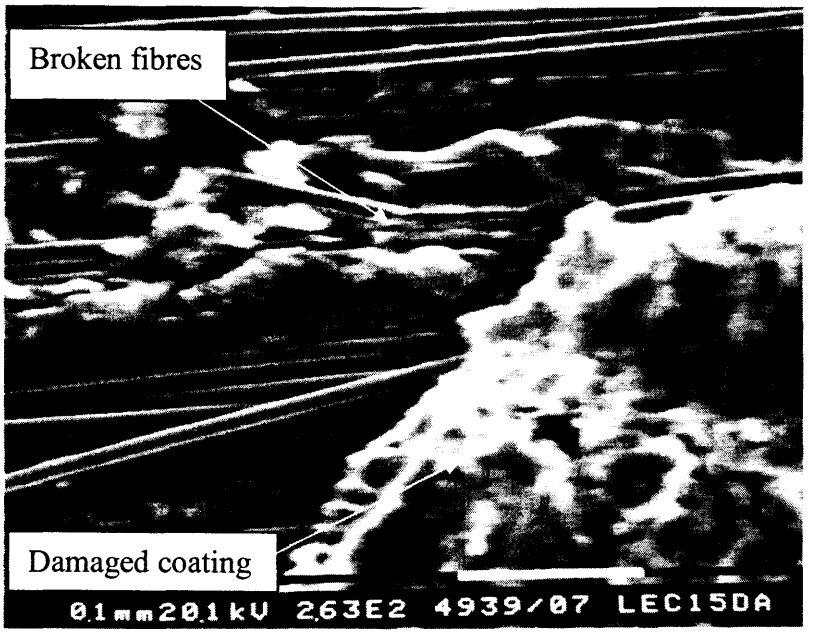

Figure 4.19. SEM image of the surface of Leadline with 75% load level (Specimen #1) after the test. Broken fibres and damaged coating are noticeable.

initially were 3.66, 2.76, 3.63, and 4.19 mm for Specimens #1 to #4, respectively. For Specimen #4, the free end slip reached a value as high as 9.95 mm and the load level dropped to 65% after 128 days at which time the load could not be maintained at the

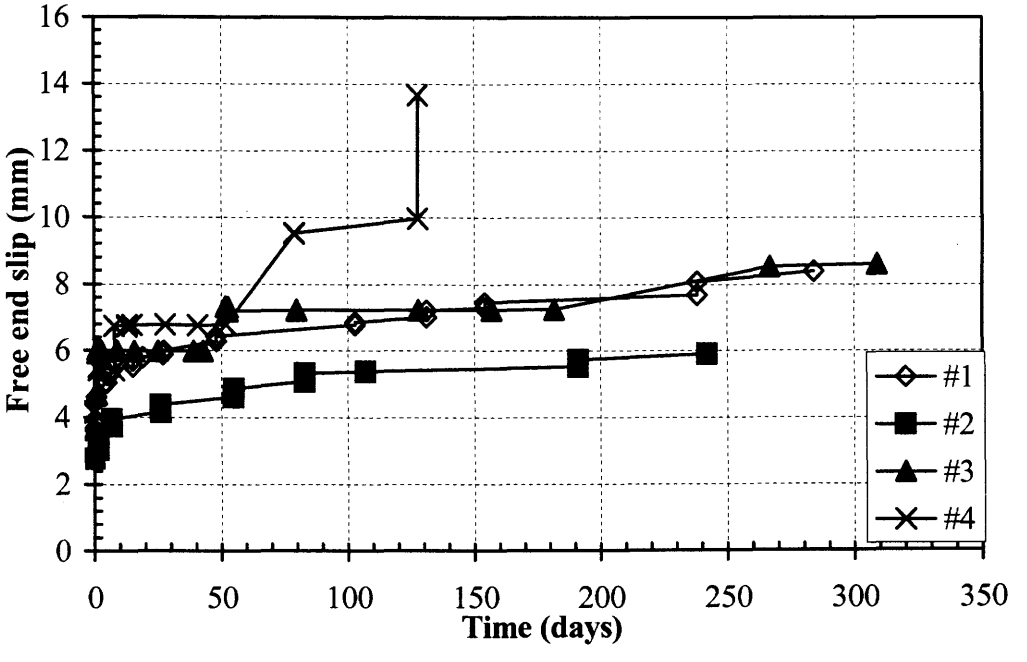

Figure 4.20. Slip-time curves for all Leadline specimens with 75% load level.

75% level. The specimen failed in pullout after 128 days while increasing the load.

Maintaining the load level at 75% in the Leadline specimens was difficult. As seen in Figure 4.20, slip of the bars occurred when adjusting the loads. The free end slip at the end of testing periods was 8.38, 5.9, and 8.59 mm for Specimens #1 to #3, respectively. The large slip values indicated bond degradation of the bars due to damage of the epoxy coating on the bars under sustained loads, as described before in SEM investigation of Specimen #1.

The steel specimen with 39% load had a bond stress of 9.4 MPa, which was a little higher than 8.8 MPa, the bond stress in Leadline specimens with 75% load. The free end slip for this steel specimen was 0.04 mm at first and 0.18 mm after 366 days (Figure 4.11). The slip values were much higher in Leadline specimens than that of the companion steel specimen since the indentations on the Leadline bars were softer than the steel lugs. The ribs on the steel rebars crushed the surrounding concrete in steel specimens while the concrete damaged the indentations on the Leadline bars in the Leadline specimens.

Typical behaviour of Leadline specimens (Specimen #3) with 60% load level is presented in Figure 4.21. Load could be maintained only with difficulty. For the specimen shown, after 148 days, the load dropped to 55% of the average ultimate static bond strength. It was required to raise the column in the loading apparatus by using shim plates underneath the base plate of the column in order to facilitate additional tightening of the nut on the aluminum rod. The load level in the specimen was measured at 26% after releasing the jacking system. The load level was then increased to 60%. This explains the large drop in load level in Figure 4.21 at 148 days. The free end slip after 329 days was 3.17 mm, whereas the initial slip was 0.95 mm (a change of 2.22 mm in slip).

Free end slip versus time curves for the four specimens with a load level of 60% of the average ultimate static bond strength are provided in Figure 4.22. Specimen # 4 had larger slip values than those of other three specimens. This could be because of

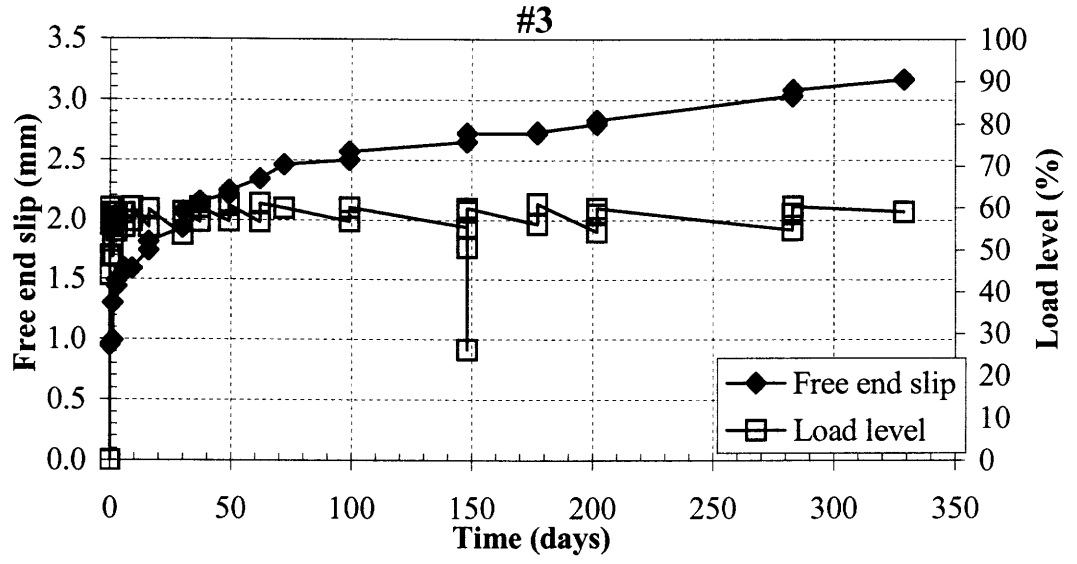

Figure 4.21. Load-slip curve for Leadline Specimen #3 with 60% load level (typical).

problems with fabrication of that specimen. Specimen #4 had a slip of 2.46 mm at the start of the test, which increased to 5.54 mm after 309 days. Specimens #1 to #3 showed similar behaviours at the start, but had somewhat different slip values as time increased. Initial free end slip values were 1.52, 1.05, and 0.95 mm, whereas the changes in slip were 1.34, 2.65, and 2.22 mm after 242, 328, and 329 days for Specimens #1, #2, and #3, respectively.

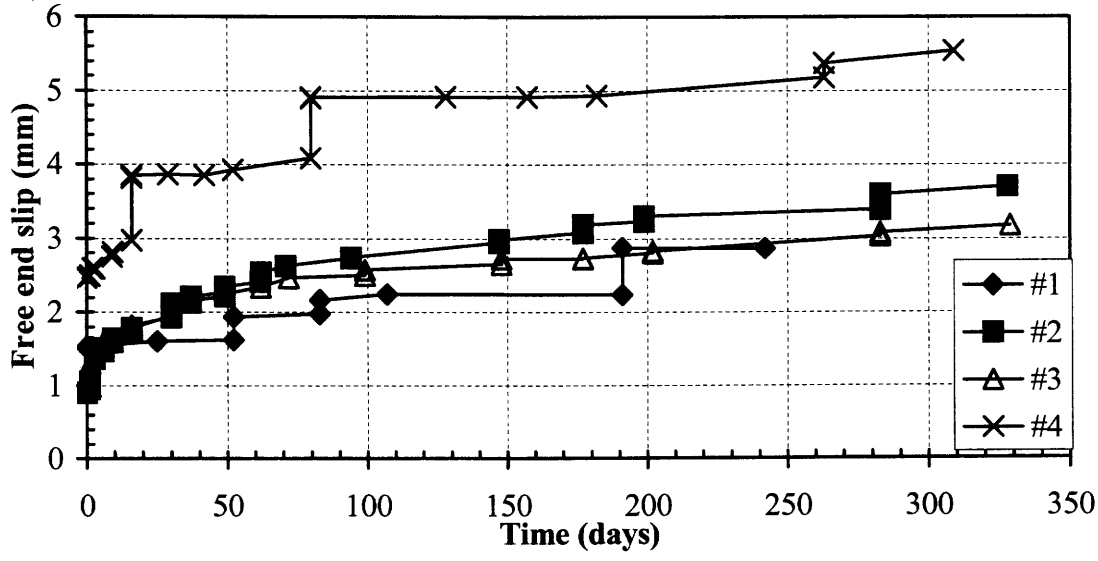

Figure 4.22. Slip-time curves for all Leadline specimens with 60% load level.

The bond stress in all those specimens was approximately 7.0 MPa. The companion steel specimen with a 39% load level had a bond stress of 7.9 MPa, which was close to 7.0MPa. However, the free end slip values in the Leadline specimens were much higher than those of the steel specimen with 39% load level (0.09 mm initially and 0.19 mm after 366 days). Also, slippage of the Leadline bars was not stabilized and continued to increase to the end of the tests, as shown in Figure 4.22. Mechanical interaction between the concrete and the Leadline bars was the bond mechanism causing damage to the indentations on the bars. When the indentations are damaged at one point of the bar (starting at the loaded end), stresses on the bar are redistributed, causing higher stresses on the indentations at other points of the bar, which lead to damage to some of these indentations. This non-stop process explains the continuous slippage of the Leadline bars.

Large free end slip values in Leadline specimens with 60% and 75% load levels over the testing period indicated that the sustained bond stresses (7.0 and 8.8 MPa) were high relative to usable service values, although no allowable bond stress was provided in the product specification (Mitsubishi Corporation 1993). Recent publications (ACI 2001, JSCE) gave allowable bond stresses of 4.63 MPa and 6.57 MPa for FRP bars and Leadline, respectively. Therefore, both stress levels used in this test program exceeded suggested allowable values. Also, allowable bond stress of 6.57 MPa seems to be high, considering the test results obtained for the Leadline specimens with sustained bond stress of 7.0 MPa (60% load level), which is close to 6.57 MPa.

4.3.5. Isorod bars

A total of nine Isorod specimens were tested under sustained loads. Four specimens were loaded to 60% of the average ultimate bond strength obtained from static tests (8.0% of the ultimate tensile strength of the bar). Out of five remaining specimens, two specimens experienced premature failures at 37% and 32% load levels. One specimen to be loaded to 75% of the static strength failed at only a 66% load level. Another specimen could hold the 75% load for only one day, at which point the load dropped to 58% of the static strength, a level that could not be increased. All failed

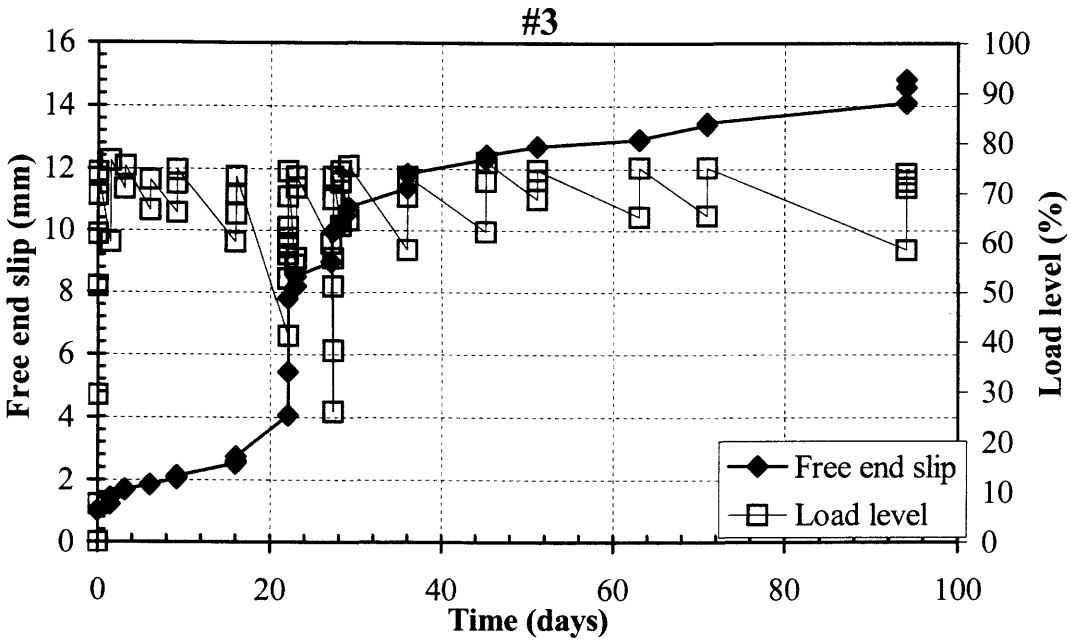

Figure 4.24. Slip-time curve for the Isorod specimen with 75% load level.

at final). Large slips represented bond degradation between the bar and the concrete due to separation of the lugs from the bar shaft.

After the test, the Isorod bar was taken out of the concrete cylinder (Section 3.2.9) at the test end of the specimen with 75% load level (Specimen #3). Primary observations revealed that the helical wrappings (lugs) on the bar had either been separated from the shaft of the bar completely in some areas or had a loose bond with the bar shaft in other areas. Further investigation under a scanning electron microscope indicated that there was damage to the coating and also to the longitudinal fibres of the bar. Figure 4.25 shows the bar surface after the test. The damaged coating as well as some broken fibres are visible. The results of the visual examination were consistent with large slips measured during the test, verifying severe bond degradation between the Isorod bar and the concrete.

The four Isorod specimens with a 60% load level demonstrated better performance than that of the Isorod specimen with a 75% load level (#3). Figure 4.26 displays slip-time curve for Specimen #2, illustrating a typical behaviour of the Isorod specimens with a 60% load.

Figure 4.25. SEM image of surface of the Isorod (75% load level) after the test. Coating is totally damaged and fibres are broken.

As shown in Figure 4.26, the load level could be readily maintained between 57 to 60% during the test period. At first, the free end slip was 0.4 mm, increasing to 1.41 mm after 329 days. Slip values were much smaller than observed for the Isorod

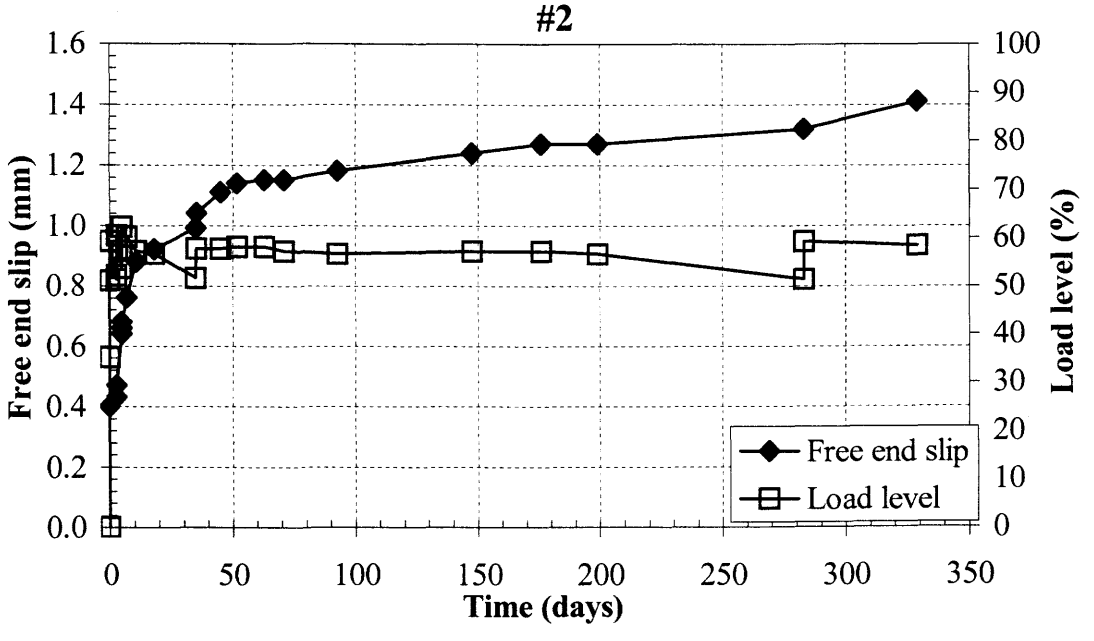

Figure 4.26. Load-slip curve for Isorod Specimen #2 with 60% load level (typical).

specimen with 75% load.

All Isorod specimens with 60% load had slips at the free ends that were smaller than those in the Isorod specimen with 75% load (Figure 4.27). Initial free end slips ranged from 0.03 mm to 1.23 mm. Changes in slip values were 0.76, 0.88, 0.21, 0.28 mm after 330 days for the Specimens #1, 2, 3, and 4, respectively. These slip values, though, were higher than those of the companion steel specimen (0.03 mm initially and 0.12 mm after 431 days in the steel specimen with 14% load and a bond stress of 3.4 MPa). A visual inspection following the sustained load tests revealed that the lugs on the Isorod bars were separated from the main shaft of the bars due to mechanical interaction between the concrete and the bars and also, weak bond between the lugs and the main shaft of the bars. After separation of the lugs at one point (starting at the loaded end due to higher stresses), redistribution of the stresses produces higher stresses at the lugs at other points, which leads to separation of the lugs at some of these points (progressing towards free end). This continuous process describes the increase of slips throughout the tests, as shown in Figure 4.27.

The sustained bond stresses in the Isorod specimens with 60% and 75% load

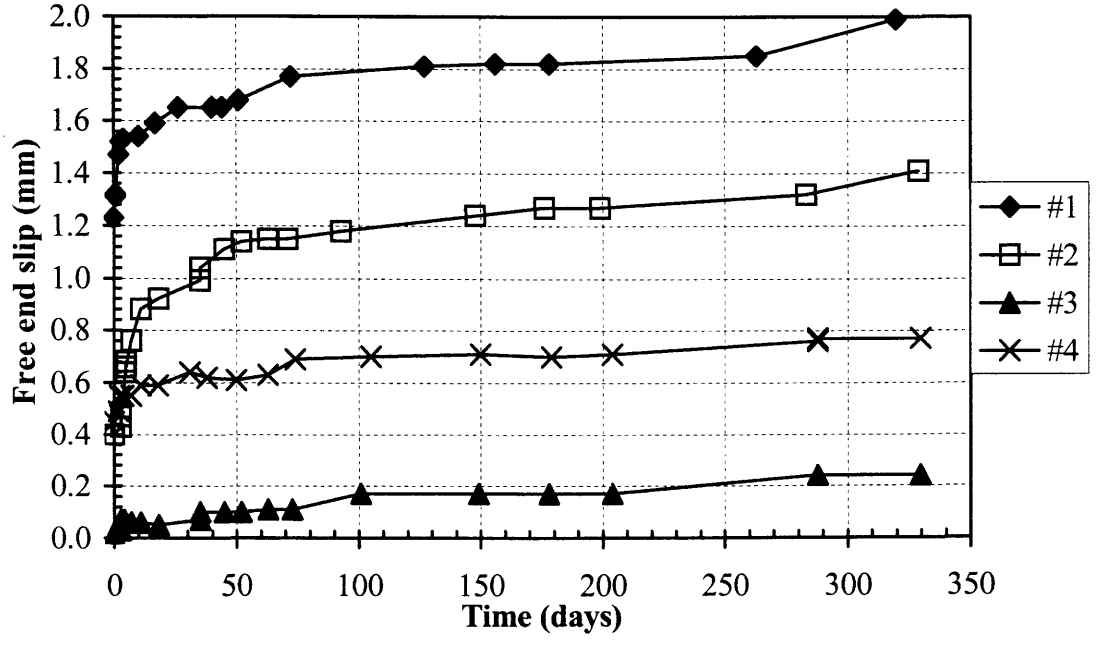

Figure 4.27. Slip-time curves for all Isorod specimens with 60% load level.

levels (3.4 and 4.3 MPa) were much less than 15 MPa, the bond strength given by the manufacturer (Pultrall Inc. 1992), and also less than 4.63 MPa, the value given by American Concrete Institute (ACI 2001). However, slip values obtained over the testing period, especially in the specimen with a bond stress of 4.3 MPa, indicated that Isorod bars had weak long-term bond properties. As mentioned in Section 4.2, subsequent investigation revealed that the manufacturer has modified the design of this reinforcement to improve its bond resistance (Pultrall Inc.).

In conclusion, the Isorod bars showed poor bond properties under sustained bond stresses lower than the bond stress given by ACI (2001). Obtained slip values under applied sustained loads, especially in the specimen with a load of 75% of the static bond strength, indicated weak long term bond performance.

Chapter 5

Test results and discussions (Phase II)

5.1. Introduction

A total of 45 pullout specimens were made in Phase II of the experimental program (Sections 3.3.4 and 3.3.5) using three types of glass fibre reinforced polymer (GFRP) bars: HB manufactured by Hughes Brothers Inc., C-bar manufactured by Marshall Industries Composites Inc., and Isorod with a new design (i.e. different from Phase I) manufactured by Pultrall Inc. Nine specimens were tested under static loads to obtain ultimate static loads (Section 3.3.6). Then, 36 specimens were tested under sustained loads of 25 and 50% of the ultimate static pullout loads in three different environments (air or room conditions, water, and alkaline), as described in Section 3.3.7. The test results obtained from static and long term tests are presented in this chapter. Investigations were done to analyze the failures at the micro-mechanical scale using a scanning electron microscope and an electron microprobe analyzer. Observations and results of these investigations are also given and discussed herein.

5.2. Static tests

Nine pullout specimens (three from each bar type) were tested in laboratory conditions under static loads (Section 3.3.6). As mentioned in Section 3.3.4, the embedment length of the pullout specimens was 75 mm (3 inches) instead of the 50 mm (2 inches) used in Phase I of the program. Also, no spirals were used in the test end and anchor end concrete cylinders.

Static test results are summarized in Table 5.1. The Isorod specimens had the highest average ultimate loads while average load for HB specimens was the lowest

Table 5.1. Summary of static test results.

Material	Diam. (mm)	Free end slips close to ultimate loads (mm)	Ultimate loads (kN)	Average ultimate load (kN)	Ave. bond strength (MPa)	Specified bond strength (MPa)	Ave. bond / Spec. bond
Isorod	12.7	0.11, 0.20, 0.07	60, 52, 62.5	58.2	19.1	-	-
C-bar	12.7	-, 0.05, 0.05	-, 48.4, 46	47.2	15.5	17	0.91
HB	12.7	5.08, 1.55, 0.10	40.3, 40.2, 45	41.8	13.8	11.6	1.19

among the specimens. As expected, all specimens experienced pullout failure and no significant damage was observed in the concrete surrounding the bars.

The three types of GFRP reinforcing bars had average bond strengths ranging from 13.8 to 19.1 MPa. These bond strengths were higher than those of the FRP bars tested in Phase I (Table 4.1) due to different configurations and longer embedment length. In Phase II, the HB bar had the weakest average bond strength of 13.8 MPa, which was 19% higher than the specified bond strength given by the manufacturer (Hughes Brothers, Inc.). The average bond strength of C-bar rods was 15.5 MPa, which was 9% lower than the specified bond strength (Marshall Industries Composites Inc.). Isorod had the highest average bond strength of 19.1 MPa. No specified bond strength was given for Isorod (Pultrall Inc.). Isorod bars had a very rough surface (Figure 3.24), which resulted in good frictional resistance between the bars and the concrete, therefore producing a high bond strength. In C-bar rods, the mechanical interaction between the lugs and the concrete was the main bond mechanism since the lugs were separated from the shaft of the bars; however, the lugs could not provide bond strength as high as that of Isorod bars. HB bars had the lowest bond strength, implying that the indentations on the bar surface and rough surface of the bar could provide mechanical interaction and friction, respectively, but not to the same extent as C-bar and Isorod rods.

The average ultimate load for HB specimens was 41.8 kN. As shown in Figure 5.1, Specimens #1 and #2 showed similar behaviours and there was no significant slip at the free end of the bar below a 32 kN load. Specimen #3 failed at a higher load (45 kN) than that of other two specimens and the free end of the bar did not experience

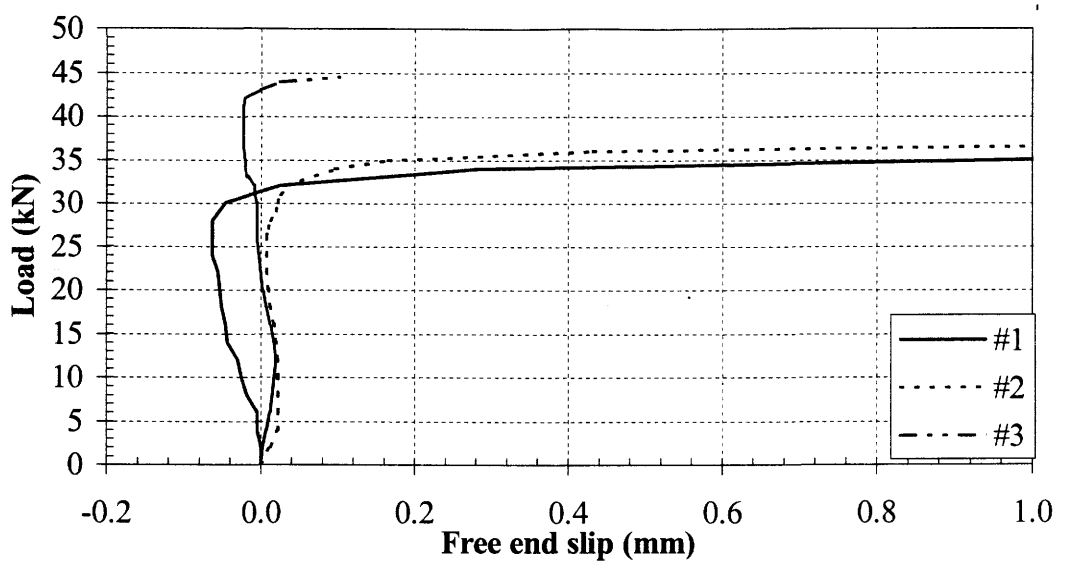

Figure 5.1. Load versus free end slip curves for HB specimens.

significant slip below a load of 42 kN. Small negative slip values shown in Figure 5.1 were due to uneven movement of the jig plate on which the dial gauge was mounted and should be ignored. However, the points on the curves where the change in slip values were positive could be considered as starting points of slips occurring at the free ends. Free end slips at ultimate loads could not be recorded for the specimens since the specimens failed shortly after the last gauge readings.

Damage to the coating of the bars due to applied loads was apparent. Bonded and unbonded portions of the bar after the test are shown in Figure 5.2(a). No coating could be seen on the bar surface which had been bonded to the concrete. After the test, the concrete cylinder at the test end of the specimen was split to observe the concrete where the bar had been. The remainder of the coating of the bar could be seen still bonded to the concrete, as shown in Figure 5.2(b). Further investigation revealed that the longitudinal crack seen in Figure 5.2(b) did not extend into the concrete.

Load versus free end slip curves for C-bar Specimens #2 and #3 are presented in Figure 5.3. Uneven movement of the jig plate on which the dial gauge was mounted caused the small negative readings shown in the figure. Free end slips started at 42 kN for Specimen #2 and at 36 kN for Specimen #3, where slips changed direction and increased at a higher rate.

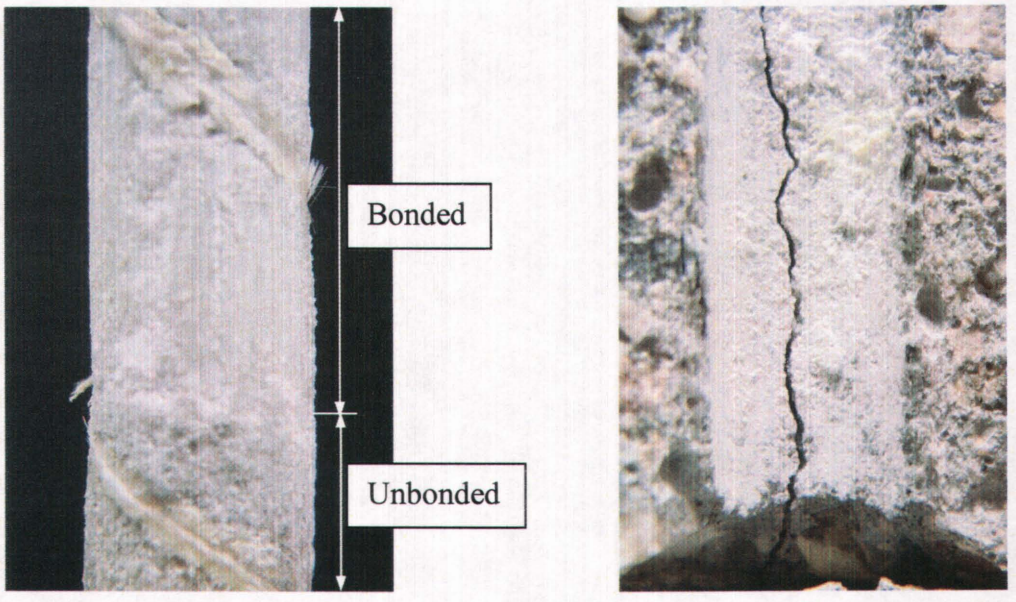

(a) (b)

Figure 5.2. HB Specimen #1 after static test: (a) surface of the bar showing damage to the coating; (b) remainder of the coating of the bar inside concrete cylinder.

C-bar specimens failed in pullout as the main shaft of the bars slipped through the concrete while the lugs sheared off and remained inside the concrete (Figure 5.4(a)). The lugs were separated from the concrete during splitting of the concrete cylinder to examine the slip surface. No significant damage to concrete was observed and traces of the bar lugs could be seen on the concrete (Figure 5.4(b)).

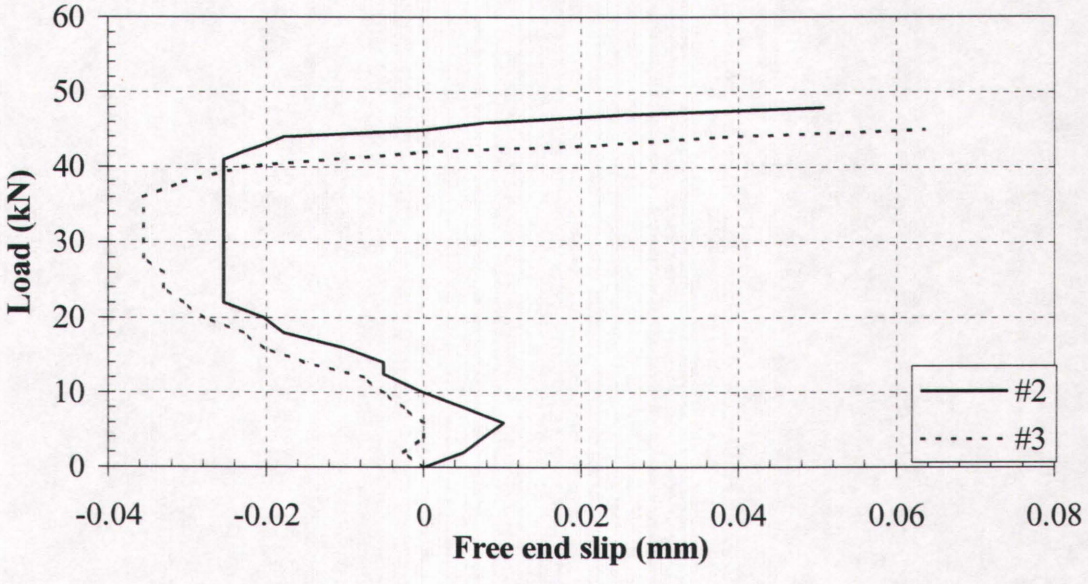

Figure 5.3. Load-free end slip curves for C-bar specimens.

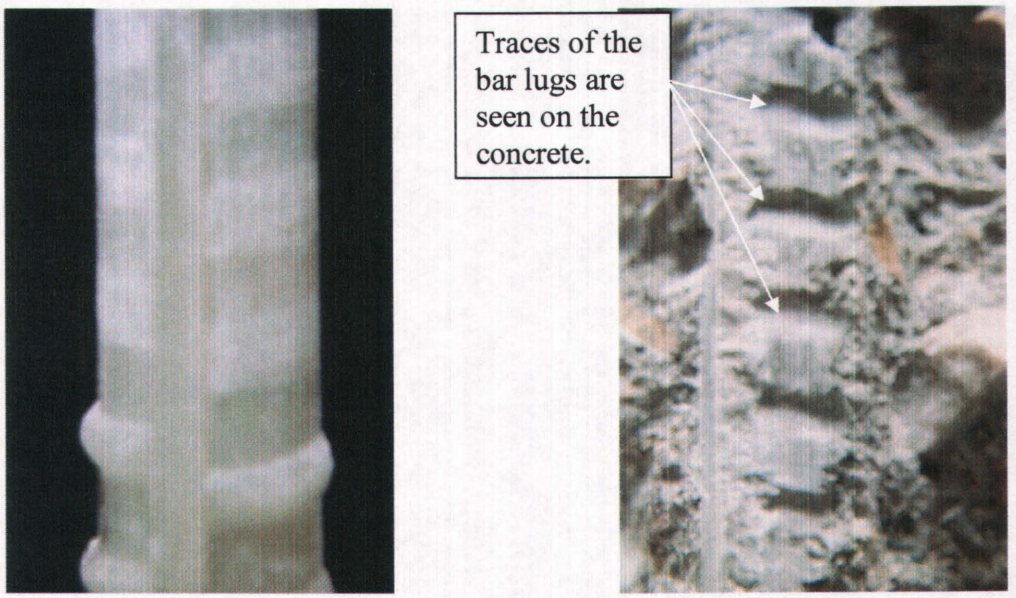

Figure 5.4. Photos of the test end of C-bar Specimen #2: (a) bar lugs are sheared off and separated from the main shaft of the bar; (b) inside of concrete cylinder showing no visible damage to the concrete surrounding the bar.

One of the three C-bar specimens (#1), tested statically, experienced pullout failure at the anchor end, which was not expected. Splitting the anchor end concrete cylinder indicated that large voids existed in the concrete around the bar due to improper compaction of the concrete (Figure 5.5). This caused pullout failure at the anchor end because of insufficient bond between the bar and concrete. The data for this specimen was not used in calculating the average ultimate static load.

Isorod specimens also experienced pullout failure. Load-slip curves are given in Figure 5.6. Similar to other specimens, negative slip values are due to uneven movement of the jig plate on which the dial gauge was mounted. Free end slips start at 40 kN for Specimen #2 and at 48 kN for Specimens #1 and #3, where the changes in slip values are positive and increase at a higher rate. Free end slips at ultimate loads could not be recorded because sudden slippage caused the gauge to fall before reaching the ultimate load. An average ultimate load of 58.2 kN and average bond strength of 19.1 MPa were obtained for the three Isorod specimens. No bond strength is given by the manufacturer (Pultrall Inc.). However, a development length of 240 mm is specified which gives a bond strength of 9 MPa if full tensile strength is to be carried by the bar.

Figure 5.5. Photos showing inside of concrete cylinder at the anchor end of C-bar Specimen #1. Large voids could be seen in concrete surrounding the bar.

No damage to the concrete was observed during the pullout tests. The coating of the bar sheared off (Figure 5.7(a)) and remained in the concrete (Figure 5.7(b)) while the main shaft of the bar pulled out of the concrete. As shown in Figure 5.7(a), sudden slip caused the coating of the bar in the unbonded portion to crack. This cracking only occurred in Specimen #1.

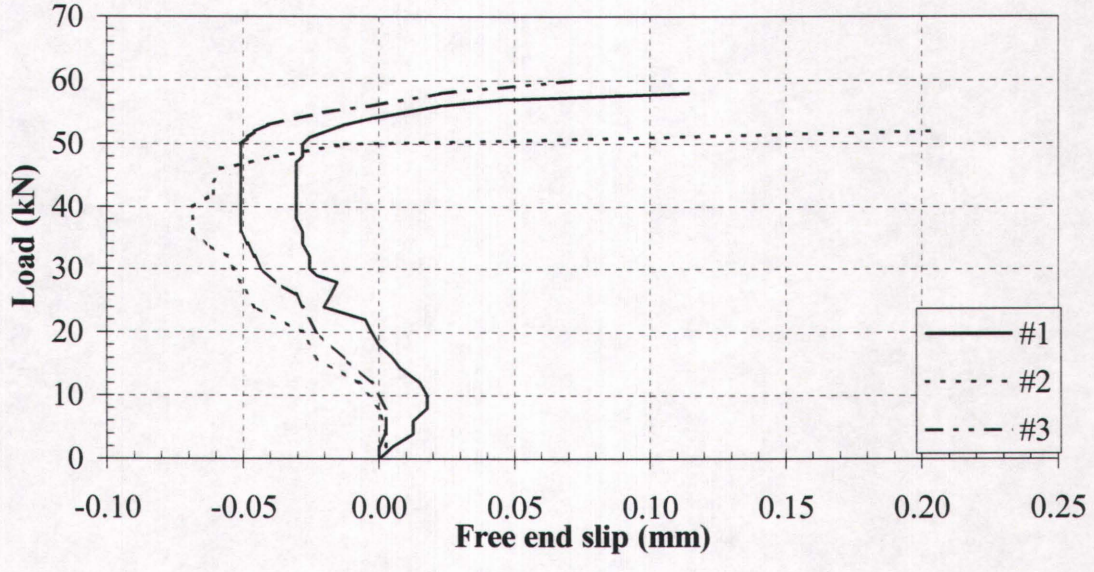

Figure 5.6. Load-slip curves for Isorod specimens.

(a) (b)

Figure 5.7. Test end of Isorod Specimen #1: (a) damage to the bar coating; (b) coating of the bar remaining inside concrete.

5.3. Long term tests

5.3.1. Introduction

Long term tests were performed to investigate the effect of sustained loads and different environments on the bond between GFRP bars and concrete, as well as on the bars themselves. A total of 36 pullout specimens were made and tested under sustained loads in three different environments (Section 3.3.7). Two load levels — 25% and 50% of ultimate loads obtained from static pullout tests — were applied to the specimens. Tests were performed in three environments: air (room conditions), tap water, and high pH alkaline solution (Section 3.3.2). The same three types of GFRP bars as were tested statically were used to make the pullout specimens (Section 3.3.4). For each type of reinforcing bar, two specimens were tested at the same load level in each environment. Long term test results are summarized in Table 5.2. Details of the test results are presented and discussed in the following sections. Also, failure analyses of the specimens are included and compared.

Table 5.2. Summary of long term test results (Phase II).

Specimen	Load (kN)	Load/ Static load (%)	Load/ Max. tensile load (%)	Bond stress (MPa)	Specified bond stress (MPa)	Test period (days)	Results
HB 25% Air #1	10.5	25	11	3.5	11.6	470	Static test. Pullout failure. Splitting cracks in concrete (120 degrees). Failed at 55.5 kN>41.8 kN.
HB 25% Water #1						473	Static test. Pullout failure. No cracks on concrete or bar. Failed at 42 kN>41.8 kN.
HB 25% Alkaline #1						465	Static test. Pullout failure followed by splitting failure. Concrete cylinder broke in two pieces. Failed at 40 kN<41.8 kN.
HB 50% Air #1	20.9	50	22	6.9	11.6	538	SEM showed no cracks. X-ray map did not indicate calcium ions in matrix.
HB 50% Water #2						531	SEM showed no cracks. X-ray map did not indicate calcium ions in matrix.
HB 50% Alkaline #1						548	Static test. Pullout failure followed by splitting failure. Concrete cylinder broke in two pieces. Failed at 42.3 kN>41.8 kN. Significant reduction in the cross section of the bar.
HB 25-75% Air #2	10.5 & 31.4	25 & 75	11 & 33	3.5 & 10.4	11.6	337 & 224	Static test. Pullout failure. No cracks on bar or concrete. Failed at 41.5 kN<41.8 kN.

Table 5.2. (Continued).

Specimen	Load (kN)	Load/ Static load (%)	Load/ Max. tensile load (%)	Bond stress (MPa)	Specified bond stress (MPa)	Test period (days)	Results
HB 25-75% Water #2	10.5 & 31.4	25 & 75	11 & 33	3.5 & 10.4	11.6	345 & 135	SEM showed circumferential cracks at bonded and unbonded portions of the bar.
HB 25-75% Alkaline #2						334 & 86	Failed in tension. No longitudinal cracking of the bar.
HB 50-75% Air #2	20.9 & 31.4	50 & 75	22 & 33	6.9 & 10.4	11.6	337 & 225	Static test. Pullout failure at 45.3 kN>41.8 kN. No cracks on bar and concrete.
HB 50-75% Water #1						344 & 210	Static test. Pullout failure. No cracks on bar or concrete. Failed at 49.5 kN>41.8 kN.
HB 50-75% Alkaline #2						331 & 141	SEM showed cracks. X-ray maps did not indicate calcium or sodium ions in matrix.
C-bar 25% Air #1	11.8	25	14	3.9	17	470	Static test. Pullout failure was associated with longitudinal cracking of the bar. No cracks on concrete. Failed at 53 kN>47.2 kN.
C-bar 25% Water #1						469	Static test. At 50 kN bar cracked longitudinally, which was followed by pullout failure. Failed at 51 kN>47.2 kN.
C-bar 25% Alkaline #1						462	Static test. Longitudinal cracking of the bar. Failed in tension at 45 kN<47.2 kN.
C-bar 50% Air #2	23.6	50	27	7.8	17	538	SEM showed no cracks. X-ray map did not indicate calcium ions in matrix.

Table 5.2. (Continued).

Specimen	Load (kN)	Load/ Static load (%)	Load/ Max. tensile load (%)	Bond stress (MPa)	Specified bond stress (MPa)	Test period (days)	Results
C-bar 50% Water #1	23.6	50	28	7.8	17	311	Breakage of outer layer of the bar. Failed in tension.
C-bar 50% Water #2						326	Breakage of outer layer of the bar. Failed in tension.
C-bar 50% Alkaline #1						433	SEM showed cracks. X-ray maps did not indicate calcium or sodium ions in matrix.
C-bar 25-75% Air #2	11.8 & 35.4	25 & 75	14 & 41	3.9 & 11.6	17	338 & 224	Static test. Longitudinal crack on the bar. Extension of the crack was followed by pullout failure at 45.2 kN<47.2 kN. No cracks on the concrete.
C-bar 25-75% Water #2						344 & 22	Bar cracked longitudinally. Failed in tension.
C-bar 25-75% Alkaline #2						336 & 21	Longitudinal cracks on the bar. Failed in tension.
C-bar 50-75% Air #1	23.6 & 35.4	50 & 75	28 & 41	7.8 & 11.6	17	337 & 202	SEM showed crack in bonded portion of the bar.
C-bar 50-75% Alkaline #2						336	Breakage of outer layer of the bar. Failed in tension while increasing the load. Load was close to 75%.
Isorod 25% Air #2	14.5	25	16	4.8	-	470	Static test. Pullout failure. No cracks on concrete or bar. Failed at 58 kN<58.2 kN.
Isorod 25% Water #1						473	Static test. Pullout failure. No cracks on concrete or bar. Failed at 58 kN<58.2 kN.

Table 5.2. (Continued).

Specimen	Load (kN)	Load/ Static load (%)	Load/ Max. tensile load (%)	Bond stress (MPa)	Specified bond stress (MPa)	Test period (days)	Results
Isorod 25% Alkaline #1	14.5	25	16	4.8	-	460	Static test. Pullout failure followed by splitting failure. Concrete cylinder broke in half. Failed at 60 kN>58.2 kN.
Isorod 50% Air #1	29.1	50	33	9.5	-	457	SEM showed no cracks. X-ray map did not indicate calcium ions in matrix.
Isorod 50% Water #1						532	SEM showed no cracks. X-ray map did not indicate calcium ions in matrix.
Isorod 50% Alkaline #1						426	Longitudinal cracking of the bar. Failed in tension.
Isorod 25-75% Air #1	14.5 & 43.6	25 & 75	16 & 49	4.8 & 14.3	-	337 & 17	Longitudinal cracks on the bar. Failed in tension.
Isorod 25-75% Water #2						347 & 0.7	Breakage of part of outer layer at 545 mm from anchor end. Failed in tension.
Isorod 25-75% Alkaline #2						333 & 0.2	Breakage of part of outer layer at 545 mm from anchor end. Failed in tension.
Isorod 50-75% Air #2	29.1 & 43.6	50 & 75	33 & 49	9.5 & 14.3	-	336 & 21	Longitudinal crack on the bar. Failed in tension.
Isorod 50-75% Water #2						345 & 71	Longitudinal crack on the bar. Failed in tension.
Isorod 50-75% Alkaline #2						333 & 1	Longitudinal crack on the bar. Failed in tension.

5.3.2. HB bars

5.3.2.1. Specimens with 25% load

All HB specimens with 25% load levels performed well in the three specified environments. As shown in Figure 5.8, initial slips ranged from 0.03 to 0.15 mm. Final slips under 25% load were 0.1 to 0.3 mm and there were no significant changes in slip values for the specimens after about 20 days.

Specimens Air #1, Water #1, and Alkaline #1 were tested statically after being under 25% load for 470, 473, and 465 days, respectively. These specimens experienced pullout failures giving ultimate loads of 55.5, 42, and 40 kN, in that order. The failure load for Specimen Air #1 (55.5 kN) was significantly higher than the average ultimate pullout load (41.8 kN) obtained from initial static tests, probably due to more compaction of the concrete accidentally during fabrication of the specimen. Three splitting cracks at 120° angles around the circumference were observed in the concrete cylinder after the test. The failure loads for other two specimens (42 kN for Water #1 and 40 kN for Alkaline #1) were close to the average ultimate static load (41.8 kN). A pullout failure in Specimen Alkaline #1 was followed by splitting failure of the concrete cylinder, which was broken in two pieces. Although the failure load of Specimen Air #1

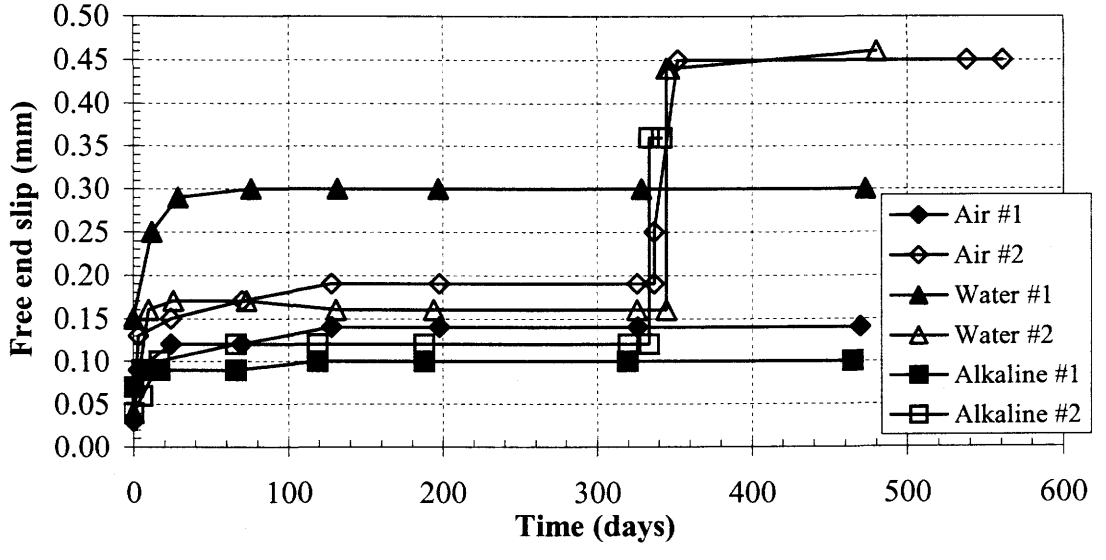

Figure 5.8. Free end slip-time curves for HB specimens with 25% load level.

was higher, the pullout failures of the specimens showed that being under 25% load for about 470 days had no apparent effect on the bond between the HB bars and concrete. Also, comparing the specimens in water and alkaline with the specimen in air indicated that there was no significant effect on bond due to exposure to solutions within this time period.

The load levels in the other three specimens with 25% load (#2's) were increased to 75% after about 340 days to accelerate the tests. As seen in Figure 5.8, slip values changed by 0.24 to 0.28 mm when the loads were increased to 75%. Slip values in Specimens Air #2 and Water #2 did not alter after being under 75% load for an additional 224 and 135 days, respectively. Specimen Alkaline #2 failed in tension after 420 days and before the free end slip was measured.

Specimen Air #2 was tested statically after being under load for 561 days, i.e. 337 days at 25% load and 224 days at 75% load. The specimen failed in pullout and there was no evidence of any visible cracks on the bar or on the concrete cylinder. An ultimate load of 41.5 kN was recorded, which was almost equal to the average ultimate load (41.8 kN) obtained from initial static tests. Therefore, for this specimen, sustained load had no major effect on bond between the bar and concrete.

Specimen Water #2 was unloaded and taken out of the apparatus after being under load for 480 days, i.e. 345 days at 25% load and 135 days at 75% load. By using a diamond saw, the concrete cylinder at the test end of the specimen was cut and the bar was taken out of the concrete (Section 3.3.8). A total of six samples from the bonded and unbonded portions of the bar were cut and prepared for observation using a scanning electron microscope (SEM). The purpose was to see the possible effects of sustained load and environment on the bar at the micro structural scale.

For the bonded portion, a crack could be observed in the cross section of the bar at approximately 0.6 mm from the surface (Figure 5.9(a)). The crack extended longitudinally and could be seen in the longitudinal section of the bar (Figure 5.10). As shown in Figure 5.9, cracking between the matrix and the fibres was evident and the

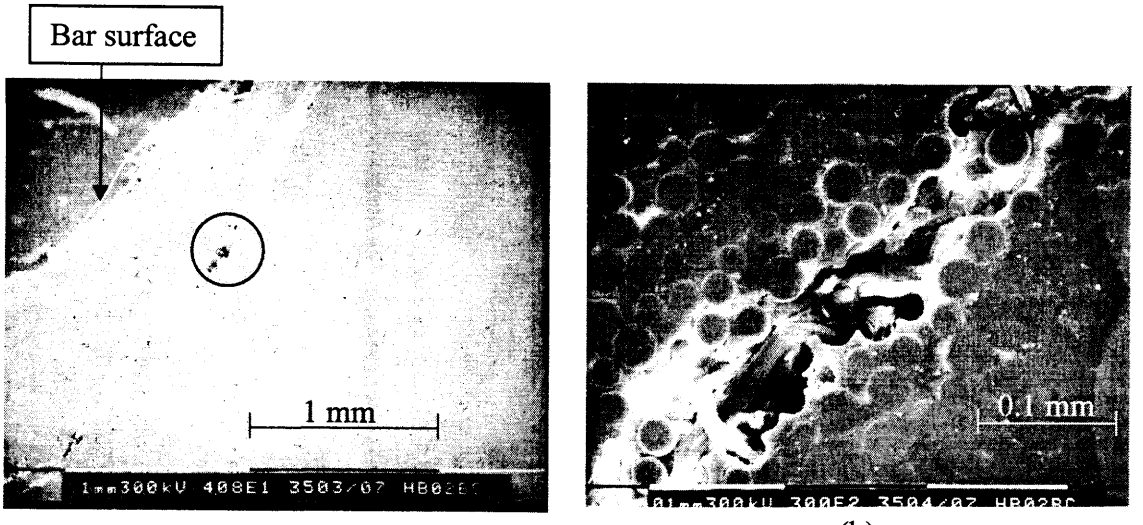

(a) (b)

Figure 5.9. SEM images of the bar cross-section at the bonded portion of Specimen HB 25-75% Water #2 showing: (a) the entire crack; (b) magnified view of the crack.

fibres did not appear to be broken. No damage to the surface of the bar was apparent (Figure 5.11).

Investigation of samples taken from the unbonded portion of the bar (Specimen HB 25-75% Water #2) revealed that the cracking seen in the bonded portion extended into the unbonded portion as well. Figure 5.12 illustrates a major circumferential crack

Figure 5.10. Longitudinal section of the sample taken from Specimen HB 25-75% Water #2 (bonded portion) displaying extension of the crack longitudinally.

Figure 5.11. Image of the bar surface (Specimen HB 25-75% Water #2 – bonded portion). No damage to the coating of the bar is visible.

at a distance of about 0.6 mm from the bar surface in the bar cross section. A magnified view of the major crack shows separation between the fibres and the resin matrix. Cracking had expanded longitudinally towards the other end of the bar (Figure 5.13(a)). Breaking of one fibre could be seen in the magnified image of the longitudinal crack (Figure 5.13(b)).

Comparing the two HB specimens (25% Water #1 and 25-75% Water #2) revealed that increasing load level from 25% to 75% resulted in separation between the fibres and the resin, and cracking of the bar in Specimen #2. As mentioned earlier,

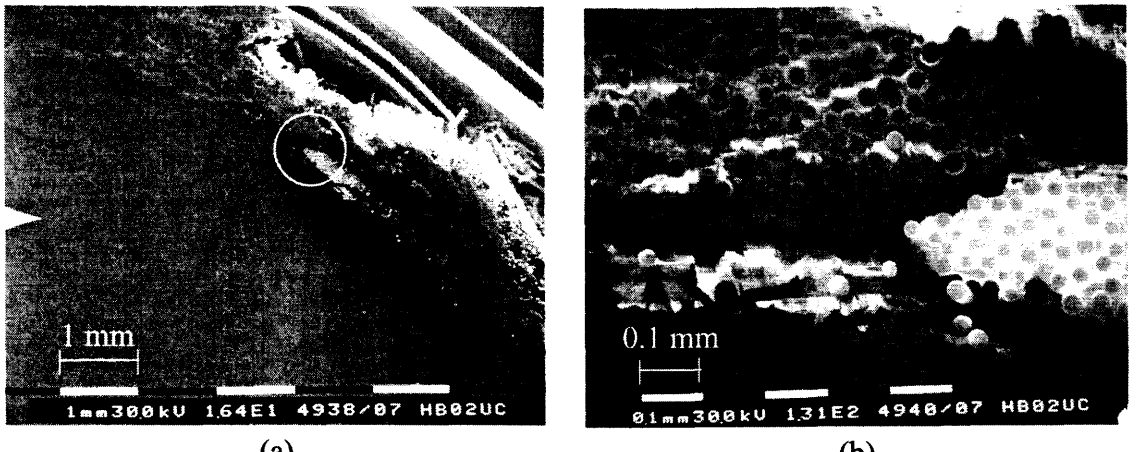

(a) (b)

Figure 5.12. Specimen HB 25-75% Water #2 (unbonded portion) showing images of the bar cross-section: (a) view of the cracks; (b) magnified view of the major crack.

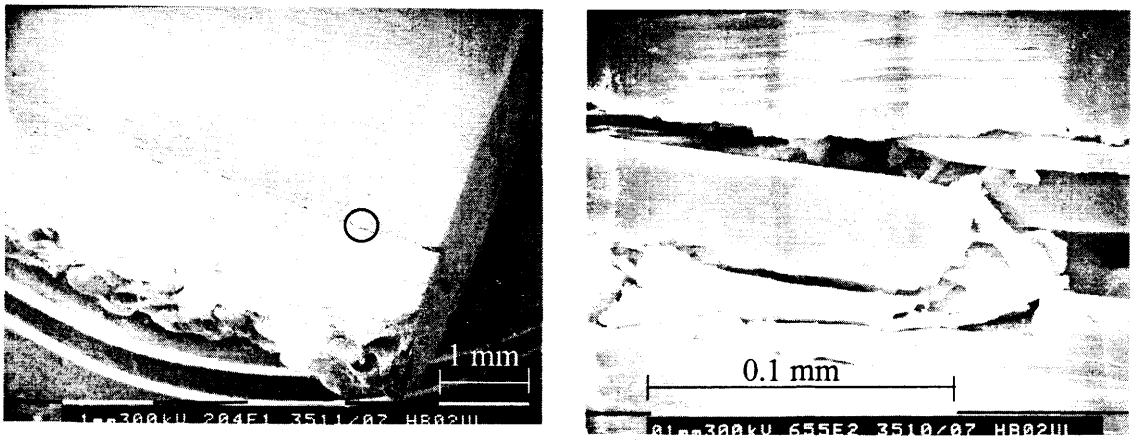

(a) (b)

Figure 5.13. Images of the extension of crack in longitudinal direction of the bar for Specimen HB 25-75% Water #2 (unbonded portion): (a) general view; (b) magnified view of the crack displaying one broken fibre.

Specimen #1 was tested statically after 473 days and experienced pullout failure at a load close to the average ultimate static load. Also, as will be shown later, no sign of calcium ions was found in another HB specimen immersed in water.

As mentioned before, the load was increased to 75% in Specimen HB 25% Alkaline #2 after 334 days. After a few days at 75% load, the alkaline solution was leaking out through the gap around the bar inside the bearing plate hole due to broken sealant in the gap. The solution could be seen on the bar surface outside the concrete cylinder at the test end. This showed that seepage of the solution between the concrete and the bearing plate was possible because of bad or broken sealant around the bar and around the base of the concrete cylinder. The specimen failed in tension after being under 75% load for 86 days.

Investigation of the failed specimen indicated that the initiation point for failure was at the indentation on the bar surface at the location of the concrete cylinder base where the leakage started. The crack extended along the indentation on the bar surface (Figure 5.14). The failed section, seen outside the circles in Figure 5.14, was due to accidental shear failure of the bar that occurred when trying to separate the bearing plate from the concrete. Since the solution had already penetrated into the failed section, it was not possible to verify whether the degradation of glass fibres had occurred before

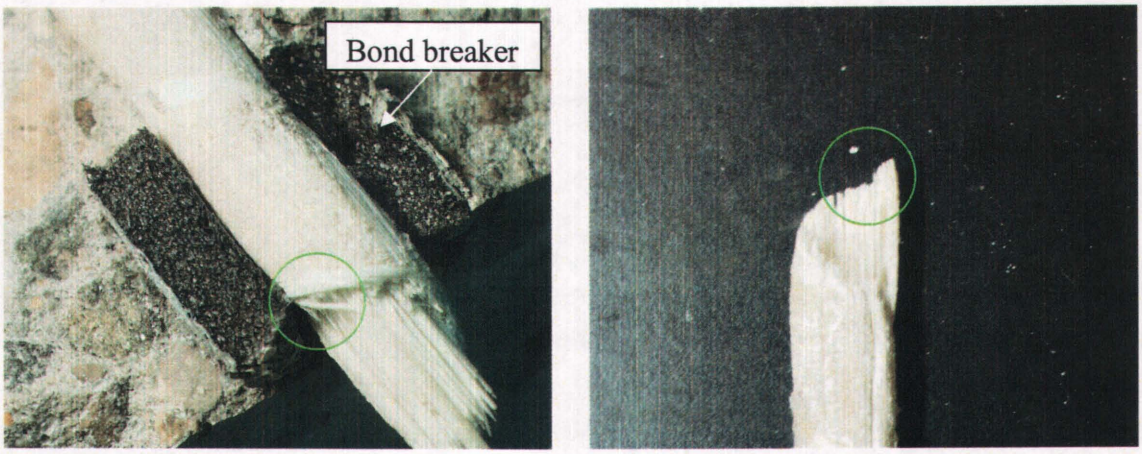

(a) (b)

Figure 5.14. Photos of Specimen HB 25-75% Alkaline #2 showing the starting point of failure (inside circles): (a) top portion of the bar at the test end of the specimen; (b) bottom portion of the bar outside the concrete.

the failure. As shown in Table 5.2, HB specimens subjected to the 75% load level showed pullout failures at loads close to or higher than the average ultimate static load. Therefore, it is possible that the leakage of the solution had some effects on Specimen HB 25-75% Alkaline #2, considering that the coating was thinner at the location of the indentation on the bar where the leakage started.

5.3.2.2. Specimens with 50% load

Figure 5.15 illustrates the free end slip versus time curves for the HB specimens with 50% loads. Initial slips varied between 0.13 mm and 0.2 mm. Free end slips became almost stable after being under 50% load. There were no changes in slip values after 120 days. Final slips under 50% loads had a range of 0.19 mm to 0.35 mm. Minimum slip change occurred for Specimen Air #2 (0.07 mm) while Specimen Water #1 exhibited a maximum slip change of 0.18 mm. All HB specimens under 50% loads showed an acceptable performance with respect to bond between the bars and concrete since there were no significant changes in slip.

Specimens Air #1 and Water #2 were unloaded and taken out for SEM investigation after being under 50% load for 538 and 531 days, respectively. No cracks could be seen on the samples taken from bonded and unbonded portions of the bars at the test end of the specimens.

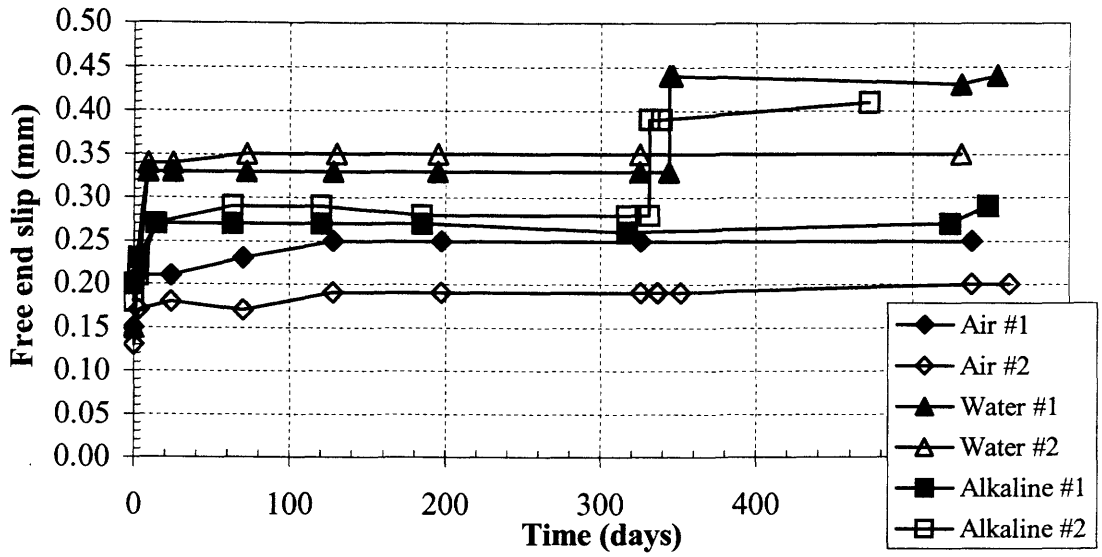

Figure 5.15. Free end slip-time curves for HB specimens with 50% load level.

After SEM observation, the cross sectional samples taken from bonded portions of Specimens HB Air 50% #1 and HB Water 50% #2 were investigated using electron microprobe analyzer. The hydroxyl ions of calcium hydroxide, which exists in the pore water solution of the concrete, could cause damage to glass fibres of the bar (Section 2.2.3.2). It is not possible to trace hydroxyl ions by electron microprobe analyzer since fluorescent x-rays for oxygen and hydrogen atoms that are produced by electron transitions can not be detected and counted by energy-dispersive x-ray analyzer (Section 3.3.9). Therefore, calcium ions, which also exist in the calcium hydroxide solution and could be detected by microprobe and x-ray maps, were acquired. Wavelength dispersive x-ray maps did not indicate any penetration of calcium ions into the bars.

A calcium x-ray map for Specimen HB 50% Water #2 is presented in Figure 5.16. Lighter points in the x-ray map indicate the presence of calcium. The calcium ions seen in the image are inside the fibres and actually exist in the E-glass fibre composition, since examination of an undisturbed sample indicated that calcium ions were present in the glass fibres. The bottom right corner of the image shows a portion of the bar coating; there is no trace of calcium ions in this area. Since both calcium and

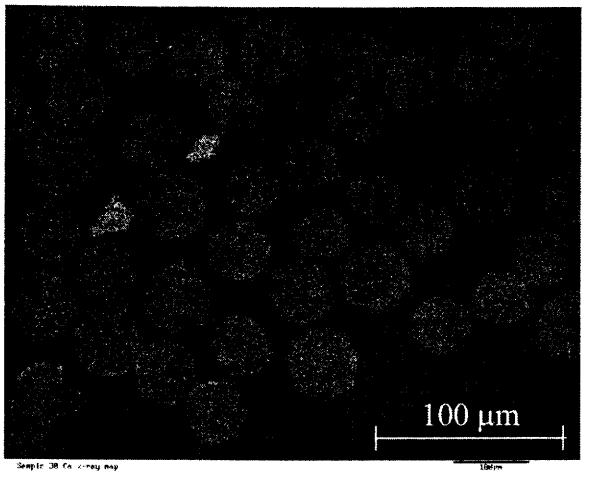

Figure 5.16. X- ray map for Specimen HB 50% Water #2 showing calcium ions (light points) in fibres. Bottom right corner shows the coating area of the bar.

hydroxyl ions exist together in pore water solution, no penetration of calcium ion means it is unlikely that hydroxyl ions could have penetrated into the bars.

Specimen HB 50% Alkaline #1 was unloaded and taken out of the apparatus to be tested under static load after 548 days. When tested statically, the specimen failed at a load of 42.3 kN, which was a little higher than the average ultimate load (41.8 kN) obtained from initial static tests. The specimen experienced pullout failure followed by splitting failure of the concrete cylinder, which was broken in two pieces. Significant reduction of the bar cross section was noticeable (Figure 5.17(a)) and a large portion of the bar remained in the concrete (Figure 5.17(b)). Splitting failure of Specimen HB 50% Alkaline #1 at the end of the static test did not occur in initial static tests. The reason for splitting failure could be swelling of the free end of the bar, which was exposed to alkaline solution. The thicker bar diameter of the bar due to swelling may have induced higher radial stresses in the concrete, resulting in higher hoop tensile stresses and splitting of the concrete cylinder.

The loads of the other three HB Specimens with 50% load (Air #2, Water #1, and Alkaline #2) were increased to 75% to accelerate the tests after the specimens had been under 50% loads for 337, 344, and 331 days, respectively. As shown in Figure 5.15, there was a change of 0.11 mm in slip values for Specimens Water #1 and Alkaline #2 when the loads were increased to 75%. After the initial slip change, the

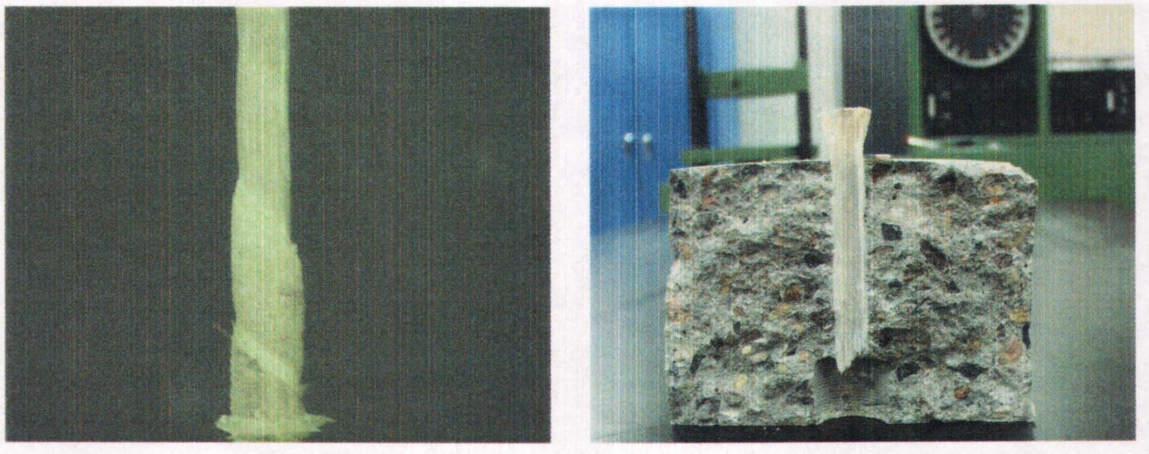

(a) Reduction of bar cross section. (b) Part of the bar seen in the concrete.

Figure 5.17. Photos of Specimen HB 50% Alkaline #1 (test end) after static test.

slips did not change significantly until the end of the testing periods. Free end slip did not change significantly for Specimen Air #2 after increasing the load and remained almost constant until the end of the test.

Specimen HB 50-75% Air #2 was tested statically after being under 50% load for 337 days and under 75% load for 225 days. The failure mode was pullout failure and there were no visible cracks on the bar or the concrete. The failure load (45.3 kN) was higher than the average static load (41.8 kN).

Specimen HB 50-75% Water #1 was under 50% load for 344 days and under 75% load for 210 days. Static testing of this specimen resulted in a higher load (49.5 kN) than the average ultimate load (41.8 kN) attained from initial static tests. The specimen failed in pullout and there were no signs of cracks on the bar or the concrete.

Specimen HB 50-75% Alkaline #2 was used for SEM and microprobe investigation after being under load for 472 days, i.e. 331 days at 50% load and 141 days at 75% load. SEM images of the bar cross section at the bonded portion of the bar are displayed in Figure 5.18. There was one micro-crack at a distance of about 0.5 mm from the bar surface that divided into two cracks. The magnified view (Figure 5.18b) illustrates separation between fibres and matrix at the interface of the two constituents. Although one broken fibre could be seen in the magnified image, observation of the

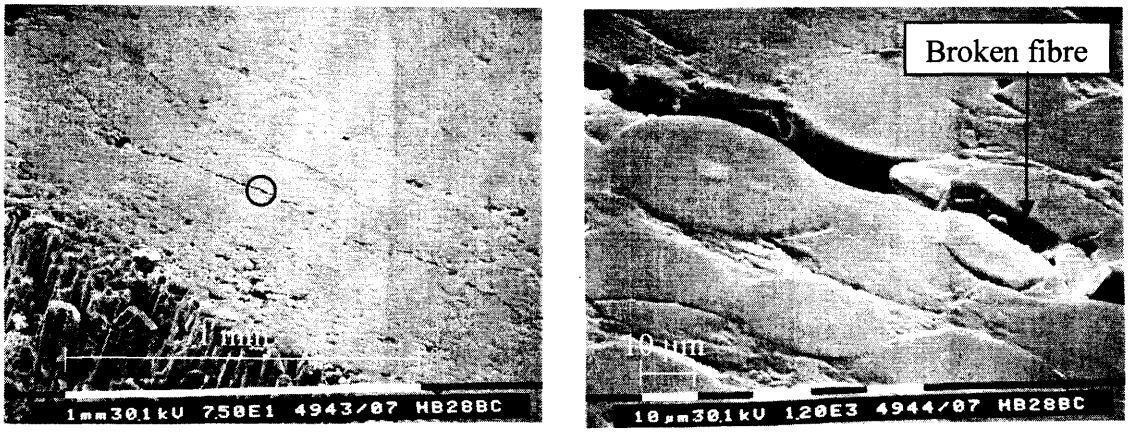

(a) (b)

Figure 5.18. SEM images of the cross section of the bonded portion of Specimen HB 50-75% Alkaline #2 showing: (a) general view of cracks; (b) magnified view of crack. Separation at fibre-matrix interface and one broken fibre could be seen.

entire crack length revealed that the cracking was due to separation between fibres and matrix mostly and only a few broken fibres could be detected.

As shown in Figure 5.19, the micro-crack extended longitudinally and changed direction by passing through fibres at a few points. The crack shown started at about 1.0 mm and ended at about 1.7 mm from the bar surface. The entire length of the micro-crack was investigated and a few broken fibres could be seen. Fibre-matrix separation

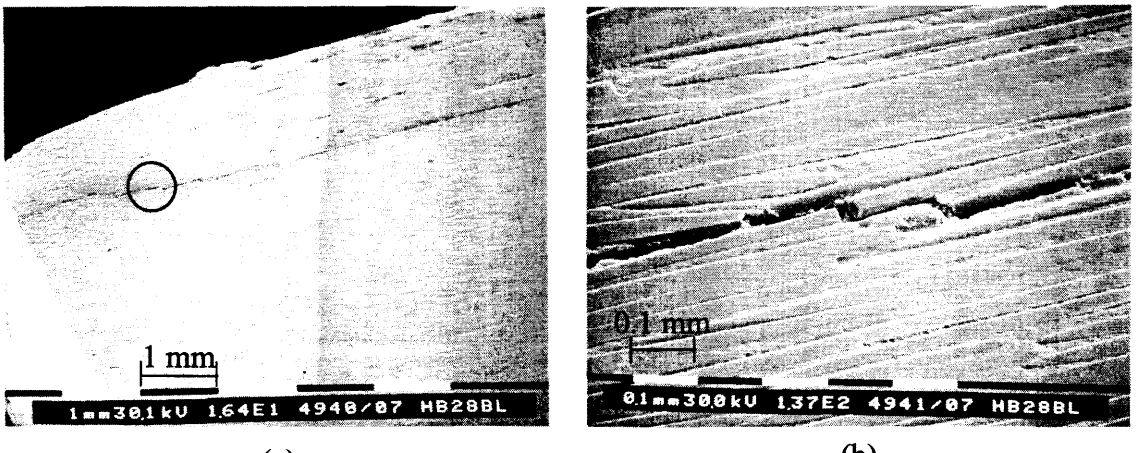

(a) (b)

Figure 5.19. SEM images of a longitudinal section of the bonded portion of Specimen HB 50-75% Alkaline #2 illustrating: (a) extension of the micro-crack in the longitudinal direction; (b) broken fibres and separation between fibres and matrix at higher magnified.

was found to be the cause for cracking at most parts, resulting from failure due to shear stresses transferring stresses from the outside to the inside of the bars.

A few micro-cracks were spotted on the bar surface at the bonded portion of Specimen HB 50-75% Alkaline #2. Some fibres were visible through the micro-cracks and there was no evidence of any damage to the exposed fibres (Figure 5.20). Most probably, surface cracking occurred when the bar was being separated from the concrete for SEM investigation. As mentioned before, no cracks were found on the surface samples taken from Specimens Air #1 and Water #2.

SEM investigation of Specimen HB 50-75% Alkaline #2 disclosed a micro-crack at the unbonded portion of the bar at a distance of about 2 mm for the bar surface (Figure 5.21(a)). The micro-crack could be an extension of the same crack found in unbonded portion, which ended at a distance of about 1.7 mm from the bar surface. Like the bonded portion, cracking was due to separation at fibre-matrix interface (Figure 5.21(b)).

The same cross sectional sample used for the SEM investigation was polished again and coated with carbon to be used in the electron microprobe analyzer. This sample was from the bonded portion of the bar used in Specimen HB 50-75% Alkaline #2. Wavelength dispersive x-ray maps did not indicate any trace of calcium (Figure 5.22) or sodium ions in the coating or in the matrix. Calcium and sodium ions could be

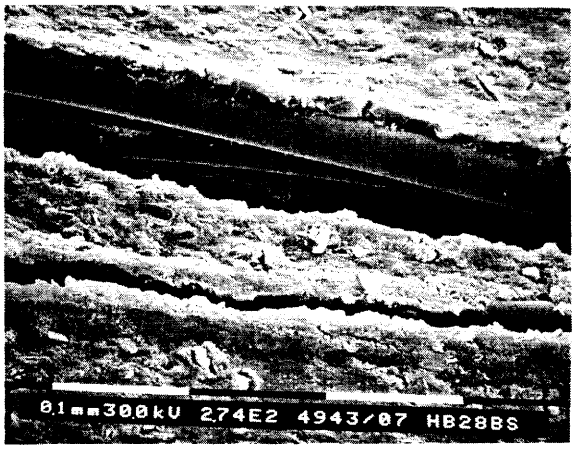

Figure 5.20. SEM image of the bar surface at the bonded portion (Specimen HB 50-75% Alkaline #2). Micro-cracks and exposed fibres are visible.

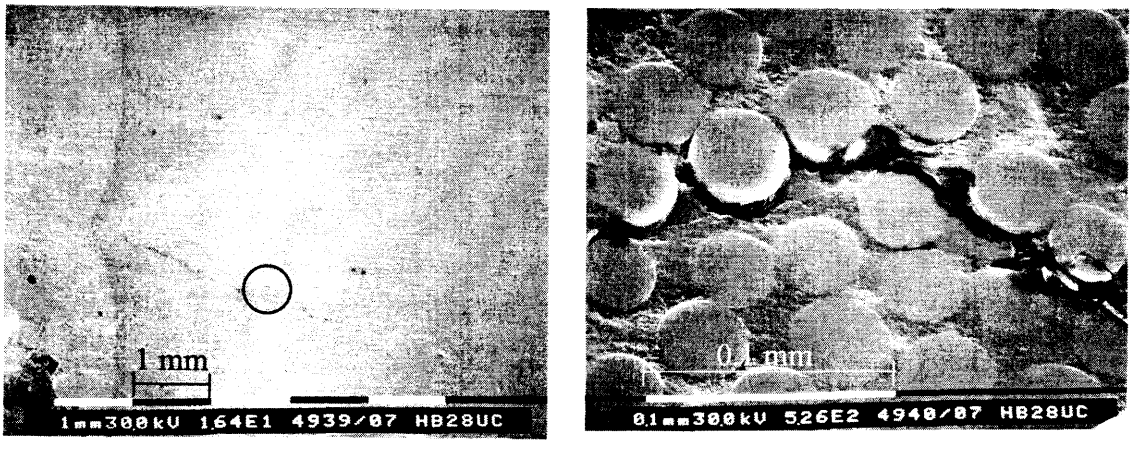

(a) (b)

Figure 5.21. Images of bar cross section at the unbonded portion of Specimen HB 50-75% Alkaline #2: (a) general view; (b) magnified view.

seen in the glass fibres since they can be found in the composition of E-glass fibres that are a main constituent of the bar. To verify this, a sample of an undisturbed bar was examined using the electron microprobe analyzer. Calcium and sodium x-ray maps were similar to the ones obtained before in which the ions were found in the glass fibres. Both hydroxyl and calcium ions are found in the alkaline solution, and if calcium ions could not penetrate to the bars, it is likely that hydroxyl ions could not either. Therefore, it is unlikely that hydroxyl ions could have penetrated into the bars.

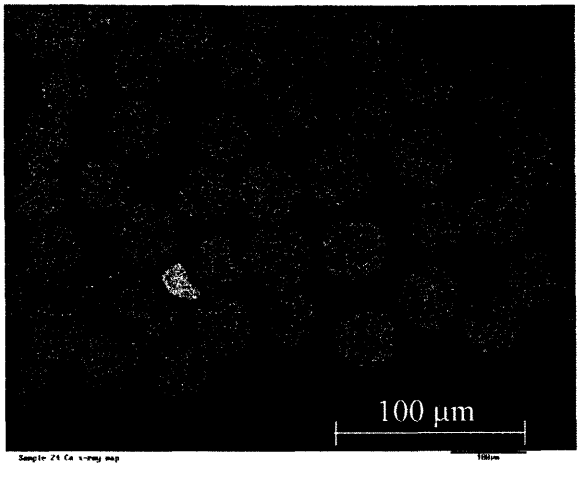

Figure 5.22. Calcium x-ray map for bonded portion of the bar (Specimen HB 50-75% Alkaline #2).

5.3.2.3. Summary

Static tests of the three specimens with 25% load after being about 460 days in the three environments resulted in failure loads that were close to or higher than the average ultimate loads obtained from initial static tests and pullout failure (followed by splitting failure in some cases) was the failure mode. Therefore, it can be concluded that sustained loads of 25% and exposure to the environments had no significant effect on the bond between the HB bars and concrete.

The static test of one specimen with 50% load in alkaline environment resulted in a slightly higher load than the average static load and the failure mode was pullout followed by splitting failure. SEM investigation of the two specimens with 50% load indicated no damage or micro-cracks on the bars' cross-sections and surfaces. Therefore, bond degradation between the HB bars and concrete was not evident due to 50% sustained loads and exposure to the three environments. In addition, the environments and sustained loads had no effect on separation between the fibres and the matrix at the interface.

Static tests of three HB specimens with increased sustained loads of 75% resulted in pullout failure of the specimens at the same or higher ultimate loads than the average static load. SEM analyses of two specimens indicated longitudinal micro-cracks inside the bars close to the surface that could be due to increased loads or environmental effects, or both.

Since analyses of HB bars in air, water, and alkaline environments indicated no penetration of calcium ions, and as a result no penetration of hydroxyl ions, the micro-cracking of the bars at the matrix-fibre interface is not likely due to the effects of the environments on the bars. It is most possible that increased sustained loads were the cause of micro-cracking.

No cracks were found in the samples taken from specimens with 50% load. When the loads increased from 25% or 50% to 75%, the micro-cracks could be seen in the samples taken from these specimens. The average bond stress between the bar and concrete, assuming a uniform distribution, increased from 3.5 or 6.9 MPa to 10.4 MPa

in these specimens. Based on the test results and findings in the literature, the following factors possibly contributed to the formation of micro-cracks.

Firstly, studies show that the bond stress is not uniform and is higher (about 40% higher than average bond stress) at the loaded end of embedment length of the bar (see Section 2.4.3). This higher stress must be transferred to the fibres through the matrix at the fibre-matrix interface. Micro-cracks appeared to initiate at the loaded end of embedment length where the bond stress was a maximum.

Secondly, cracking occurred only after application of sustained loads. Therefore, time-dependent (creep) effects are suggested. Studies show that thermosetting resins like epoxy exhibit creep behaviour under sustained loads at room temperature (Section 2.2.2.1). It should be mentioned that no information was available on creep properties of the resin used in HB bars (Hughes Brothers Inc.). On the other hand, glass fibres exhibit little creep at room temperature (Section 2.2.3.2). The resulting strain incompatibility may have contributed to the observed failures.

Finally, circumferential micro-cracks at the fibre/matrix interface were an indication of a shear failure along the interface at the location of the micro-cracks which occurred close to the surface of the bar. The circumferential cracking started at the loaded end of the bar and then extended along the bar. This suggests that additional shear stresses were induced in the matrix and at fibre-matrix interface, probably due to differential creep properties of the fibres and the matrix, to prevent creep of the matrix under existing high shear stresses at the loaded end of the embedment length and close to the surface of the bar (region of highest shear stress within the bar).

As mentioned before, Specimen HB 50-75% Alkaline #2 failed in tension. The failure started at an indentation on the bar surface and at the end the concrete cylinder where there was seepage of alkaline solution. This point was 25 mm from the loaded end of the embedment length the bar. Since other HB specimens with increased load level of 75% did not fail in tension, it is possible that the leakage of the solution had some effects on the bar in Specimen HB 50-75% Alkaline #2.

The maximum load in the HB specimens was 33% of the tensile strength of the bars, which is more than the 25% recommended by other researchers (Malvar 1998, Benmokrane et al. 2001a). As mentioned earlier, SEM investigation showed longitudinal cracking in the HB bars with tensile stress of 33% of the tensile strength. Therefore, test results support the recommended load limits.

5.3.3. C-bar bars

All C-bar specimens under 25% load performed well. As shown in Figure 5.23, initial slips were between 0.05 mm and 0.12 mm. Free end slips changed for about 20 days and became stable after that. Final slips ranged from 0.13 to 0.28 mm. Loads could be maintained and there was no change in sustained loads over time.

Specimens Air #1, Water #1, and Alkaline #1 were tested under static loads after 470, 469, and 462 days, respectively. Specimen Air #1 experienced pullout failure at a load of 53 kN, which was higher than the average ultimate load (47.2 kN) attained from static tests done initially. After the test, a longitudinal crack could be seen on the surface of the bar, extending from inside the concrete cylinder at the test end to a distance of 330 mm from the test end. The crack was not apparent before the test and was seen only after the test. A cross sectional sample of the bar was cut at a distance of

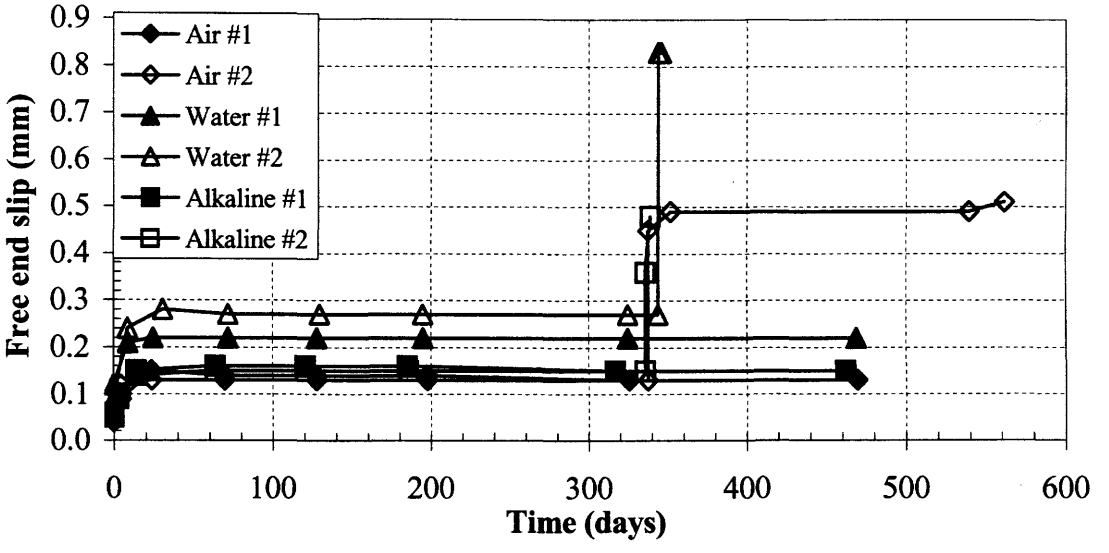

Figure 5.23. Free end slip-time curves for C-bar specimens with 25% load.

280 mm from the test end of the specimen and was polished. SEM examination showed a micro-crack on the sample (Figure 5.24). The micro-crack was at fibre-matrix interface, which was an indication of shear failure of the bar.

Specimen Water #1 cracked longitudinally at a 50 kN load when tested statically. The load could be increased after longitudinal cracking of the bar. The longitudinal cracking was followed by pullout failure and the specimen failed at 51 kN, which was higher than the average static failure load of 47.2 kN. Specimen Alkaline #1 failed in tension at 45 kN, which was lower than the average static failure load (47.2 kN). Longitudinal cracks could be seen on the bar after the static test. The test results indicate that bond degradation between the C-bar and the concrete is not a problem in Specimens Air #1, Water #1 and Alkaline #1 with 25% sustained load, since they failed in tension rather than pullout when tested statically. However, longitudinal cracking of the bars shows that the sustained load of 25% affected the C-bar itself. Due to shear failure at fibre-matrix interface, the tensile strength of the bar decreased significantly. The tensile strength of the bar given by the manufacturer (Marshall Industries Composites Inc.) was 770 MPa, i.e. tensile load of 87 kN, which was much higher than the failure loads observed (53, 51 and 45 kN).

The loads in the other three C-bar specimens with 25% loads (Air #2, Water #2, and Alkaline #2) were increased to 75% after 338, 344, and 336 days, respectively, to

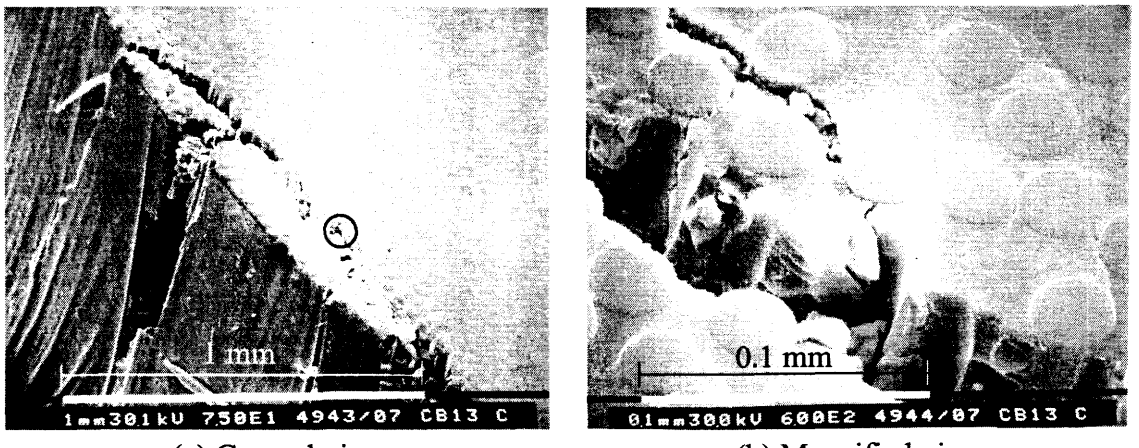

(a) General view (b) Magnified view

Figure 5.24. SEM images of bar cross section at 280 mm from the test end after static test (Specimen C-bar 25% Air #1).

accelerate the tests. The free end slips increased from 0.13 mm to 0.45 mm in Specimen Air #2, from 0.27 mm to 0.83 mm in Specimen Water #2, and from 0.15 mm to 0.36 mm in Specimen Alkaline #2 due to increased loads (see Figure 5.23).

Specimen Air #2 had a total free end slip of 0.51 mm after being under 75% load for 224 days. The specimen was tested statically after a total of 562 days, i.e. 338 days at 25% load and 224 days at 75% load. The bar cracked longitudinally when the loading started. The crack could be seen on the bar close to the plate at the test end and it had spread from inside to outside of the concrete for a distance of about 60 mm from the plate (Figure 5.25(a)). In spite of the initial cracking, the specimen could carry more load, and as the load increased, the crack extended along the bar (Figure 5.25(b)). The longitudinal cracking was followed by pullout failure at 45.2 kN, which was lower than the average static load (47.2 kN).

Specimen Water #2 cracked longitudinally after 344 days under 25% load and 22 days under 75% load. The specimen failed in tension 3 days after cracking. Investigation showed that part of the coating of the bar at the interface of bonded and unbonded portions of the bar (25 mm above the sealing around the bar) broke due to separation of matrix and fibres (shear failure). The cracking then extended longitudinally due to unbalanced load in the bar (Figure 5.26).

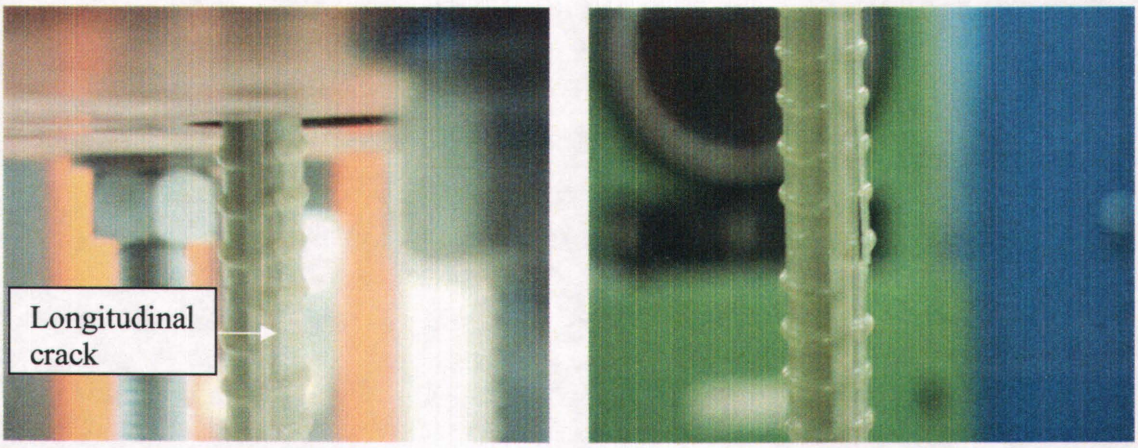

(a) Initial cracking at loaded end just after starting the static test.

(b) Extension of initial crack along the bar by increasing the load.

Figure 5.25. Longitudinal cracking in Specimen C-bar 25% Air #2 during static test.

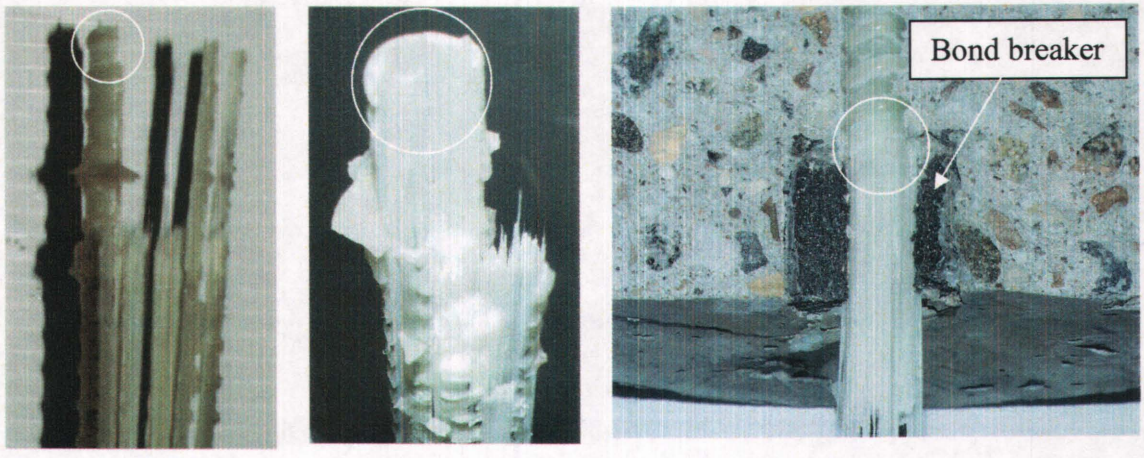

Figure 5.26. Photos of Specimen C-bar 25-75% Water #2 showing break of outer layer and longitudinal cracking. Inside circles illustrate starting point of breakage at interface of bonded and unbonded portions of the bar.

Specimen Alkaline #2 had a total slip of 0.48 mm at the free end after 3 days under 75% load. The specimen cracked along the bar and failed after being under 75% load for 21days. Longitudinal cracking of the bar was followed by vertical splitting of the bar and by blooming of the fibres. The failure pattern was similar to that of Specimen C-bar 25-75% Water #2 except that the fibres broke (tensile failure) close to the middle of the bar after longitudinal cracking.

Longitudinal cracking of the bars was observed in the C-bar specimens with 25% load when they were tested statically, and under sustained loads when the loads were increased to 75%. This common pattern indicates that sustained loads of 25% may have caused micro-cracking of the bar at the cross sectional interface of bonded and unbonded portions of the bar (shear failure), where the bond stress was maximum. As will be shown later, no trace of calcium ions could be found in the matrix. However, there was no evidence of bond degradation between the bars and concrete due to sustained load and/or exposure to aggressive environments.

Free end slip versus time curves for C-bar specimens with 50% load are illustrated in Figure 5.27. The initial free end slips were between 0.16 and 0.28 mm. Total slips were in the range of 0.26 and 0.39 mm after about 200 days. Except for Specimen Water #2, slips stabilized 20 to 60 days after loading. Loads did not change and could be maintained in all specimens except for Specimens Water #1 and Water #2.

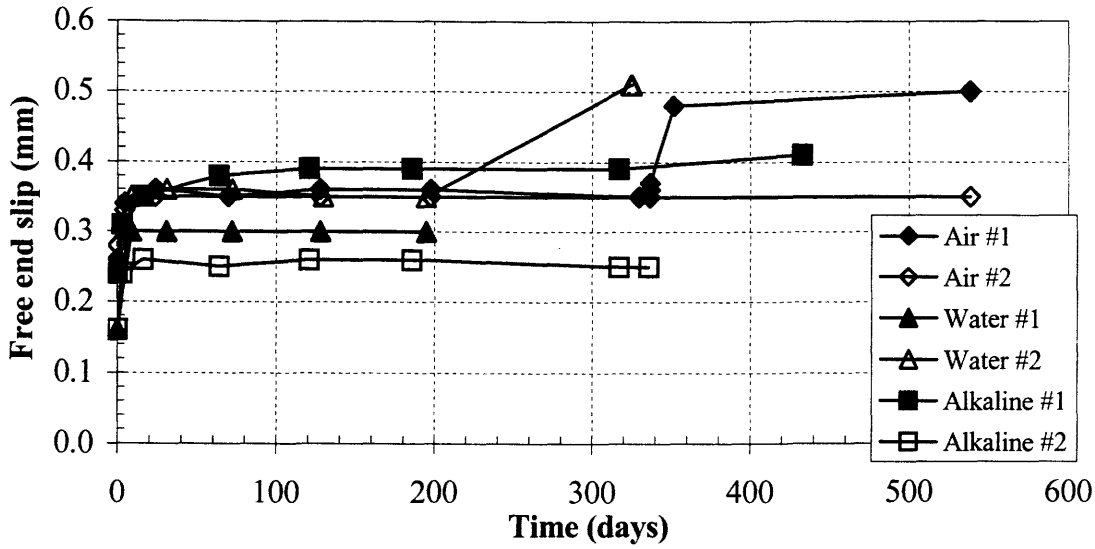

Figure 5.27. Free end slip versus time curves for C-bar specimens with 50% load.

The loads in theses specimens dropped after about 300 days due to failure in tension. In general, all specimens had acceptable performance with respect to bond between the bars and concrete since the free end slips did not change significantly and were in an acceptable range.

However, Specimen Water #1 failed in tension after about 300 days. Load had dropped to zero and there was slip of about 19 mm at the loaded end of the bar. No cracks were apparent on the bar surface between the two end concrete cylinders. The concrete cylinder at the test end of the specimen was split in order to inspect the portion of the bar inside concrete. Figure 5.28(a) shows the general view of the failed bar. The entire part seen enclosed by the circle in the figure had been located inside the bond breaker wrapped around the bar. The bond breaker was removed after taking the bar out of the concrete cylinder. The failed section shown by the arrow in Figure 5.28(b) was located at the interface of bonded and unbonded portions of the bar. Stress concentrations due to higher bond stress at this location could have caused the separation of outer and inner layers of the bar (shear failure) and then breakage of the outer layer.

The load in Specimen C-bar 50% Water #2 dropped to 45% after 325 days, at which time a total slip of 0.51 mm was measured at the free end of the bar. Cracking

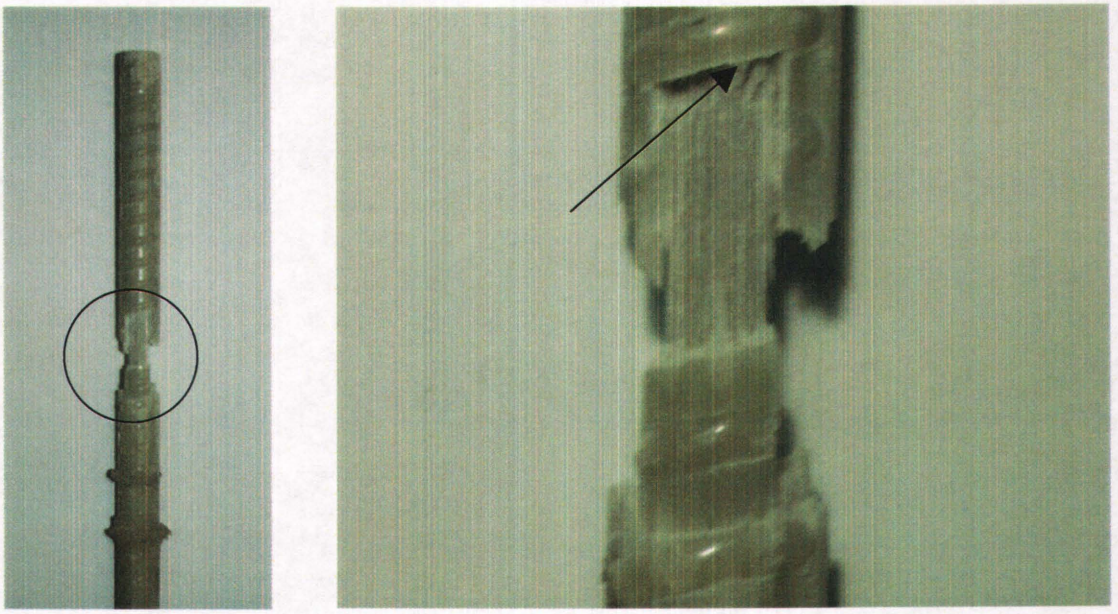

(a) General view (b) Magnified view of failed region.

Figure 5.28. Photos of the test end of Specimen C-bar 50% Water #1 showing the breakage of the bar at interface of bonded and unbonded portions of the bar (shown by arrow).

sounds were noticeable when increasing the load back to 50%. By next day, the load had dropped to 45% again. The load dropped to zero shortly after it was again increased to 50%. Slippage of the bar was about 20 mm at the loaded end. As seen in Figure 5.29, the sealant, shown inside the rectangle, which was initially attached to the bearing plate

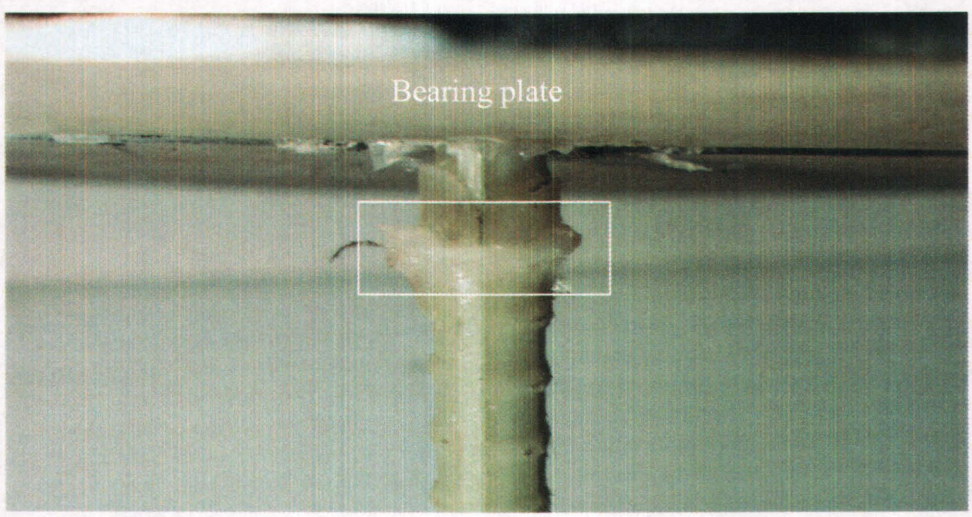

Figure 5.29. Photo of loaded end of Specimen C-bar 50% Water #2. Slip of the loaded end is visible.

had moved down. This indicated breakage of the bar inside the concrete similar to Specimen C-bar 50% Water #1. No cracks could be seen on the bar between the two end concrete cylinders.

As shown in Figure 5.27, free end slip in Specimen C-bar 50% Air #2 did not change after about twenty days under load. Total free end slip was 0.35 mm after 538 days. The specimen was unloaded and was taken out of the apparatus. Samples from bonded and unbonded portions of the bar inside the concrete were cut and polished for SEM examination. No cracks could be found on the samples (Figure 5.30) and there was no damage on the bar surface.

Although scanning electron microscopy did not show any cracks in Specimen C-bar 50% Air #2, a crack could be found in Specimen C-bar 50% Alkaline #1. Figure 5.31 displays SEM images of the bar cross-section within the bonded portion of the bar. The crack forms a circular arc and is located about 0.8 mm from the bar surface. Separation of matrix and fibres due to shear failure is visible in the magnified view of Figure 5.31(b). Although few broken fibres could be seen along the crack, separation at fibre-matrix interface was evident along most of the crack.

Cross-sectional samples from bonded portions of Specimens C-bar 50% Air #2 and C-bar 50% Alkaline #1 (used in SEM) were polished and carbon coated. These

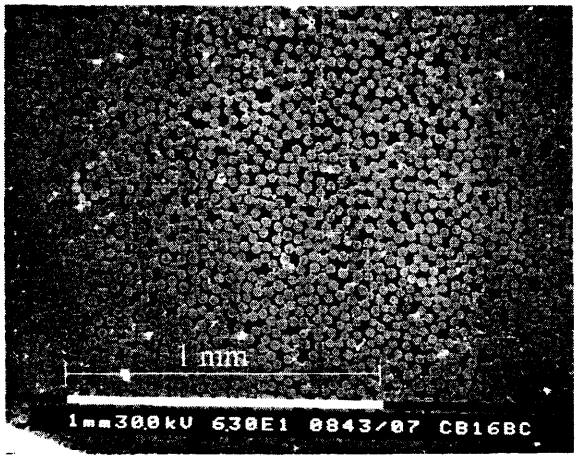

Figure 5.30. Cross section of the bonded portion of Specimen C-bar 50% Air #2 at 10 mm from loaded end of the bar. No cracks could be seen in the cross section.

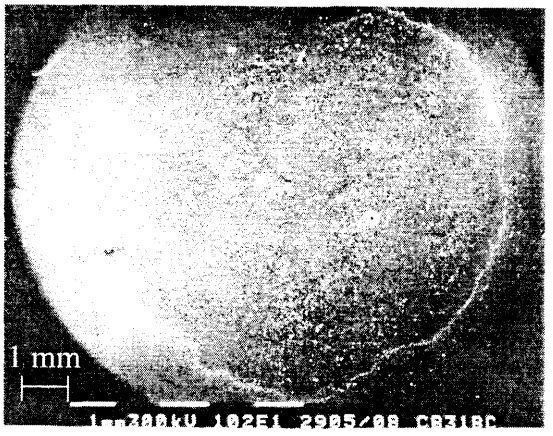

(a) General view of micro-crack.

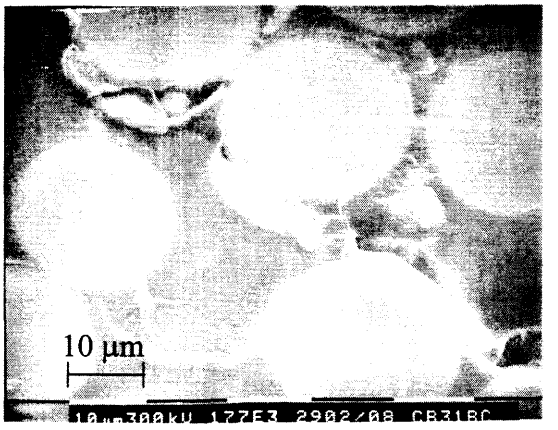

(b) Magnified view of showing separation of fibres and matrix.

Figure 5.31. SEM images of the cross-section of Specimen C-bar 50% Alkaline #1 at bonded portion of the bar.

samples were used in the electron microprobe analyzer to obtain calcium and sodium x-ray maps. Traces of calcium and sodium ions could be found in the fibres but not in the matrix. Calcium x-ray map for Specimen C-bar 50% Alkaline #1 is presented in Figure 5.32. Similar patterns were found in x-ray maps of an undisturbed C-bar sample. There was no penetration of calcium ions into the bars and as a result, it could be said that hydroxyl ions had not penetrated into the bars in the two specimens since calcium and hydroxyl ions were present in the solution simultaneously. Therefore, the cracking found in C-bar 50% Alkaline #1 was likely due to sustained load rather than to degradation as a result of alkaline attack.

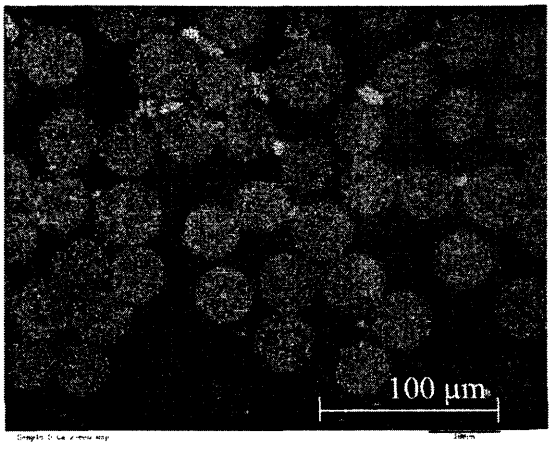

Figure 5.32. X-ray map of calcium for Specimen C-bar 50% Alkaline #1. Trace of calcium ions could be seen in fibres but not in matrix (light points).

The load on Specimen C-bar 50% Air #1 was increased to 75% after 337 days under load. The free end slip increased to 0.48 mm 15 days after the load was increased. Total free end slip in the specimen was 0.5 mm after being under 75% load for 202 days (Figure 5.27). The specimen was unloaded after 539 days and samples were prepared for SEM investigation. A micro-crack could be seen on the bar cross section within the bonded region (Figure 5.33(a)), and it extended longitudinally towards the loaded end of the bar (Figure 5.33(b)). The cracking is thought to be due to increased sustained load since no calcium ions could be found in the bar matrix of the identical Specimen C-bar 50% Air #2, as mentioned before.

Specimen C-bar 50% Alkaline #2 failed after 336 days while the load was being increased to 75%. The load was close to 75% when failure occurred. The loaded end slipped about 13 mm and load dropped to zero. No change in free end slip was measured. The location of failure was inside the concrete and the mode was similar to that of Specimens C-bar 50% Water #1 and #2. It is likely that failure was due only to increased sustained load, rather than degradation by chemical attack, because inspection of the identical specimen (C-bar 50% Alkaline #1) showed no trace of calcium and sodium ions in the matrix of the bar.

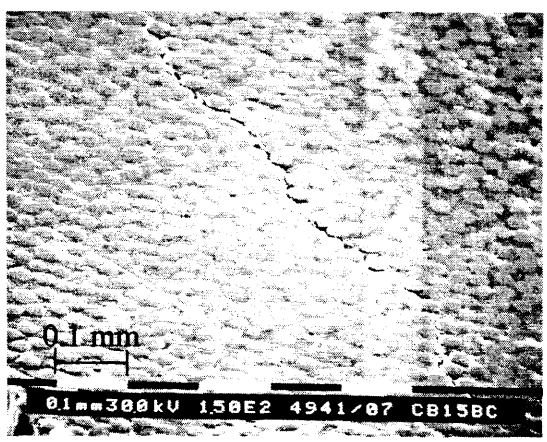

(a) Image of cross section.

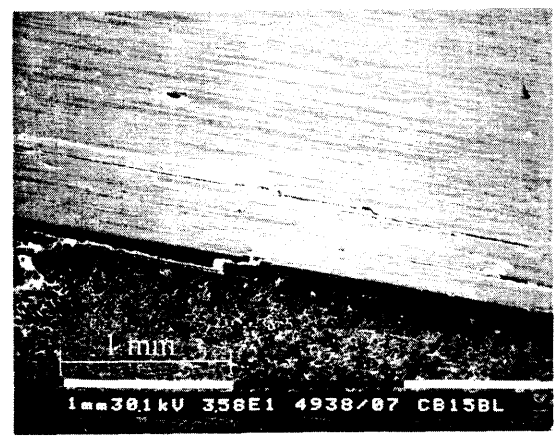

(b) Image of longitudinal section.

Figure 5.33. SEM images from bonded portion of Specimen C-bar 50-75% Air #1.

5.3.4. Isorod bars

Free end slip-time curves for Isorod specimens with a sustained load of 25% of average ultimate load obtained from static pullout tests are displayed in Figure 5.34. Free end slips were between 0.06 and 0.11 mm initially and changed by 0.1mm to 0.23 mm over the next 10 days. After that, slip remained almost unchanged. Loads did not change and could be maintained at 25%. In general, Isorod specimens with 25% load exhibited good performance with respect to bond between Isorod bar and concrete since the free end slips did not change significantly and were in an acceptable range.

Specimens Air #2 and Water #1 were tested statically after about 470 days under 25% load. The specimens experienced pullout failure at a load of 58 kN, which was almost equal to the average ultimate load (58.2 kN) attained from initial pullout tests. No cracks were apparent on the bars or concrete cylinders.

A static test of Specimen Alkaline #1 after 460 days resulted in pullout failure at a higher load (60 kN) than the average ultimate static load (58.2 kN). Pullout failure of the specimen was followed by splitting failure of the concrete cylinder at the test end, which resulted in the cylinder breaking in half. The results of static tests of Specimens Air #2, Water #1, and Alkaline #1 with 25% load confirm good bond performance of

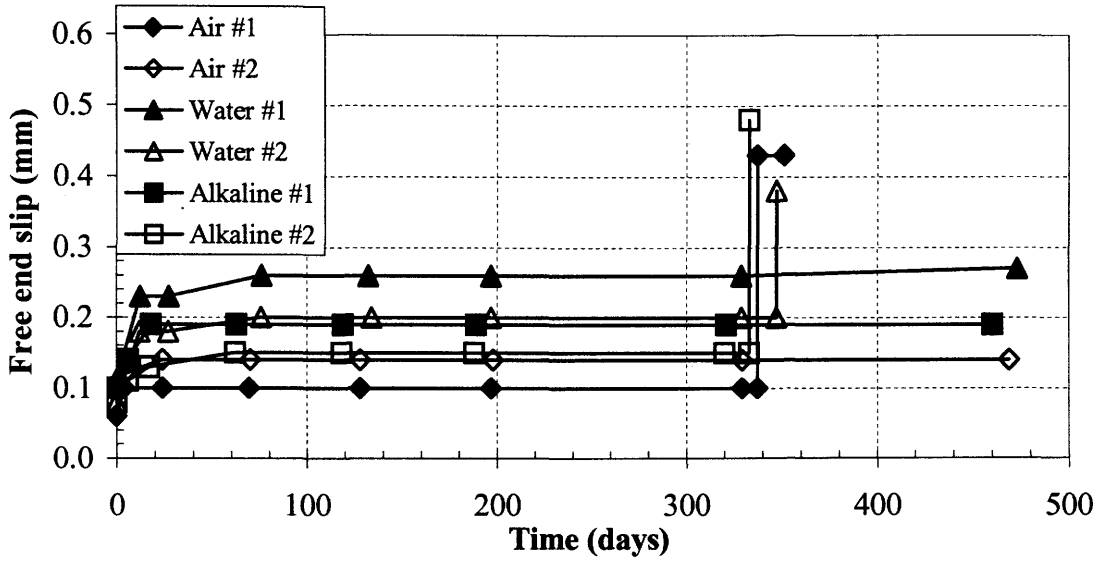

Figure 5.34. Free end slip curves for Isorod specimens with 25% load.

Isorod specimens under sustained load of 25% of the average ultimate static load.

Loads in Specimens Air #1, Water #2, and Alkaline #2 were increased from 25% to 75% after 337, 347, and 333 days, respectively to see the effects of higher loads and to speed up the tests. Specimen Air #1 failed in tension when the bar cracked longitudinally after 17 days under 75% load (Figure 5.35(a)). Further investigation revealed that shear failure of part of the outer layer of the bar at the interface of bonded and unbonded portions led to longitudinal cracking of the bar (Figure 5.35(b)).

Specimens Water #2 failed in tension after being under 75% load for 17 hours. Part of the outer layer was separated from the bar at interface between bonded and unbonded portions of the bar (545 mm from anchor end where bond stress was a maximum) due to shear failure (Figure 5.36). The bar then cracked longitudinally due to initiation of the crack at the fibre-matrix interface at the loaded end due to higher shear stresses and broke at about 495 mm from anchor end (Figure 5.36(b)).

A failure pattern similar to Specimen Water #2 occurred in Specimen Alkaline #2 after 5 hours under 75% load (Figure 5.37). Leakage of solution around the bar inside the hole of the bearing plate was visible before increasing the load. Since the alkaline solution had already penetrated through the longitudinal crack when the bar broke, it was not possible to verify whether the degradation of glass fibres had occurred

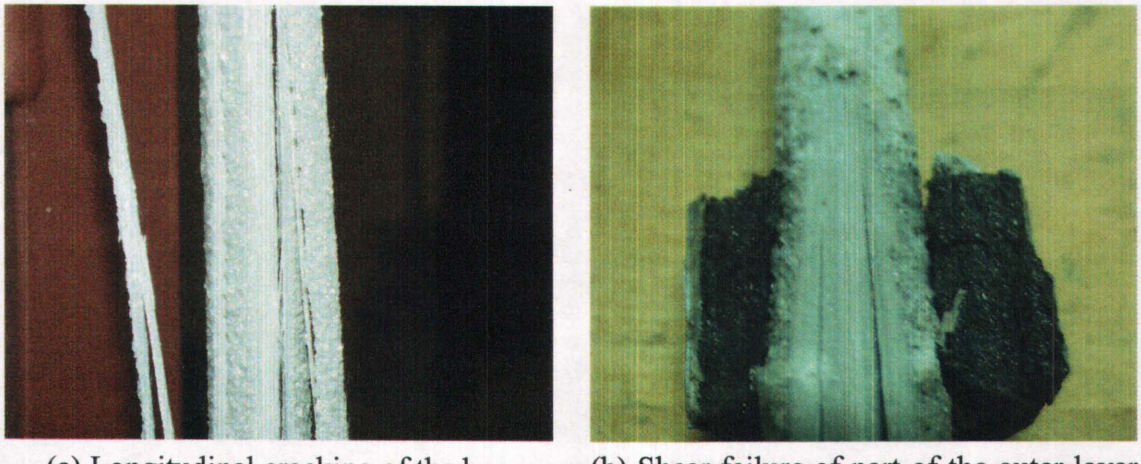

(a) Longitudinal cracking of the bar.

(b) Shear failure of part of the outer layer of the bar.

Figure 5.35. Photos of failed Specimen Isorod 25-75% Air #1.

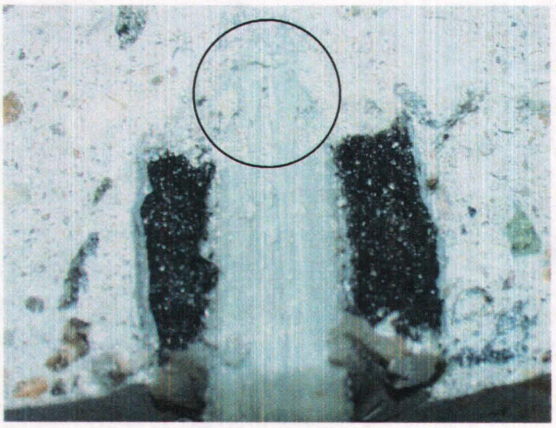

(a) Partial breakage of the outer layer of the bar at interface of bonded and unbonded portions (inside circles).

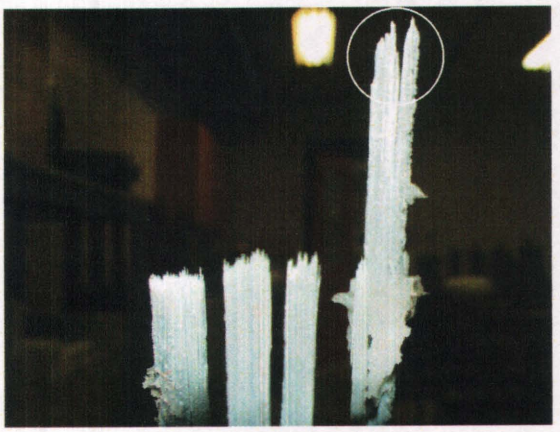

(b) Longitudinal cracking and tensile failure of the bar.

Figure 5.36. Photos of failed Specimen Isorod 25-75% Water #2.

before the failure. However, since the failed bar was similar to Specimen Water #2, it is unlikely that leakage of alkaline solution could have had any effects on the bar.

Isorod specimens with 50% load exhibited acceptable performance with respect to bond between the bars and concrete, since free end slips did not change significantly after initial slips of 0.14 to 0.45 mm (Figure 5.38). The final slips were between 0.25 and 0.50 mm under 50% loads.

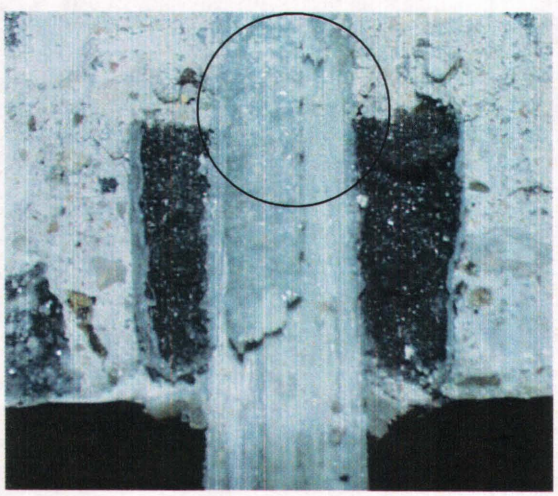

(a) Partial breakage of the outer layer of the bar at interface of bonded and unbonded portions (inside circles).

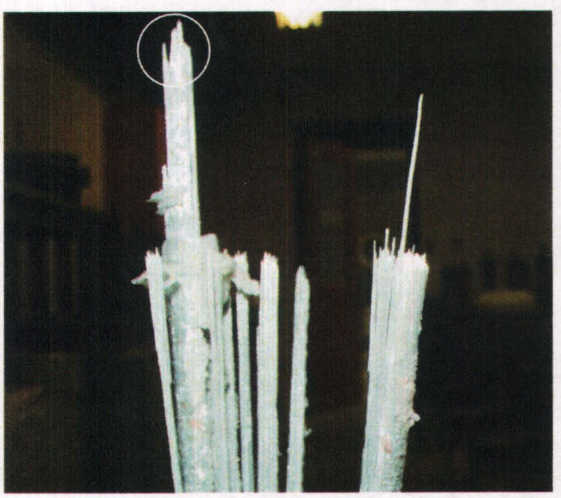

(b) Longitudinal cracking and tensile failure of the bar.

Figure 5.37. Photos of failed Specimen Isorod 25-75% Alkaline #2.

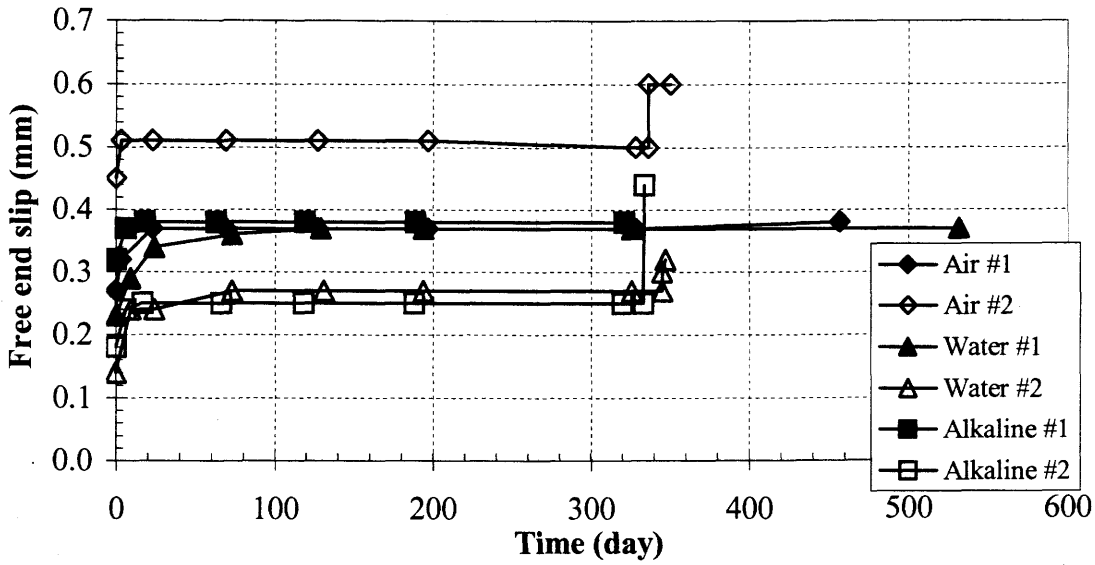

Figure 5.38. Free end slip-time curves for Isorod specimens with 50% load.

Specimens Air #1 and Water #1 were unloaded after 457 and 532 days, respectively, and were used to make samples for SEM observation. No cracks could be found on longitudinal and cross sections of the bar at bonded and unbonded portions. Also, no damage was visible on bar surfaces.

Figure 5.39 illustrates the SEM images for Specimen Water #1. Examination of cross sectional samples from bonded portions of the bars using electron microprobe

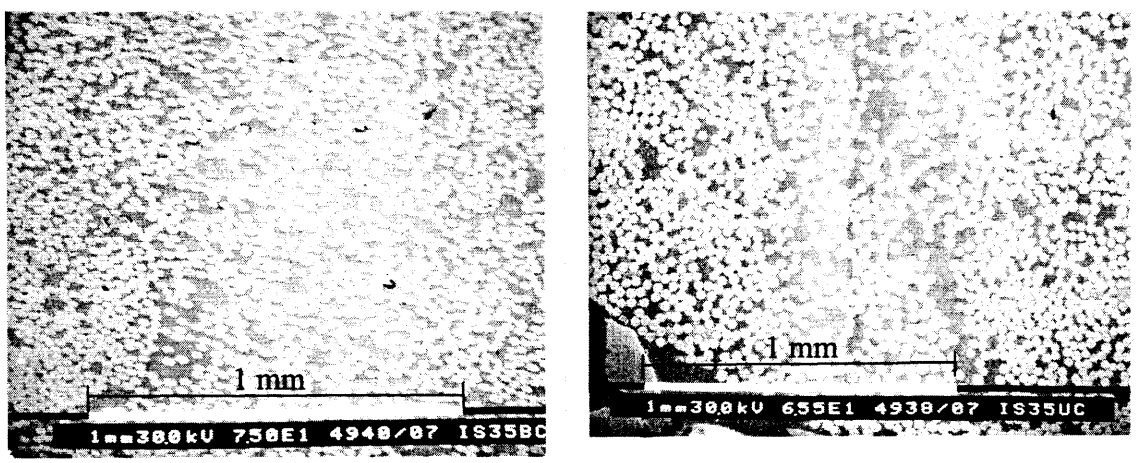

(a) Bonded portion. (b) Unbonded portion.

Figure 5.39. SEM images of the bar cross-sections at bonded and unbonded portions for Specimen Isorod 50% Water #1.

showed calcium ions in the fibres, but no trace of calcium ions in the matrix (Figure 5.40). Specimen Isorod 50% Alkaline #1 was under 50% load for 426 days when it failed. Alkaline solution was leaking out around the bar inside the hole of the bearing plate shortly after loading the specimen. Examination of the failed specimen indicated that the outer layer of the bar was broken partially at the interface of bonded and unbonded portions of the bar (540 mm from anchor end) and most of the fibres experienced tensile failure at the location close to the top of the bearing plate (515 mm from anchor end) at the test end of the specimen (Figure 5.41) where alkaline solution was leaking.

Breakage of half of the outer layer of the bar at the interface of bonded and unbonded portions suggests that sustained load may have caused separation between fibres and matrix at that location (shear failure), where the bond stress between the bar and concrete was maximum. The micro-crack extended along the bar towards the unbonded portion of the bar. Then, failure of the fibres may have occurred due to unbalanced load in the bar and/or due to alkaline attack.

Loads in Specimens Air #2, Water #2, and Alkaline #2 were increased from 50% to 75% after 336, 345, and 333 days, respectively. Specimen Air #2 cracked longitudinally after 21 days under 75% load and then fibres broke at a location close to bottom of the bearing plate due to unbalanced load in the bar. Investigation of the failed

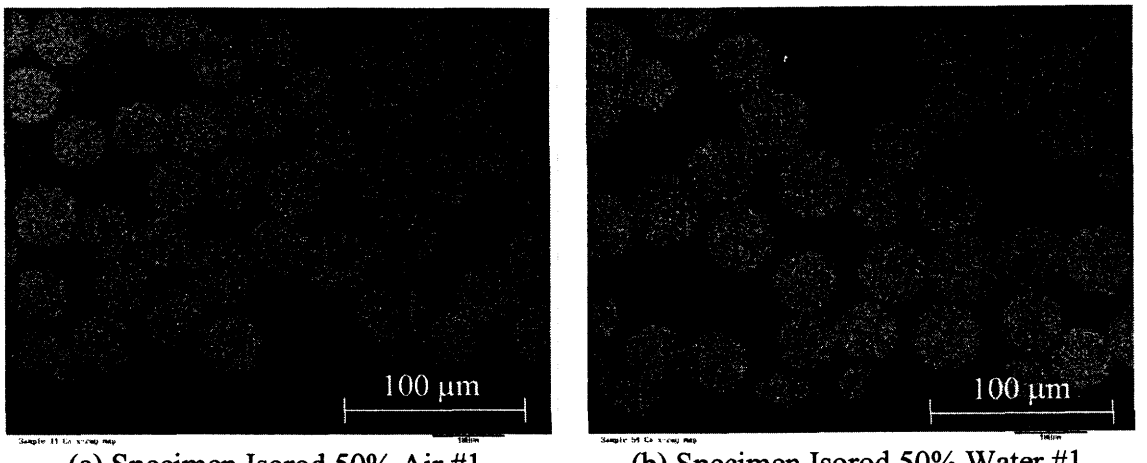

(a) Specimen Isorod 50% Air #1. (b) Specimen Isorod 50% Water #1.

Figure 5.40. Wavelength energy dispersive x-ray maps showing calcium ions in the fibres but not in the matrix.

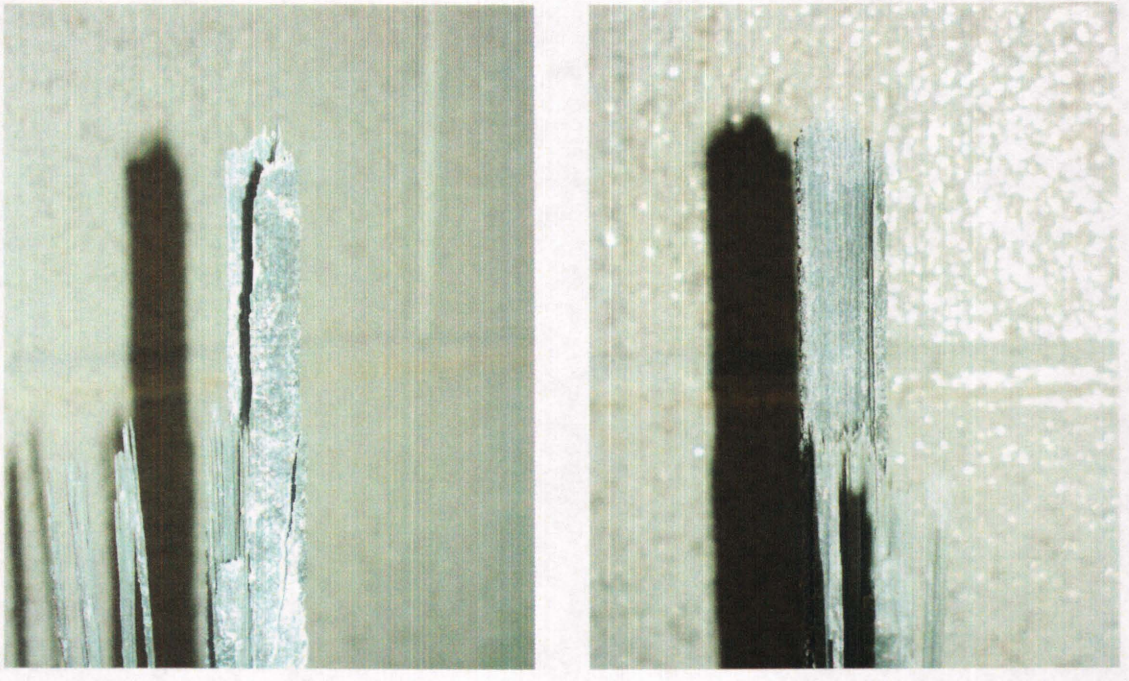

Figure 5.41. Breakage of half of the outer layer of the bar and broken fibres in Specimen Isorod 50% Alkaline #1.

specimen revealed shear failure between an outer layer and the inner portion of the bar had occurred at a location close to the interface of bonded and unbonded portions of the bar, where the bond stress was a maximum (Figure 5.42(a)). A broom shaped splitting failure of the bar could be seen on the other piece of the failed specimen (Figure 5.42(b)).

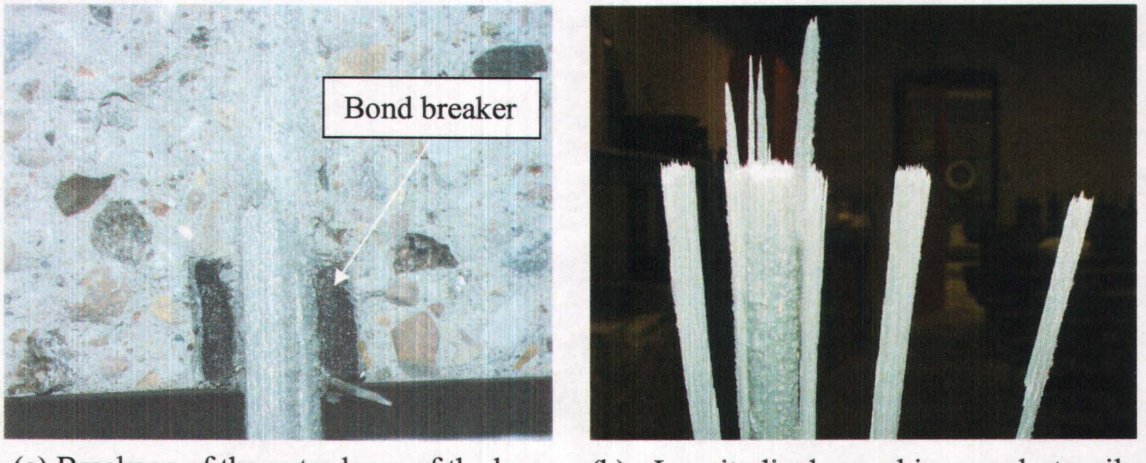

(a) Breakage of the outer layer of the bar.

(b) Longitudinal cracking and tensile failure of the bar.

Figure 5.42. Photos of failed Specimen Isorod 50-75% Air #2.

As shown in Figure 5.43(a), Specimen Water #2 cracked longitudinally after it was under 75% load for 71 days. Eighteen days after that, the specimen failed in tension. A similar failure pattern occurred for Specimen Alkaline #2. This specimen experienced longitudinal cracking after only one day under 75% load (Figure 5.43(b)). A cracking sound from the specimen was noticeable. A slippage of about 7 mm was seen at the loaded end (Figure 5.44). The specimen was holding 70% load at this point. Half an hour later, widening of the crack associated with a cracking sound occurred. The specimen failed in tension the next day. Broom shaped splitting of the bar could be seen on the failed specimen. Splitting of the concrete cylinder at the test end revealed that the breaking line of the outer layer of the bar was close to the interface of bonded and unbonded portions of the bar, as seen in Figure 5.45.

The similar failure patterns in Isorod specimens with increased sustained load of 75% indicate that the increased load caused shear failure at the interface of the bonded and unbonded portions of the bars, where the bond stress was a maximum. A crack then extended longitudinally along the bar and unbalanced load in the bar caused the breakage of the fibres.

(a) Specimen Isorod 50-75% Water #2.

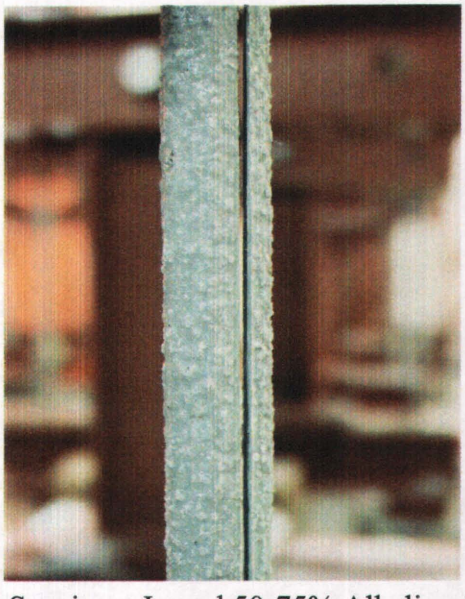

(b) Specimen Isorod 50-75% Alkaline #2.

Figure 5.43. Longitudinal cracks are apparent in the bars.

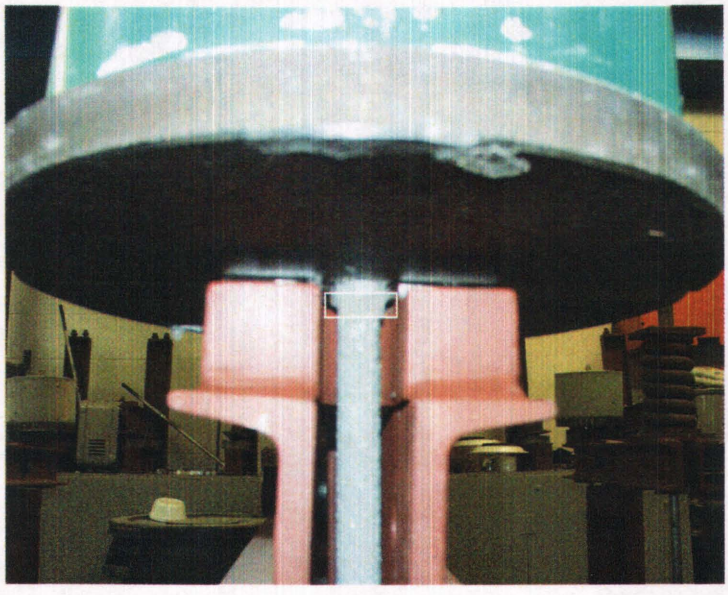

Figure 5.44. Slippage of the bar (Specimen Isorod 50-75% Alkaline #2) at the loaded end is visible. The sealant (inside the rectangle) was previously attached to the plate.

5.3.5. Summary

HB bars did not exhibit any degradation in bond between the bars and concrete. No significant changes in free end slip were measured under sustained loads in different environments. Static tests of some specimens that had been under sustained loads resulted in pullout failures at loads close to or higher than the average ultimate load

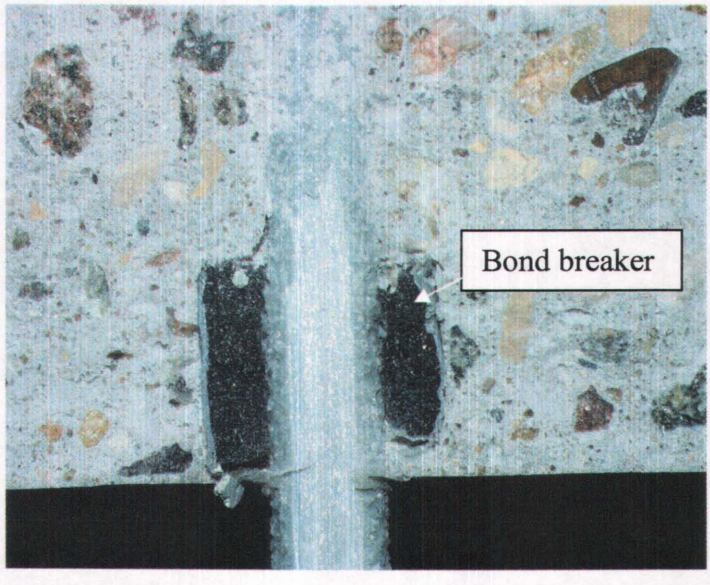

Figure 5.45. Photo of failed Specimen Isorod 50-75% Alkaline #2.

obtained from initial static tests.

However, SEM investigations indicated the initiation of micro-cracks in the bars when the loads were increased to 75%. The cracks were circumferential and extended over a longitudinal distance near the bonded-unbonded transition. They were consistent with a longitudinal shear failure, as the matrix attempted to transfer stresses to interior fibres by shear. X-ray maps did not show any calcium ions in the matrix, so it was unlikely that any hydroxyl ions could have penetrated into the bars to attack the glass fibres. Therefore, micro-cracks were thought to be due to increased sustained loads and not to degradation due to chemical attack. Micro-cracks in the bars were mostly at the matrix–fibre interfaces, showing separation between the two constituents. Because of the higher bond stress at the loaded end, higher shear stress existed between the matrix and the fibres at this location, which could have caused shear failure at the fibre-matrix interface. If the shear strength at fibre-matrix interface is less than bond stress between the bar and the concrete, it will cause shear failure and longitudinal cracking of the bar at the matrix-fibre interface.

C-bar specimens performed well when considering the bond between the bars and concrete. No major changes in free end slips were identified due to sustained loads in different environments. Although static tests of some of the specimens with 25% sustained load exhibited pullout failures which were associated with longitudinal cracking of the bars, the failure loads were close to or higher than the average static loads obtained initially. Longitudinal cracking of the bars or pullout failure associated with longitudinal cracking on the bars defined the failure modes in these specimens. Therefore, sustained loads of 25% could have caused longitudinal shear failure between fibres and matrix. Longitudinal cracking was an indication of partial breakage (separation) of the outer layer of the bar at higher loads since two specimens with 50% load in water failed due to complete breakage or shear failure of the outer layer of the bar at the transition between bonded and unbonded portions. Also, SEM investigations showed micro-cracks in Specimens C-bar 50% Alkaline #1 and C-bar 50-75% Air #1. X-ray maps did not show any calcium ions in the matrix of the bars. Therefore, sustained loads of 50% are believed to have caused shear failure most possibly at the

interface of bonded and unbonded portions of the bars due to higher bond stress at this location. This micro-cracking extended within the bar circumferentially and longitudinally along the bars and led to complete or partial necking of the bars. In some specimens (e.g. C-bar 50% Water), complete circumferential separation of the outer layer at interface region between bonded and unbonded portions of the bar caused the failure. In other specimens (e.g. C-bar 50-75% Alkaline #2), partial separation of the outer layer in this same region caused longitudinal cracking and failure of the bar.

The performance of Isorod specimens with respect to bond between the bars and concrete was good and acceptable since free end slips did not change appreciably under sustained loads in different environments. Static testing of some specimens caused pullout failures at loads close to or higher than the average ultimate loads found from initial static tests. SEM examination of two specimens with 50% load did not detect any cracks in the bars. Also, no calcium ions were found in the matrix using x-ray maps. All the specimens with increased load of 75% failed in tension under sustained loads within a relatively small length of time. Failures started by cracking of the bars longitudinally, which was followed by breaking of the bars in tension in some specimens. Examination of the failed specimens revealed that the high bond stress at the interface of bonded and unbonded portions of the bars caused shear failure between the fibres and the matrix resulting in micro-cracks which extended along the bar. Partial breakage or separation of the outer layer of the bars led to longitudinal cracking of the bars and failure of the specimens.

As mentioned in Section 5.3.2.3, circumferential cracking of the GFRP bars started under sustained loads; therefore, time-dependent (creep) effects are suggested. Although there was no information available on creep properties of the resins used in the GFRP bars, studies show that epoxy resins exhibit creep behaviour under sustained loads at room temperature (2.2.2.1). On the other hand, glass fibres do not creep significantly under sustained loads at room temperature (Section 2.2.3.2).

Furthermore, micro-cracks appeared to initiate at the loaded end of embedment length where the bond stress was a maximum. The bond stress is not uniform and is

higher (about 40% higher than average bond stress) at the loaded end of embedment length of the bar (see Section 2.4.3).

Therefore, it is suggested that circumferential micro-cracks at the fibre/matrix interface at the loaded end of the embedment length and close to the surface of the bar (region of highest shear stress within the bar) were due to shear fracture at or near the fibre/matrix interface for fibres close to the surface of the bar. Shear strain incompatibility may have been induced in the matrix and at fibre-matrix interface due to differential creep behaviour of the fibres and the matrix under existing high shear stresses.

In conclusion, bond degradation between the GFRP bars and concrete did not occur under sustained loads in the different environments used in this study. Shear failure between the glass fibres and the resin matrix occurred under sustained loads due to incompatibility in creep properties of the two constituents. For HB bars, separation of fibres and matrix could be seen at sustained bond stresses higher than 6.9 MPa (50% of ultimate bond strength), whereas sustained bond stresses of 3.9 MPa (25% of ultimate bond strength) resulted in shear failure along the fibre-matrix interface and through the matrix in C-bar specimens. Isorod specimens did not exhibit any decline in capacity under sustained bond stresses of 9.5 MPa (50% of ultimate bond strength).

Chapter 6

Conclusions and recommendations

6.1. Introduction

An experimental program was conducted to study the long-term bond behaviour between fibre reinforced polymer (FRP) bars and concrete under sustained loads. Also, the effects of alkaline and moist ambient conditions on the bond between FRP bars and concrete under sustained loads were investigated. The experiments were performed in two phases. In Phase I, pullout specimens were made using one type of glass FRP (GFRP) bar (Isorod manufactured by Pultrall Inc.), two types of carbon FRP (CFRP) bars (CFCC and Leadline manufactured by Tokyo Rope Mfg. Co. and Mitsubishi Corporation, respectively), and conventional steel rebar. These specimens were tested in room conditions under sustained loads of different magnitudes. In Phase II of the experimental program, three different types of GFRP bars (HB, C-bar, and improved Isorod manufactured by Hughes Brothers Inc., Marshall Industries Composites Inc., and Pultrall Inc., in that order) were used in pullout specimens that were tested under two different sustained loads in three different environments: in room conditions, water, and alkaline solution.

After the long-term tests, a failure analysis of the specimens was performed to determine the possible causes of failure. Static tests of some of the specimens that did not fail under sustained loads, along with scanning electron microscopy (SEM) and electron microprobe analysis (EMPA) techniques, were employed in this regard. SEM investigation revealed interesting results regarding the deterioration of the FRP bars on the micro structural scale.

6.2. Conclusions

The following conclusions are based on the results found in the experimental program and are limited to the materials and the conditions used in this study.

FRP reinforcing bars had average static pullout bond strengths that were 24% (Isorod), 43% (Leadline), and 48% (CFCC) of the bond strength of companion reinforcing steel specimens. The bond mechanism for CFCC bars was friction. Mechanical interlock between the bars' surface deformations (lugs or indentations) and the concrete appeared to be the main mechanism for Isorod and Leadline bars, as well as for steel rebar. In FRP specimens, the surfaces of the bars in contact with concrete were damaged during pullout while, with the steel bars, the lugs crushed the surrounding concrete.

In Phase I, under sustained loading, free end slip in the FRP specimens generally exceeded the slip in steel specimens for the same level of bond stress: 0.28 vs. 0.17 mm on average for CFCC specimens, 6.01 vs. 0.17 mm on average for Leadline specimens, and 7.97 vs. 0.19 mm on average for Isorod specimens. Compared to steel specimens, CFCC specimens showed good performance (low free end slip values) under sustained bond stresses up to 9.4 MPa (90% of static bond strength). In these specimens, free end slips were not that high (0.28 vs. 0.17 mm on average) compared to companion steel specimens tested; and also, slippage in CFCC specimens was stabilized after 150 to 250 days depending on the load level.

Isorod specimens exhibited a poor performance (large free end slip values). The Isorod specimens had large free end slips under a sustained bond stress of 4.3 MPa (75% of static bond strength), compared to companion steel specimens. Large free end slips were also experienced by Leadline specimens under sustained bond stresses of 7.0 MPa (60% of static bond strength) or higher. Slippage did not stabilize and continued to increase to the end of the tests (i.e. about 300 days) in Leadline and Isorod specimens. Post-testing investigations revealed that damage to the surfaces of Isorod and Leadline bars was apparent. Broken fibres and damaged regions of coating were noticeable.

For the bars used in Phase II, bond degradation between GFRP bars and concrete was not found to be a problem for the specimens in this test series. For these bars, no significant change in free end slip occurred under sustained loads in different environments. It should be noted that the sustained load levels were lower than the load levels applied to the FRP specimens used in Phase I.

On the other hand, sustained loads appeared to have affected the bars. Shear failure between the glass fibres and the resin matrix occurred under sustained loads possibly due to differences in creep characteristics of the two constituents. Isorod specimens did not exhibit any decline in bond between fibres and resin under sustained loads of 25% and 50% of ultimate static strength (bond stresses of 4.8 and 9.5 MPa) except for one specimen with 50% load in alkaline solution, which failed in tension after 426 days. In this specimen, alkaline solution was leaking out around the bar inside the hole of the bearing plate shortly after loading the specimen, which may have caused tensile failure of the glass fibres. SEM investigation of two specimens with 50% load in water and air environments did not show any cracks in the bars.

Increasing load levels to 75% of ultimate static strength (bond stress of 14.3 MPa) caused longitudinal circumferential cracking of Isorod bars due to apparent shear failure at the fibre-matrix interface, which was often followed by a tensile failure of the glass fibres. The longitudinal cracking started by separation of part of the outer layer of the bar at the interface of bonded and unbonded portions of the bar, where the bond stress between the bar and the concrete was a maximum. These specimens (one from each load level in each environment) failed after being under 75% load for 5 hours (25-75% alkaline) to 71 days (50-75% water).

Sustained loads of 25% and 50% of ultimate static strength (bond stresses of 3.5 and 6.9 MPa) did not result in any observable effects for the HB specimens in any of the specified environments. Initiation of circumferential micro-cracks in HB bars occurred when the sustained load was increased to 75% (bond stress of 10.4 MPa). SEM observation of Specimens 25-75% Water #2 and 50-75% Alkaline #2 revealed that the micro-cracks were mostly at fibre-matrix interfaces and had extended over a

longitudinal distance near the bonded-unbonded transition (location of maximum bond stress).

However, static testing of Specimens HB 25-75% Air #2, HB 50-75% Air #2, and HB 50-75% Water #1 did not indicate any cracking of the bars. The specimens experienced pullout failure at loads close to or higher than the average ultimate static loads obtained from the initial static tests. Specimen HB 25-75% Alkaline #2 failed in tension at an indentation on the bar surface at the location of the concrete cylinder base where leakage of alkaline solution had started a few days after increasing the load. It is possible that the alkaline solution had caused failure of the bar by attacking glass fibres since the coating of the bar was thinner at the location of the indentation. The fact that a similar specimen (25-75% Air #2) failed in pullout when tested statically supports this hypothesis.

In C-bar specimens, a sustained load of 25% of the ultimate static strength (bond stress of 3.9 MPa) resulted in weakening the bars. Static testing of three specimens (after about 467 days) caused longitudinal cracking (shear failure) of the bars along the fibre-matrix interface and through the matrix that ultimately resulted in pullout failure or tensile failure of the bars.

Longitudinal cracking also occurred when the load was increased from 25% to 75% in C-bar Specimens Water #2 and Alkaline #2. The specimens were under 75% load for about 22 days when they cracked longitudinally. Longitudinal shear failure between the fibres and the matrix was a result of partial breakage (separation) of the outer layer of the bar at the transition between the bonded and unbonded portions of the bar, which was the location of maximum bond stress. Specimen 25-75% Air #2 experienced longitudinal cracking when tested statically after 338 days under 25% load and 224 days under 75% load.

Under sustained load of 50% (bond stress of 7.8 MPa), complete breakage of the outer layer of the bars at the interface of the bonded and unbonded portions of the bars (location of maximum bond stress) caused the tensile failure of C-bar rods in the specimens in water (#1 and #2) after about 320 days. In addition, SEM investigation

showed circumferential cracking in the bar cross-section in Specimen C-bar 50% Alkaline #1. Cracks were also observed in the bonded portion of the bar in Specimen 50-75% Air #1. Similar to the specimens 50% Water #1 and #2, breakage of outer layer of the bar occurred after 336 days when the load was being increased to 75% in Specimen 50-75% Alkaline #2.

No sign of calcium ion ingress could be found in any of the specimens tested in Phase II. However, C-bar specimens under 50% and 75% sustained loads in water and alkaline environments showed tensile failure or cracking between the fibres and the matrix in shorter periods compared to C-bar specimens in air. This may have been because of degradation of the matrix due to absorption of water, although no evidence of deterioration of matrix could be found. Isorod specimens in water and alkaline solution under 75% load (except for Specimen Isorod 50-75% Water #2) exhibited similar behaviour. The specimens failed in tension sooner than the specimens tested in air.

In general, the performance of CFCC bars with respect to bond between the bars and concrete was satisfactory when compared to that of steel rebars. Maximum bond stress in these bars could be as high as 9.4 MPa. However, Isorod (used in Phase I) and Leadline rods did not exhibit good performance under sustained loads of 60% or higher. Bond stresses in these bars (for the configurations tested) should not reach 3.4 MPa and 7.2 MPa, respectively, based on the test results.

Bond degradation between concrete and GFRP bars used in Phase II was not a problem. All bars performed well under sustained loads up to 50% of ultimate static bond strength of the bars. However, shear failure between the fibres and the matrix occurred in the bars, especially under increased sustained loads of 75% of ultimate static bond strength. Based on the test results, maximum bond stress should not exceed levels of approximately 6.9, 3.9, and 9.5 MPa in HB, C-bar, and Isorod (used in Phase II) bars, respectively. ISIS Canada (2000) and ACI (2001) give a value of 4.63 MPa as maximum allowable bond stress for FRP bars.

6.3. Recommendations

The following recommendations are made for future studies. The recommendations are based on the findings of the experiments conducted in this thesis.

The bond between the fibres and matrix under sustained loads needs more research and specific considerations should be made in defining the maximum bond stress that should be applied to the GFRP bars. High bond stresses between FRP bars and concrete could cause shear and/or tensile failure of bars due to bond degradation between the fibres and the matrix under sustained loads in structural elements within the first few years of being in service.

Modeling of the FRP bars under sustained loads, using finite element method and mechanical properties of the constituents, gives a better understanding of shear stress transfer inside the bar and shear stresses at fibre/matrix interaction region. A complete bond between the fibres and the matrix could be assumed in the model.

Free end slips and loads were measured and monitored manually during the long-term tests. The measurements were subjective and human error was always involved. Use of a data acquisition system to collect data and to monitor the constant and variable parameters in long-term tests is more reliable and much easier if an appropriate system is chosen. The measurements will be taken and recorded in shorter periods. The loads can be checked every day and adjusted if necessary. Time of failure for specimens could be obtained within few hours error, instead of few days error with manual measurements. Also, variables such as free end slip can be recorded at failure.

References

Abrishami, H. H. and Mitchell, D. 1996. "Analysis of bond stress distributions in pullout specimens." Journal of Structural Engineering, V. 122, No. 3, pp. 255-261.

ACI. 1996. State-of-the-Art Report on Fiber Reinforced Plastic (FRP) Reinforcement for Concrete Structures. Reported by American Concrete Institute, committee 440R.

ACI. 2001. Guide for the design and construction of concrete reinforced with FRP bars. ACI 440.1R-01. Reported by American Concrete Institute, committee 440.

Al Cheikh, A. and Murat, M. 1988. "Kinetics of non-congruent dissolution of E-glass fiber in saturated calcium hydroxide solution." Cement and concrete research, V. 18, No. 6, pp. 943-950.

ASM. 1986. Failure analysis and prevention. Metals handbook, 9th ed., v11, American Society for Metals, Materials Park, Ohio.

Bakis, C. E. 1993. "FRP reinforcement: materials and manufacturing." Fiber-reinforced-plastic (FRP) reinforcement for concrete structures: properties and applications. Nanni, A., Editor, Elsevier Science Publishers B.V. Amsterdam, The Netherlands, pp. 13-58.

Ballinger, C. A. 1992. "Development of fibre-reinforced plastic products for the construction market – How has and can it be done?" Advanced composite materials in bridges and structures, 1st International Conference, Sherbrooke, Quebec, Edited by K.W. Neale and P. Labossiere, pp. 3-13.

Bank, L. C., Puterman, M., and Kutz, A. 1998. "The effect of material degradation on bond properties of fiber reinforced plastic reinforcing bars in concrete." ACI Materials Journal, V 95, No. 3, pp. 232-243.

Benmokrane, B., Tighiouart, B., and Chaallal, O. 1996. "Bond strength and load distribution of composite GFRP reinforcing bars in concrete." ACI Materials Journal, V 93, No. 3, pp. 246-253.

Benmokrane, B., Xu, H., and Nishizaki, I. 1997. "Aramid and carbon fibre-reinforced plastic prestressed ground anchors and their field applications." Canadian Journal of Civil Engineering, V 24, No. 6, pp. 968-985.

Benmokrane, B., Wang, K., Laoubi, J., Robert, F., and Ton-That, M. T. 2001a. "Stress corrosion behaviour of composite reinforcing bars in alkaline environment." 29th Annual Conference of the Canadian Society for Civil Engineering, Proceedings, A10, 8 pp.

Benmokrane, B., Zhang, B., Laoubi, K., Tighiouart, B., and Lord, I. 2001b. "Mechanical and bond properties of new generation CFRP reinforcing bars for concrete structures." 29th Annual Conference of the Canadian Society for Civil Engineering, Proceedings, A11, 8 pp.

Bentur, A. and Mindess, S. 1990. Fibre reinforced cementitious composites. Elsevier Science Publishing Ltd., New York.

Callister, W. D., Jr. 2000. Materials science and engineering: an introduction, Appendices B and C. Wiley, New York.

Chaallal, O. and Benmokrane, B. 1993. "Physical and mechanical performance of an innovative glass fibre reinforced plastic rod for concrete and grouted anchorages." Canadian Journal of Civil Engineering, V. 20, No. 2, pp. 254-268.

CHBDC. 1996. Fiber reinforced structures. Canadian Highway Bridge Design Code, Final draft. Ministry of Transportation , Downsview, Ontario.

Chin, J. W., Haight, M. R., Hughes, W. L., and Nguyen, T. 1998. "Environmental effects on composite matrix resins used in construction." Durability of fibre reinforced polymer (FRP) composites for construction (CDCC'98). 1st international conference, Proceedings, Canada. Benmokrane, B., Rahman, H., Editors, pp. 229-241.

Chin, J. W., Nguyen, T., and Aouadi, K. 1997. "Effects of environmental exposure on fiber-reinforced plastic (FRP) materials used in construction." Journal of Composites Technology & Research, V. 19, No. 4, pp. 205-213.

Clark, J. L., O'Regan, D. P., and Thirugnanendran, C. 1996. Modification of design rules to incorporate non-ferrous reinforcement, Draft. Eurocrete Project, London.

Cosenza, E., Manfredi, G., and Realfonzo, R. 1997. "Behavior and modeling of bond of FRP rebars to concrete." Journal of composites for construction, V. 1, No. 2, pp. 40-51.

Daniali, S. 1992. "Development length for fibre-reinforced plastic bars." Advanced composite materials in bridges and structures, 1st International Conference, Sherbrooke, Canada. Neale, K. W. and Labossiére, P., Editors, pp. 179-188.

Domenico, N. G., Mahmud, Z. I., and Rizkalla, S. H. 1998. "Bond properties of carbon fiber composite pre-stressing strands." ACI Structural Journal, V. 95, No. 3, pp. 281-290.

Doremus, R. H. and Mehrotra, Y. 1983. "Reaction of water with glass: influence of a transformed surface layer." Journal of materials science, V. 18, No. 2, pp. 612-622.

Dutta, P. K. and Hui, D. 2000. "Creep rupture of a GFRP composite at elevated temperatures." Computers and structures, V. 76, No. 1, pp. 153-161.

Ehsani, M. R., Saadatmanesh, H., and Nelson Thompson, C. 1997a. "Transfer and flexural bond performance of aramid and carbon FRP tendons." PCI Journal, V. 42, No. 1, pp. 76-86.

Ehsani, M. R., Saadatmanesh, H., and Tao, S. 1997b. " Bond behavior of deformed GFRP bars." Journal of Composite Materials, V. 31, No. 14, pp. 1413-1430.

Faza, S. and GangaRao, H.V.S. 1993. "Glass FRP reinforcing bars for concrete." Fiber-reinforced-plastic (FRP) reinforcement for concrete structures: properties and applications. Nanni, A., Editor, Elsevier Science Publishers B.V. Amsterdam, The Netherlands, pp. 167-188.

FIP. 1992. High-strength fiber composite tensile elements for structural concrete. Federation International de la Précontrainte Commission on Prestressing Materials and Systems. Institute of Structural Engineering, London.

Gdoutos, E. E., Pilakoutas, K., and Rodopoulos, C. A. 2000. Failure analysis of industrial composite materials. McGraw-Hill, New York.

Gilstrap, J. M., Burke, C. R., Dowden, D. M., and Dolan, C. W. 1997. "Development of FRP reinforcement guidelines for pre-stressed concrete structures." Journal of Composites for Construction, V. 1, No. 4, pp. 131-139.

Goto, Y. 1971. "Cracks formed in concrete around deformed tension bars." Journal of the American Concrete Institute, V. 68, No. 4, pp. 244-251.

Hattori, A., Inoue, S., Miyagawa, T., and Fuji, M. 1995. "A study on bond creep behaviour of FRP rebars embedded in concrete." Non-metallic (FRP) reinforcement for concrete structures. Taerwe, L. Editor, E & FN Spon, London, pp. 172-179.

Hollaway, L. 1993. Polymer composites for civil and structural engineering. Chapman & Hall, Cambridge, Great Britain.

Hollaway, L. C., Crowder, J. R., and Howard C. M. 1990. "End use performance and time-dependent characteristics," in Polymers and polymer composites in construction, Hollaway, L. C., Editor, Thomas Telford Ltd., London, pp. 139-165.

Hughes Brothers Inc. Glass fiber reinforced polymer rebar, 16 pp.

Hundley, A. and Dolan, C. 1996. "Non-accelerated creep-rupture of fiber-reinforced-plastics in a concrete environment." Materials for the new millennium: Proceeding of the 4th Materials Engineering Conference, Published by ASCE, New York, V. 1, pp. 519-526.

ISIS Canada. 2000. Reinforcing concrete structures with fibre reinforced polymers, Draft, Spring 2000. ISIS-M04-00, The Canadian Network of Centres of Excellence on Intelligent Sensing for Innovative Structures, Winnipeg, Manitoba.

Jerrett, C. V. and Ahmad, S. H. 1995. "Bond tests of carbon fibre reinforced plastic (CFRP) rods." Non-metallic (FRP) reinforcement for concrete structures. Taerwe, L. Editor, E & FN Spon, London, pp. 180-191.

JMC. 1995. Design guidelines for FRP prestressed concrete members. Japan Ministry of Construction, Building Research Institute, Tokyo.

JSCE. Recommendation for design and construction of concrete structures using continuous fiber reinforcing materials, Concrete Engineering Series 23, Leadline section only. Japanese Society of Civil Engineers.

JSCE. 1995. Recommendation for design and construction of reinforced concrete structures using continuous fiber reinforced materials, Draft. Japanese Society of Civil Engineers, Research Committee, Tokyo.

Kanakubo, T., Yonemaru, K., Fukuyama, H., Fujisawa, M., and Sonobe, Y. 1993. "Bond performance of concrete members reinforced with FRP bars." Fiber-reinforced-plastic reinforcement for concrete structures, International Symposium, ACI SP-138. Nanni, A. and Dolan, C. W., Editors, pp. 767-788.

Kant, T., Ramana, V. P. V., Dutta, P. K., Mukherjee, A. and Desai, Y. 1997. "Construction applications of fiber reinforced polymer composites, A survey." Proceedings of the Seventh International Offshore and Polar Engineering Conference. Honolulu, USA, pp. 657-663.

Katsuki, F. and Uomoto, T. 1995. "Prediction of deterioration of FRP rods due to alkali attack." Non-metallic (FRP) reinforcement for concrete structures. Taerwe, L., Editor, E & FN Spon, London, pp. 82-89.

Larralde, J., Burdette, J., and Harris, B. 1993. "Bond stress distribution of FRP bars in concrete." Proceedings of the 38th SAMPE Symposium and Exhibition, Covina, CA, V. 38, No. 2, pp. 1775-1788.

Larralde, J. and Silva-Rodriguez, R. 1993. "Bond and slip of FRP rebars in concrete." Journal of Materials in Civil Engineering, V. 5, No. 1, pp. 30-40.

Lutz, L. A. and Gergely, P. 1967. "Mechanics of bond and slip of deformed bars in concrete." Journal of the American Concrete Institute, V. 64, No. 11, pp. 711-721.

Makitani, E., Irisawa, I., and Nishiura, N. 1993. "Investigation of bond in concrete member with fiber reinforced plastic bars." Fiber-reinforced-plastic

reinforcement for concrete structures, International Symposium, ACI SP-138. Nanni, A. and Dolan, C. W., Editors, pp. 315-331.

Mallick, P. K. 1988. Fiber-reinforced composites: materials, manufacturing, and design. Marcel Dekker, Inc. New York.

Malvar, L. J. 1995. "Tensile and bond properties of GFRP reinforcing bars." ACI Materials Journal, V. 92, No. 3, pp. 276-285.

Malvar, L. J. 1998. "Durability of composites in reinforced concrete." Durability of fibre reinforced polymer (FRP) composites for construction (CDCC'98). 1st International Conference, Proceedings. 1998, Canada. Benmokrane, B. and Rahman, H., Editors, pp. 361-372.

Marshall Industries Composites Inc. C-bar composite reinforcing rods the future of concrete reinforcement, 7 pp.

Mashima, M. and Iwamoto, K. 1993. "Bond characteristics of FRP rod and concrete after freezing and thawing deterioration." Fiber-reinforced-plastic reinforcement for concrete structures, International symposium, ACI SP-138. Nanni, A. and Dolan, C. W., Editors, pp. 51-69.

Mathey, R. G., and Watstein, D. 1961. "Investigation of bond in beam and pull-out specimens with high-yield-strength deformed bars." ACI Journal, V. 57, No. 3, pp. 1071-1089.

McGarry, F. J. 1994. "Polymer composites." Annual Review of Materials Science, V. 24., Publisher: Annual Reviews Inc., Palo Alto, CA, USA, pp. 63-82.

Miklofsky, H. A., Gonsior, M. J., and Santini, J. J. 1965. Further studies of epoxy bonding compounds. National Academy of Sciences, National Research Council. Washington, D.C.

Mitsubishi Corporation. 1993. Leadline Carbon Fiber Tendons/Bars (Product Specification Manual), 4 pp.

Mufti, A. A., Erki, M-A., and Jaeger, L. G. 1991. Advanced composite materials with applications to bridges, Chapter One. State-of-the-Art Report, Edited by Mufti, A. A., Erki, M-A., and Jaeger, L. G., pp. 1-20.

Nagae, S. and Otsuka, Y. 1994. "Effect of sizing agent on corrosion of glass fibres in water." Journal of materials science letters, V. 13, No. 20, pp. 1482-1483.

Nanni, A., Al-Zaharani, M. M., Al-Dulaijan, S. U., Bakis, C. E., and Boothby, T. E. 1995a. "Bond of FRP reinforcement to concrete – Experimental results." Non-metallic (FRP) reinforcement for concrete structures, Taerwe, L., Editor, E & FN Spon, London, pp. 135-145.

Nanni, A., Bakis C. E., and Boothby, T. E. 1995b. "Test methods for FRP-concrete systems subjected to mechanical loads: State of the art review." Journal of Reinforced Plastics and Composites, V. 14, No. 6, pp. 524-558.

Porter, M. L., Mehus, J., and Young, K. A. 1995. Aging degradation of fiber composite reinforcements for structural composite, final report. September 1995, College of Engineering, Iowa State University.

Pultrall Inc. 1992. Isorod, glass-fiber composite rebar for concrete, technical data, 8 pp.

Pultrall Inc. Isorod composite rebar, 11 pp.

Rizkalla, S. H. and Tadros, G. 1994. " A smart highway bridge in Canada." Concrete International, V. 16, No. 6, pp. 42-44.

Saadatmanesh, H. and Tannous, F. E. 1999. "Relaxation, creep, and fatigue behavior of carbon fiber reinforced plastic tendons." ACI Materials Journal, V. 96, No. 2, pp. 143-153.

Santoh, N. 1993. "CFCC (Carbon Fiber Composite Cable)." Fiber reinforced plastic (FRP) reinforcement for concrete structures: properties and applications. Nanni, A., Editor, Elsevier Science Publishers B.V. Amsterdam, The Netherlands, pp. 223-247.

Sekijima, K., Otsuka, Y., and Konno, T. 1999. "Durability of fiber reinforced polymer reinforcement embedded in concrete." Fourth International Symposium, Fiber

reinforced polymer reinforcement for reinforced concrete structures, Proceedings. Dolan, C. W., Rizkalla, S. H., and Nanni, A., Editors, ACI international SP-188, pp. 501-513.

Sen, R., Mariscal, D., and Shahawy, M. 1993a. "Durability of fiberglass pretensioned beams." ACI Structural Journal, V. 90, No. 5, pp. 525-533.

Sen, R., Mariscal, D., and Shahawy, M. 1993b. "Investigation of S-2 glass/epoxy strands in concrete." Fiber-reinforced-plastic reinforcement for concrete structures, International Symposium, ACI SP-138. Nanni, A. and Dolan, C. W., Editors, pp. 15-33.

Shackelford, James F. 1996. Introduction to materials science for engineers, 4th ed. Prentice Hall Inc., New Jersey.

Sonobe, Y., Fukuyama, H., Okamoto, T., Kani, N., Kimura, K., Kobayashi, K., Masuda, Y., Matsuzaki, Y., Mochizuki, S., Nagasaka, T., Shimizu, A., Tanano, H., Tanigaki, M., and Teshigawara, M. 1997. "Design guidelines of FRP reinforced concrete building structures." Journal of Composites for Construction, V. 1, No. 3, pp. 90-113.

Sturgeon, J. B. 1978. "Creep of fibre reinforced thermosetting resins." Creep of Engineering Materials, Chapter 10, Pomeroy, C. D., Editor, Heffers Printers Ltd., Cambridge, England.

Tokyo Rope Mfg. Co., Ltd. 1993. Technical Data on CFCC, 12 pp.

University of Oklahoma. "What is an Electron Microprobe?" Electron Microprobe Laboratory. January 2002. <http://research.ou.edu/Microprobe/WhatIs.htm>.

Uomoto, T. and Nishimura, T. 1999. "Deterioration of aramid, glass, and carbon fibers due to alkali, acid, and water in different temperatures." Fourth International Symposium, Fiber reinforced polymer reinforcement for reinforced concrete structures, Proceedings. Dolan, C. W., Rizkalla, S. H., and Nanni, A., Editors, ACI international SP-188, pp. 515-522.

Vijay, P. V. and GangaRao, V. S. 1999. "Accelerated and natural weathering of glass fiber reinforced plastic bars." Fourth International Symposium, Fiber reinforced

polymer reinforcement for reinforced concrete structures, Proceedings. Dolan, C. W., Rizkalla, S. H., and Nanni, A., Editors, ACI international SP-188, pp. 605-614.

Appendix A

Calibration curves for loading frames (apparatus) used in long term tests

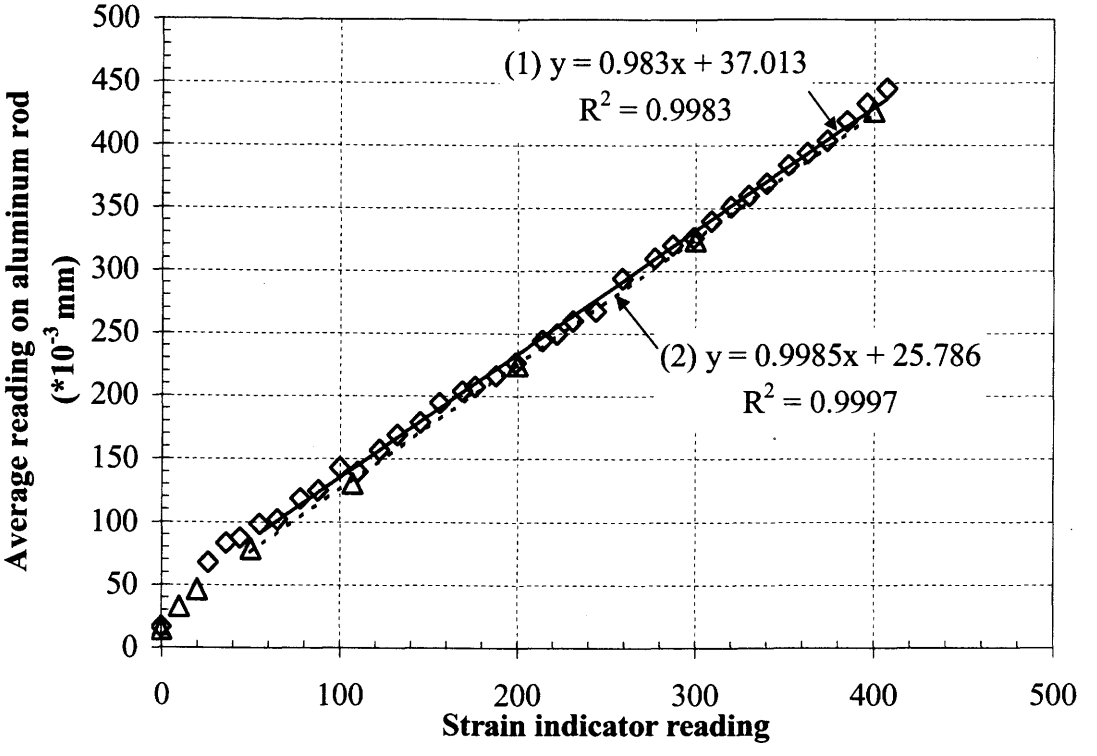

Figure A.1. Calibration curves for loading frame #1.

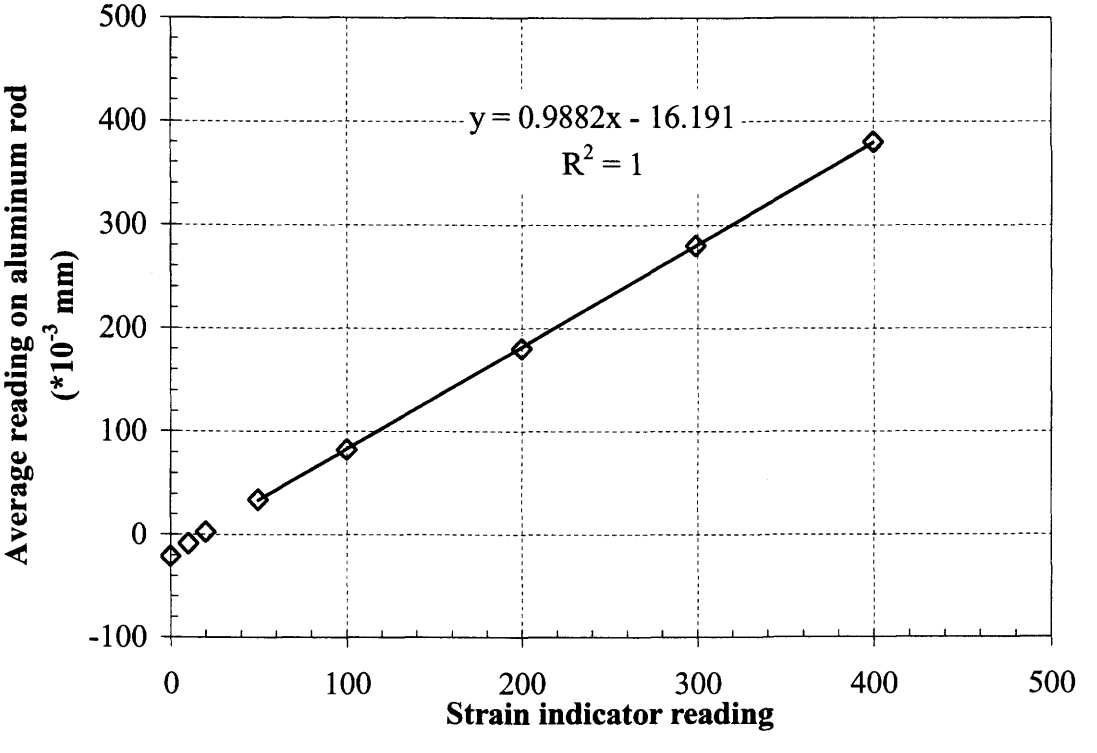

Figure A.2. Calibration curve for loading frame #2.

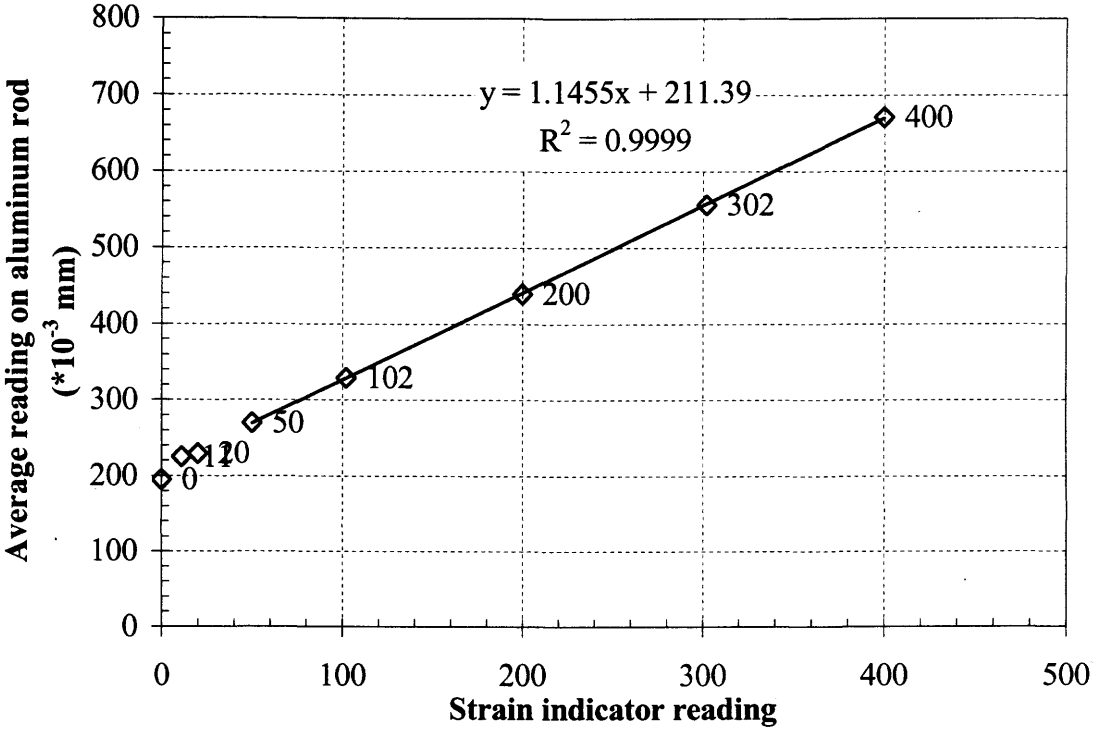

Fi26gure A.3. Calibration curve for loading frame #3.

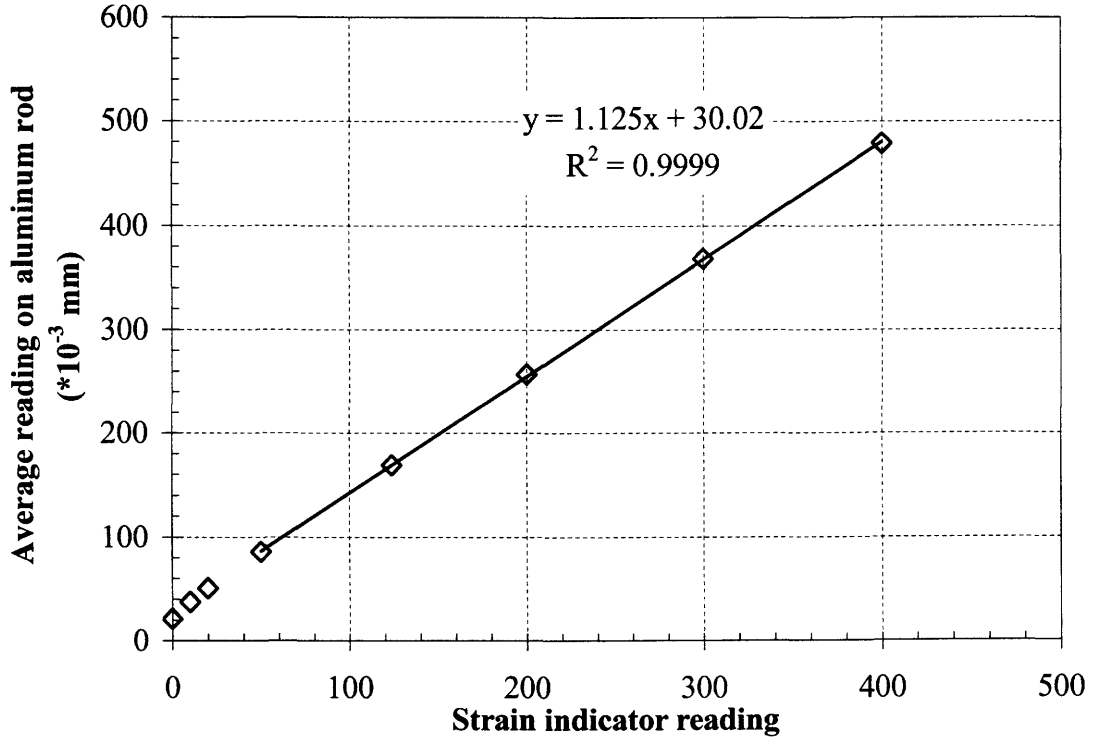

Figure A.4. Calibration curve for loading frame #4.

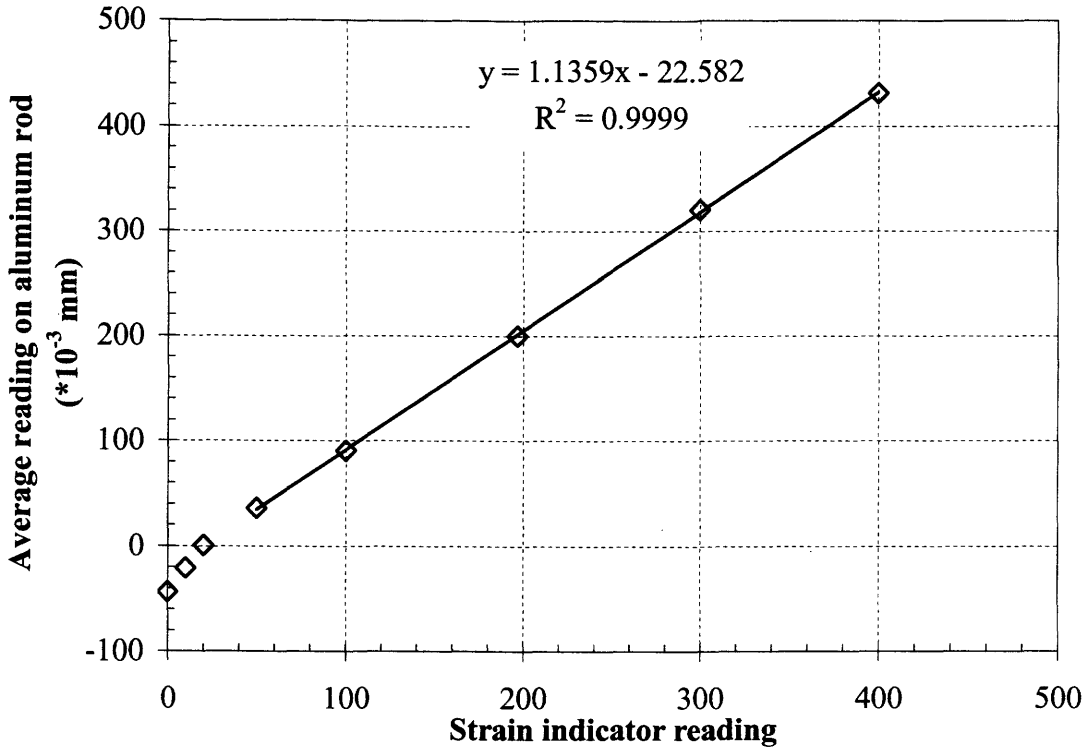

Figure A.5. Calibration curve for loading frame #5.

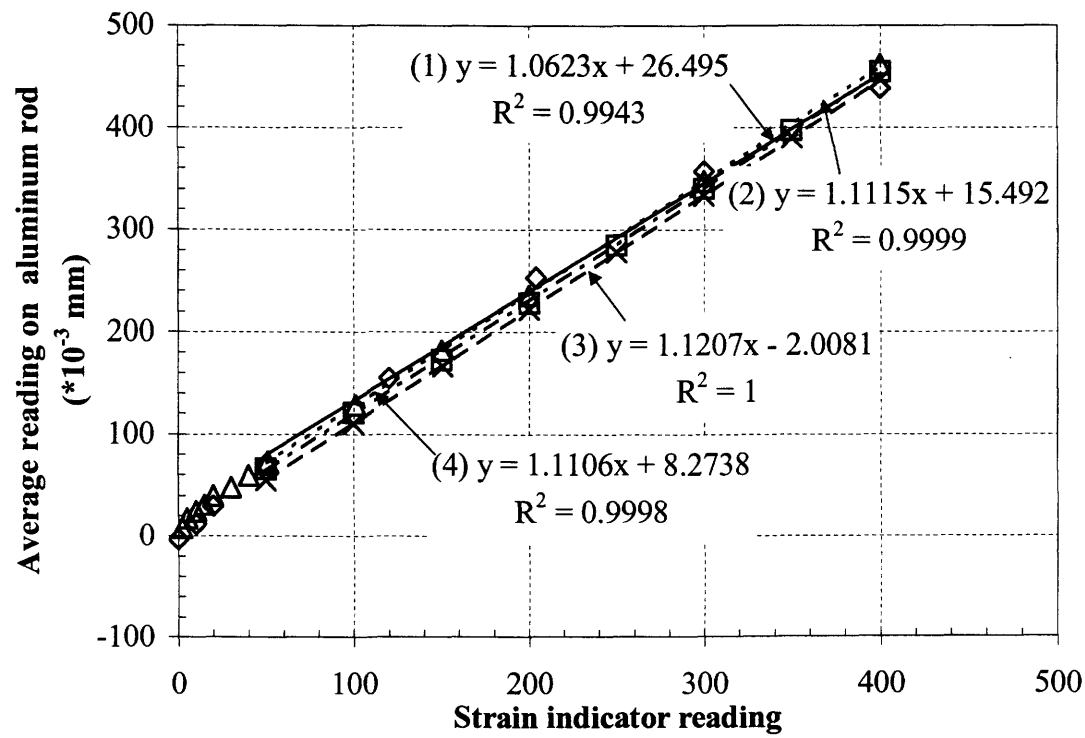

Figure A.6. Calibration curves for loading frame #6.

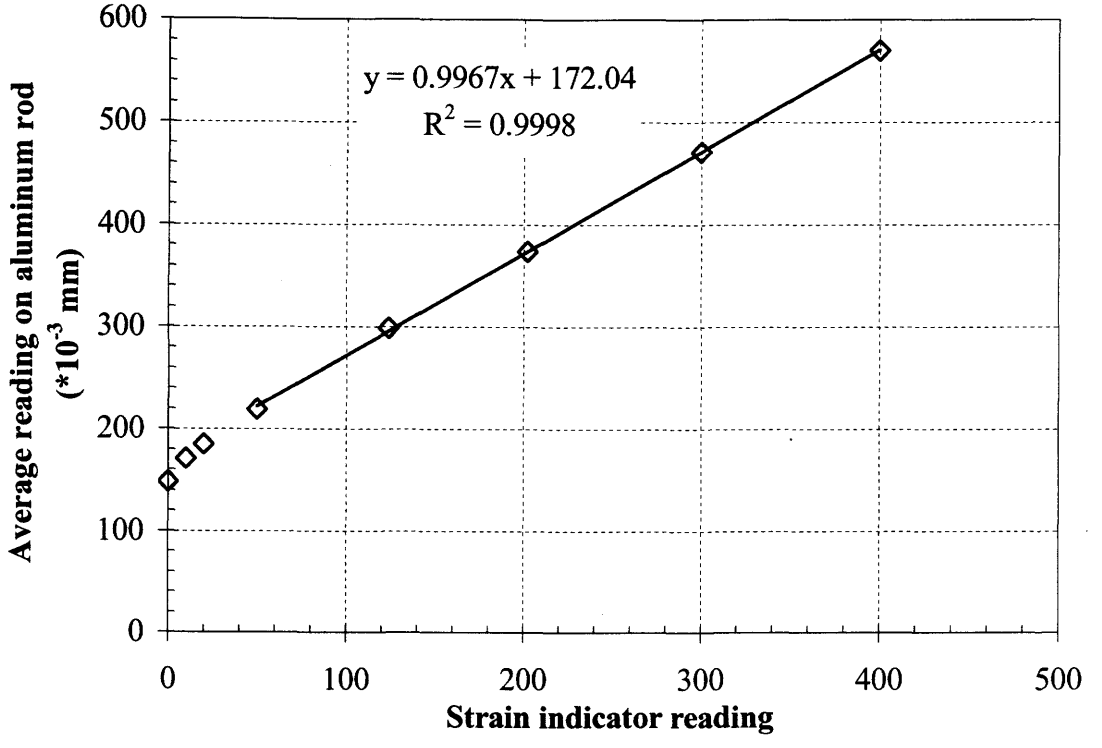

Figure A.7. Calibration curve for loading frame #7.

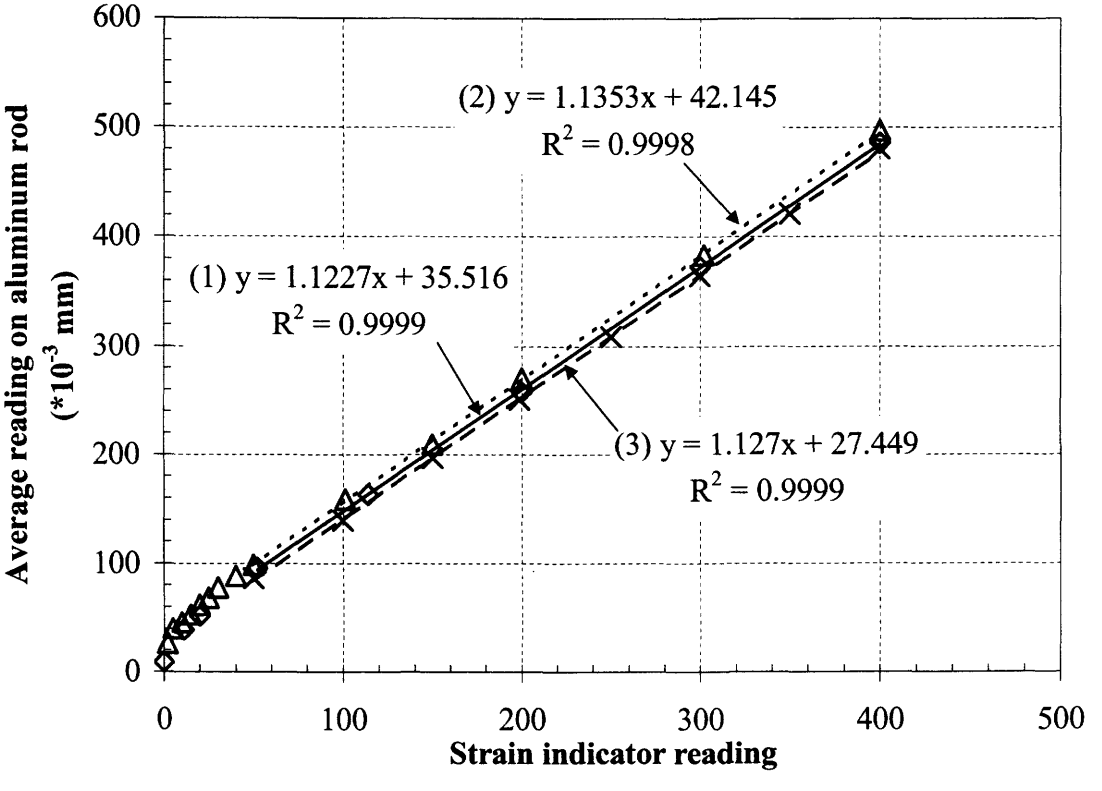

Figure A.8. Calibration curves for loading frame #8.

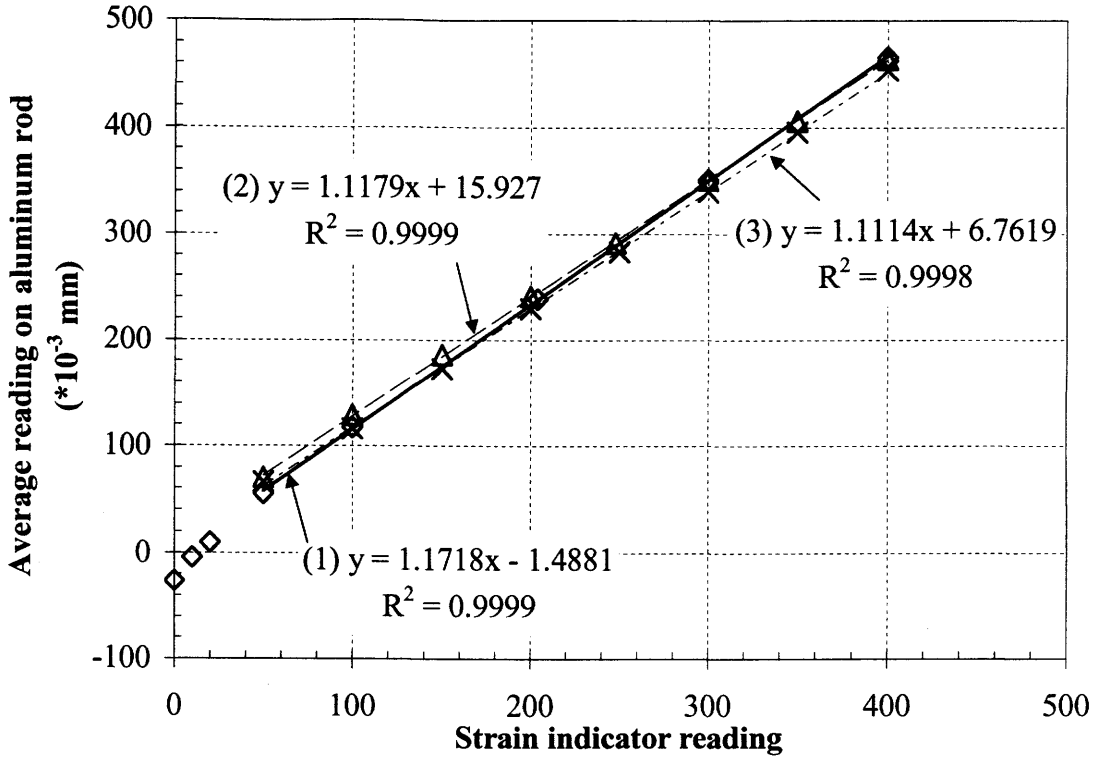

Figure A.9. Calibration curves for loading frame #9.

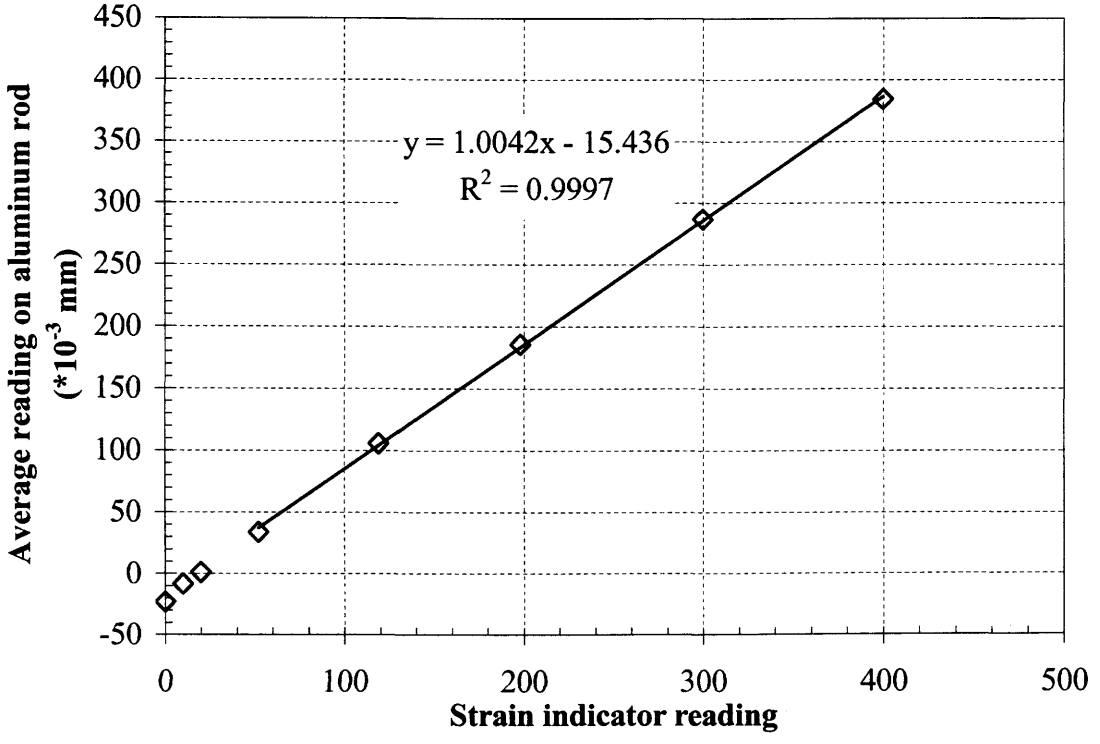

Figure A.10. Calibration curve for loading frame #10.

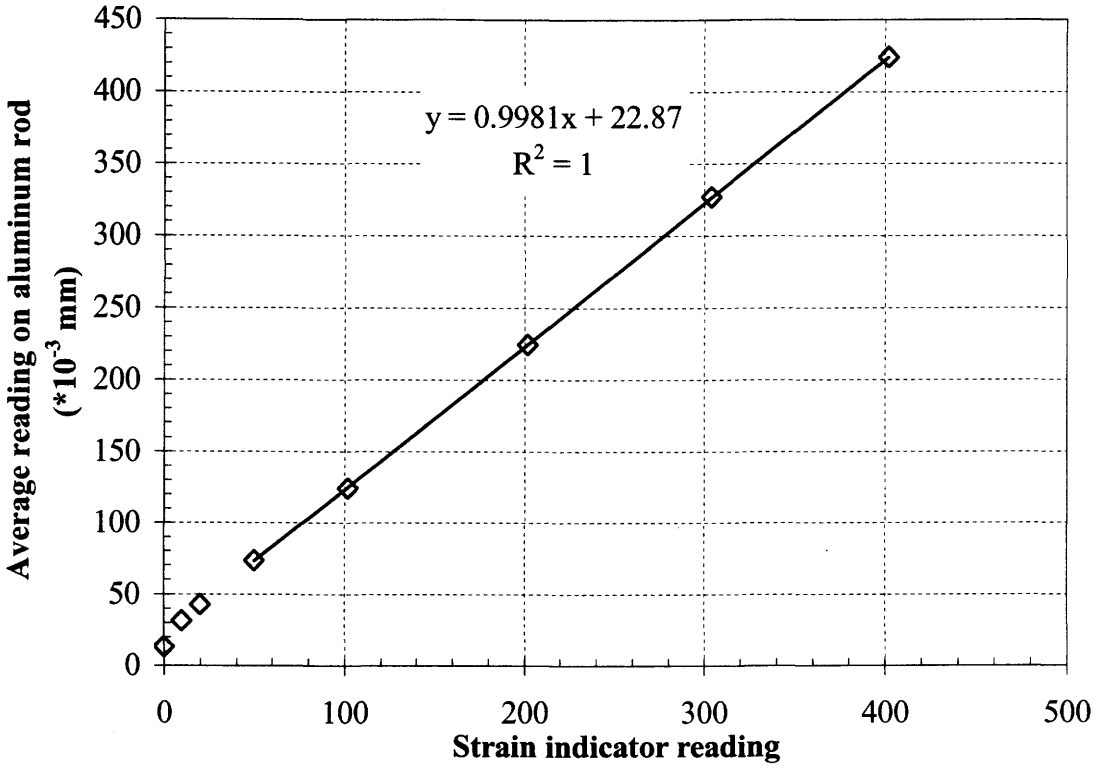

Figure A.11. Calibration curve for loading frame #11.

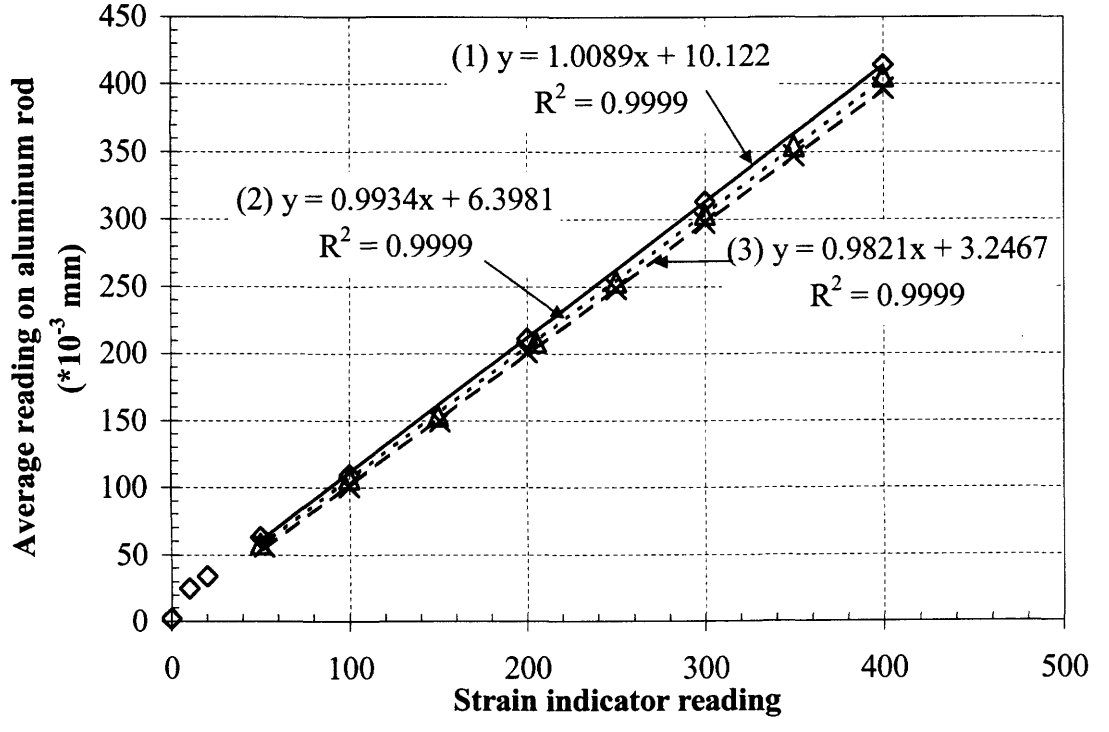

Figure A.12. Calibration curves for loading frame #12.

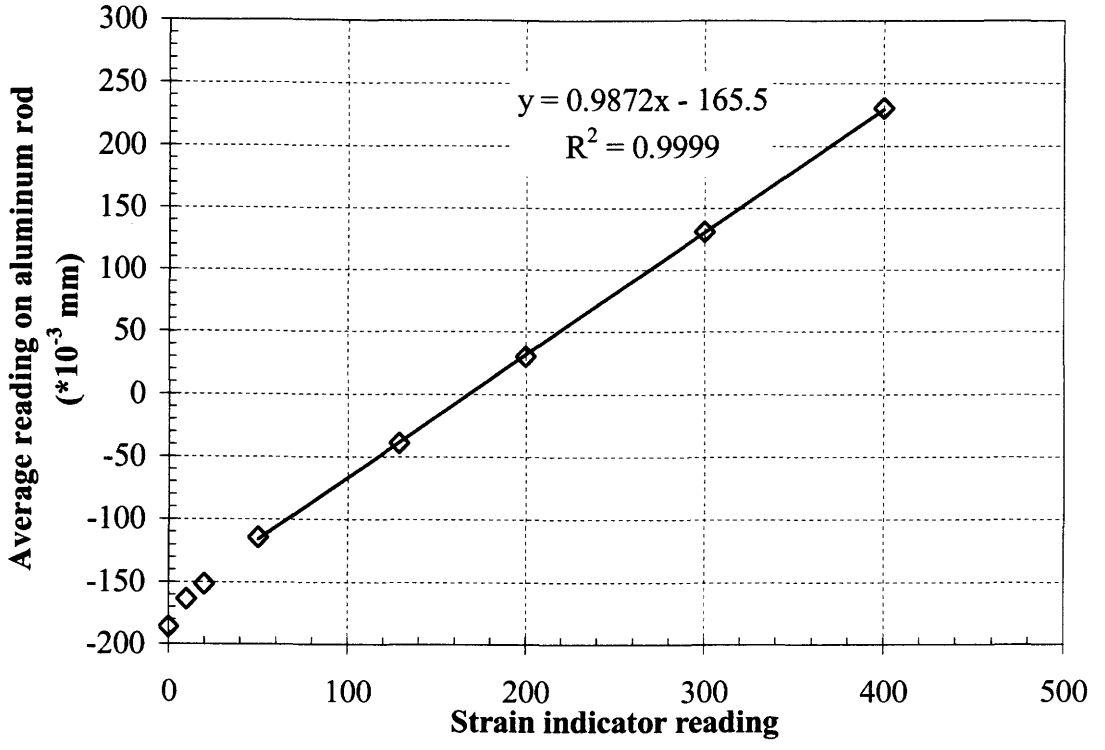

Figure A.13. Calibration curve for loading frame #13.

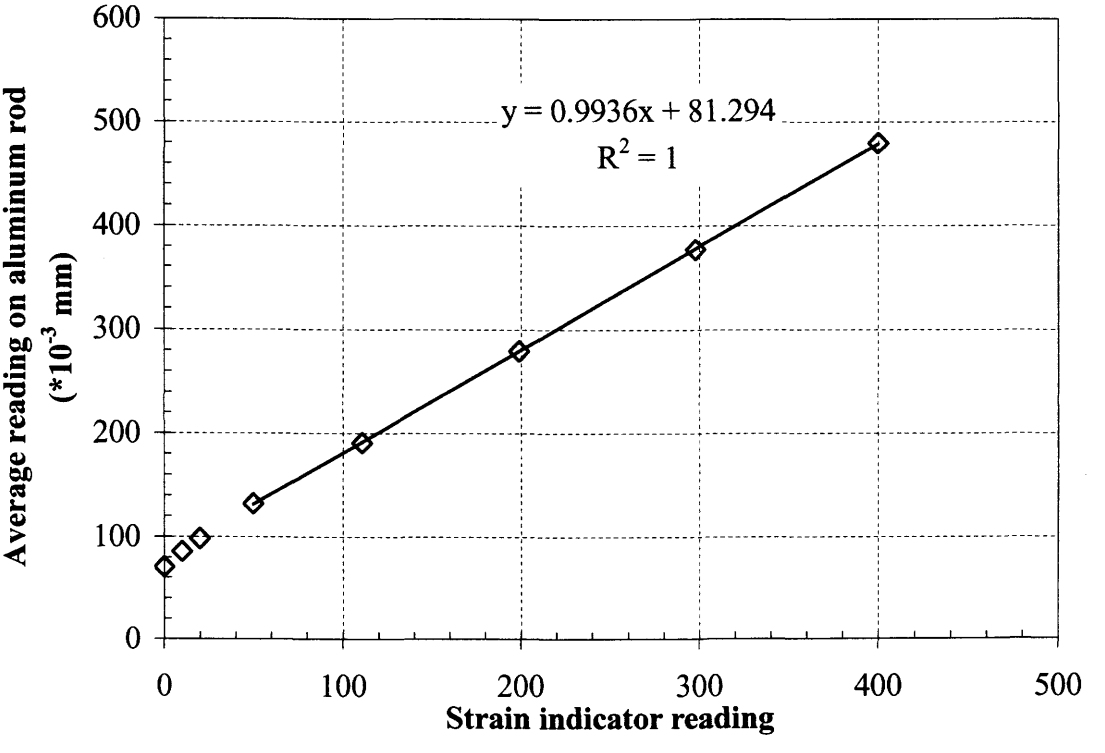

Figure A.14. Calibration curve for loading frame #14.

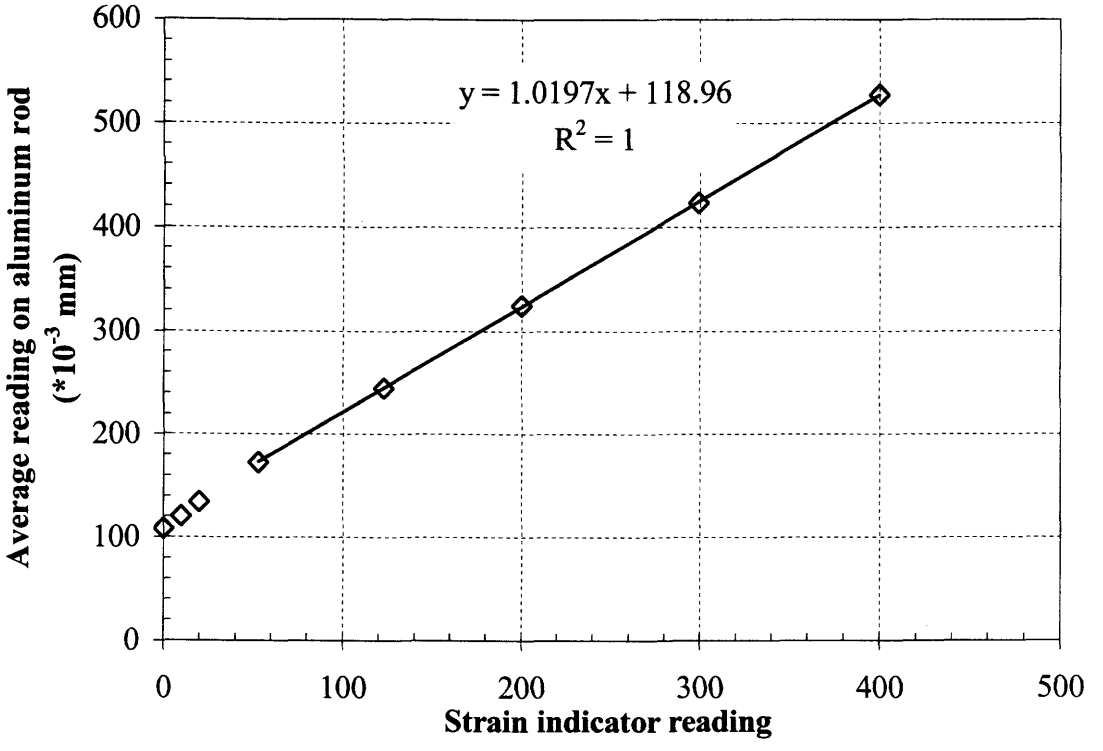

Figure A.15. Calibration curve for loading frame #15.

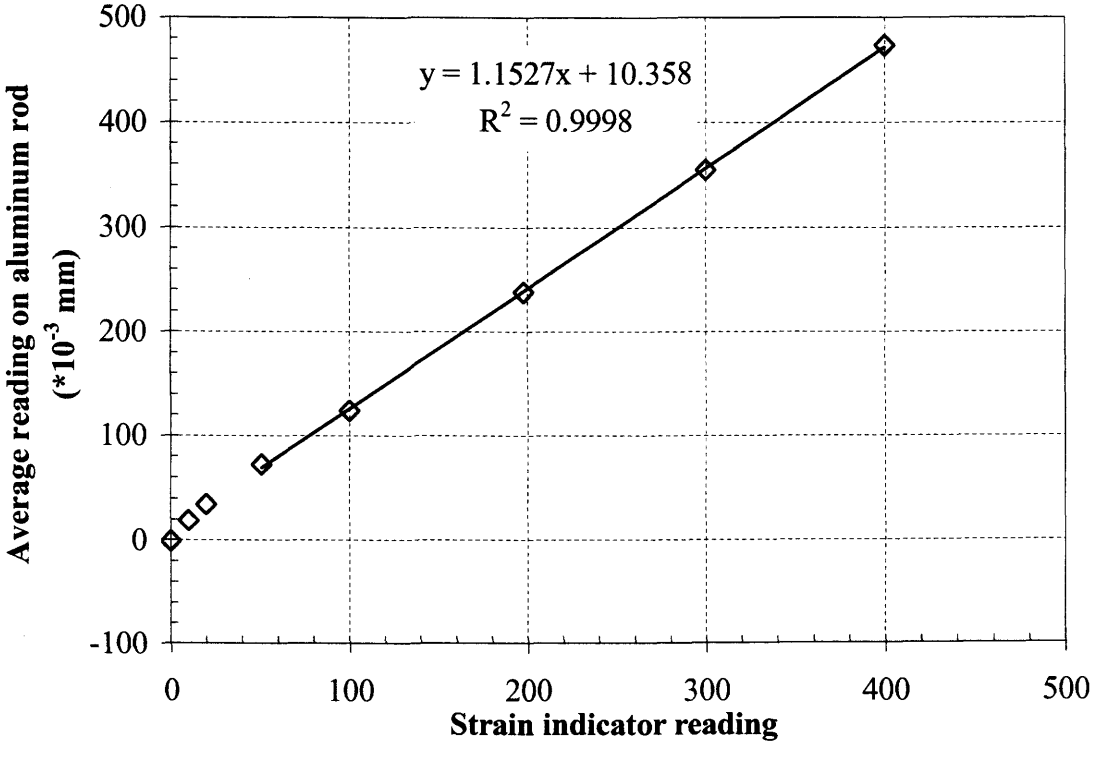

Figure A.16. Calibration curve for loading frame #16.

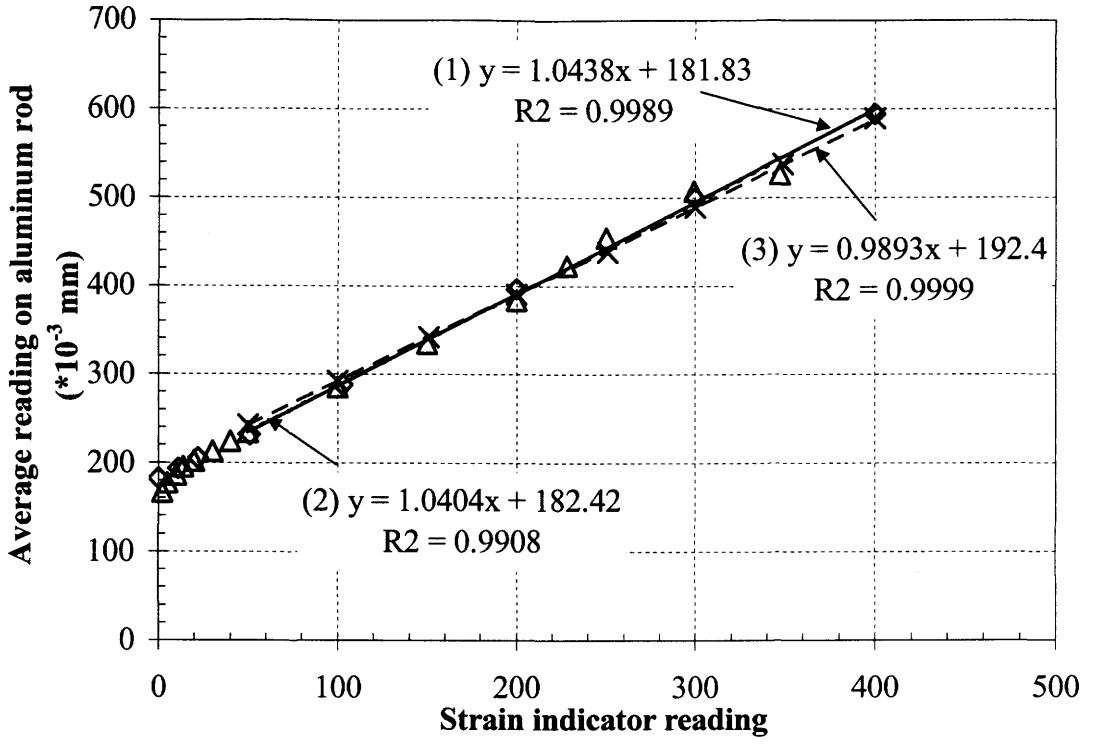

Figure A.17. Calibration curves for loading frame #17.

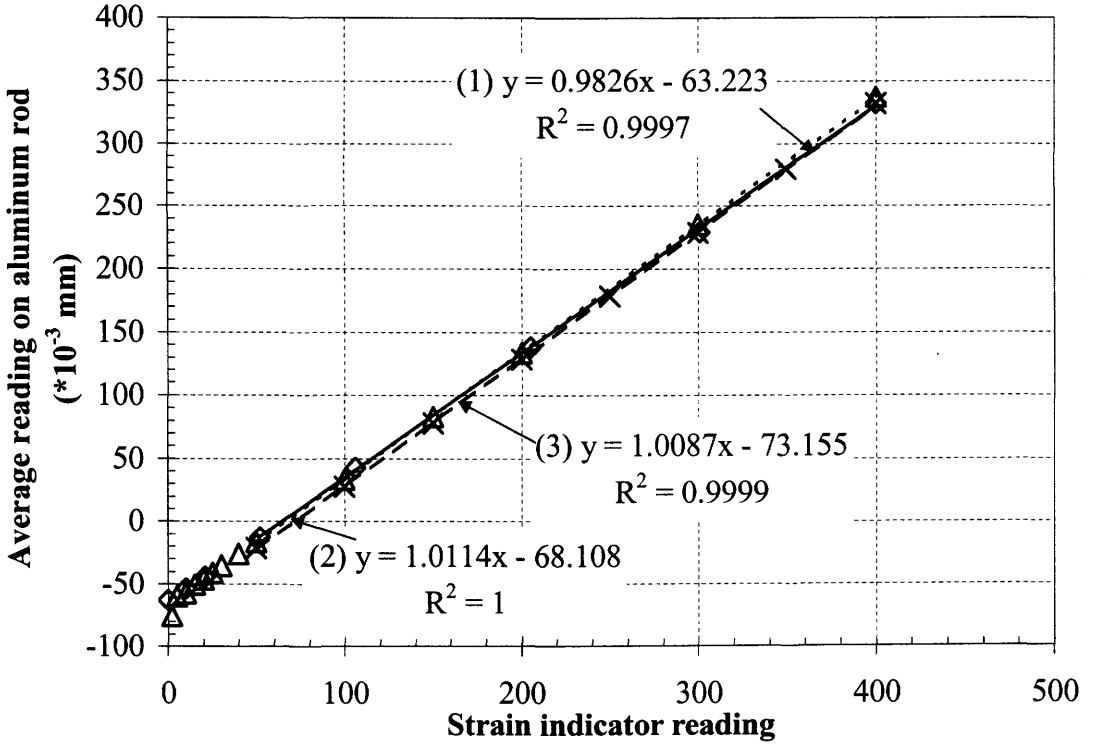

Figure A.18. Calibration curves for loading frame #18.

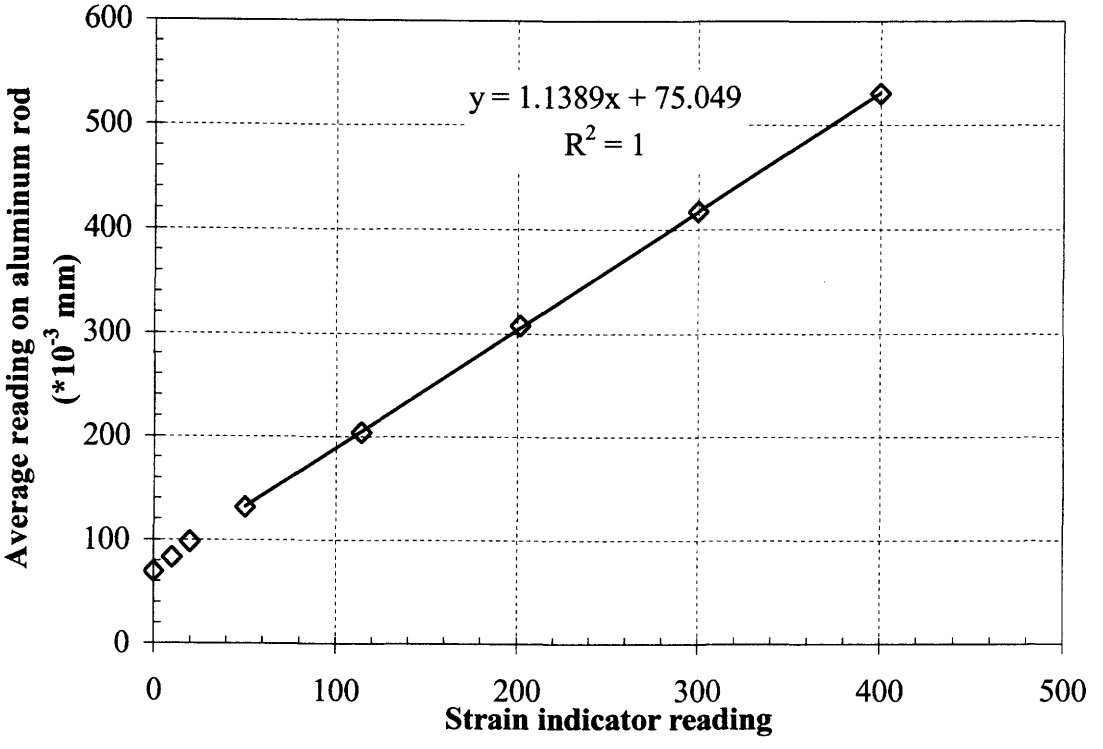

Figure A.19. Calibration curve for loading frame #19.

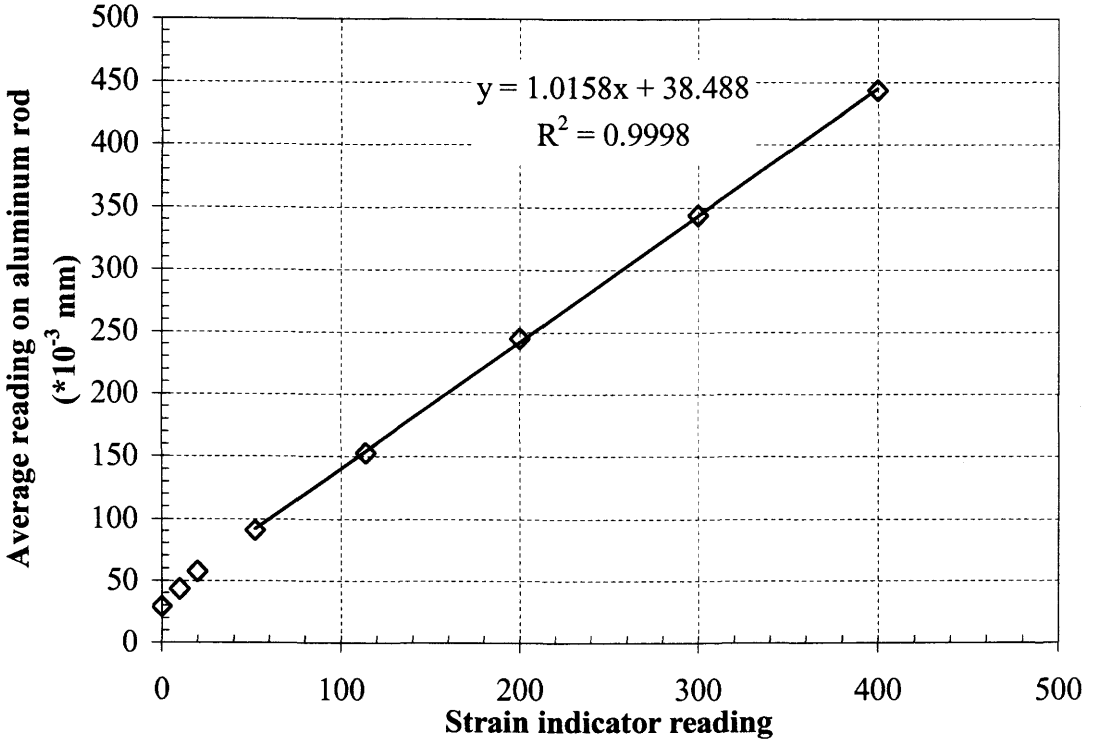

Figure A.20. Calibration curve for loading frame # 20.

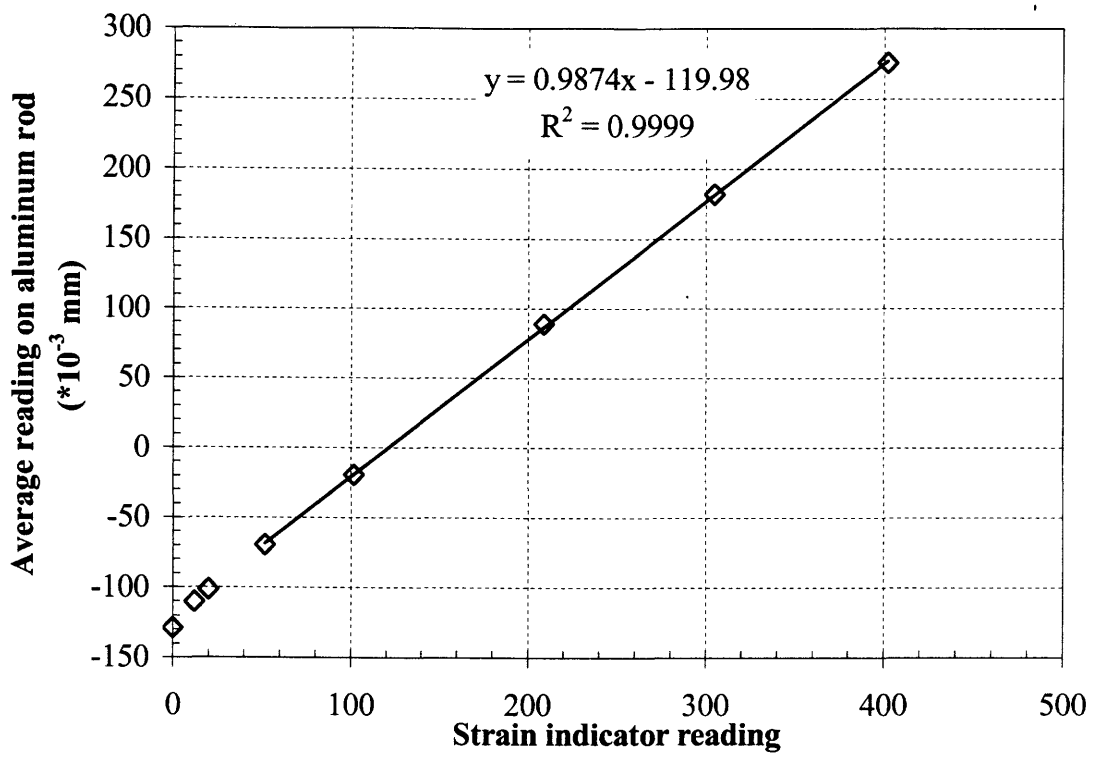

Figure A.21. Calibration curve for loading frame #21.

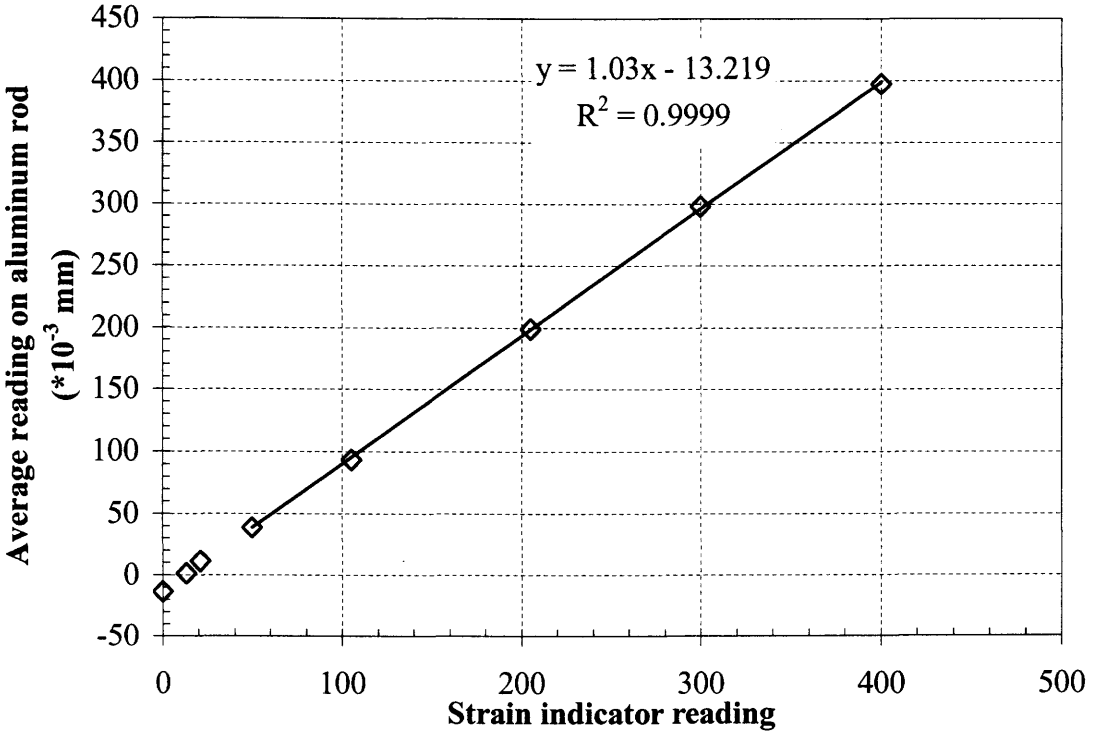

Figure A.22. Calibration curve for loading frame #22.

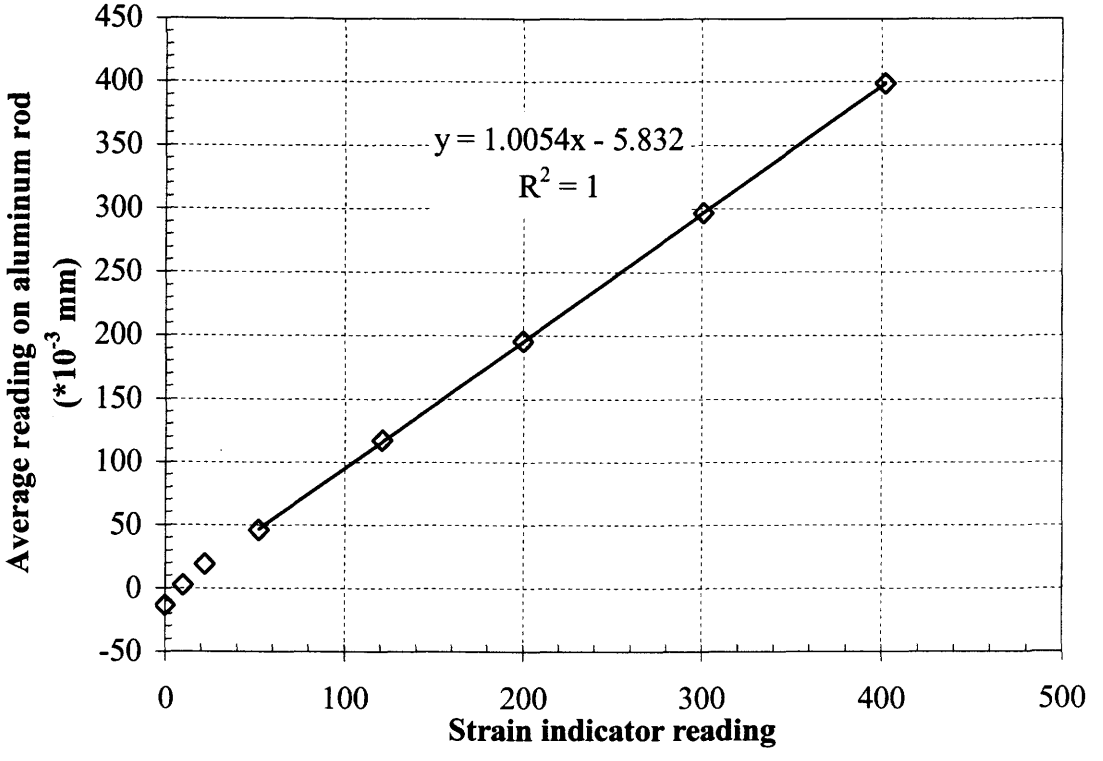

Figure A.23. Calibration curve for loading frame #23.

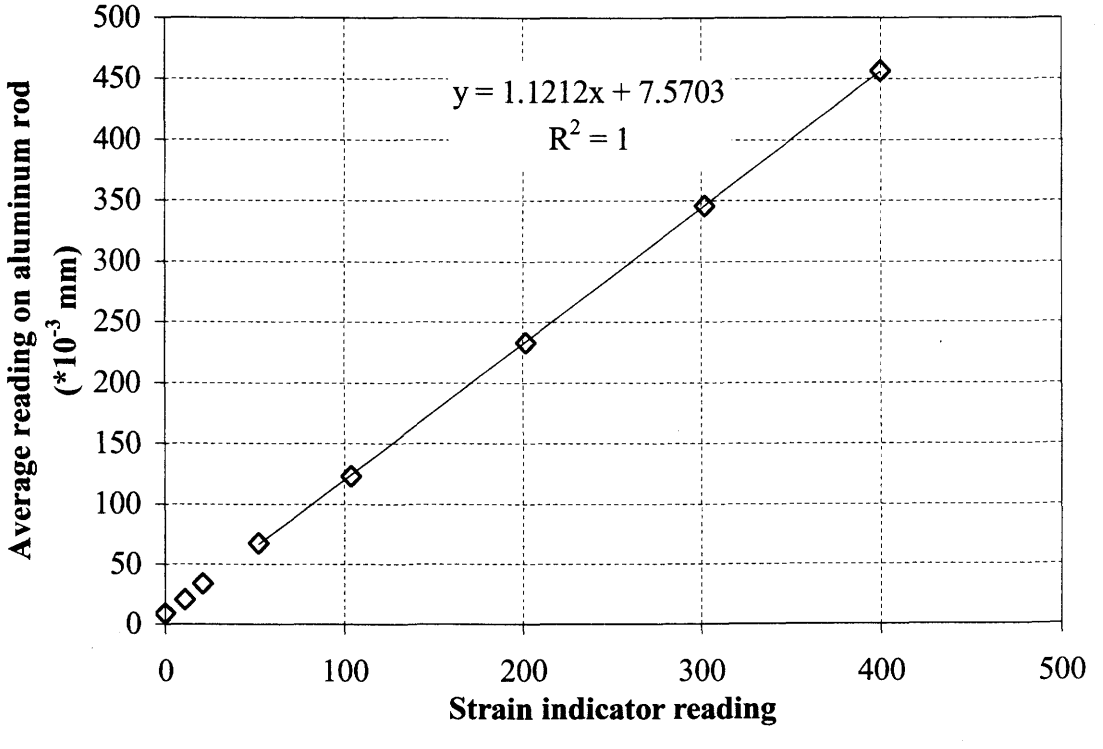

Figure A.24. Calibration curve for loading frame #24.

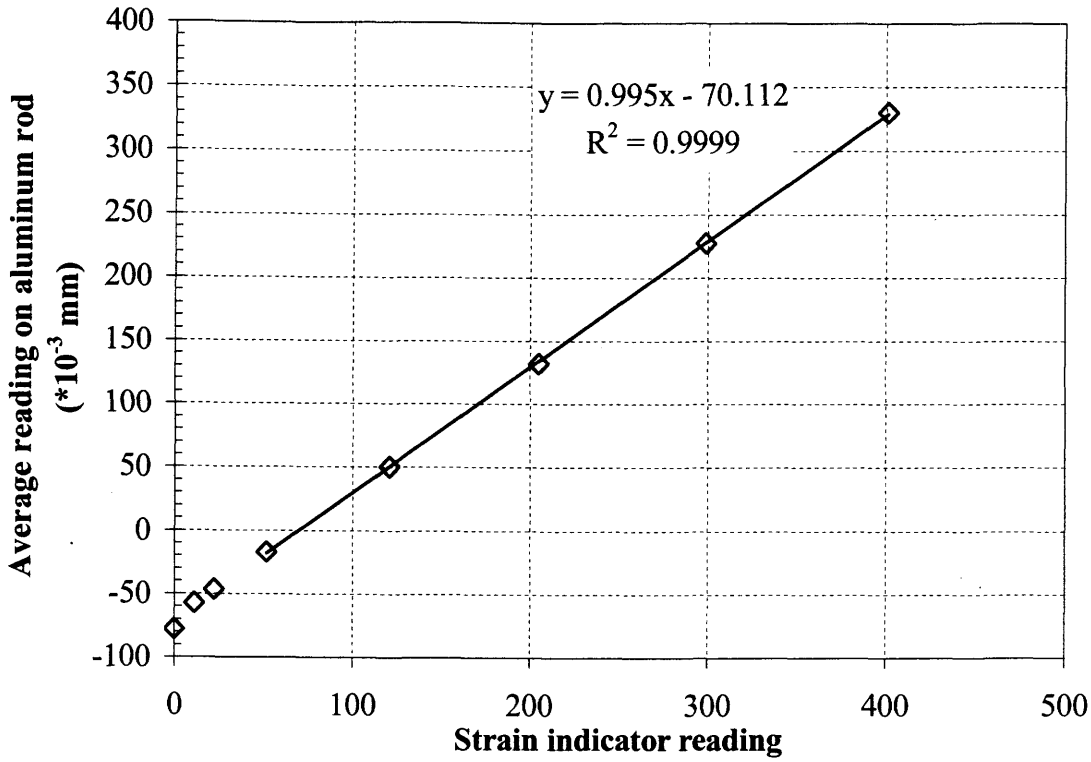

Figure A.25. Calibration curve for loading frame #25.

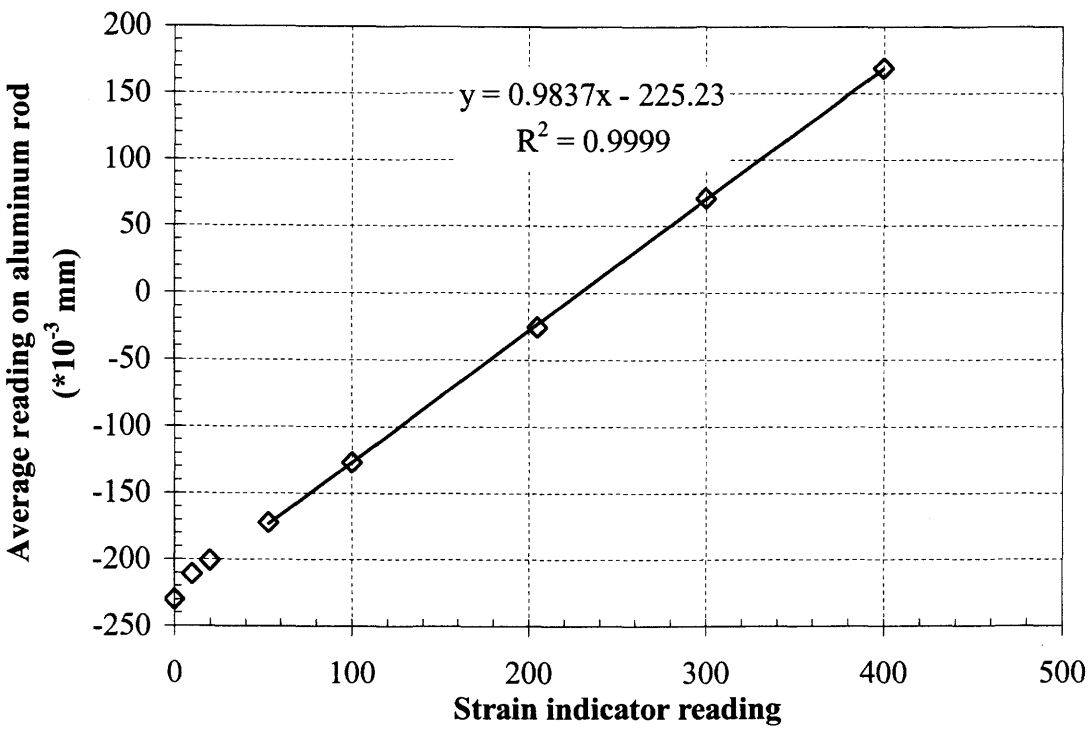

Figure A.26. Calibration curve for loading frame #26.

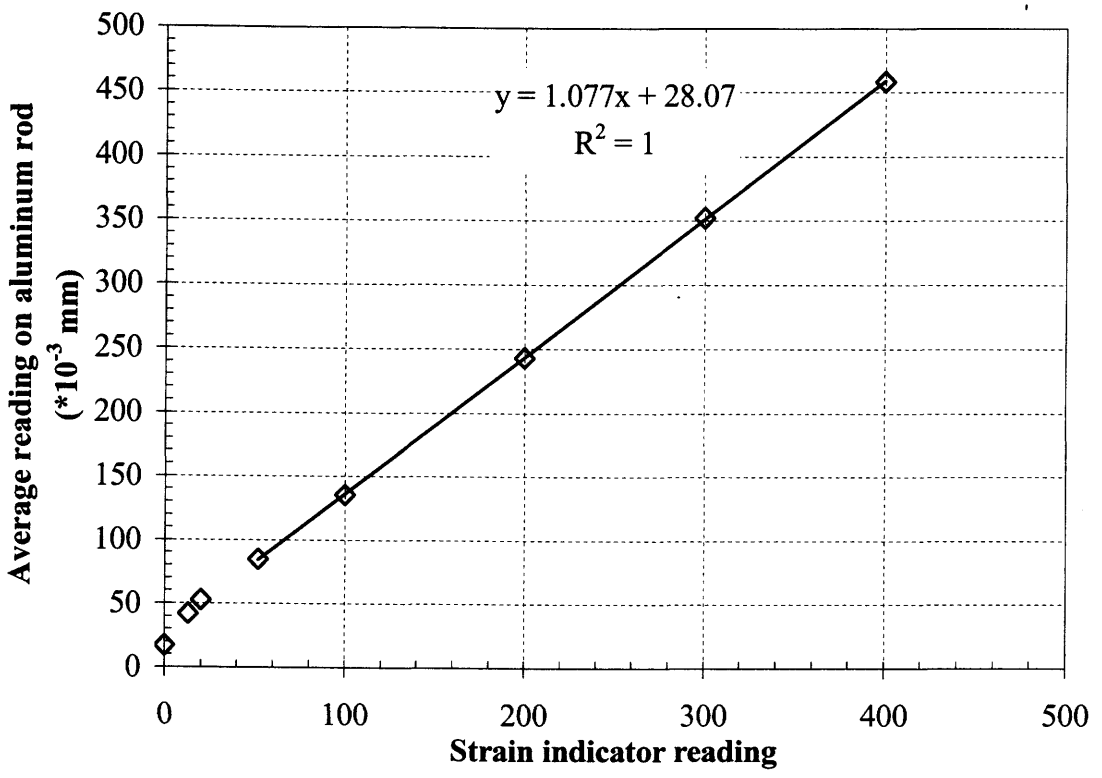

Figure A.27. Calibration curve for loading frame #27.

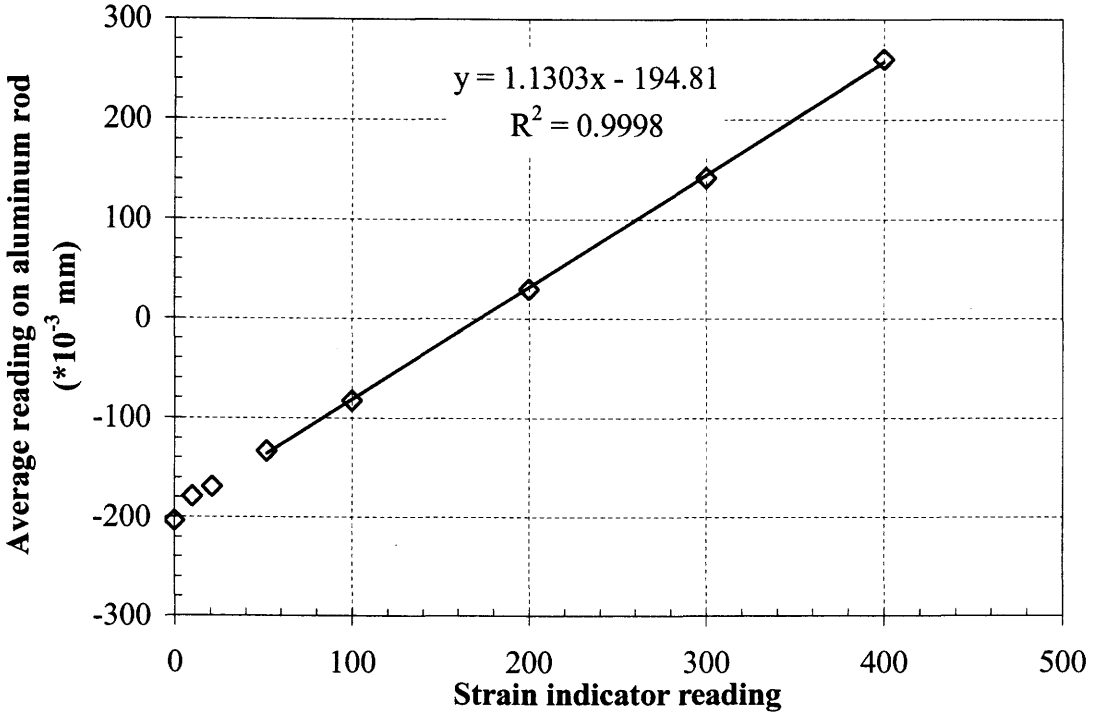

Figure A.28. Calibration curve for loading frame # 28.

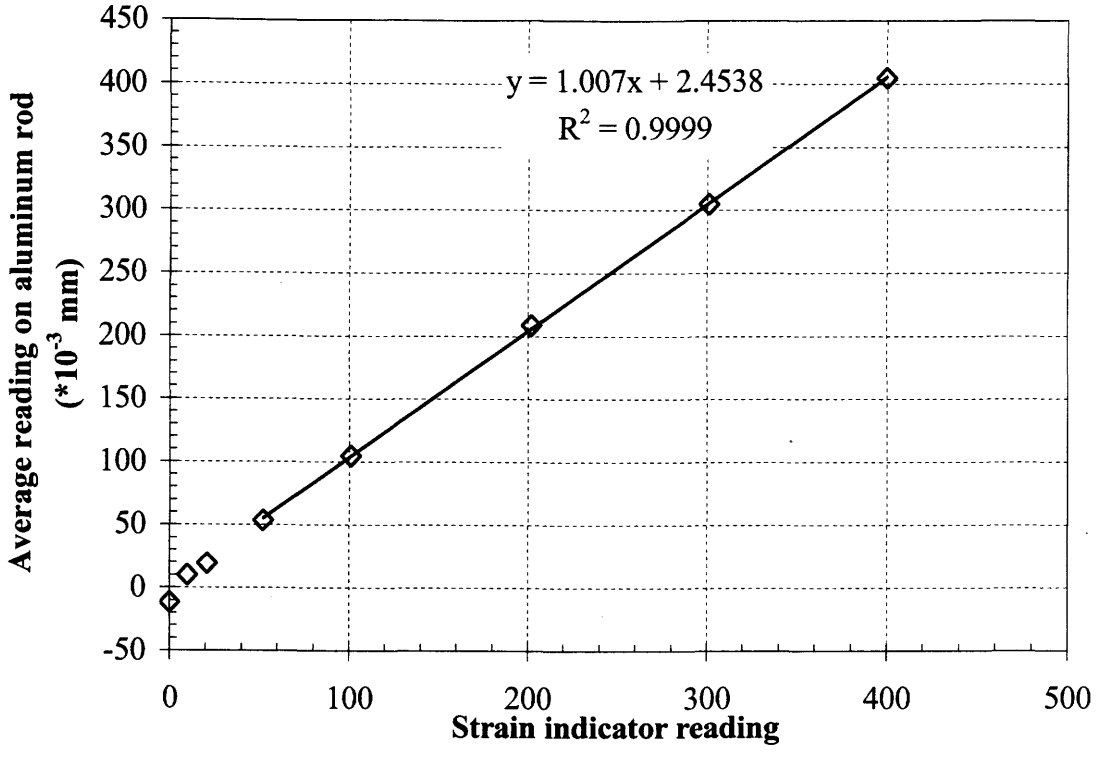

Figure A.29. Calibration curve for loading frame #29.

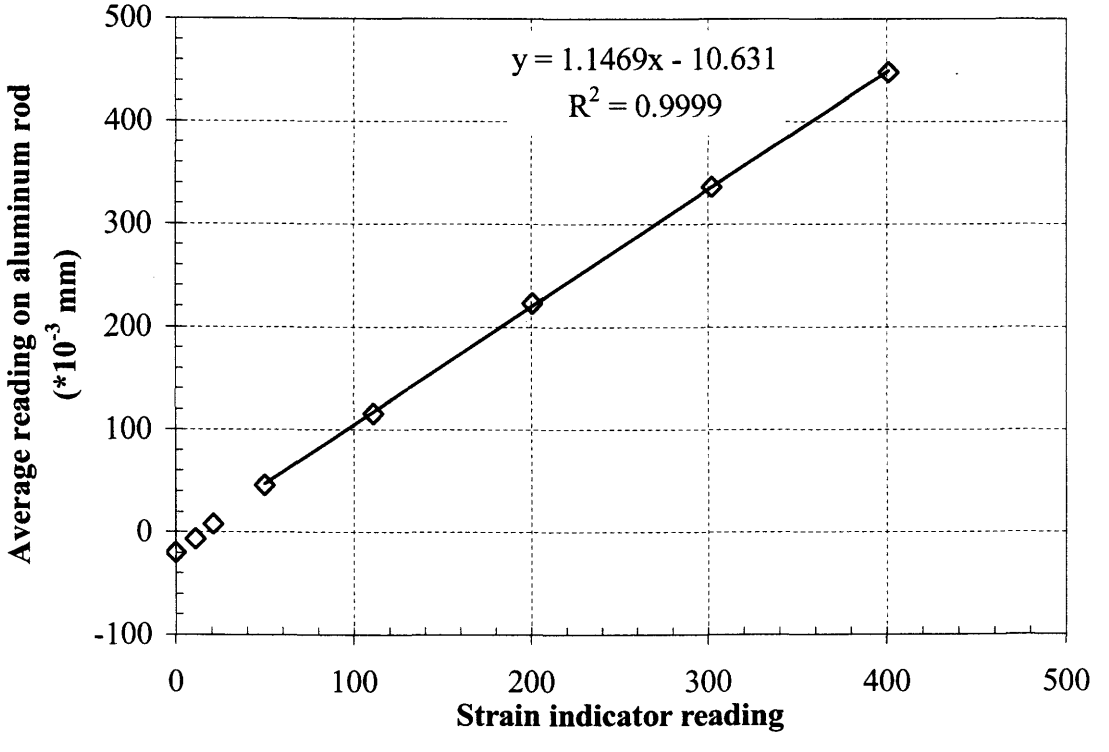

Figure A.30. Calibration curve for loading frame #30.

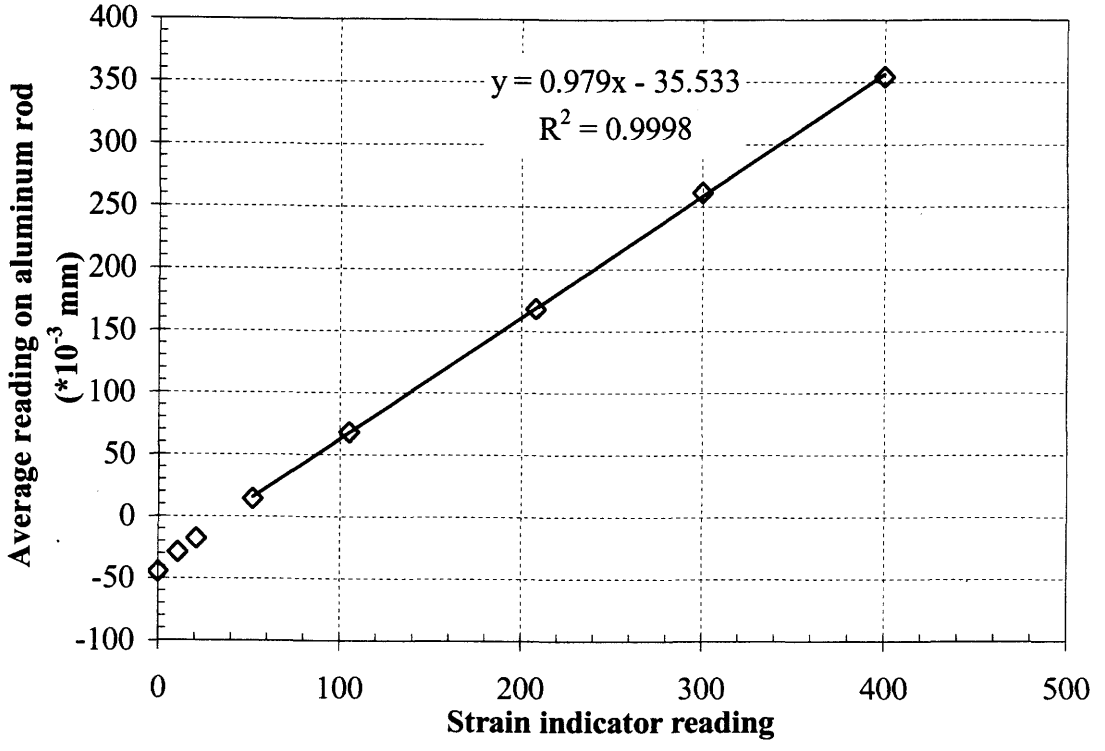

Figure A.31. Calibration curve for loading frame #31.

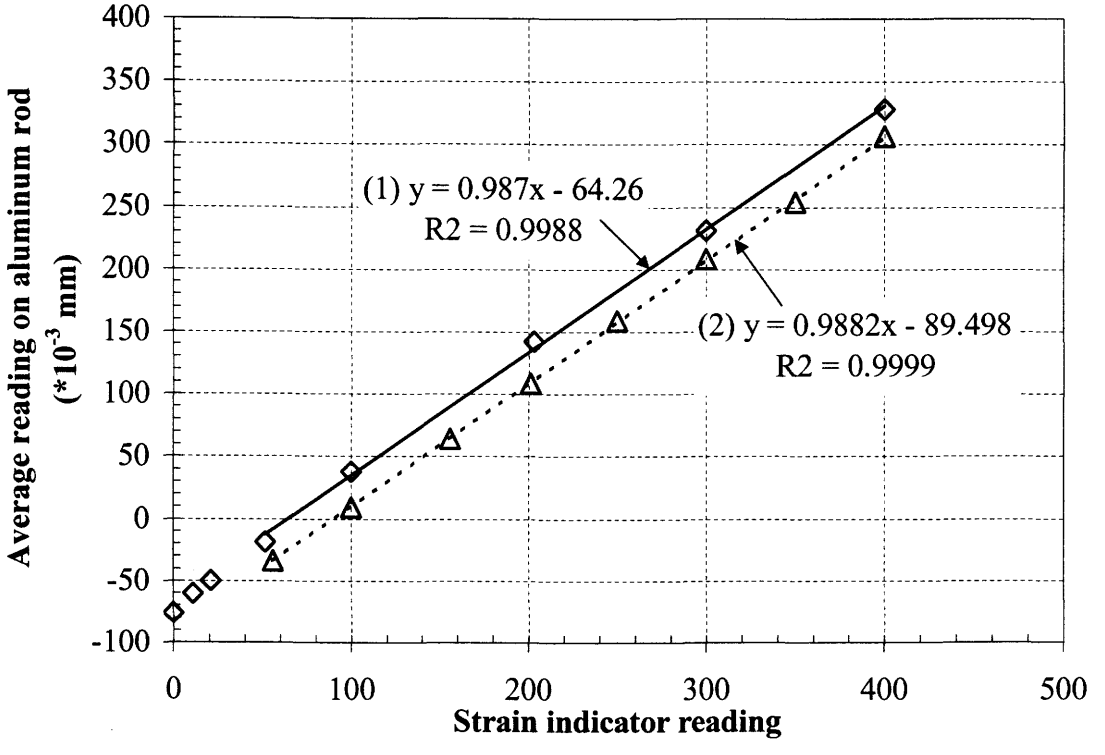

Figure A.32. Calibration curve for loading frame #32.

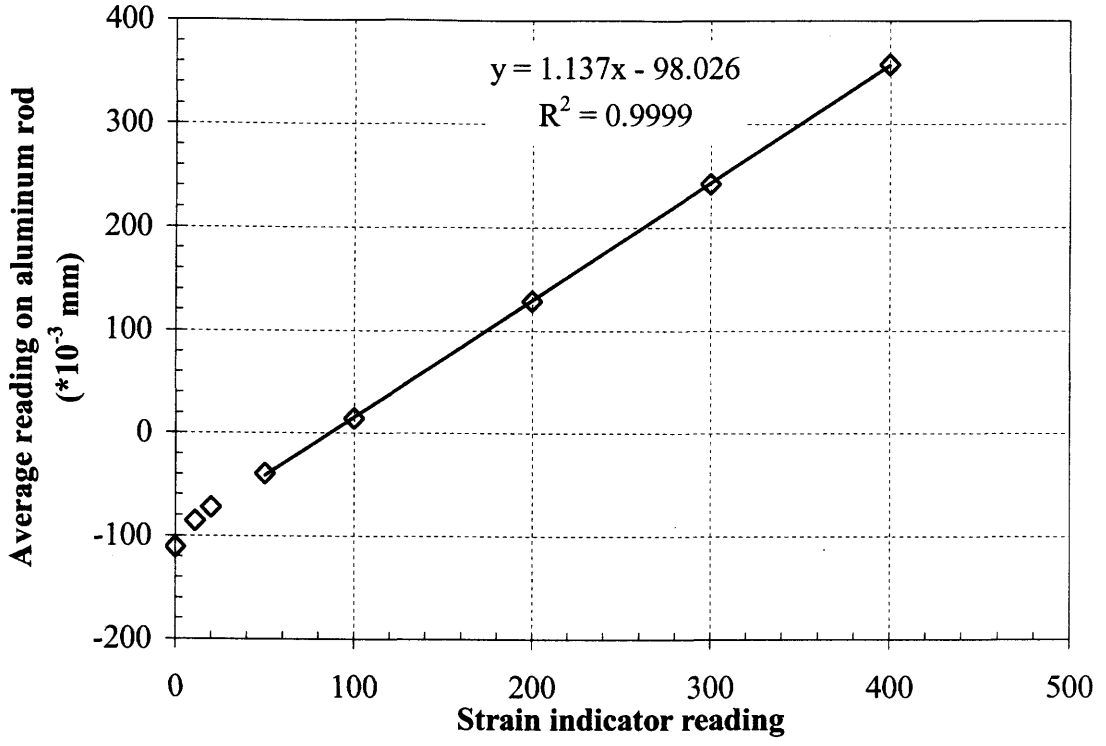

Figure A.33. Calibration curve for loading frame #33.

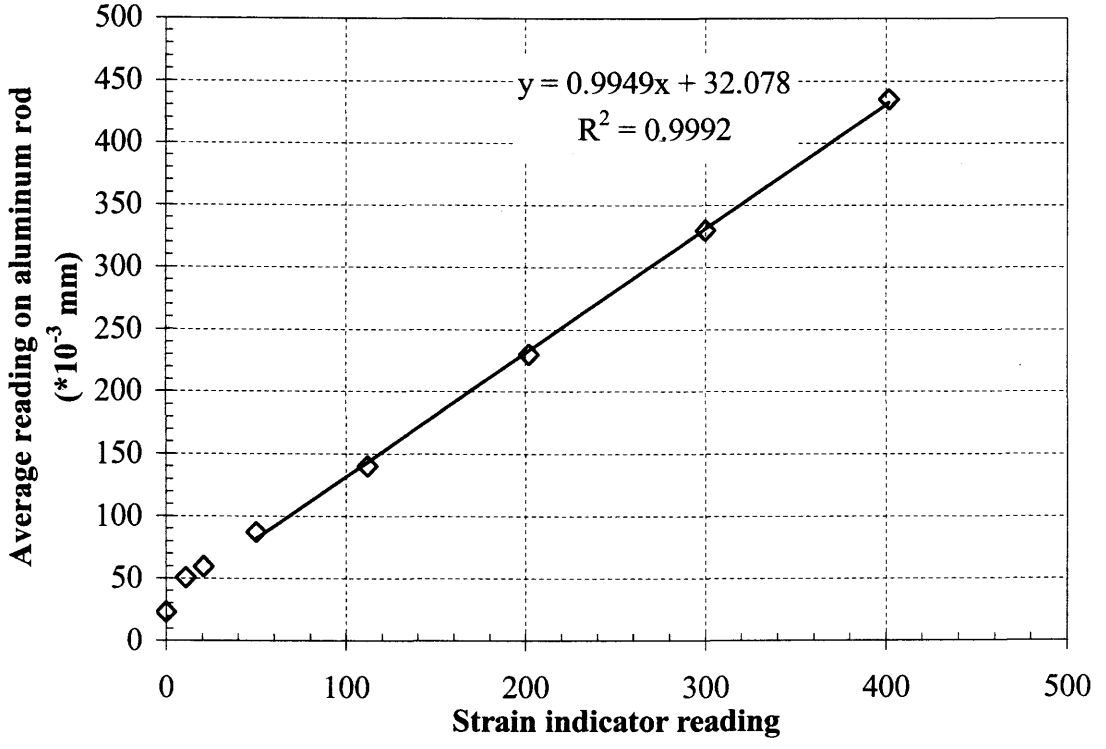

Figure A.34. Calibration curve for loading frame #34.

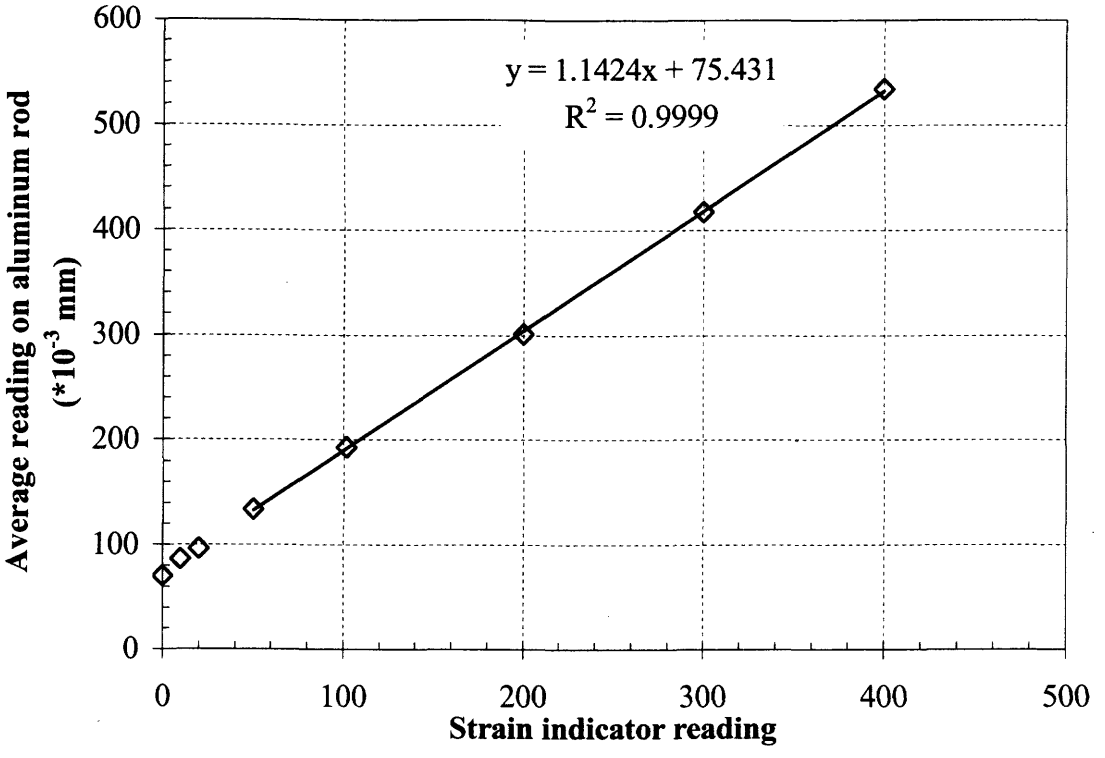

Figure A.35. Calibration curve for loading frame #35.

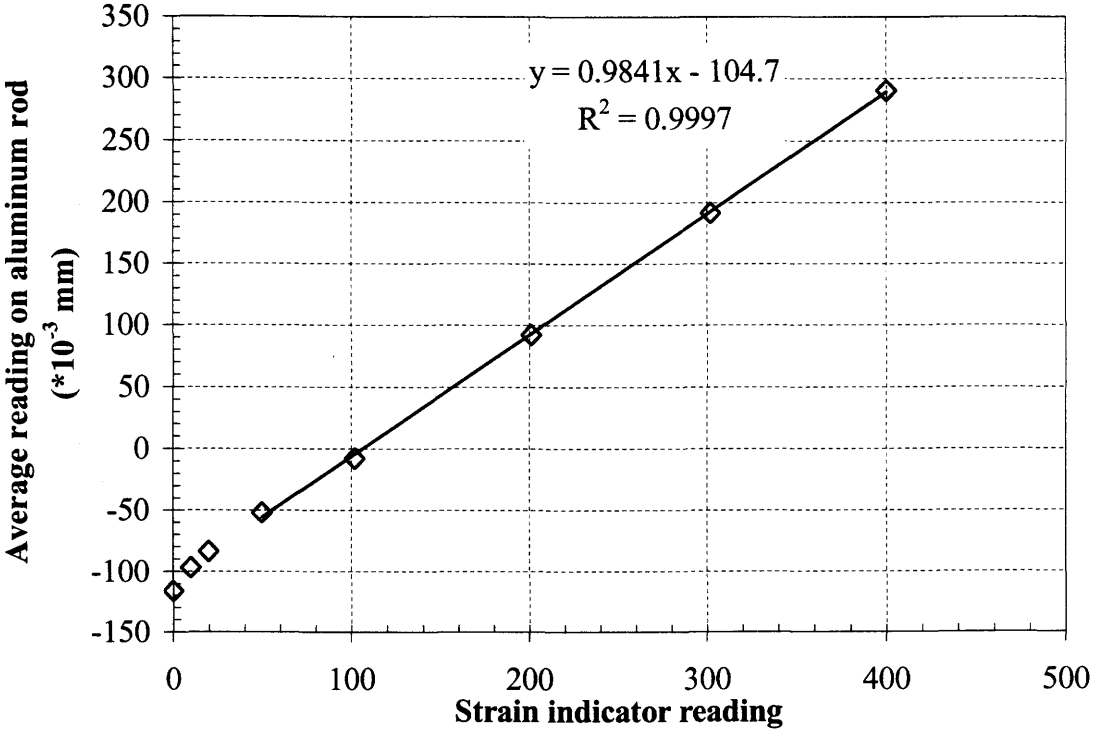

Figure A.36. Calibration curve for loading frame #36.

Appendix B

Long term test results for Phase I

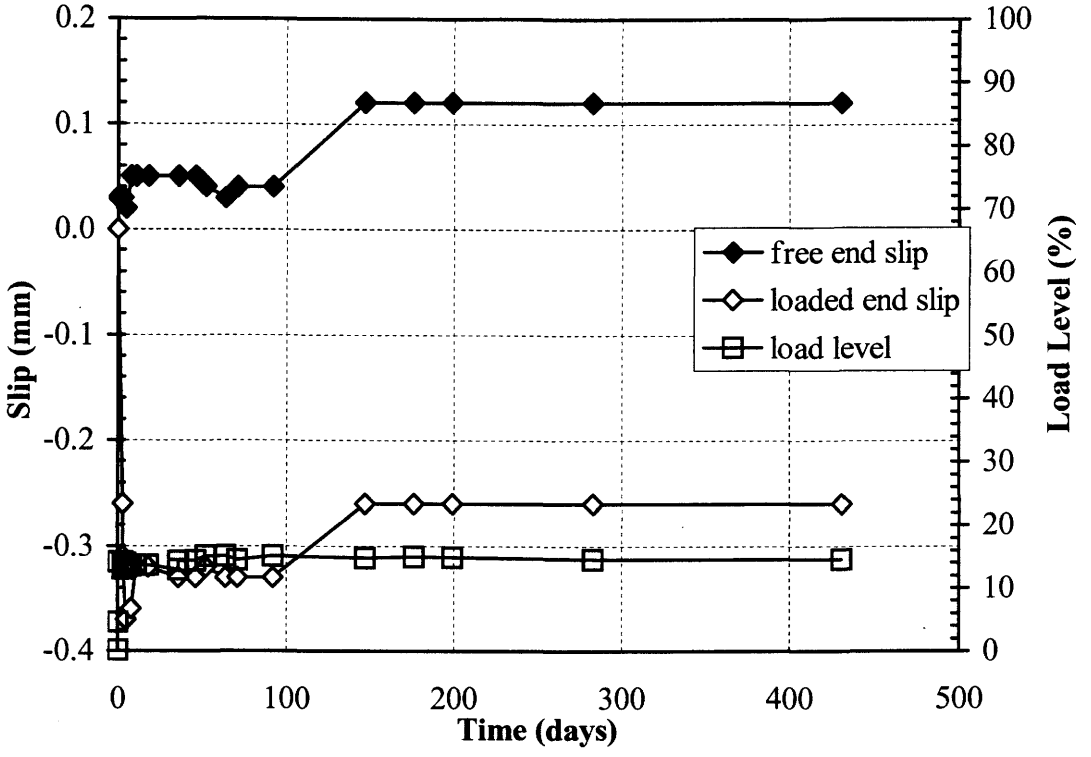

Figure B.1. Slip vs. time and load vs. time curves for Specimen Steel 14% #1.

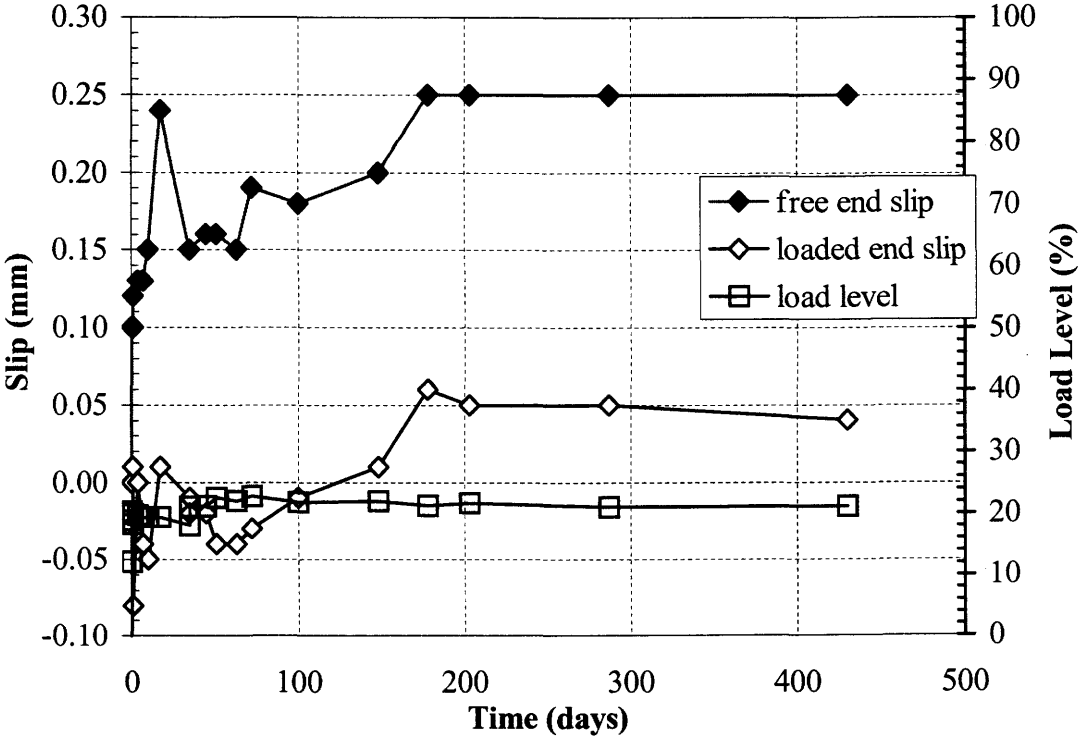

Figure B.2. Slip vs. time and load vs. time curves for Specimen Steel 20% #1.

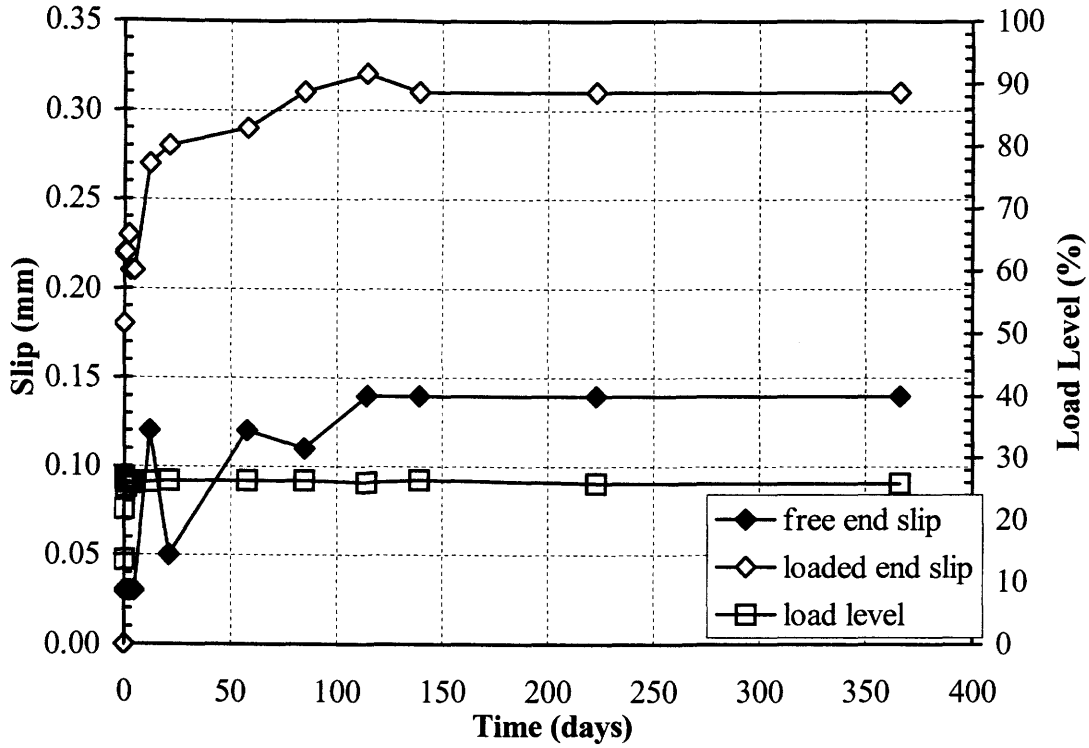

Figure B.3. Slip vs. time and load vs. time curves for Specimen Steel 26% #1.

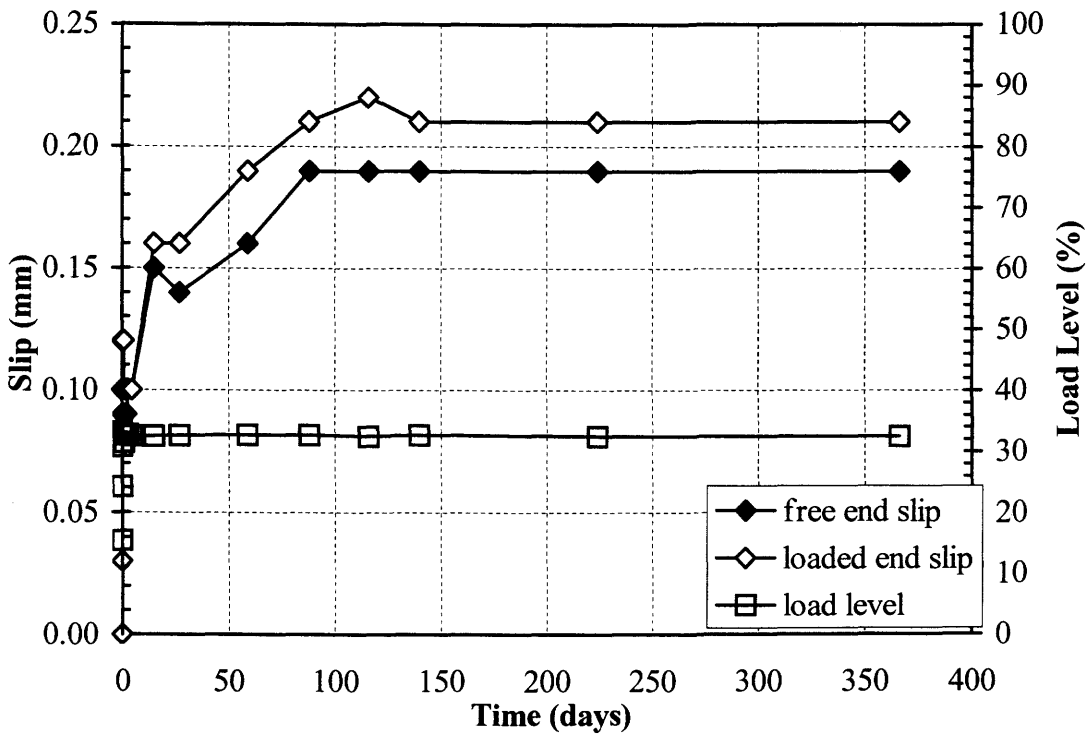

Figure B.4. Slip vs. time and load vs. time curves for Specimen Steel 33% #1.

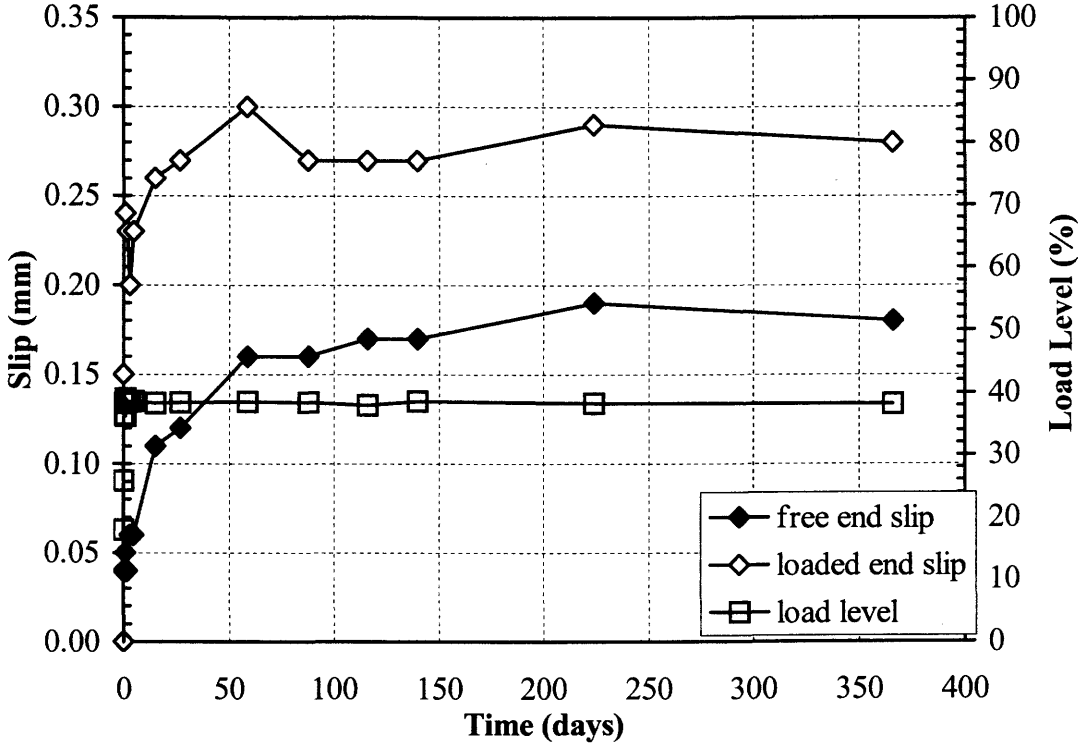

Figure B.5. Slip vs. time and load vs. time curves for Specimen Steel 39% #1.

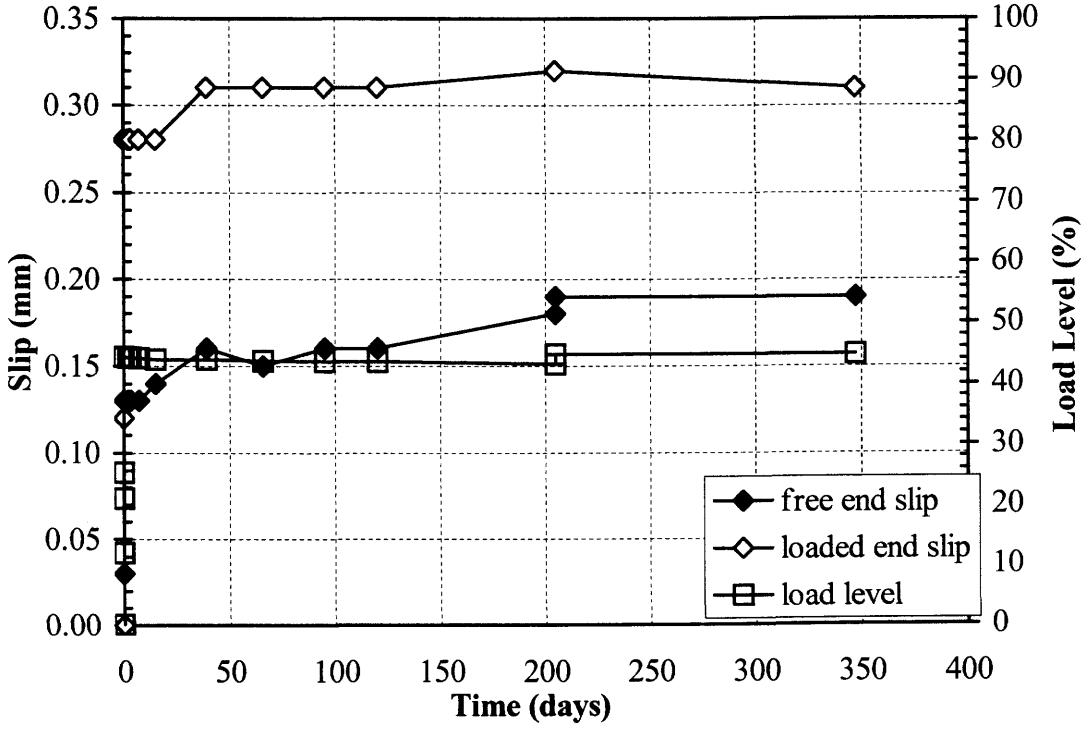

Figure B.6. Slip vs. time and load vs. time curves for Specimen Steel 45% #1.

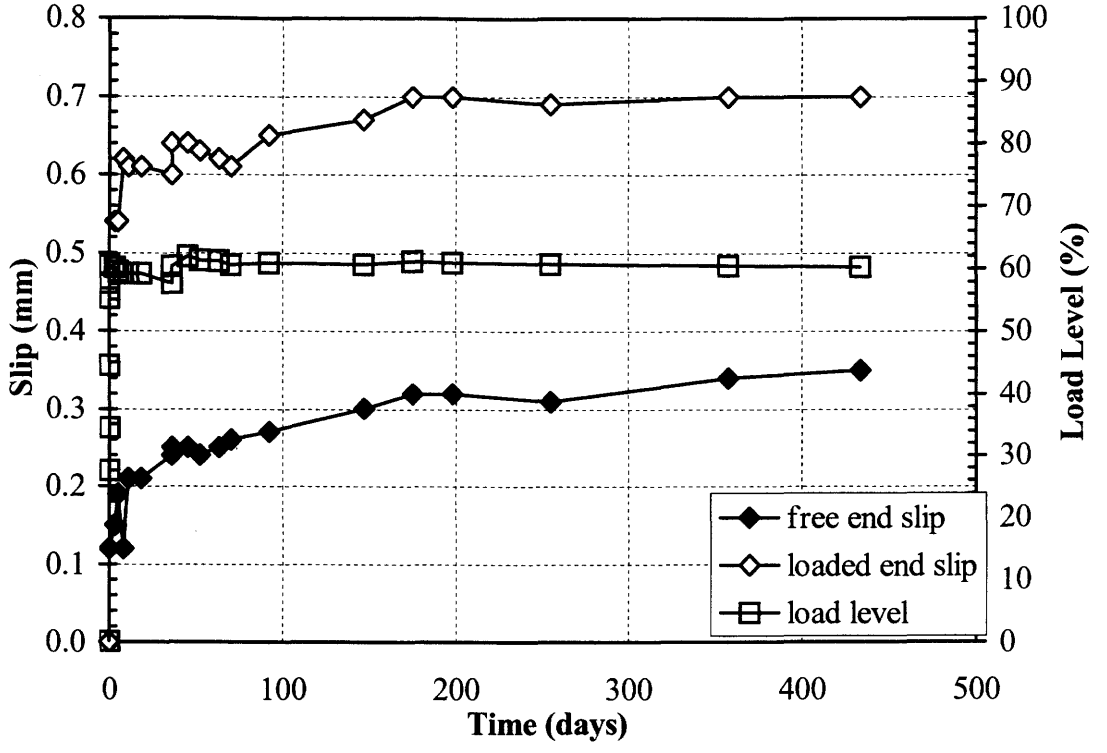

Figure B.7. Slip vs. time and load vs. time curves for Specimen Steel 60% #1.

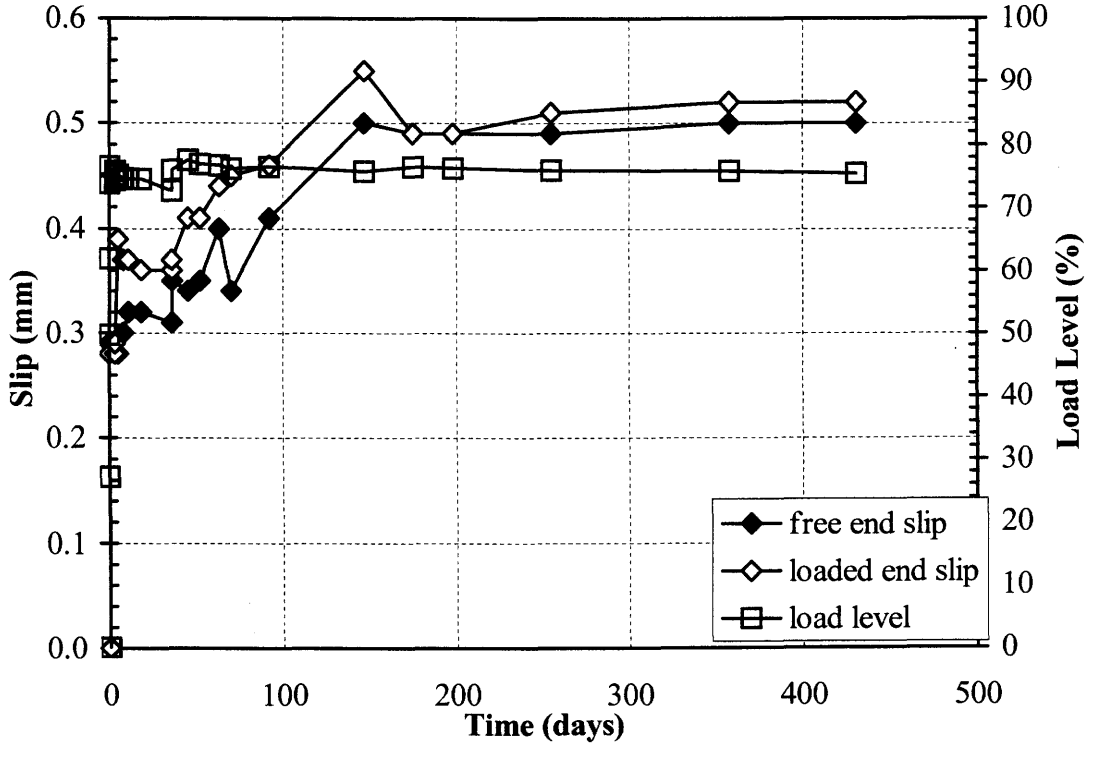

Figure B.8. Slip vs. time and load vs. time curves for Specimen Steel 75% #1.

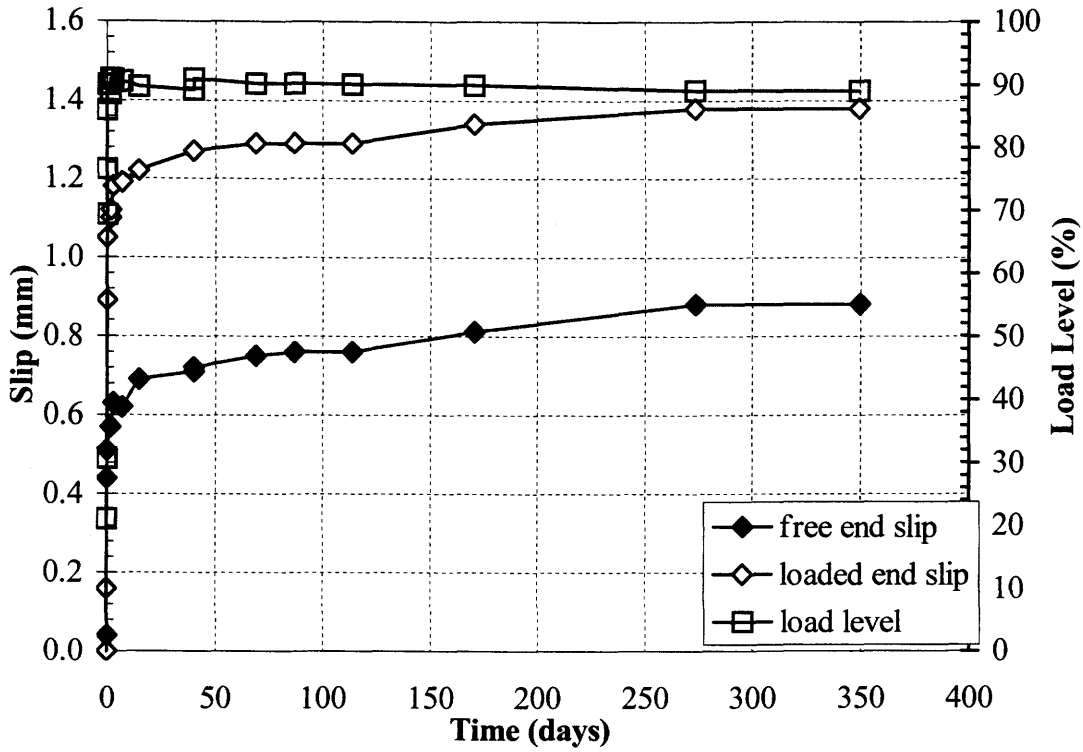

Figure B.9. Slip vs. time and load vs. time curves for Specimen Steel 90% #1.

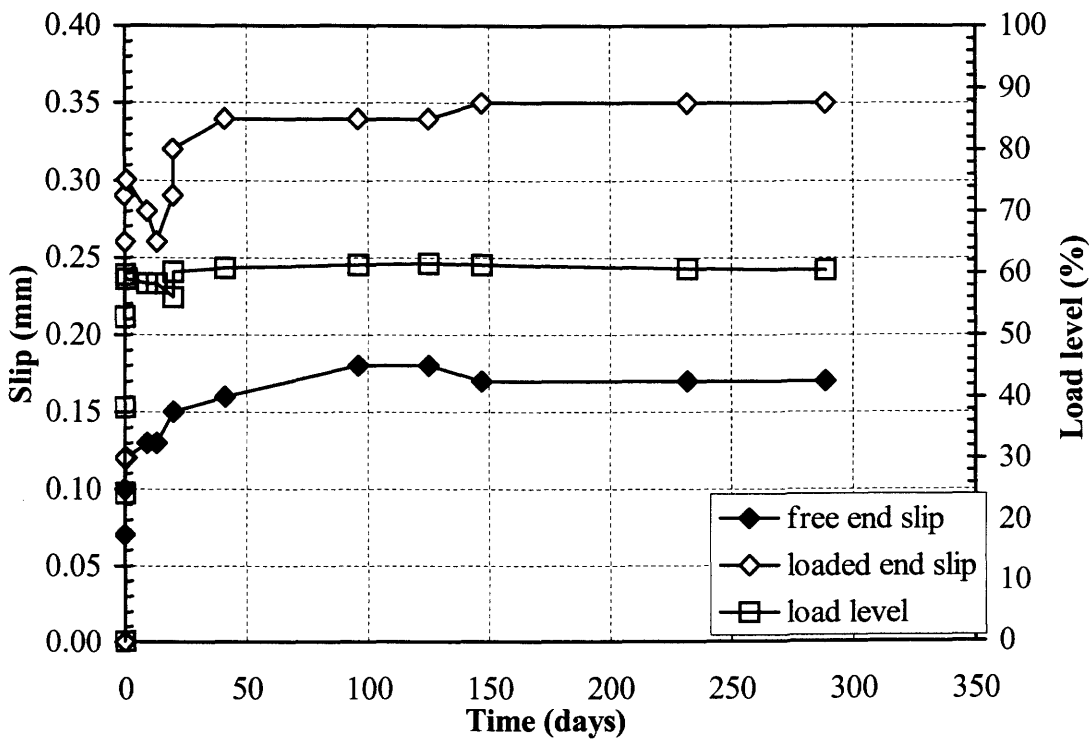

Figure B.10. Slip vs. time and load vs. time curves for Specimen CFCC 60% #1.

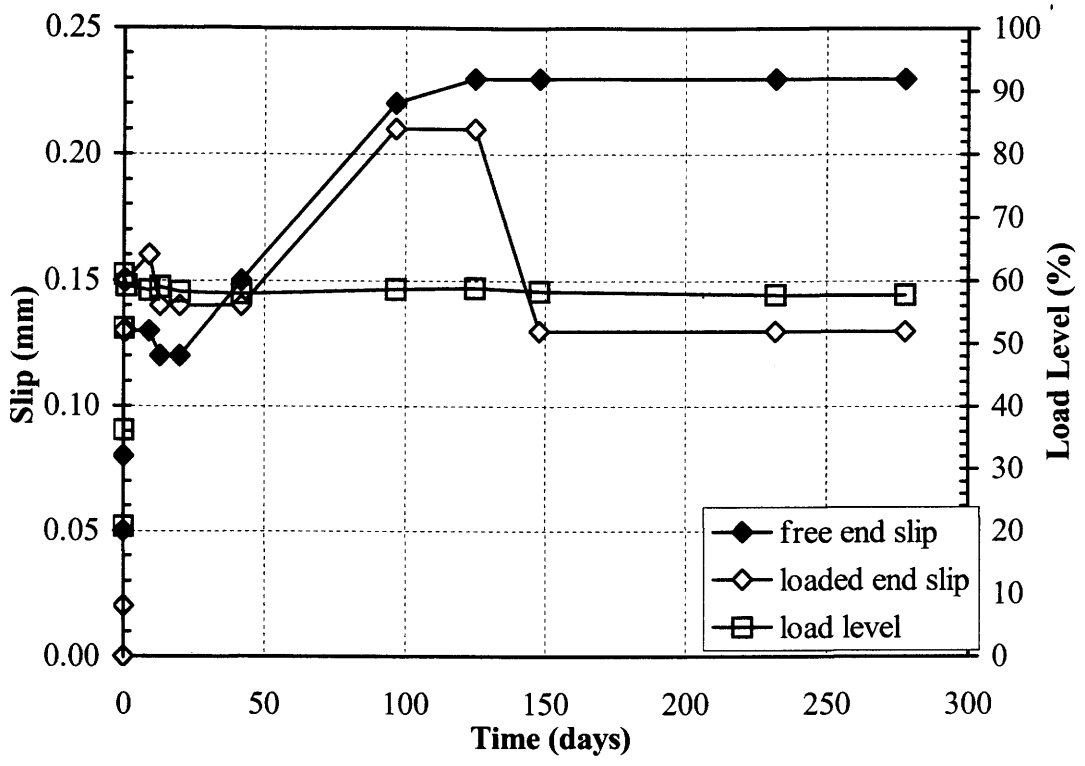

Figure B.11. Slip vs. time and load vs. time curves for Specimen CFCC 60% #2.

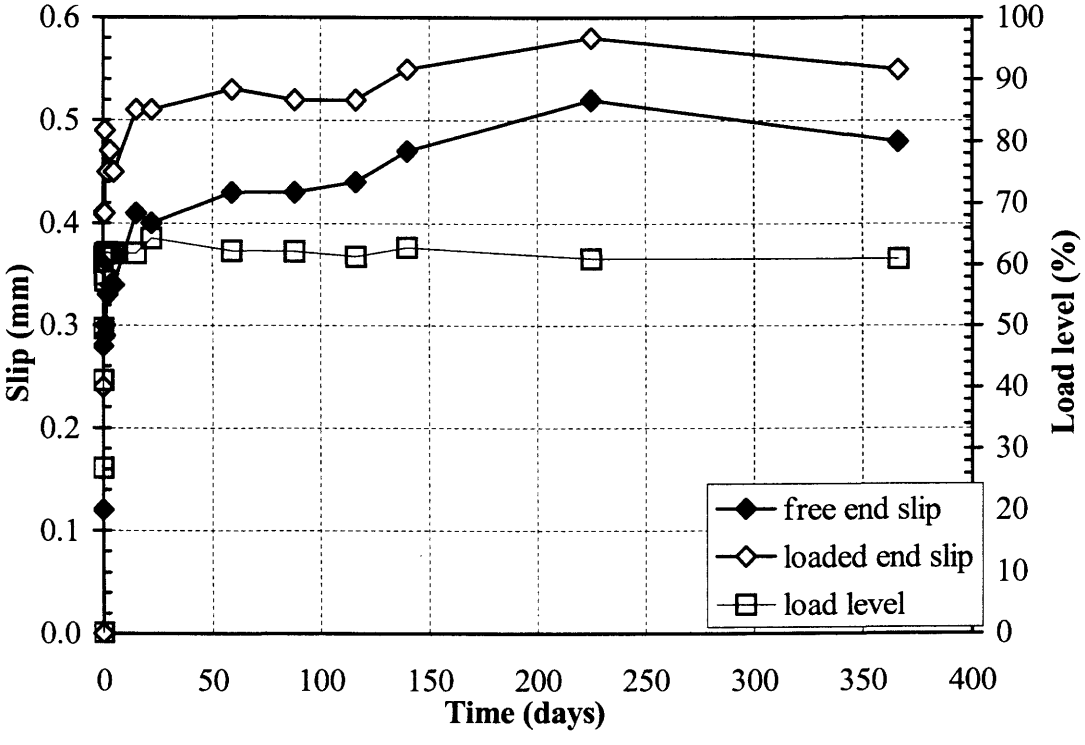

Figure B.12. Slip vs. time and load vs. time curves for Specimen CFCC 60% #3.

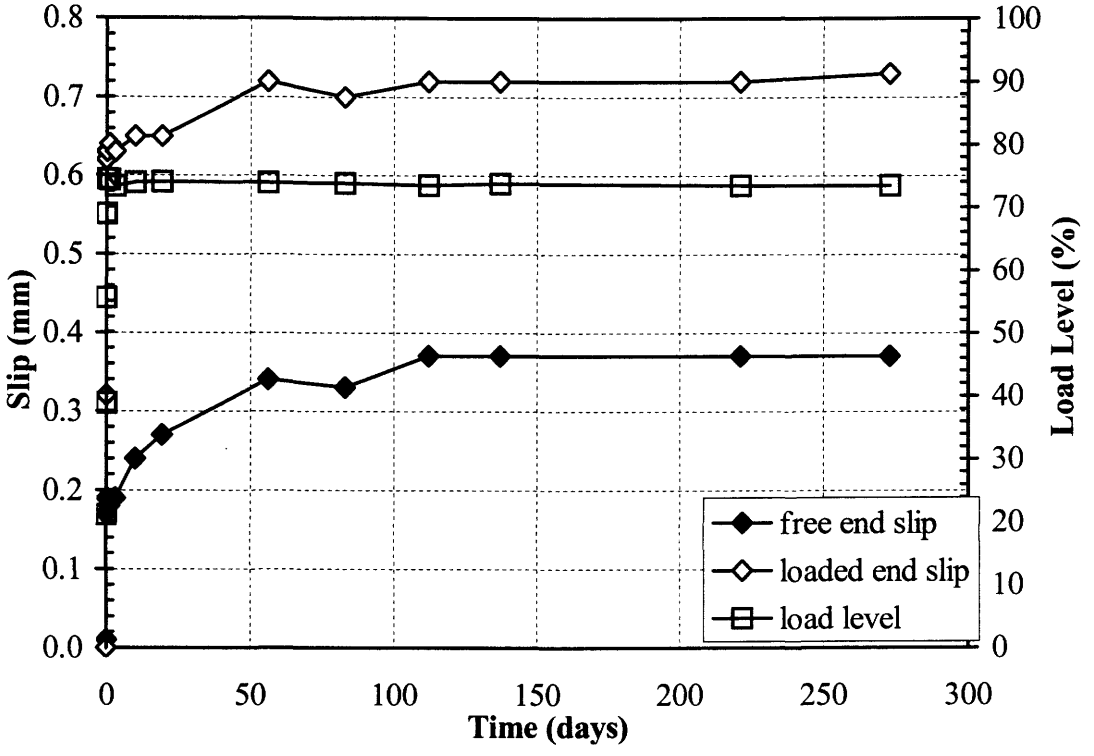

Figure B.13. Slip vs. time and load vs. time curves for Specimen CFCC 75% #1.

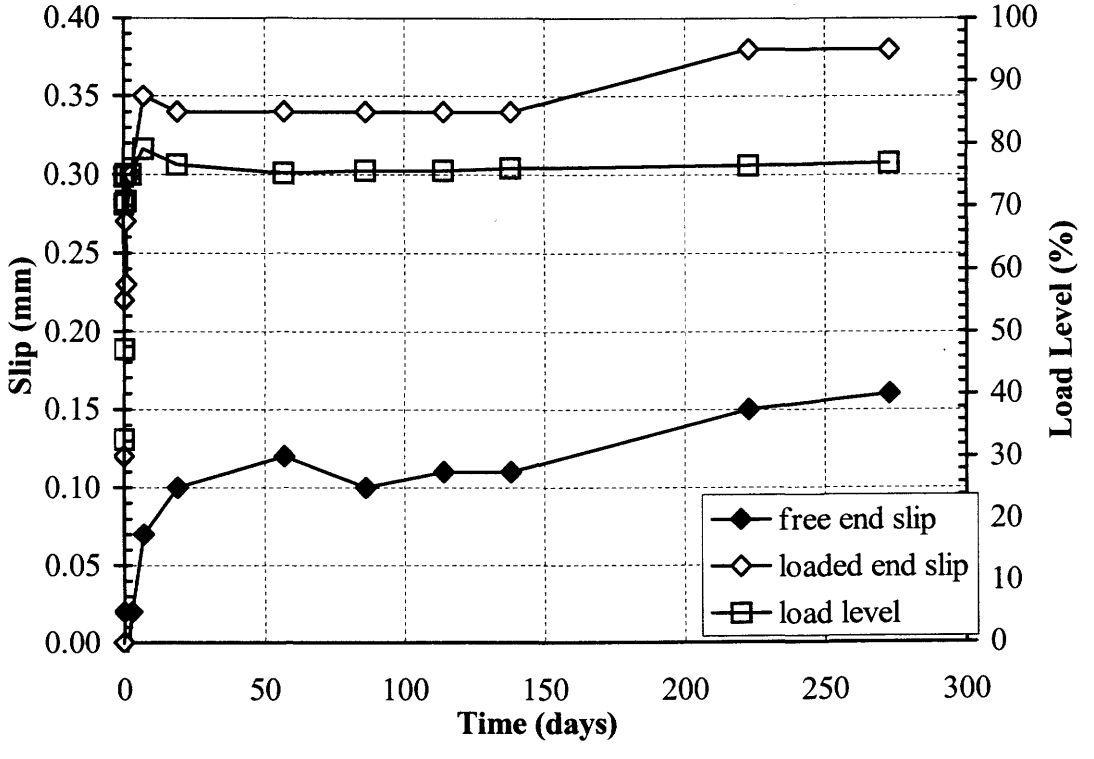

Figure B.14. Slip vs. time and load vs. time curves for Specimen CFCC 75% #2.

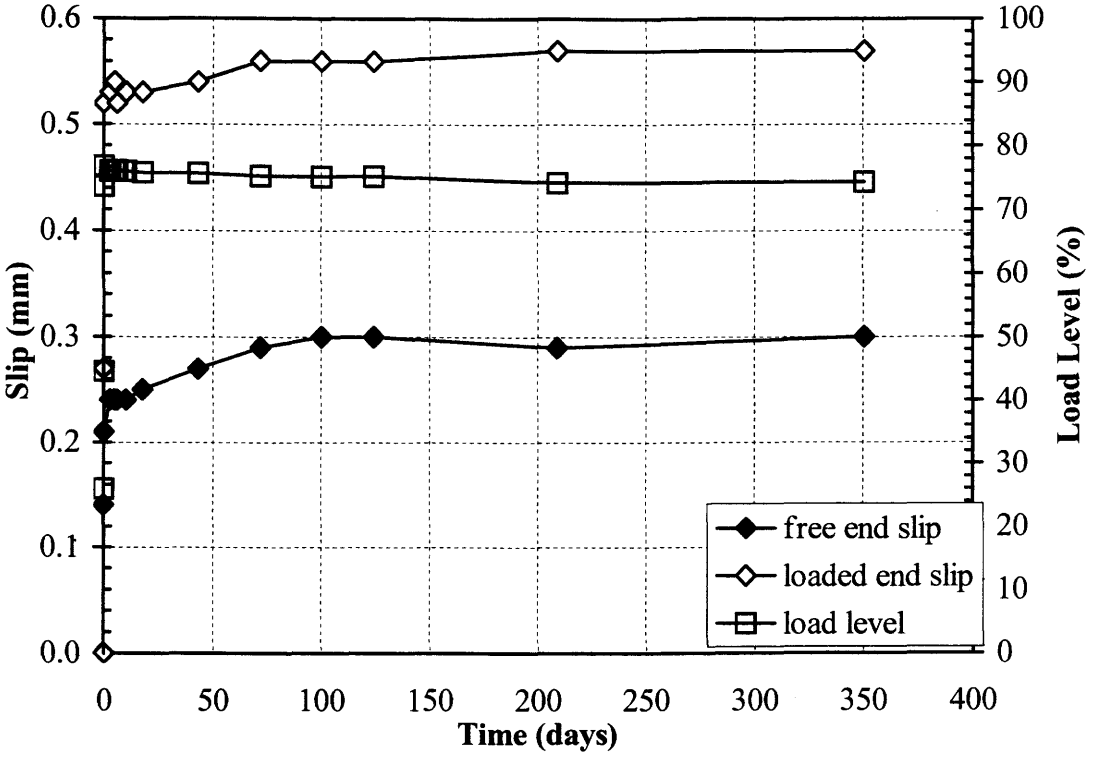

Figure B.15. Slip vs. time and load vs. time curves for Specimen CFCC 75% #3.

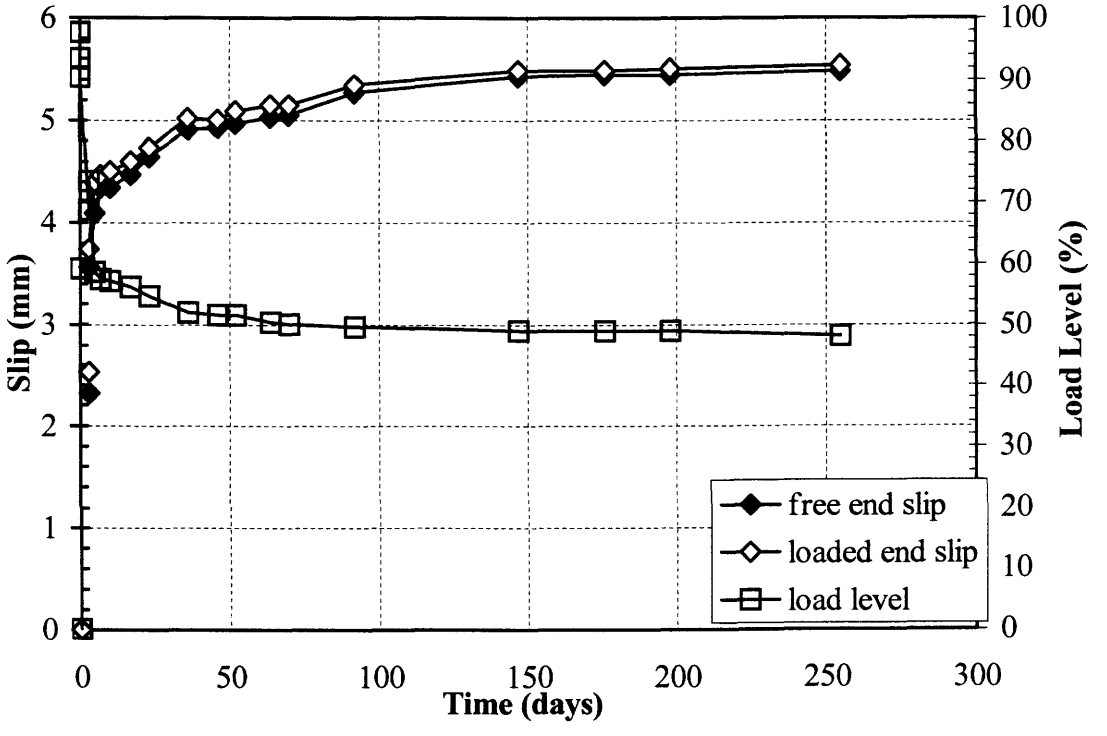

Figure B.16. Slip vs. time and load vs. time curves for Specimen CFCC 90% #1.

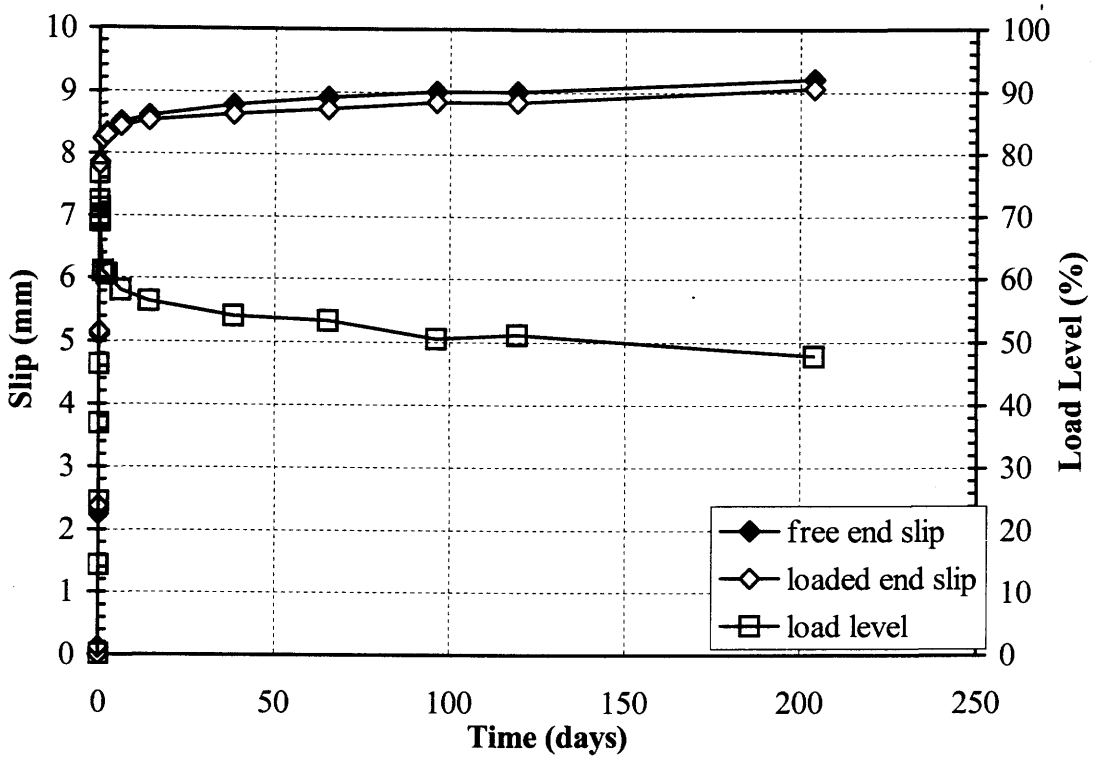

Figure B.17. Slip vs. time and load vs. time curves for Specimen CFCC 90% #2.

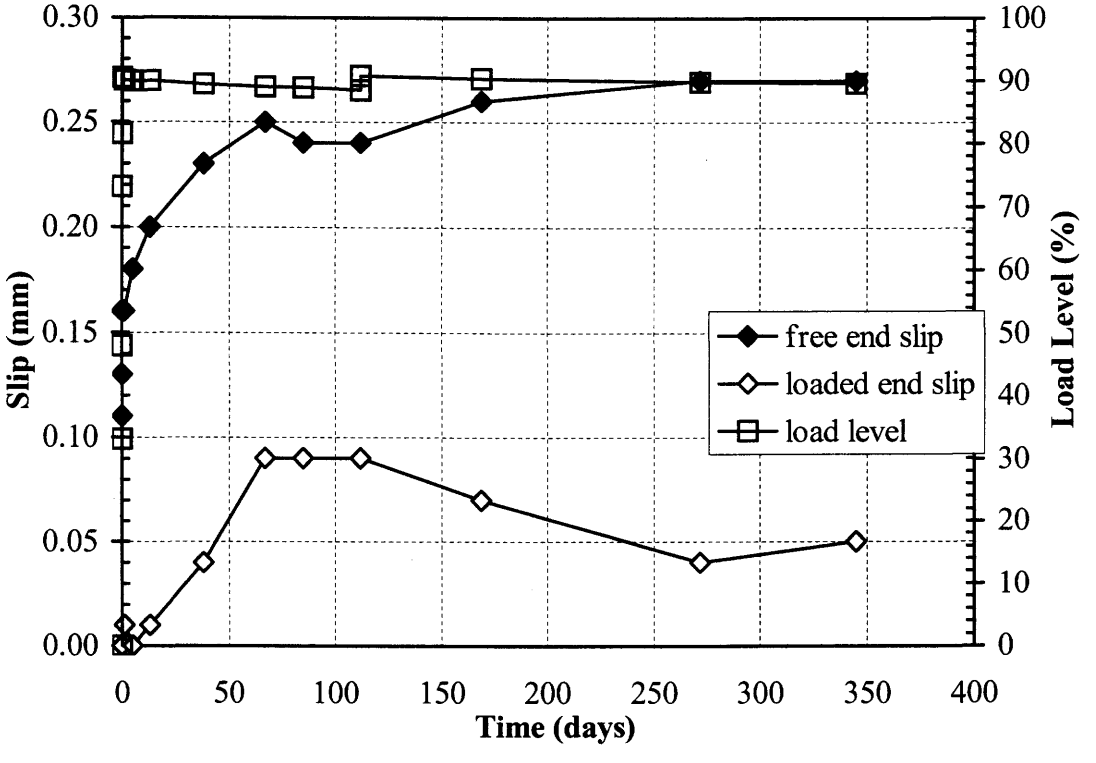

Figure B.18. Slip vs. time and load vs. time curves for Specimen CFCC 90% #3.

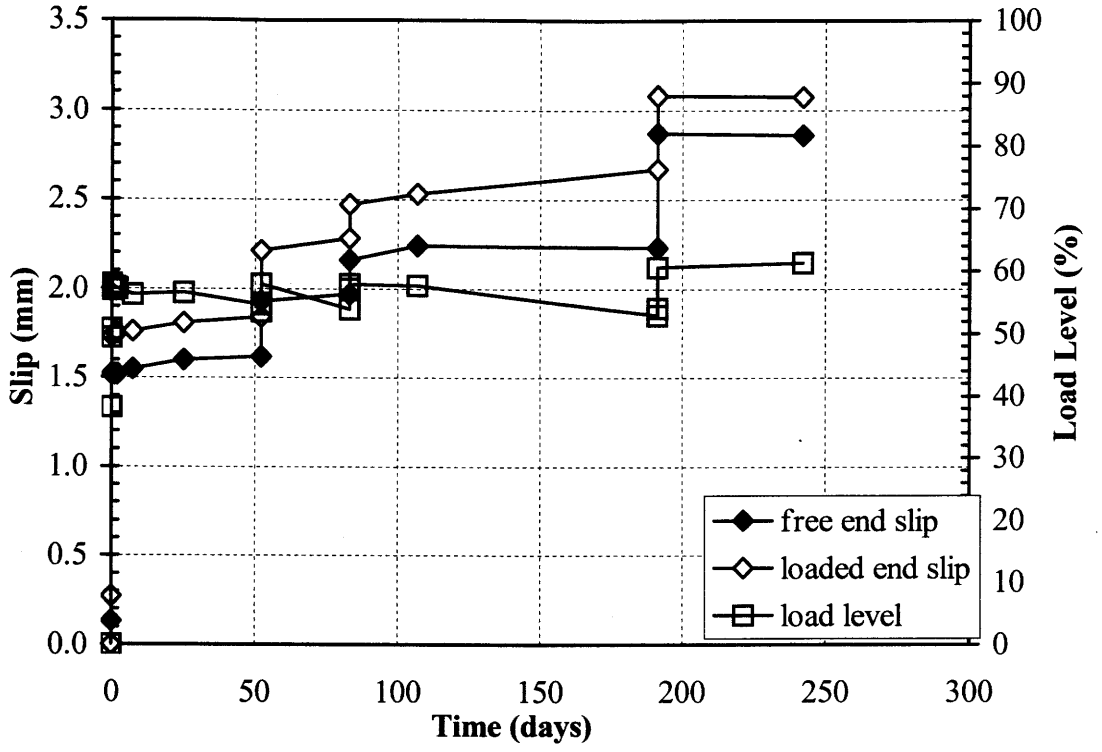

Figure B.19. Slip vs. time and load vs. time curves for Specimen Leadline 60% #1.

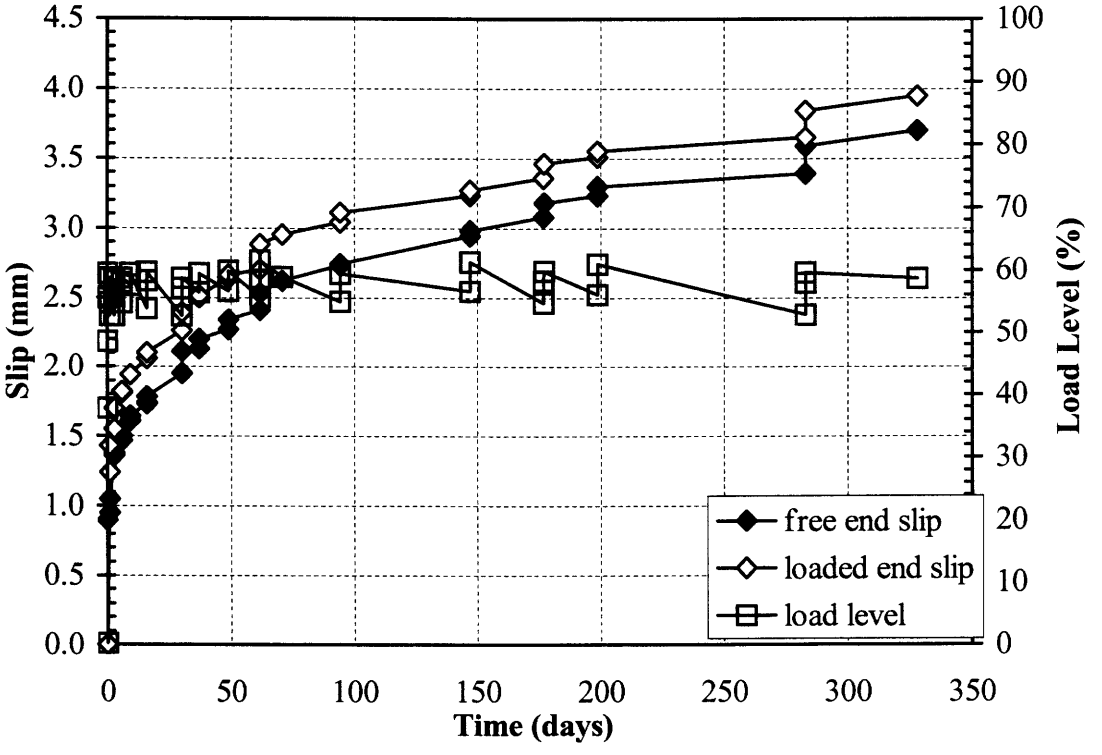

Figure B.20. Slip vs. time and load vs. time curves for Specimen Leadline 60% #2.

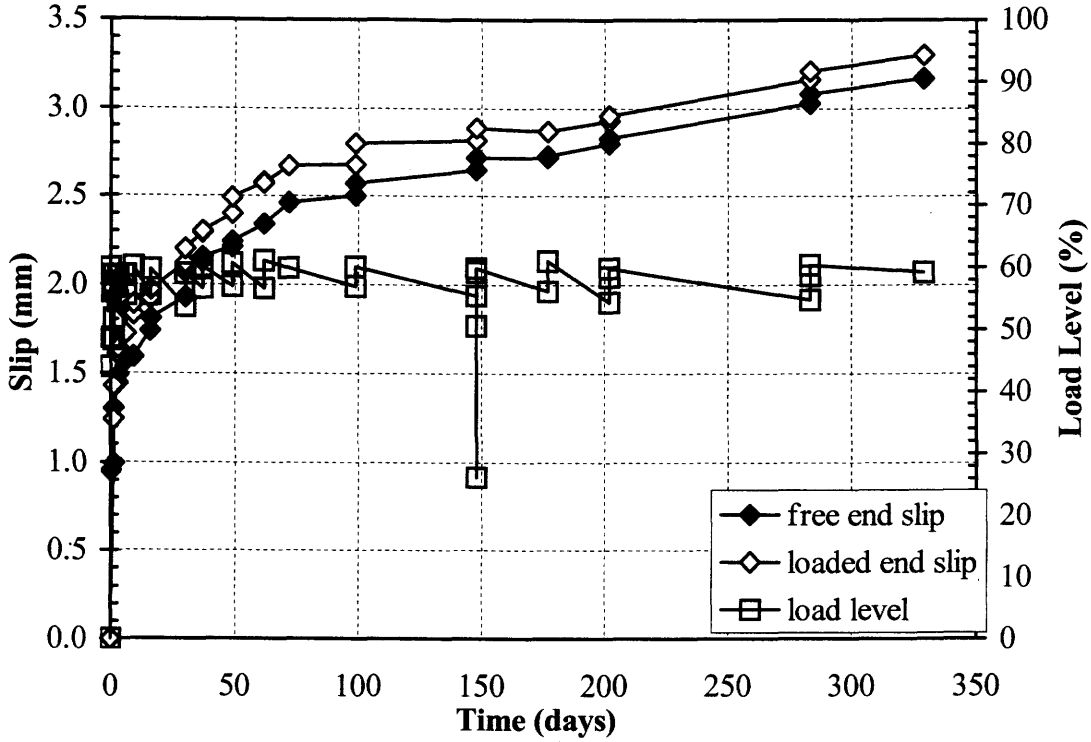

Figure B 21. Slip vs. time and load vs. time curves for Specimen Leadline 60% #3.

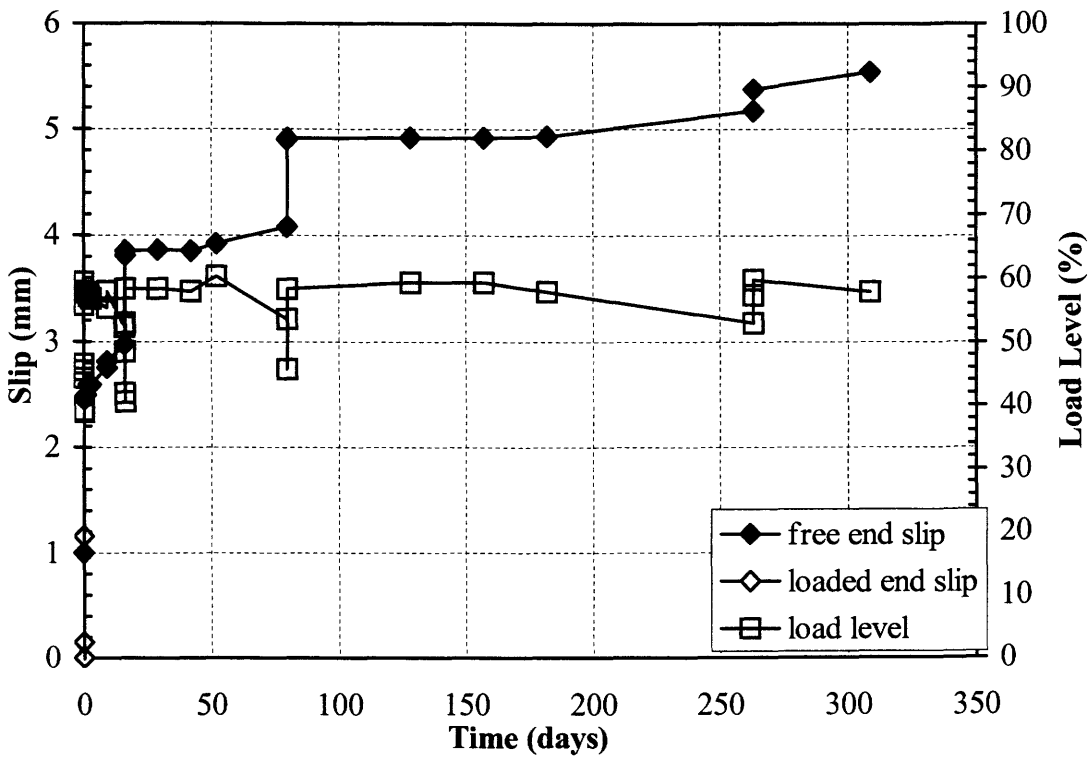

Figure B.22. Slip vs. time and load vs. time curves for Specimen Leadline 60% #4.

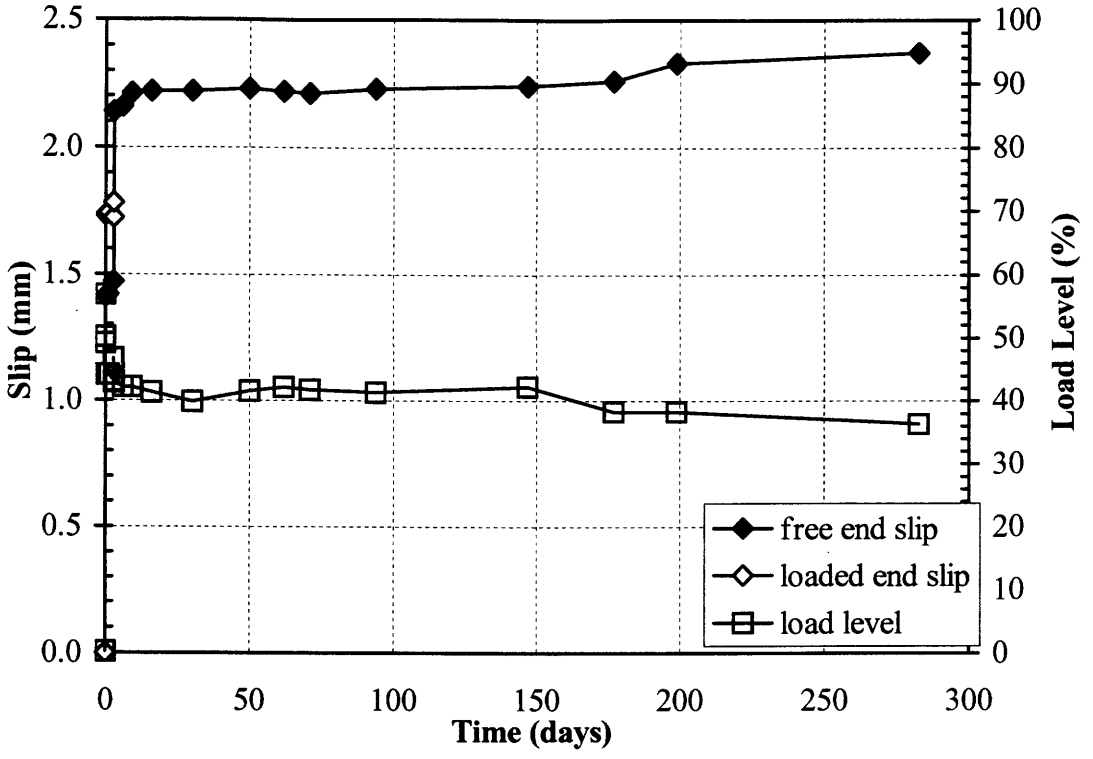

Figure B.23. Slip vs. time and load vs. time curved for Specimen Leadline 60% #5.

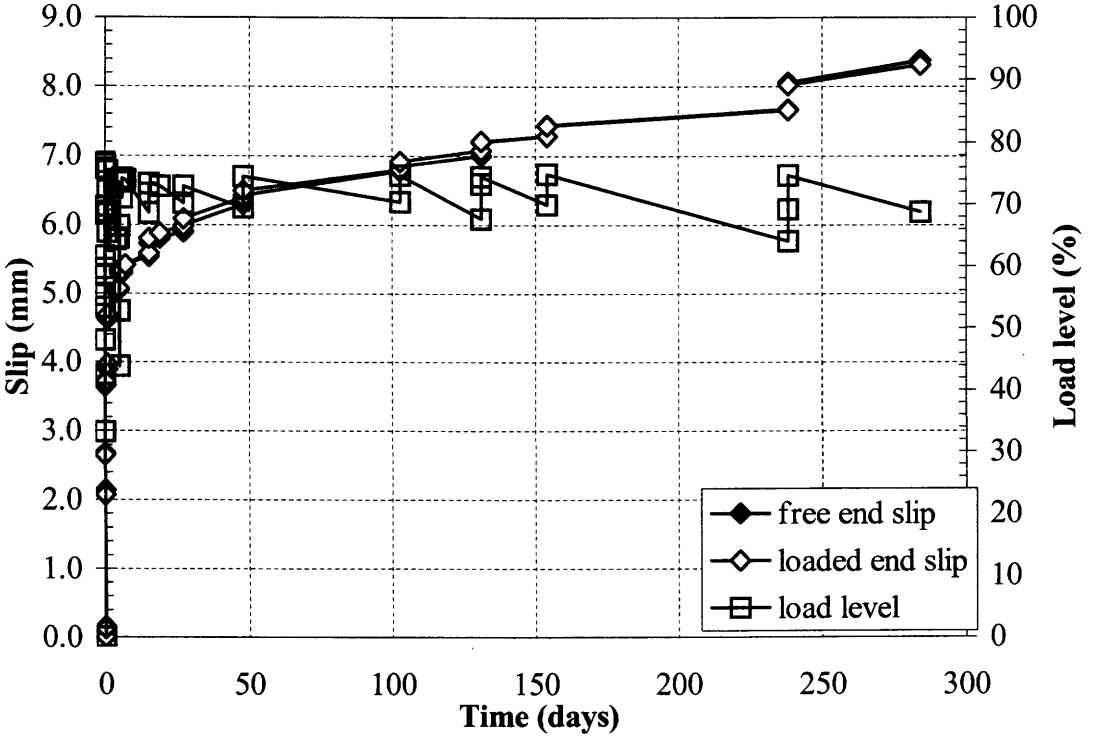

Figure B.24. Slip vs. time and load vs. time curves for Specimen Leadline 75% #1.

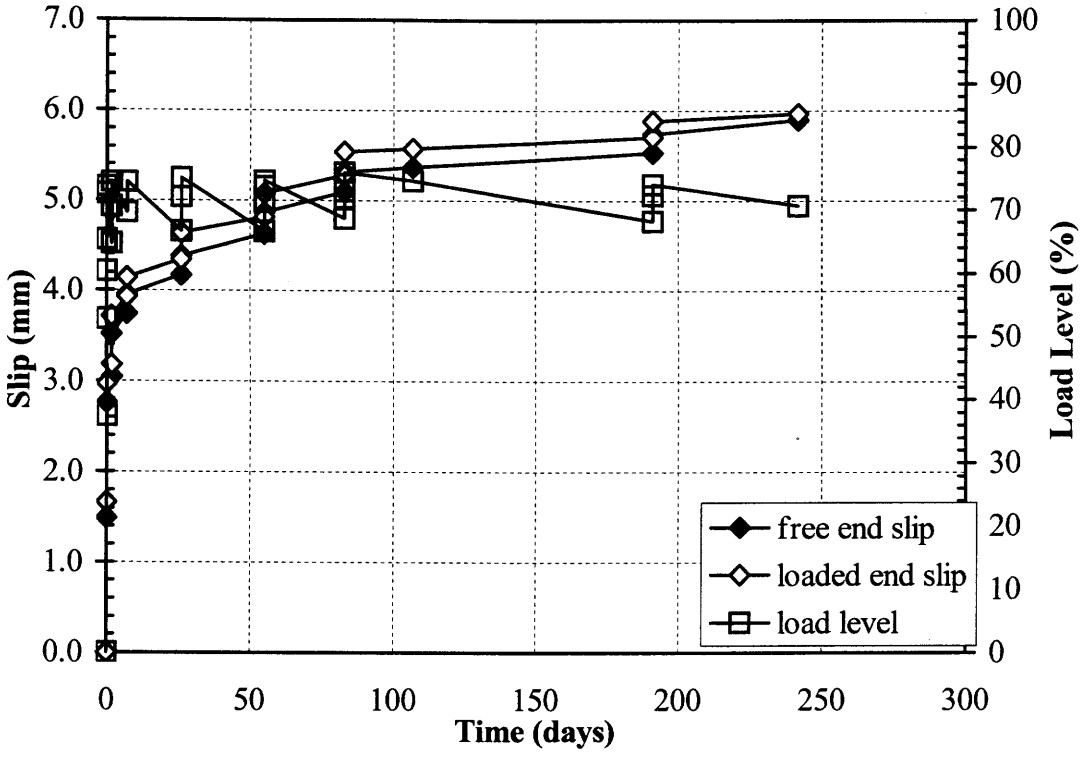

Figure B.25. Slip vs. time and load vs. time curves for Specimen Leadline 75% #2.

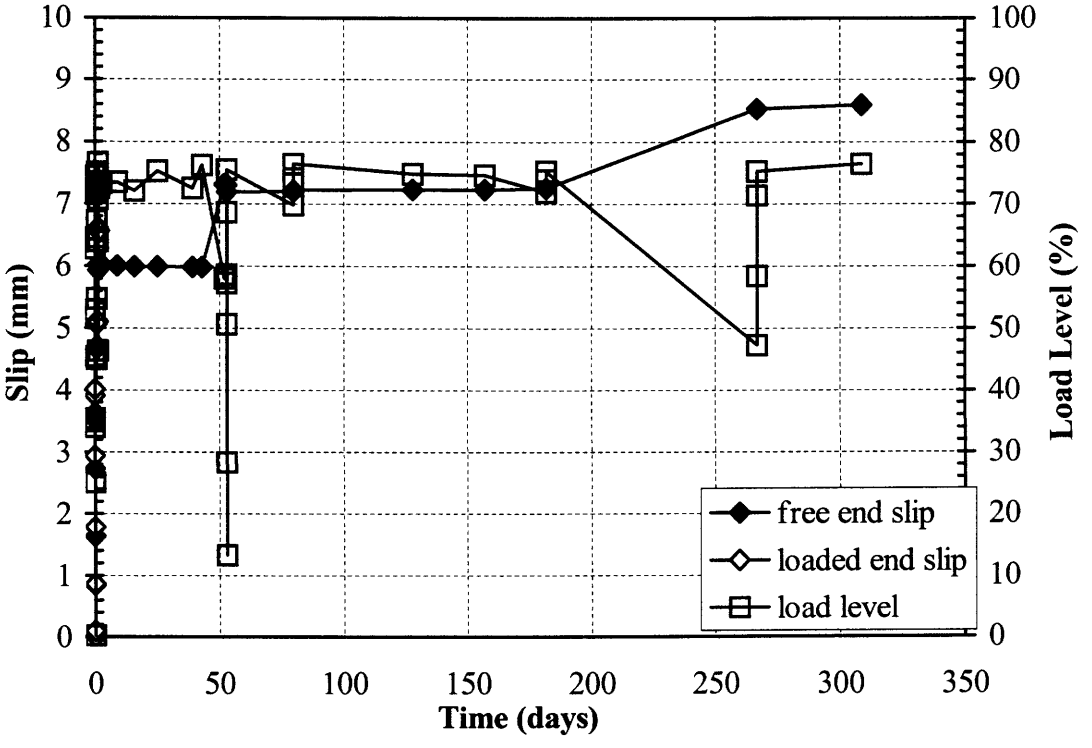

Figure B.26. Slip vs. time and load vs. time curves for Specimen Leadline 75% #3.

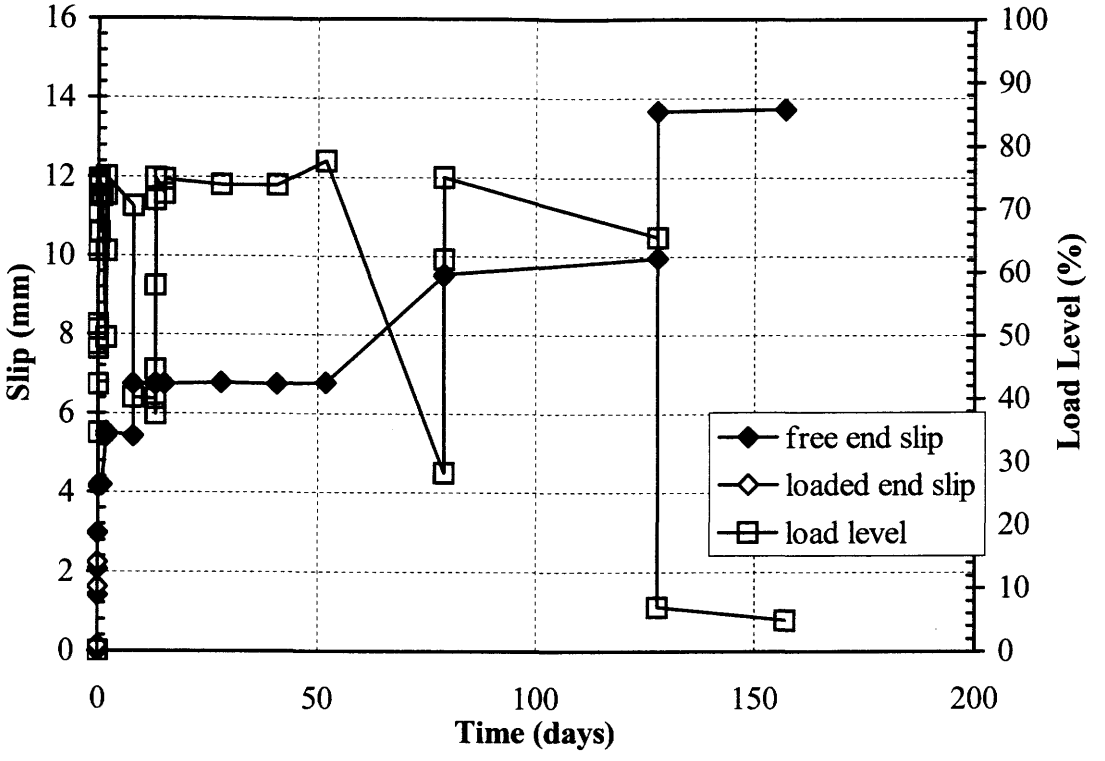

Figure B.27. Slip vs. time and load vs. time curves for Specimen Leadline 75% #4.

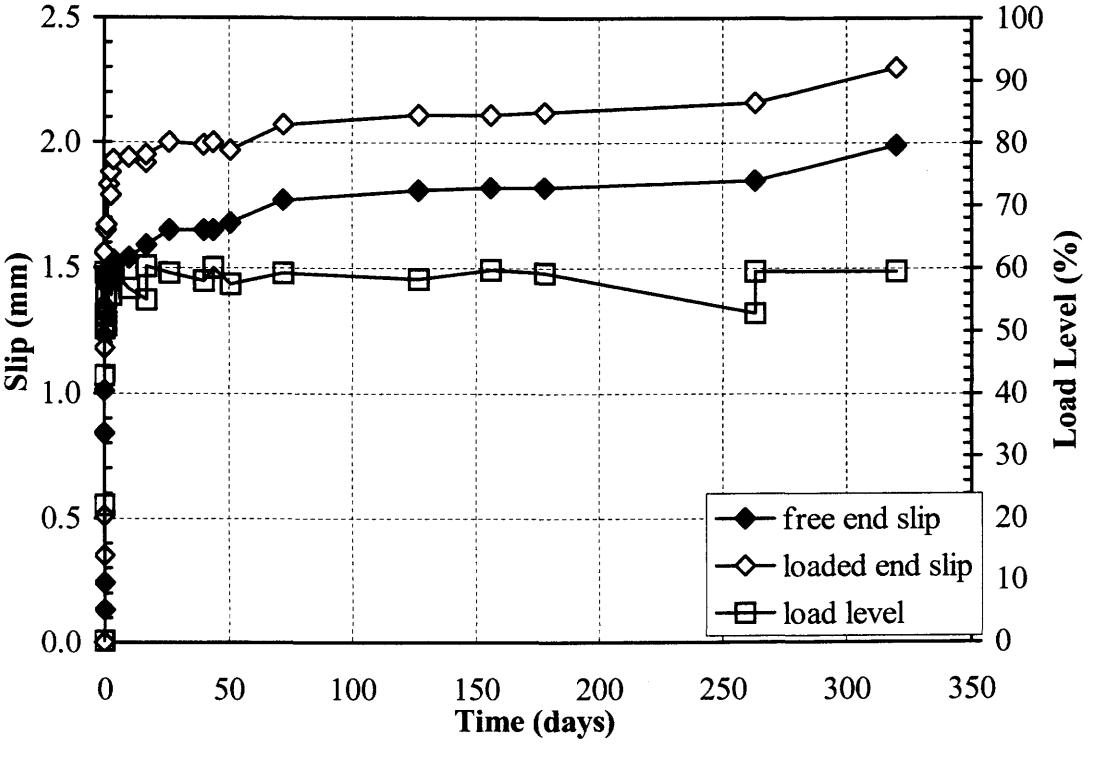

Figure B.28. Slip vs. time and load vs. time curves for Specimen Isorod 60% #1.

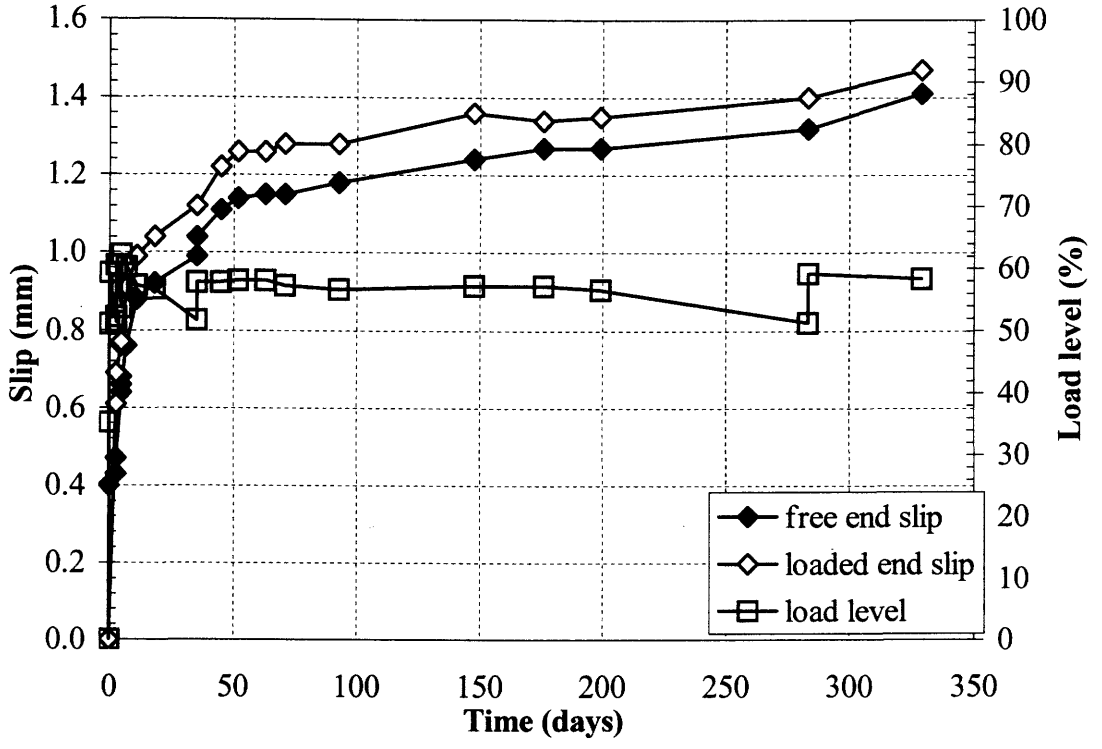

Figure B.29. Slip vs. time and load vs. time curves for Specimen Isorod 60% #2.

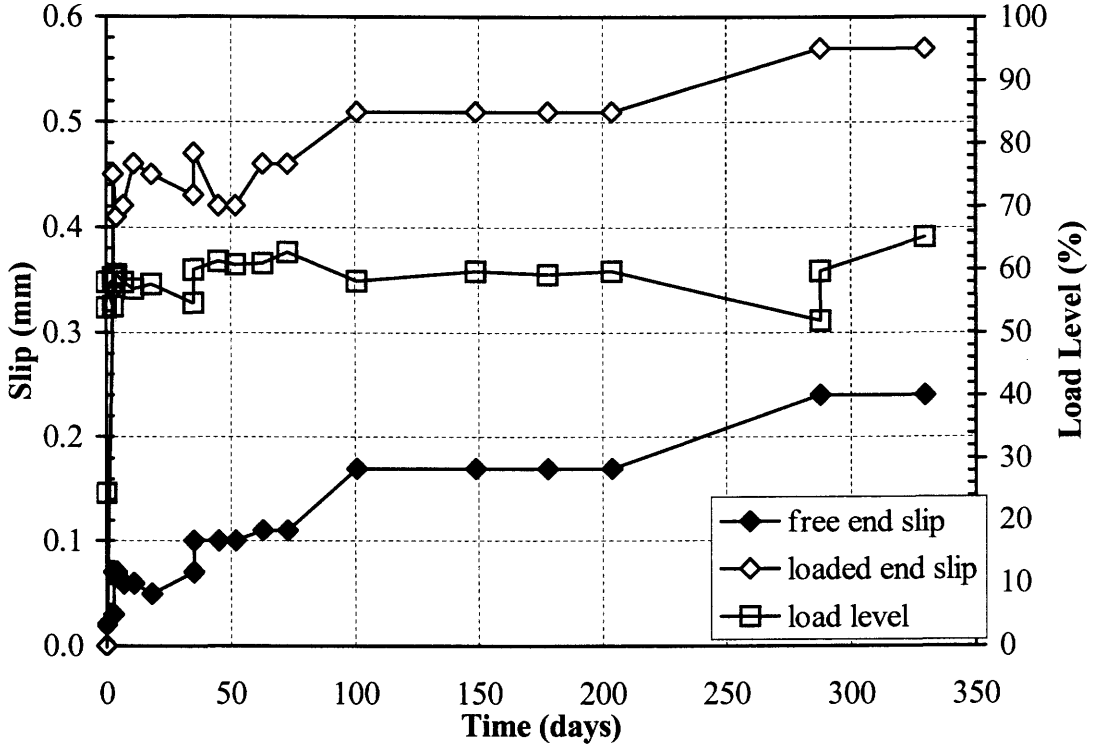

Figure B.30. Slip vs. time and load vs. time curves for Specimen Isorod 60% #3.

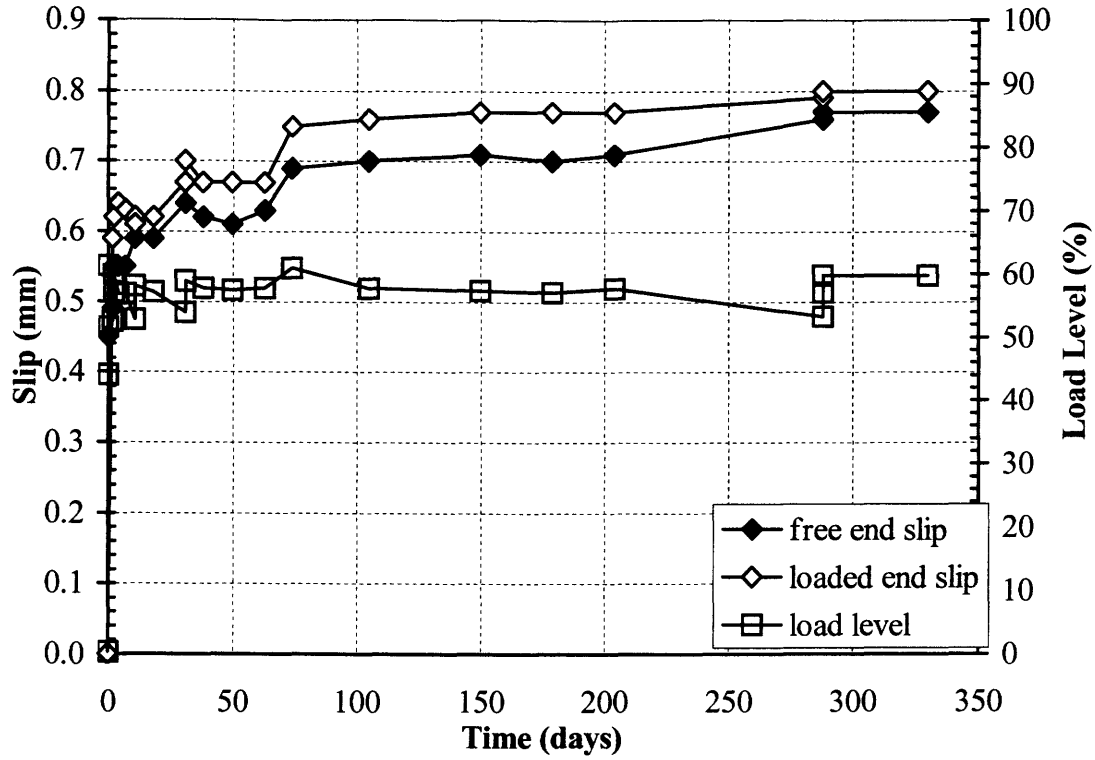

Figure B.31. Slip vs. time and load vs. time curves for Specimen Isorod 60% #4.

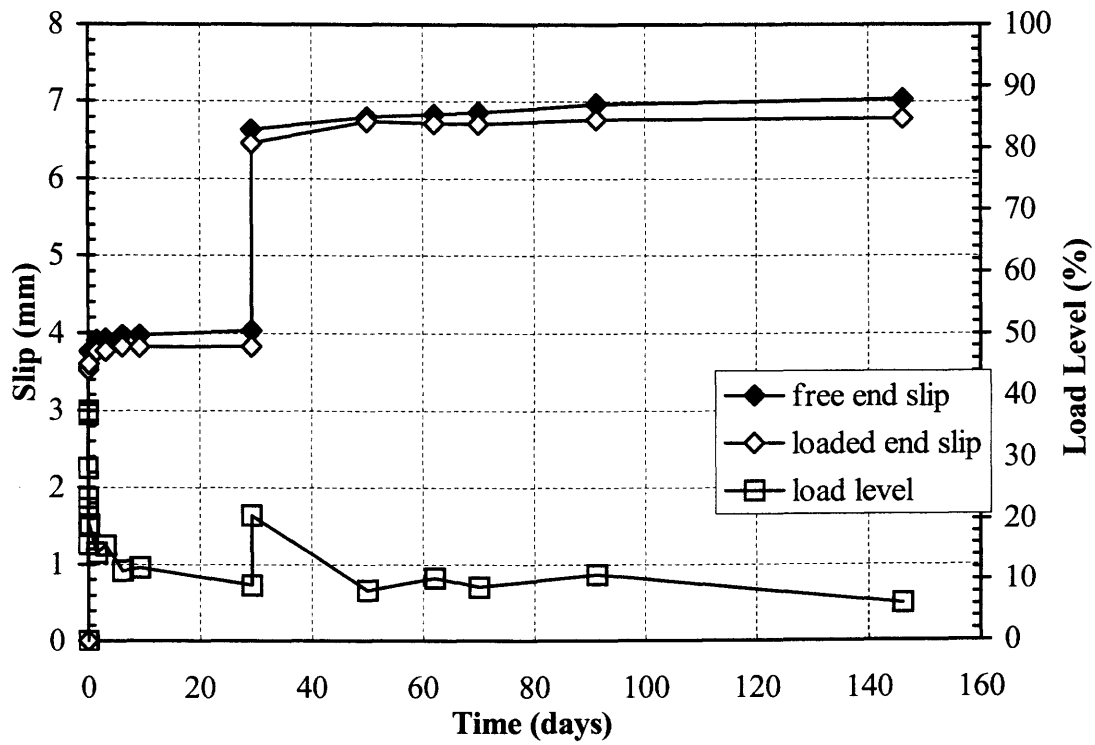

Figure B.32. Slip vs. time and load vs. time curves for Specimen Isorod 75% #1.

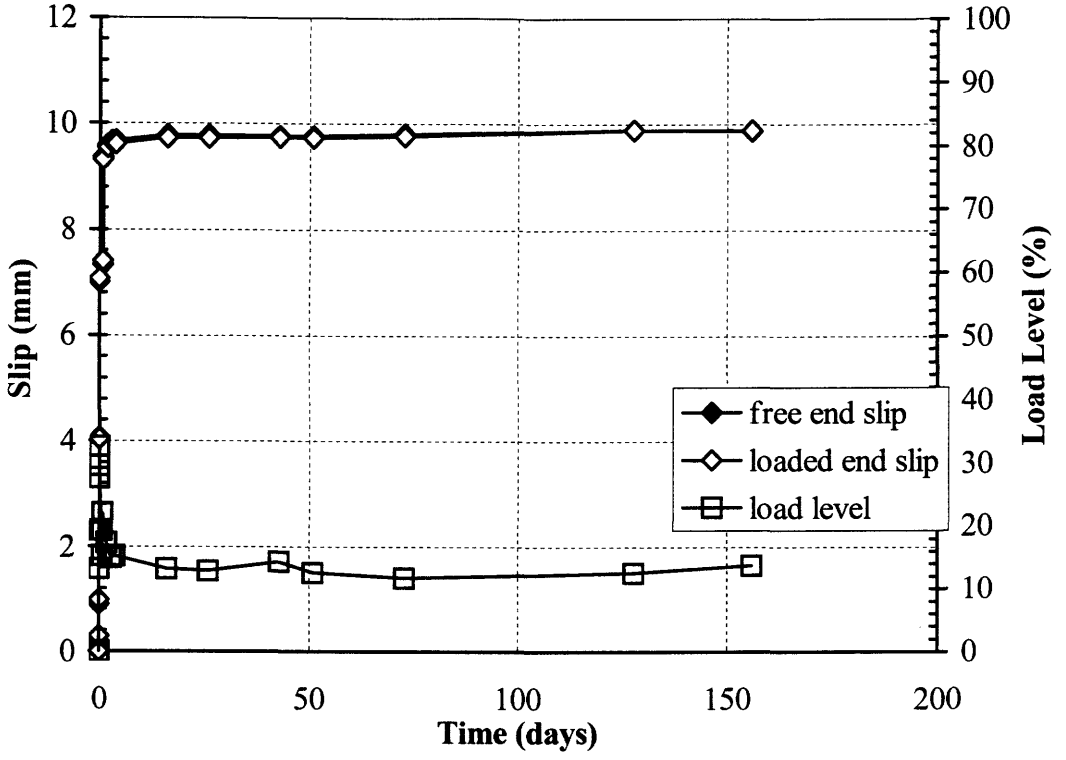

Figure B.33. Slip vs. time and load vs. time curves for Specimen Isorod 75% #2.

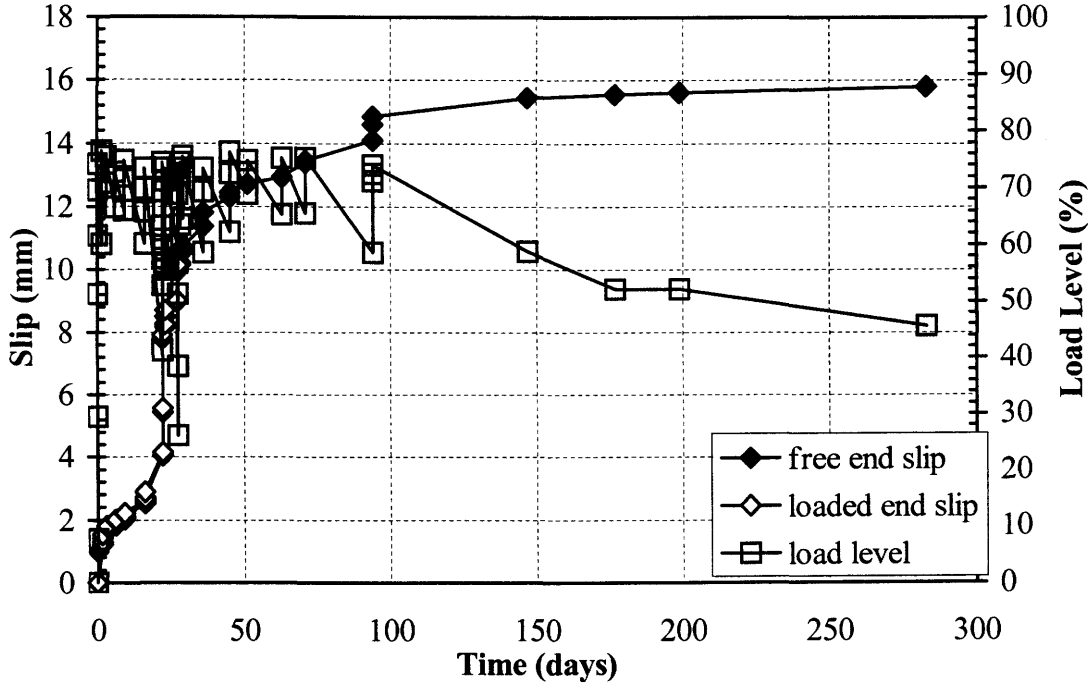

Figure B.34. Slip vs. time and load vs. time curves for Specimen Isorod 75% #3.

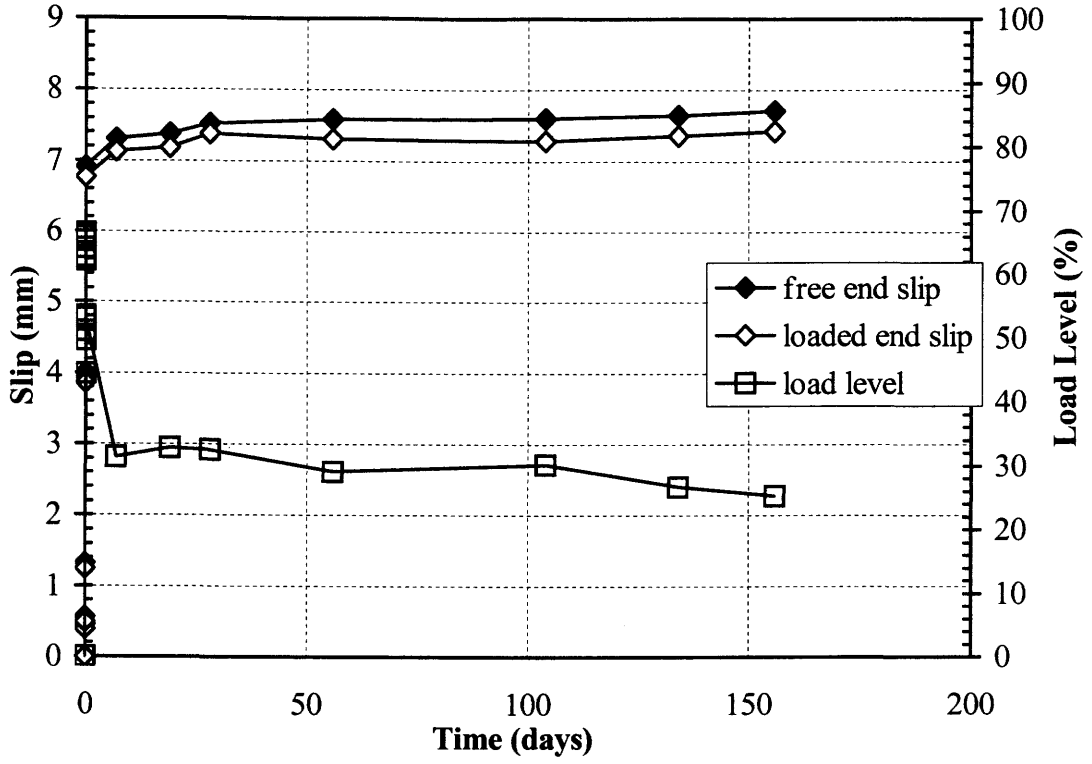

FigureB.35. Slip vs. time and load vs. time curves for Specimen Isorod 75% #4.

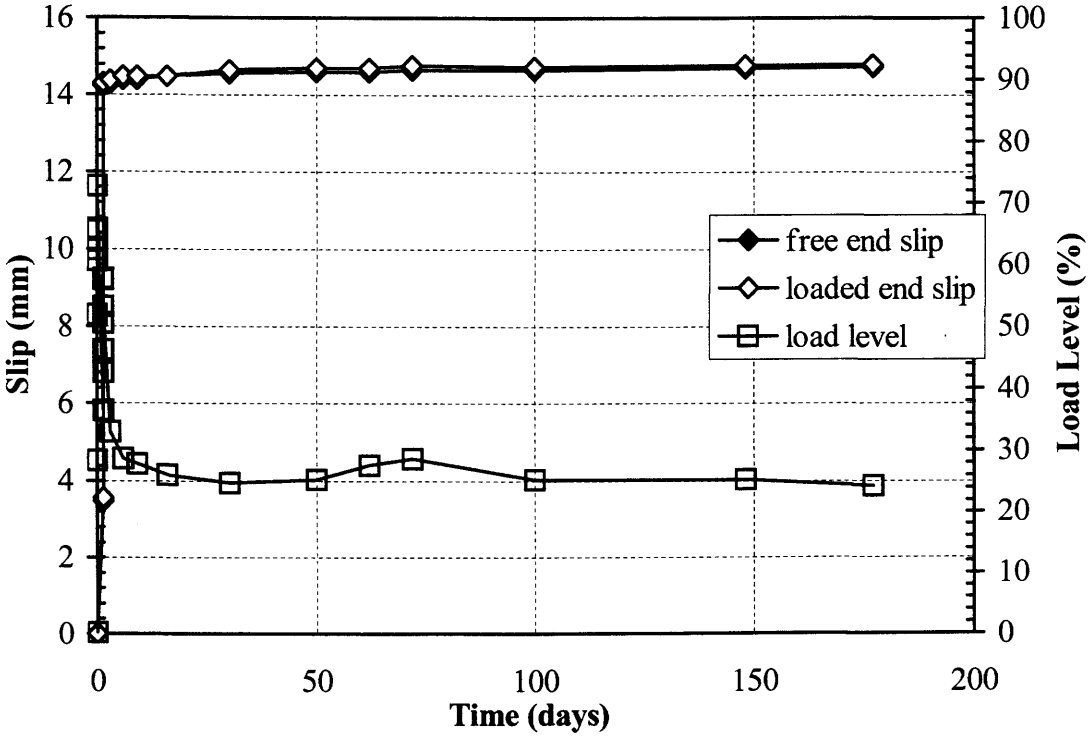

Figure B.36. Slip vs. time and load vs. time curves for Specimen Isorod 75% #5.

Appendix C

Long term test results for Phase II

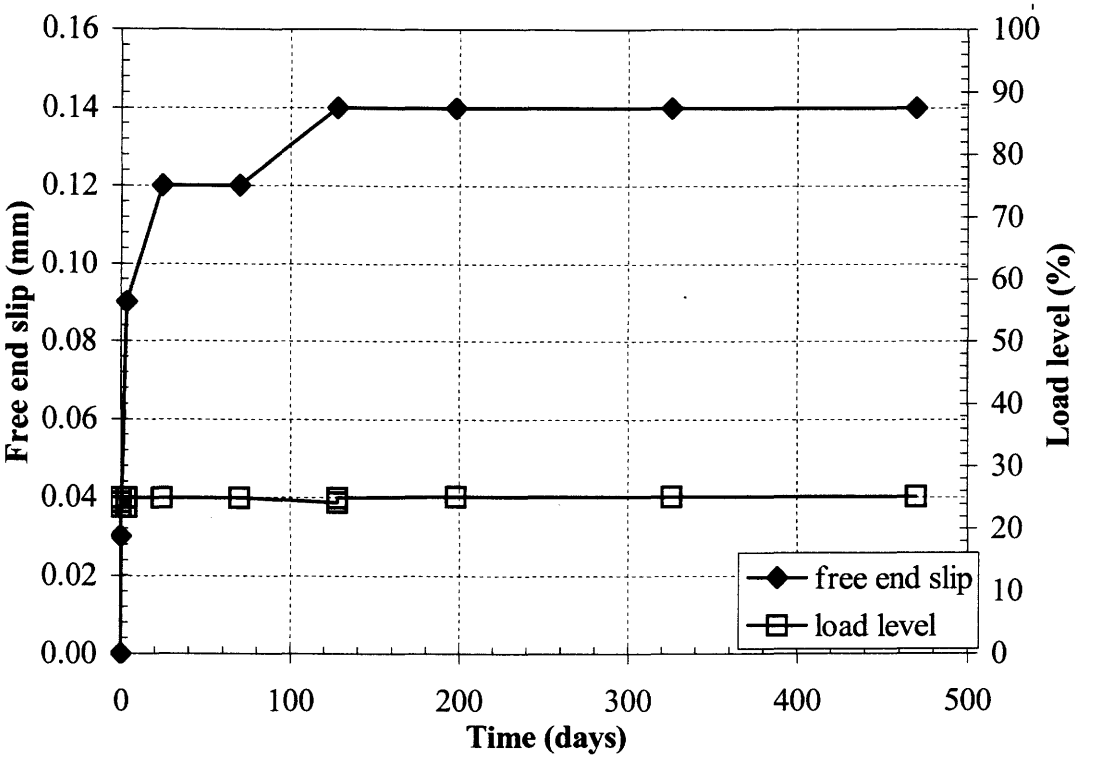

Figure C.1. Free end slip vs. time and load curves for Specimen HB 25% Air #1.

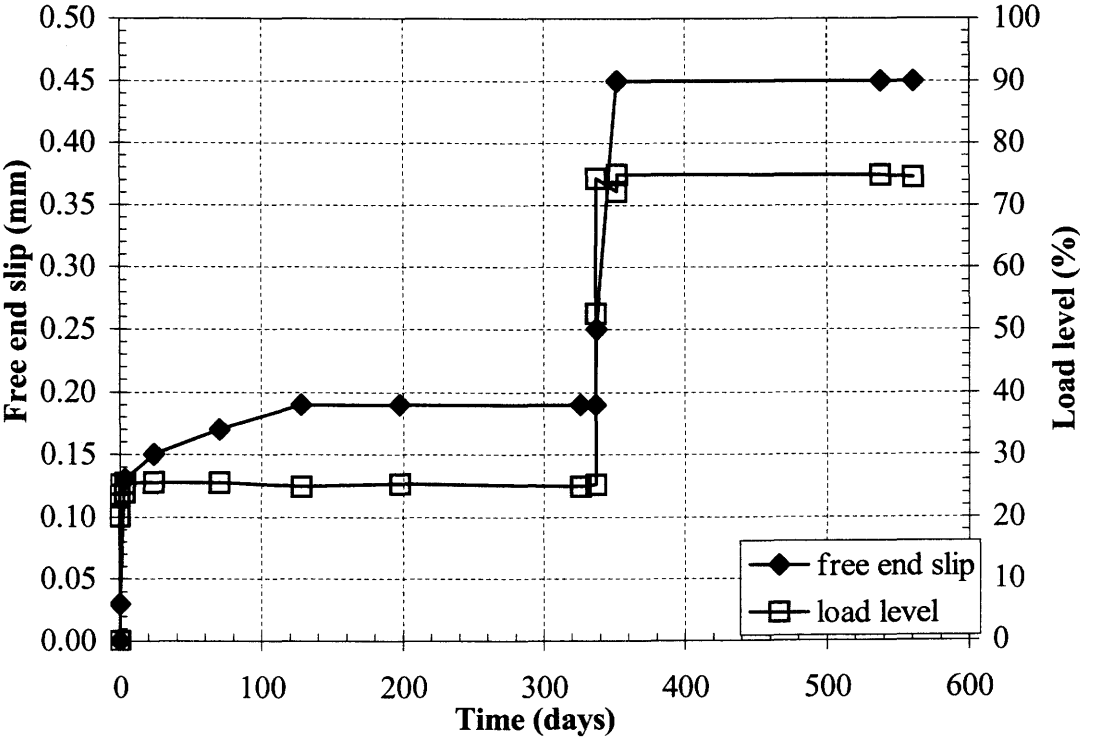

Figure C.2. Free end slip vs. time and load vs. time curves for Specimen HB 25-75% Air #2.

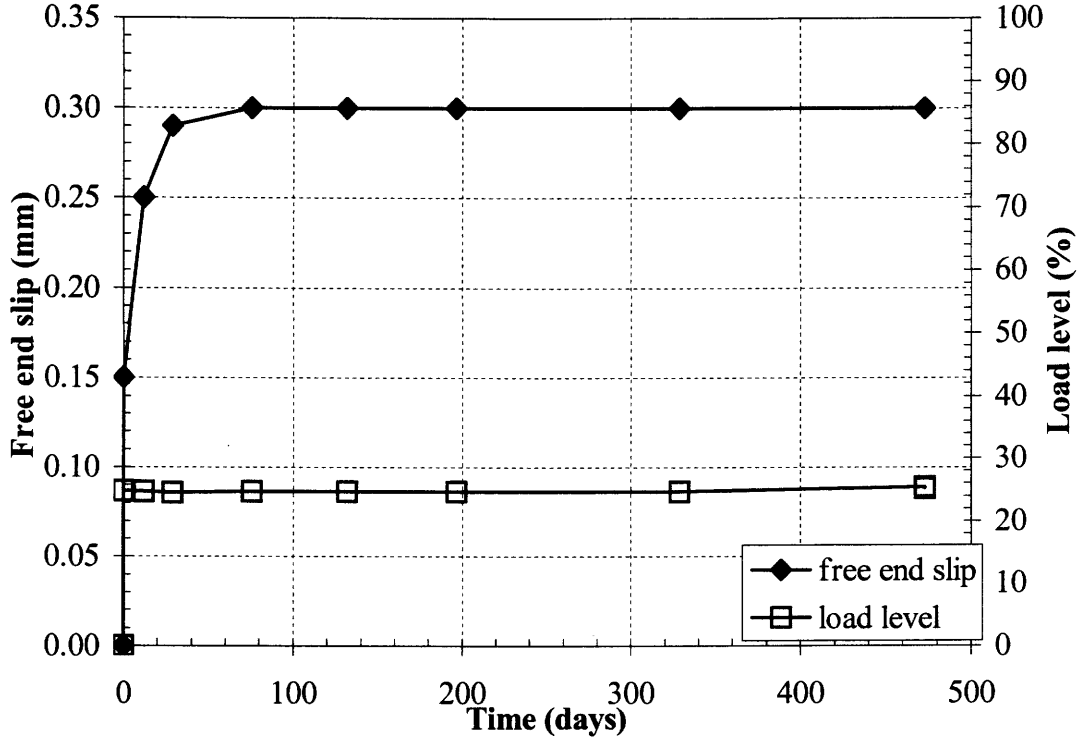

Figure C.3. Free end slip vs. time and load vs. time curves for Specimen HB 25%Water #1.

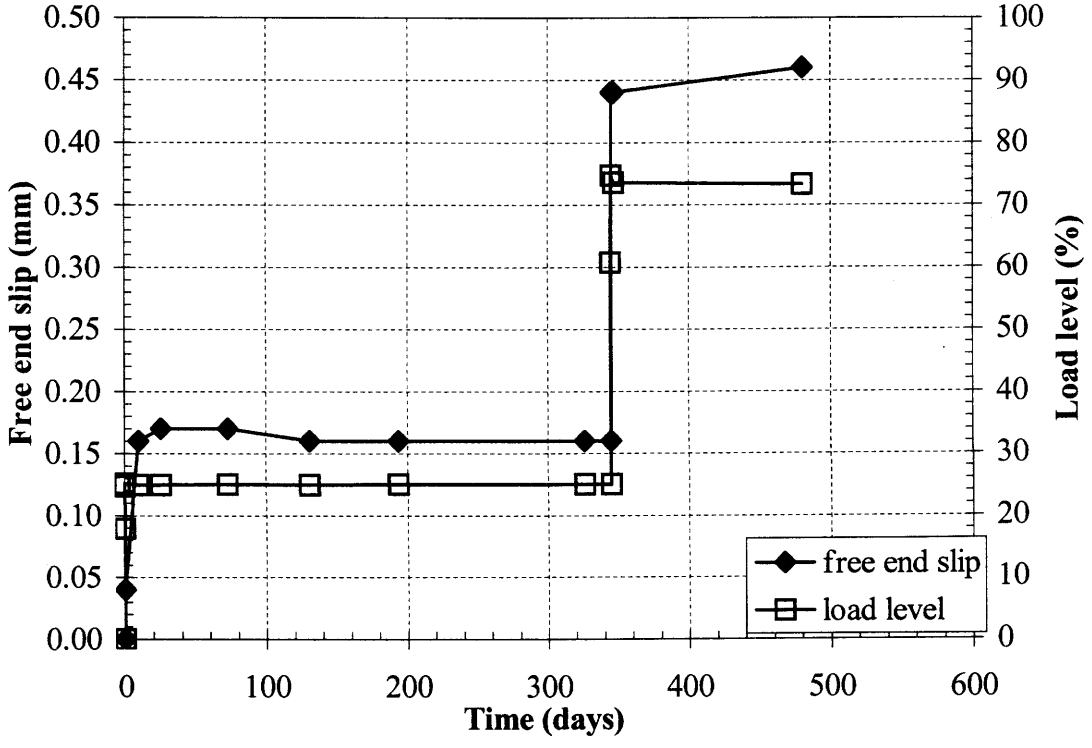

Figure C.4. Free end slip vs. time and load vs. time curves for Specimen HB 25-75% Water #2.

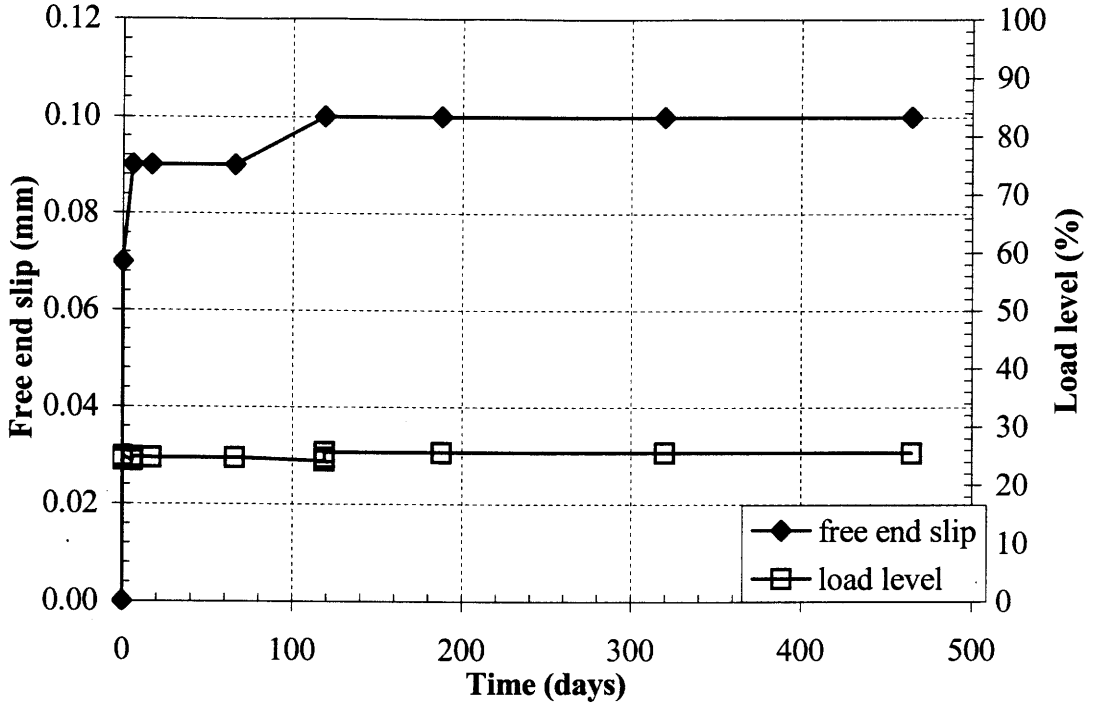

Figure C.5. Free end slip vs. time and load vs. time curves for Specimen HB 25% Alkaline #1.

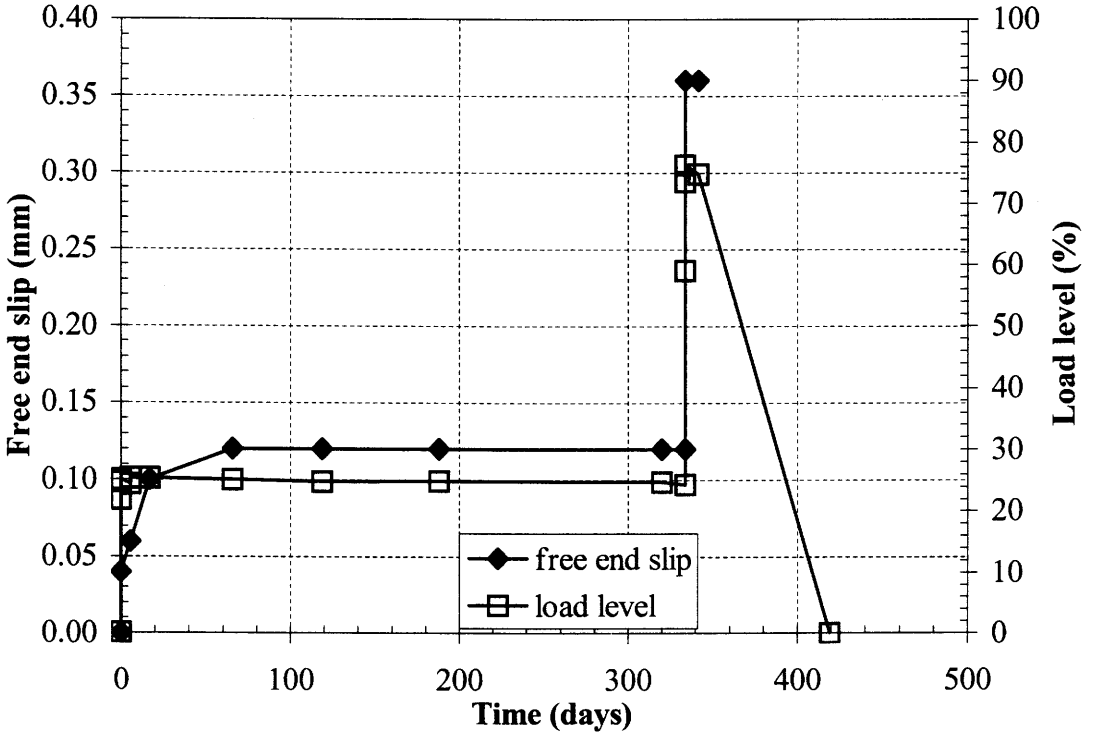

Figure C.6. Free end slip vs. time and load vs. time curves for Specimen HB 25-75% Alkaline #2.

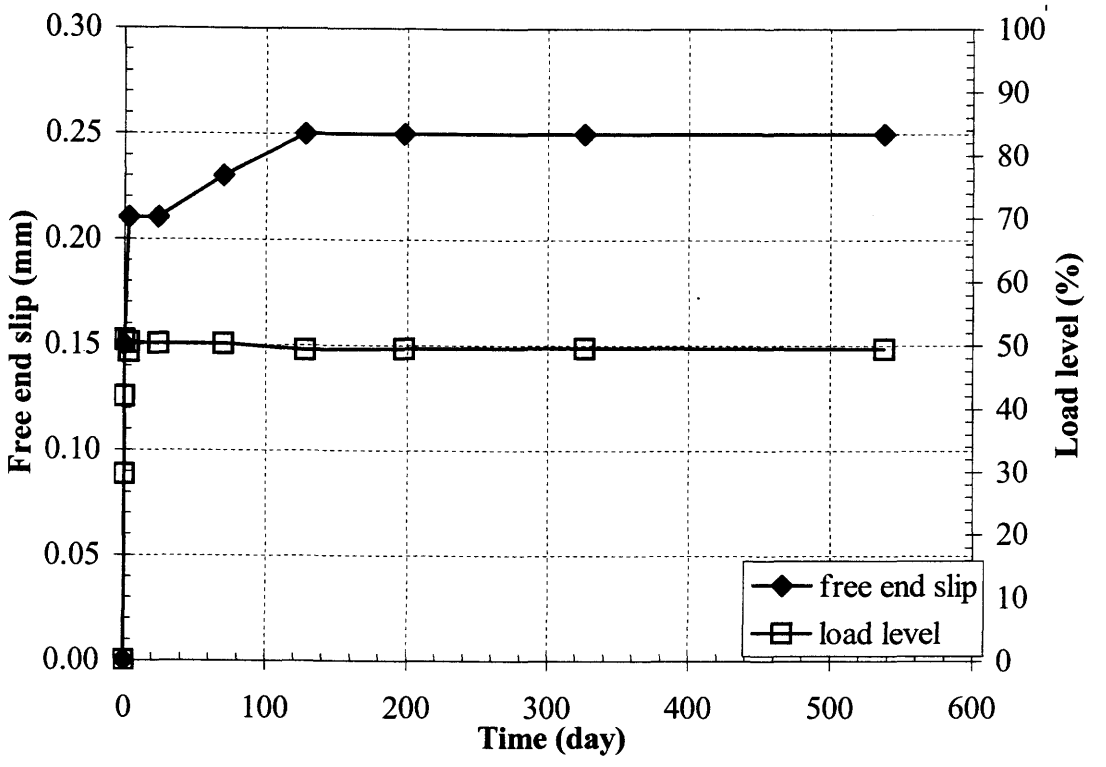

Figure C.7. Free end slip vs. time and load vs. time curves for Specimen HB 50% Air #1.

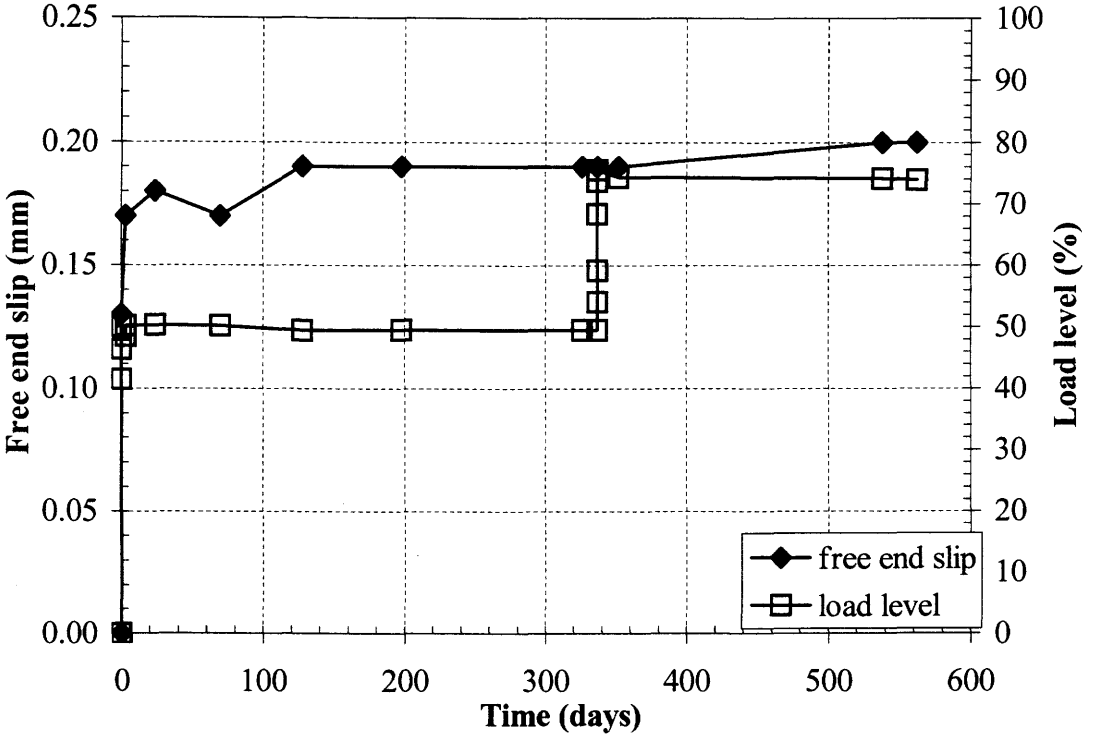

Figure C.8. Free end slip vs. time and load vs. time curves for Specimen HB 50-75% Air #2.

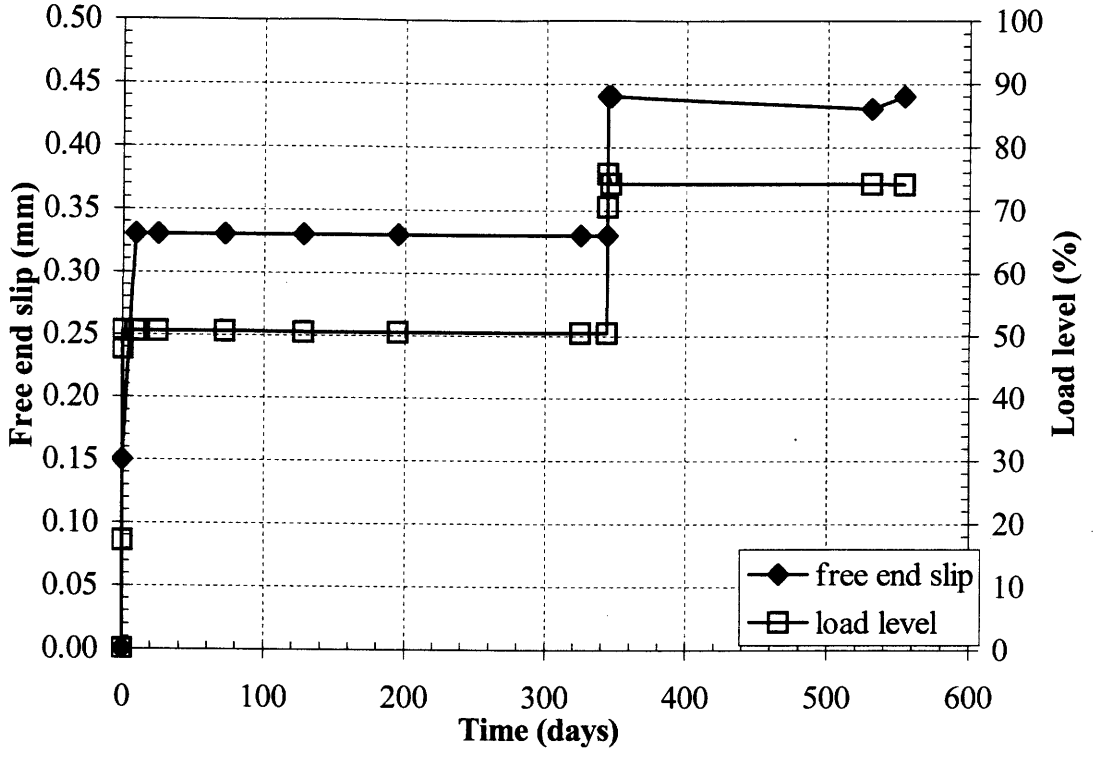

Figure C.9. Free end slip vs. time and load vs. time curves for Specimen HB 50-75% Water #1.

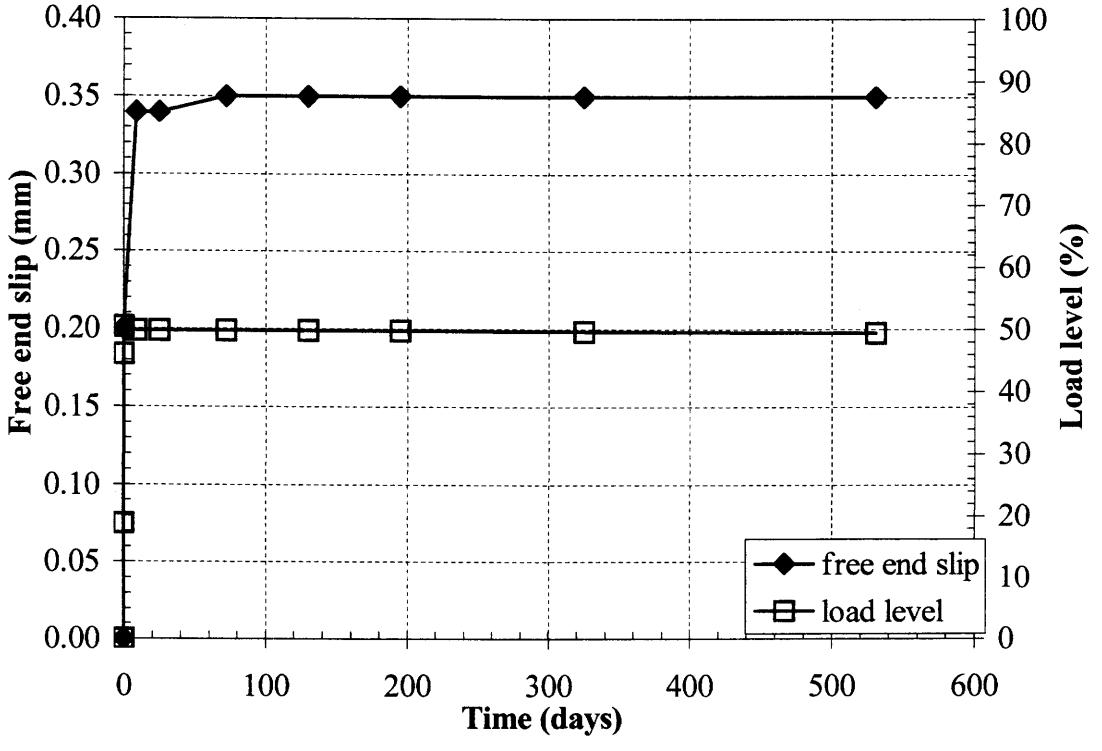

Figure C.10. Free end slip vs. time and load vs. time curves for Specimen HB 50% Water #2.

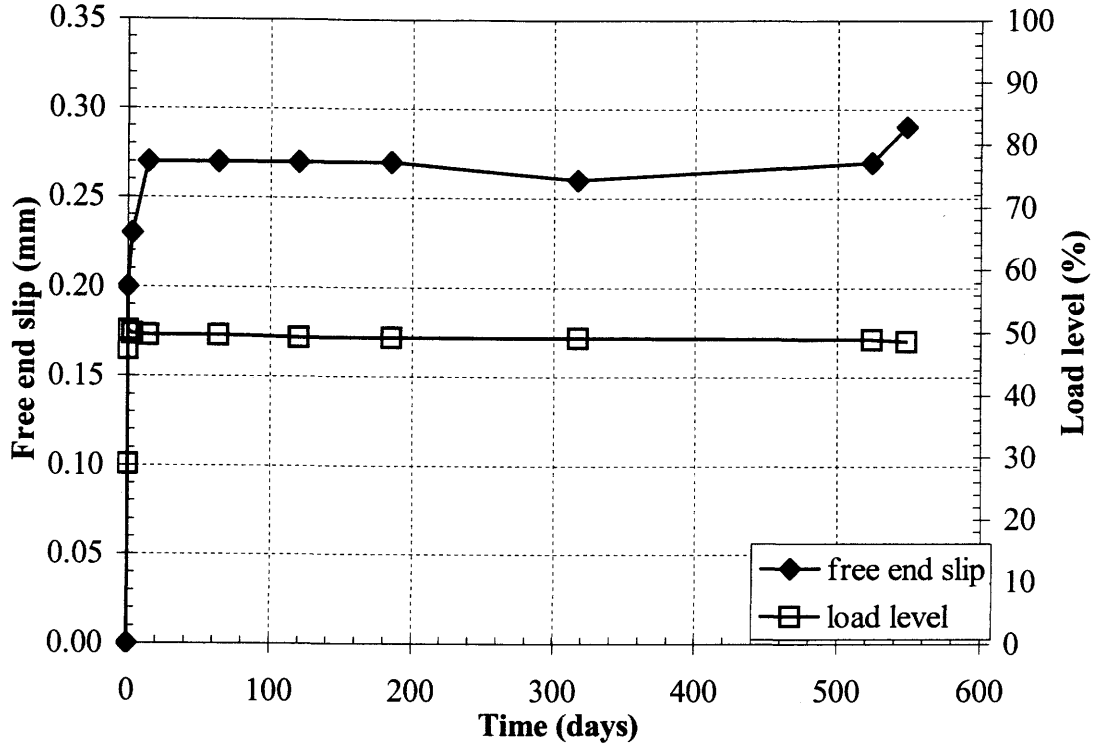

Figure C.11. Free end slip vs. time and load vs. time curves for Specimen HB 50% Alkaline #1.

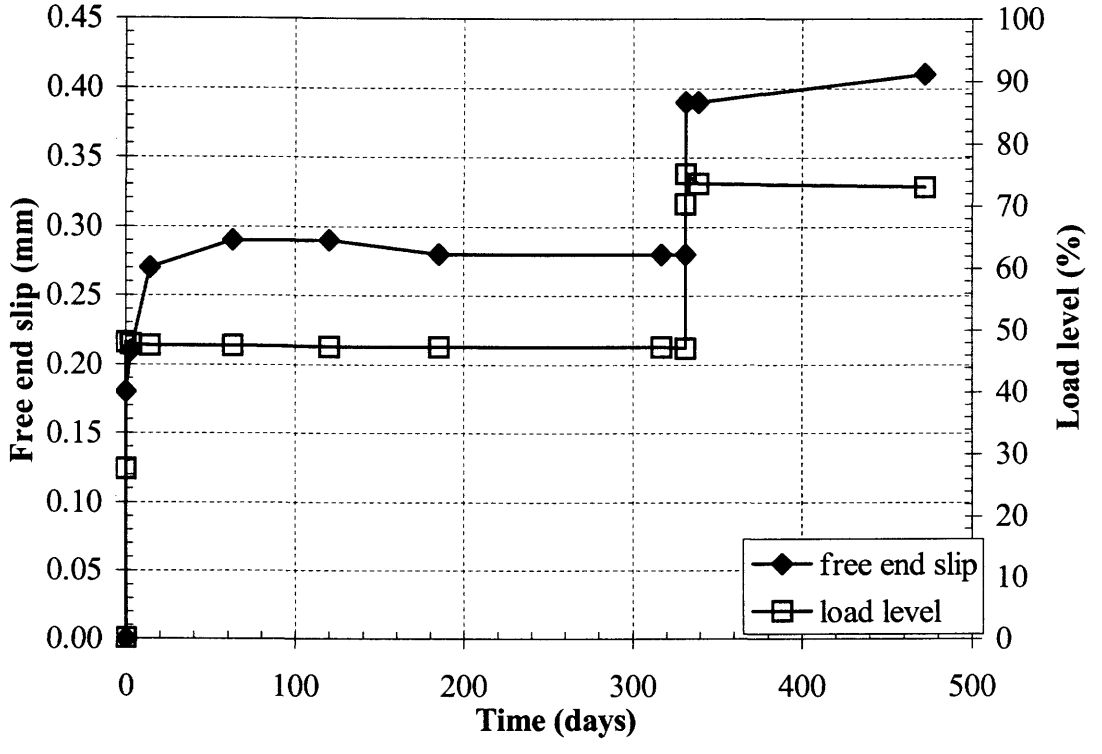

Figure C.12. Free end slip vs. time and load vs. time curves for Specimen HB 50-75% Alkaline #2.

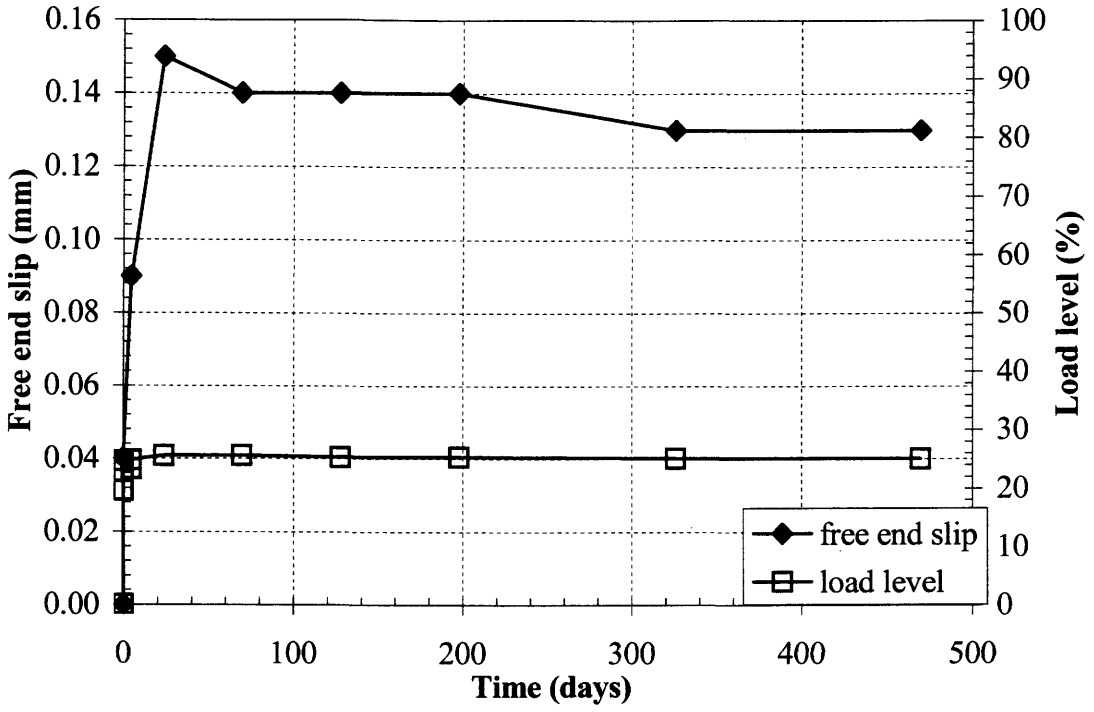

Figure C.13. Free end slip vs. time and load vs. time curves for Specimen C-bar 25% Air #1.

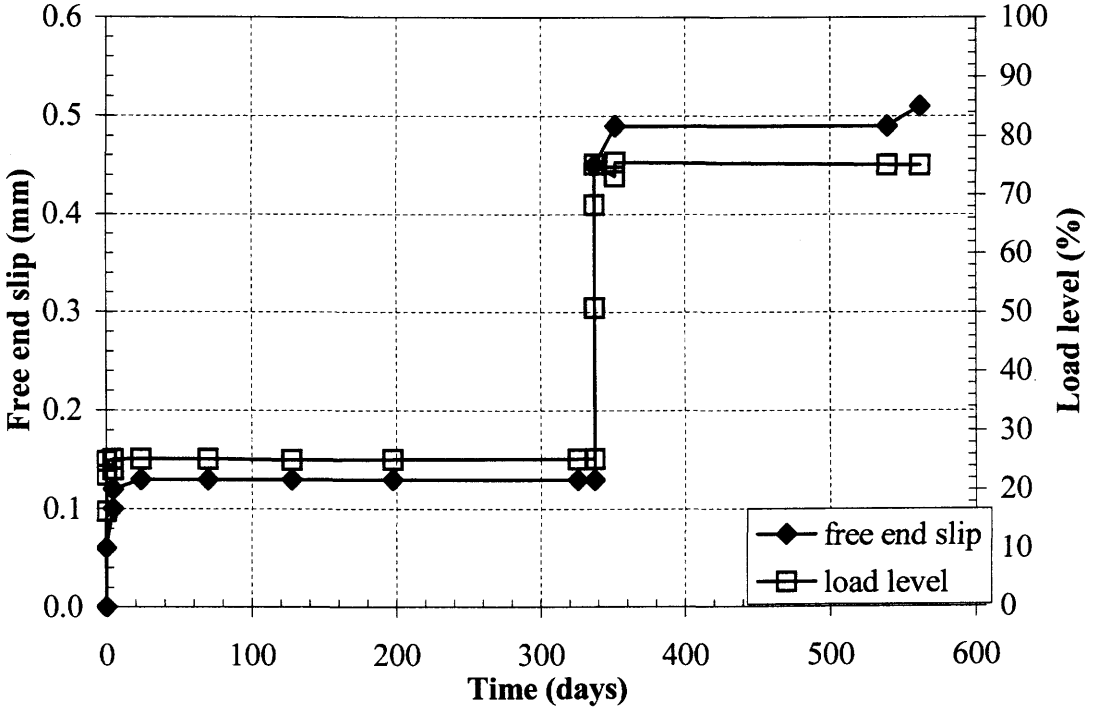

Figure C.14. Free end slip vs. time and load vs. time curves for Specimen C-bar 25-75% Air #2.

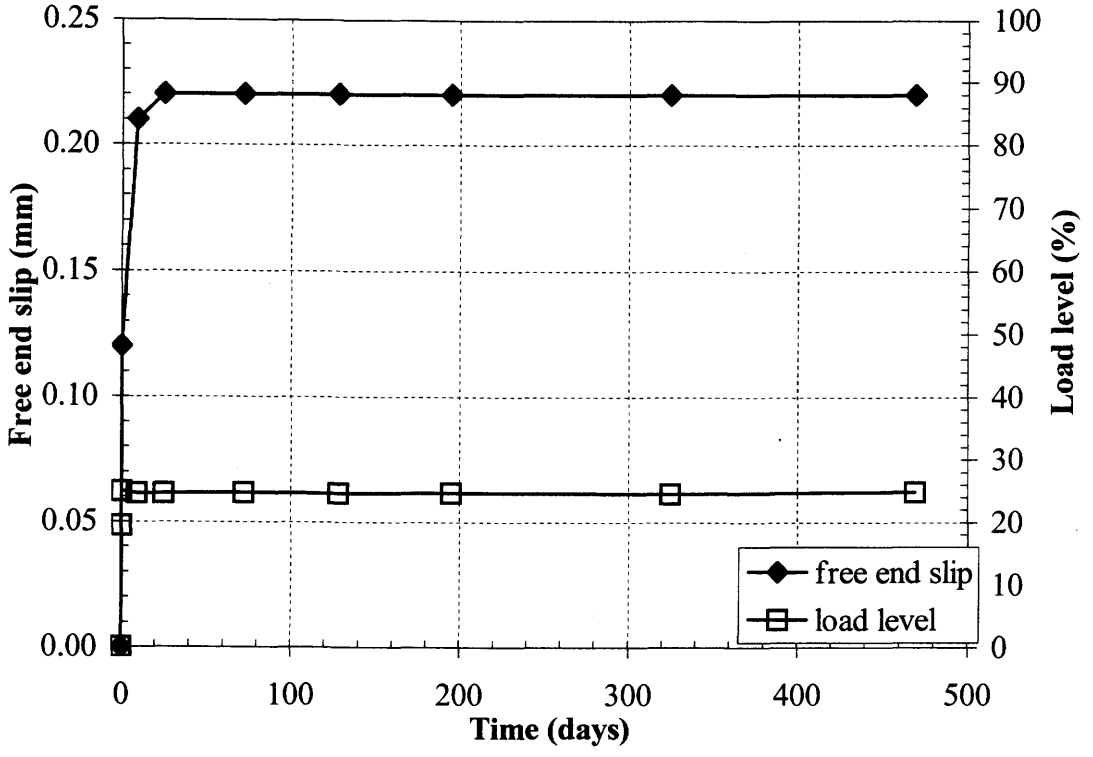

Figure C.15. Free end slip vs. time and load vs. time curves for Specimen C-bar 25% Water #1.

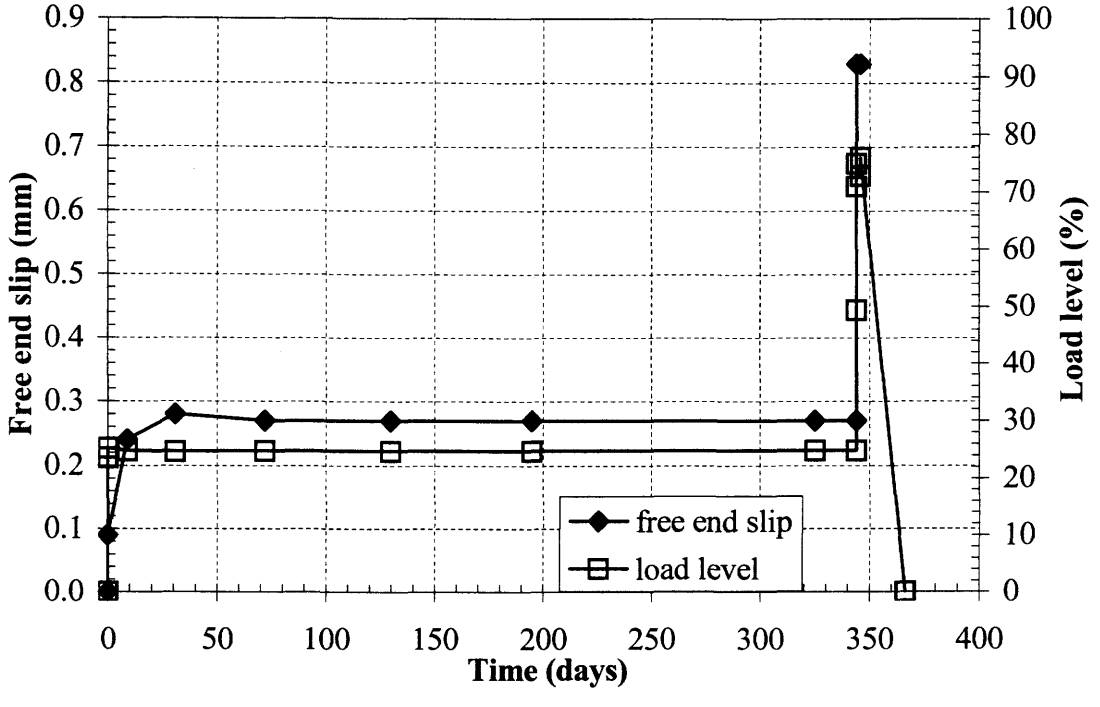

Figure C.16. Free end slip vs. time and load vs. time curves for Specimen C-bar 25-75% Water #2.

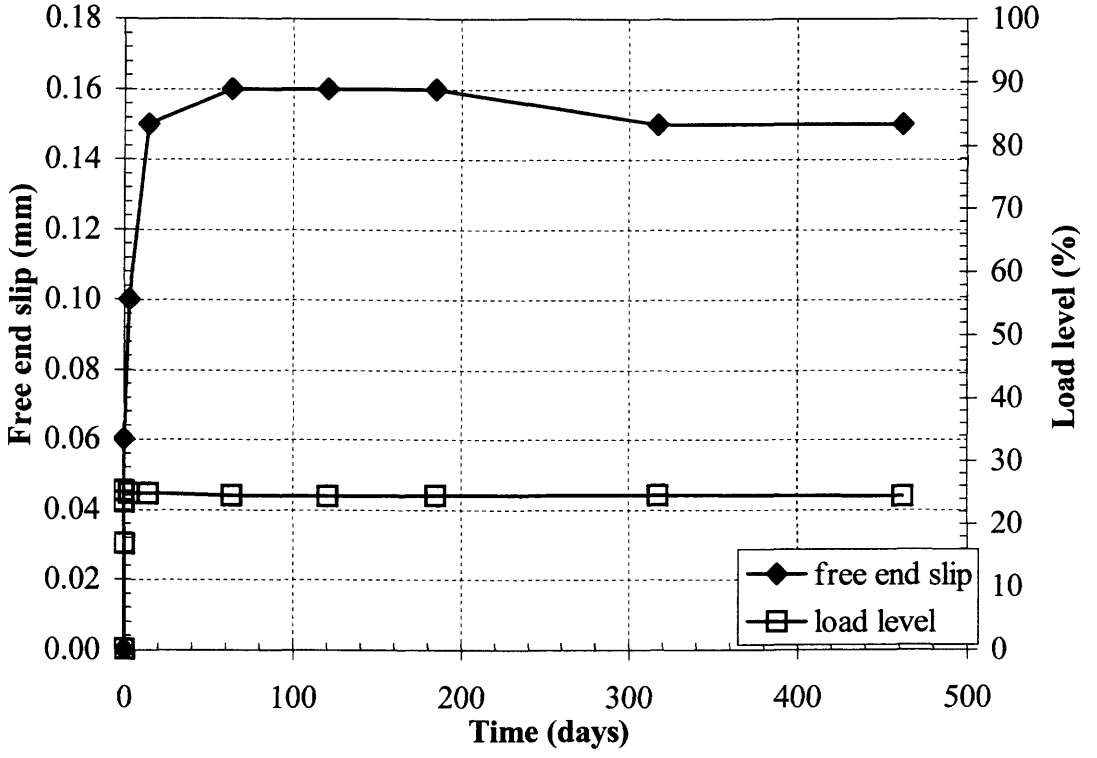

Figure C.17. Free end slip vs. time and load vs. time curves for Specimen C-bar 25% Alkaline #1.

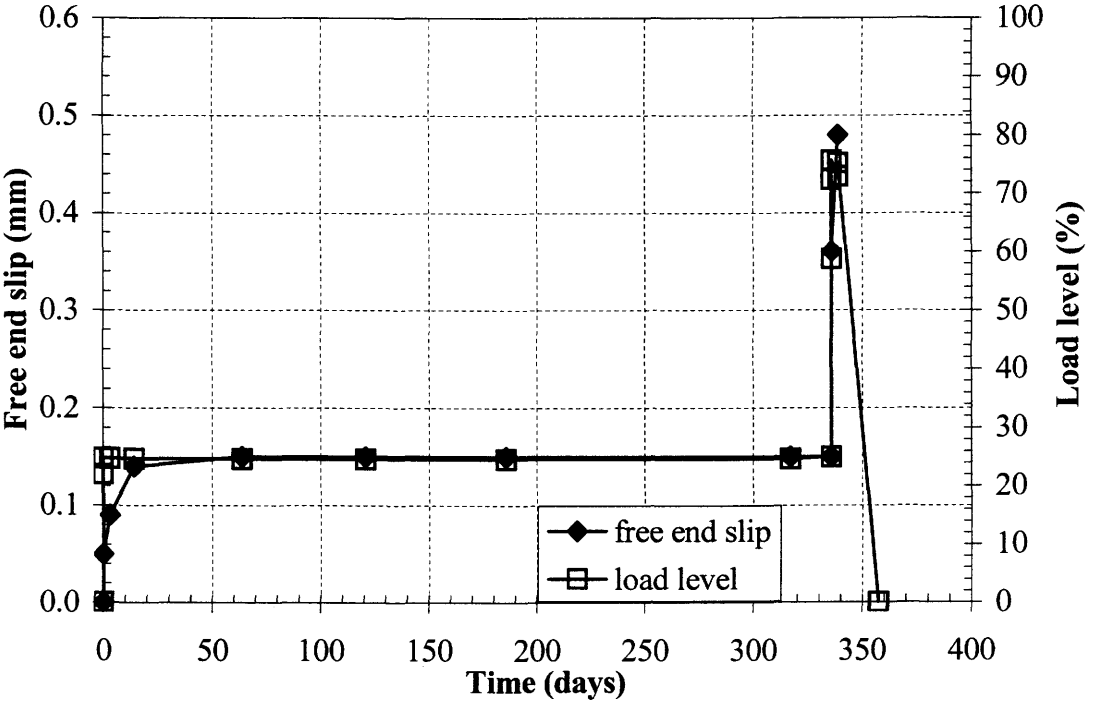

Figure C.18. Free end slip vs. time and load vs. time curves for Specimen C-bar 25-75% Alkaline #2.

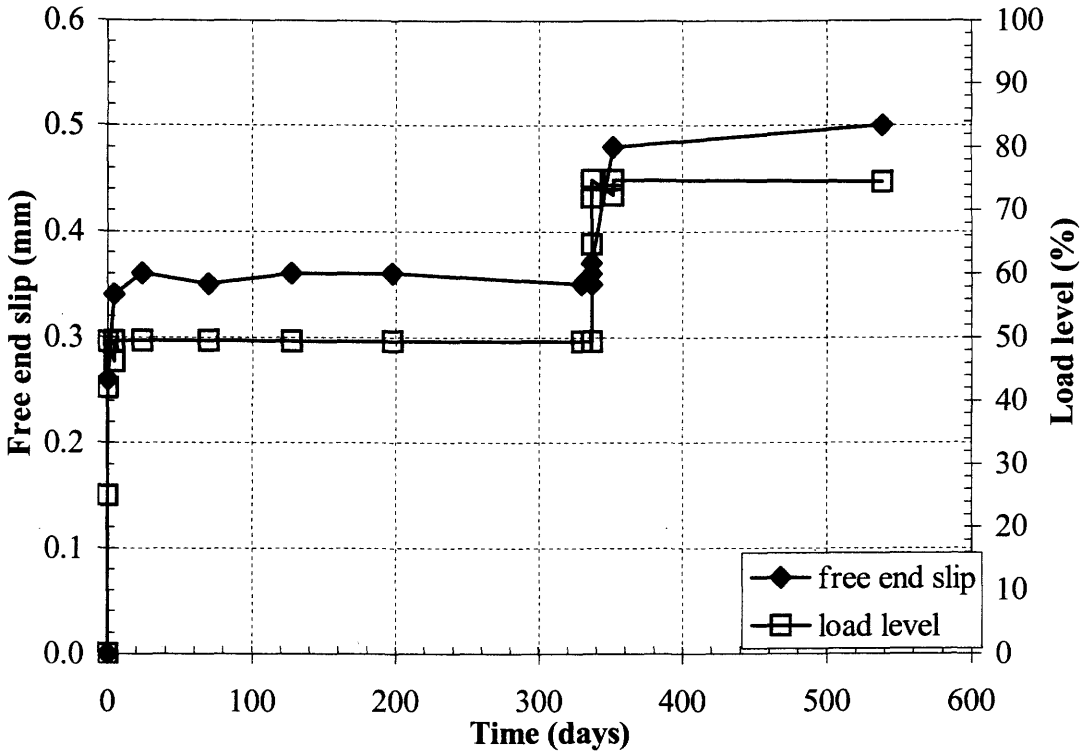

Figure C.19. Free end slip vs. time and load vs. time curves for Specimen C-bar 50-75% Air #1.

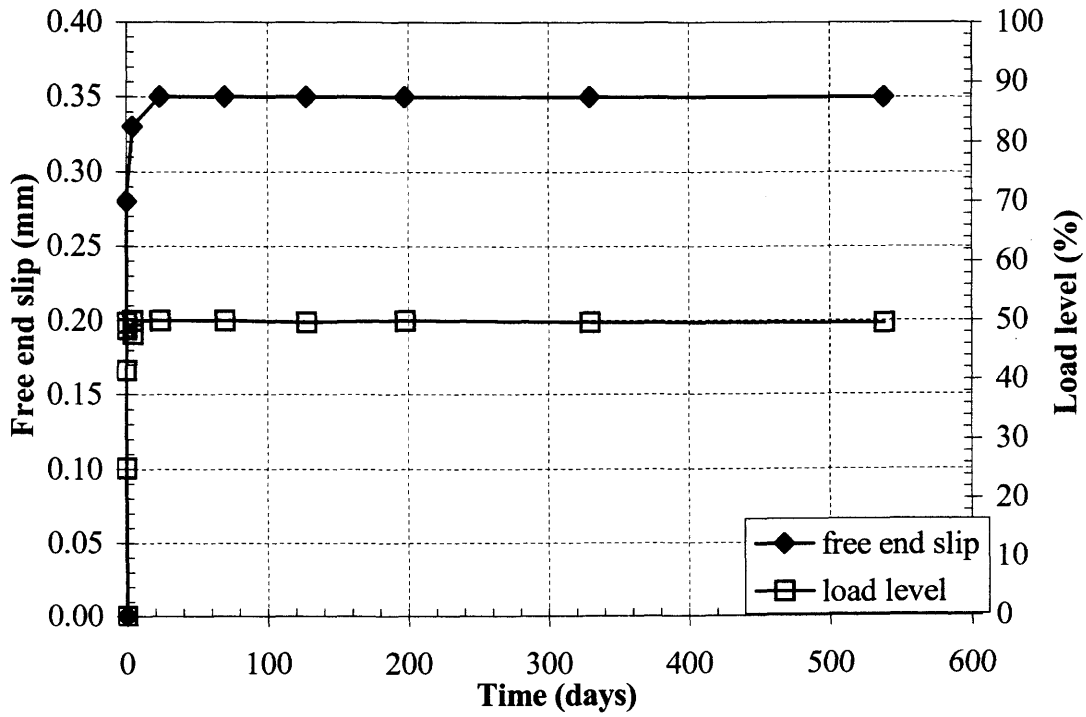

Figure C.20. Free end slip vs. time and load vs. time curves for Specimen C-bar 50% Air #2.

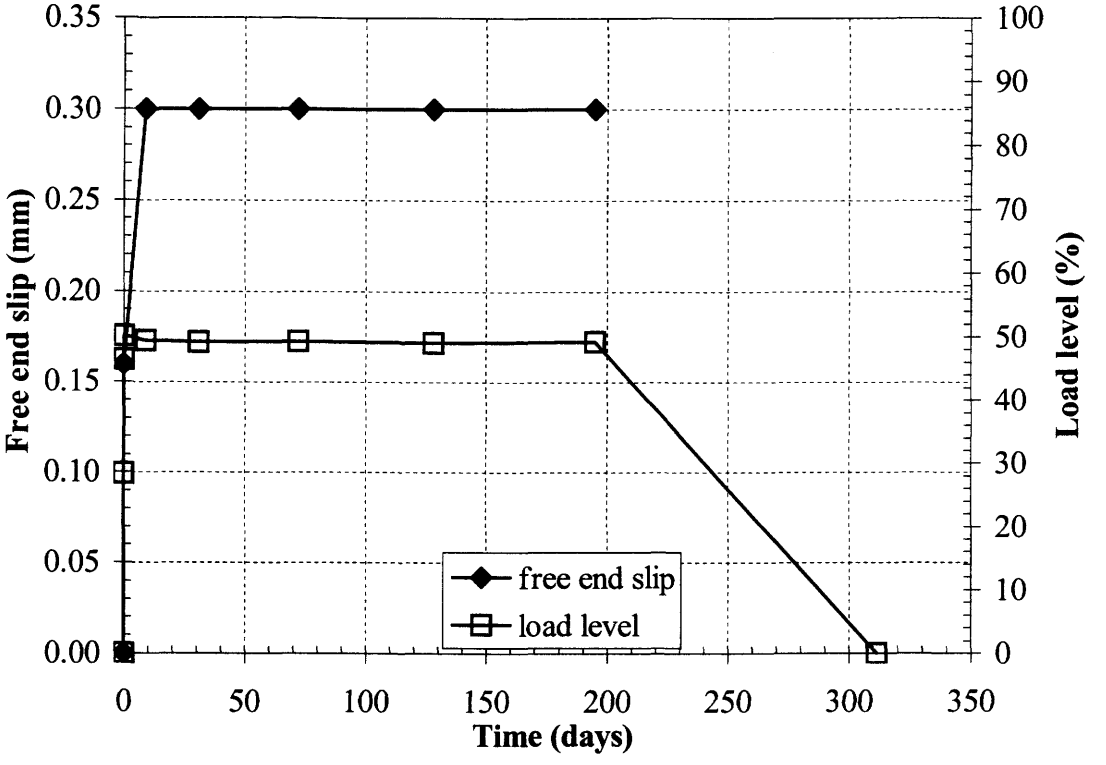

Figure C.21. Free end slip vs. time and load vs. time curves for Specimen C-bar 50% Water #1.

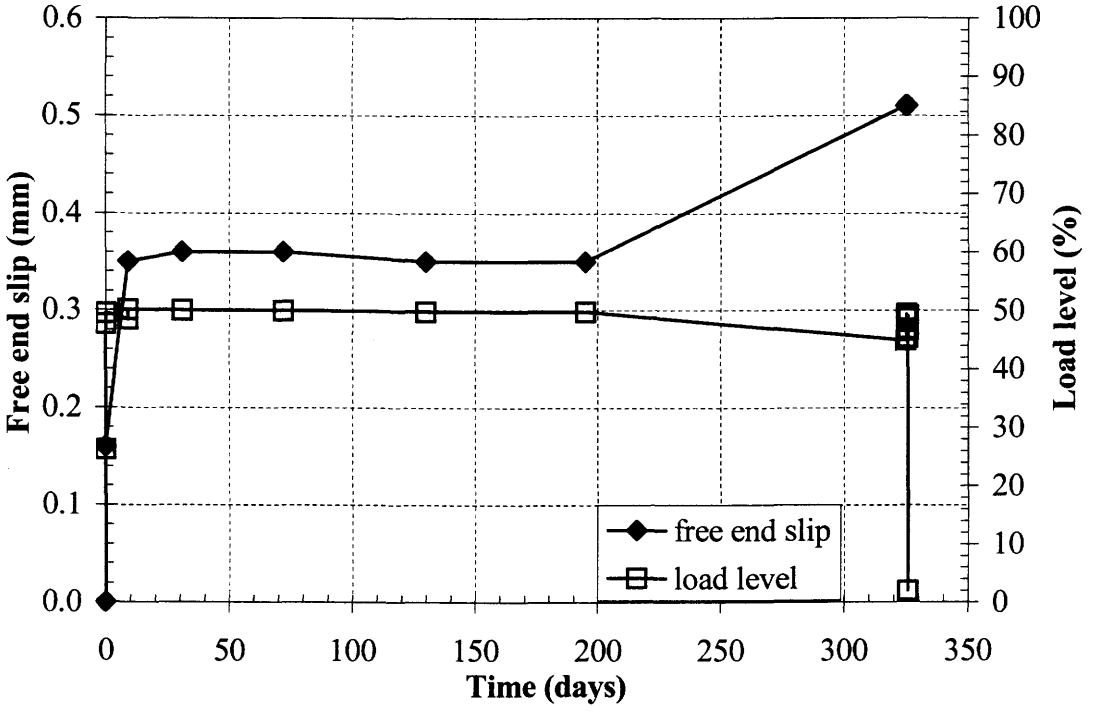

Figure C.22. Free end slip vs. time and load vs. time curves for Specimen C-bar 50% Water #2.

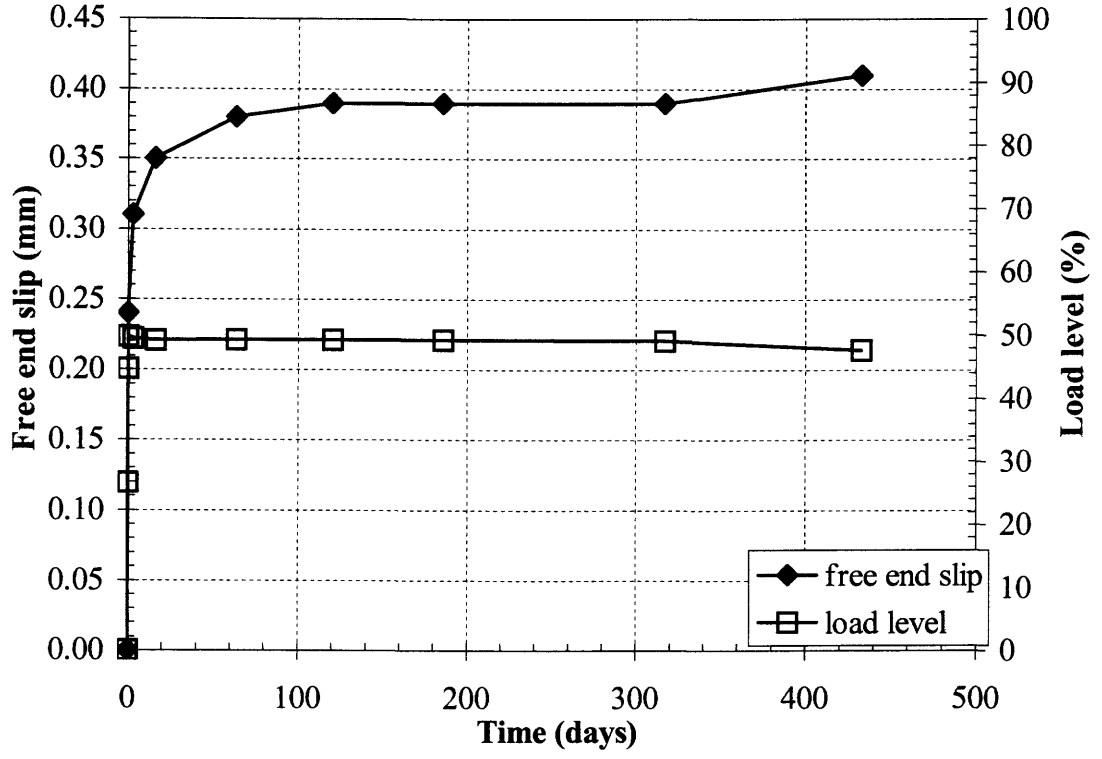

Figure C.23. Free end slip vs. time and load vs. time curves for Specimen C-bar 50% Alkaline #1.

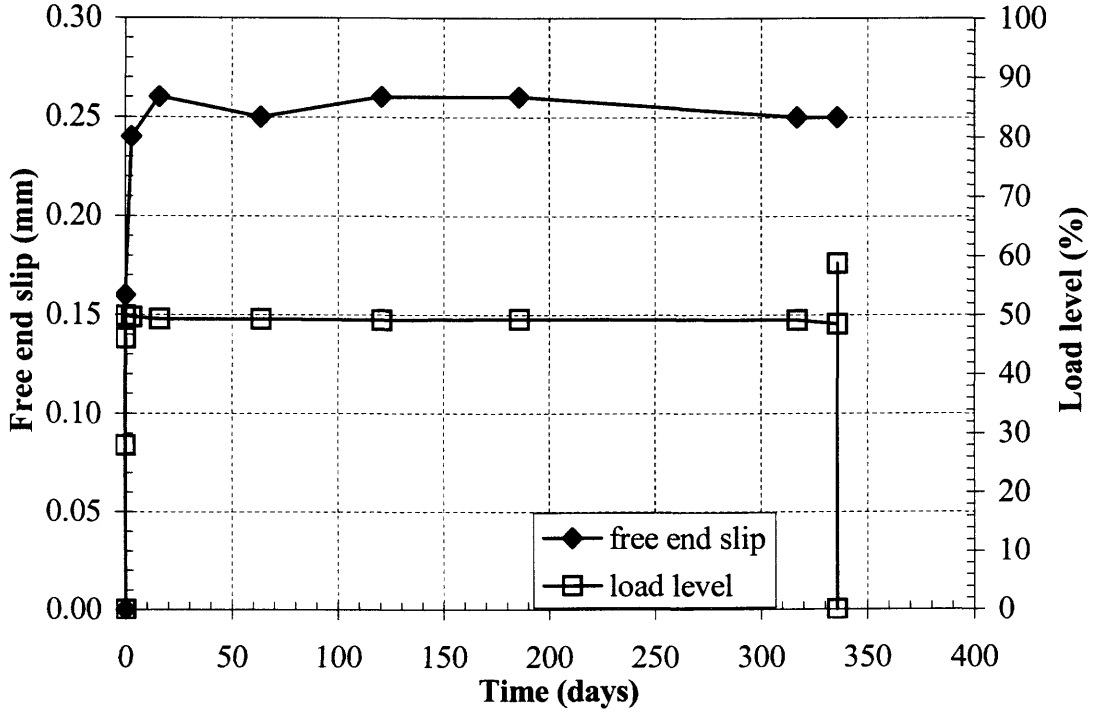

Figure C.24. Free end slip vs. time and load vs. time curves for Specimen C-bar 50-75% Alkaline #2.

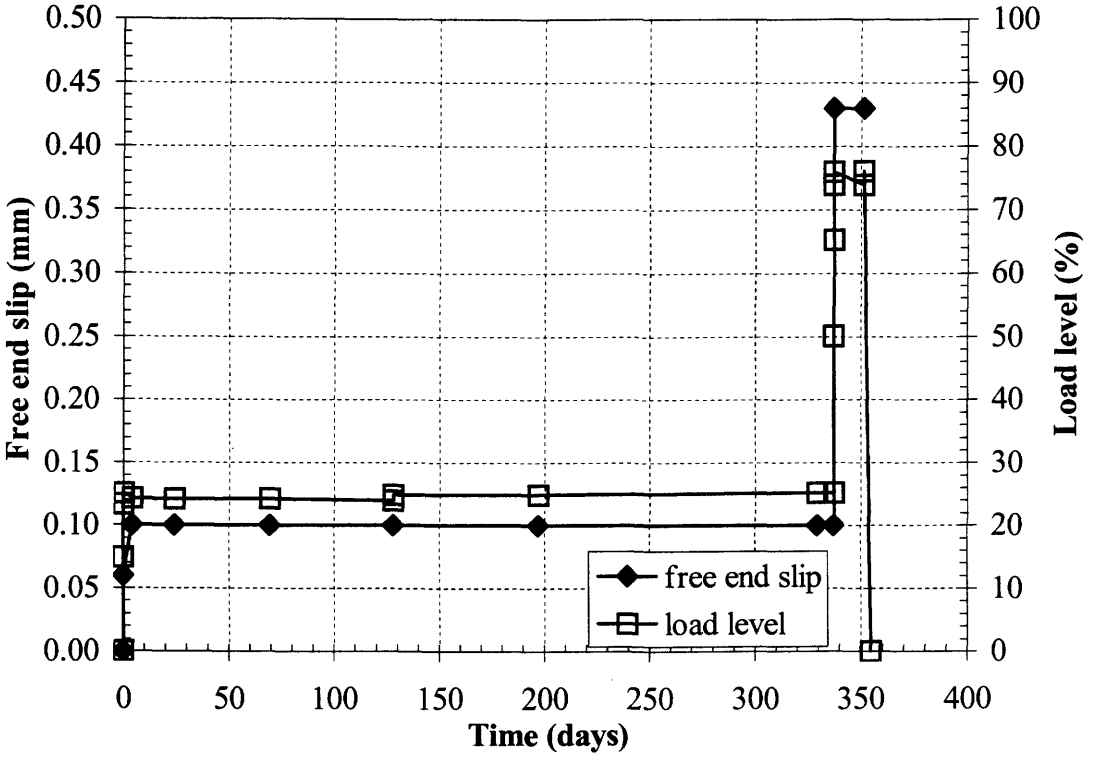

Figure C.25. Free end slip vs. time and load vs. time curves for Specimen Isorod 25-75% Air #1.

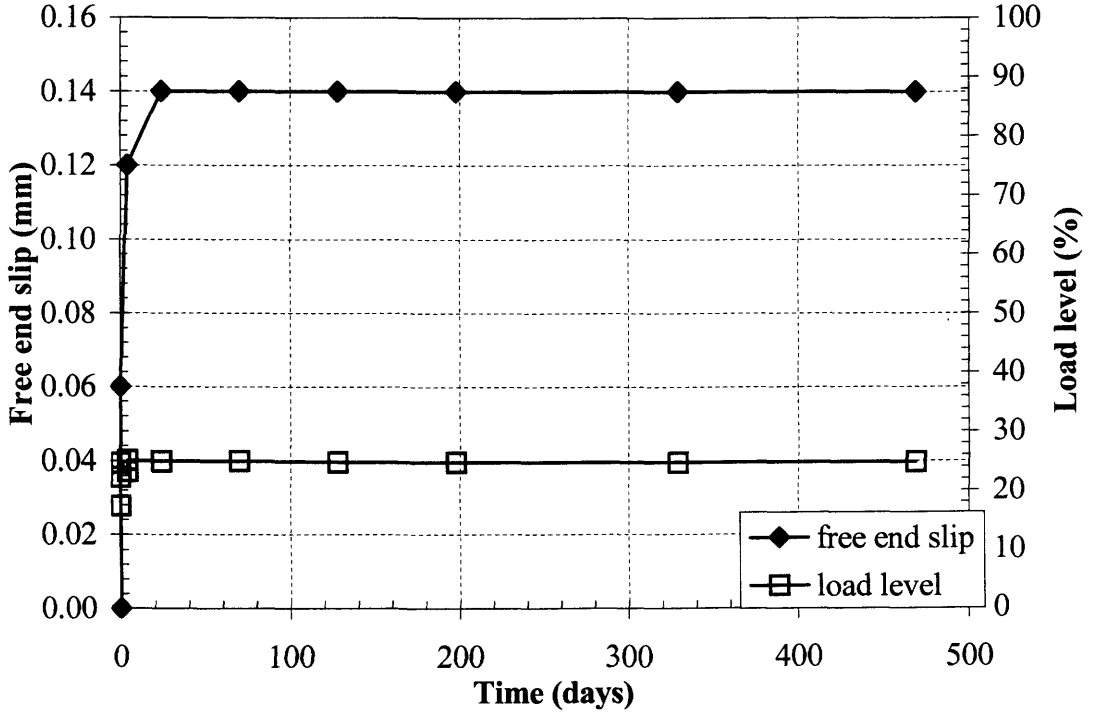

Figure C.26. Free end slip vs. time and load vs. time curves for Specimen Isorod 25% Air #2.

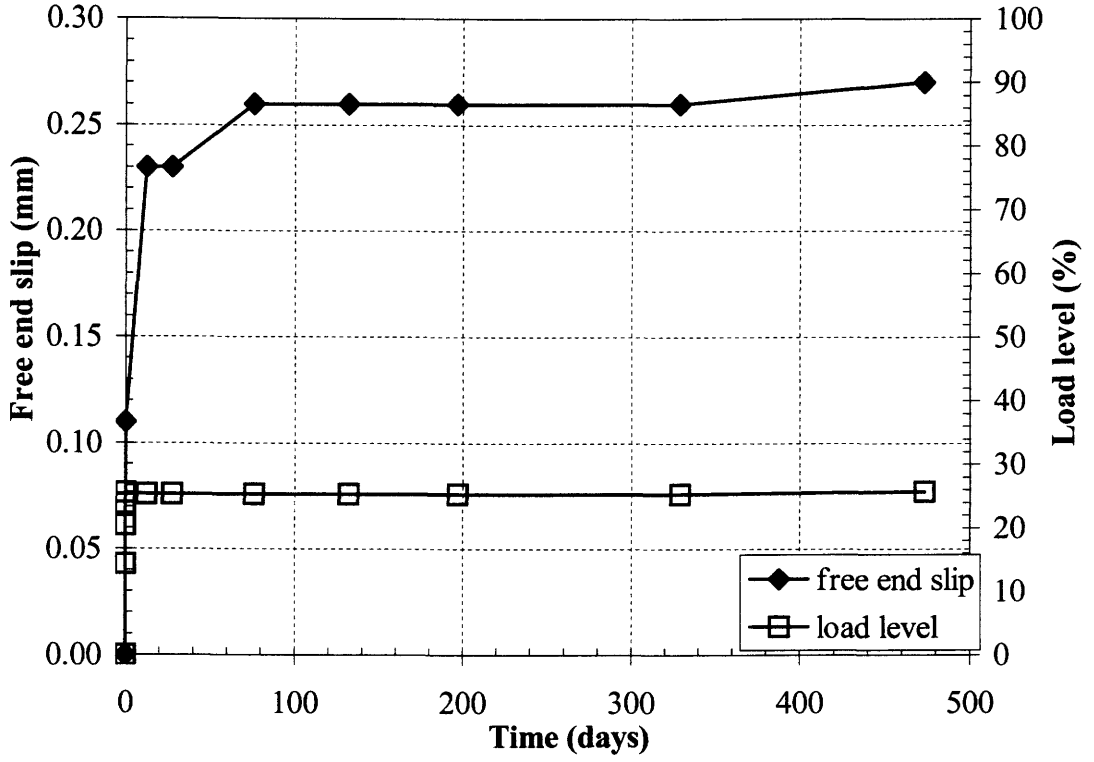

Figure C.27. Free end slip vs. time and load vs. time curves for Specimen Isorod 25% Water #1.

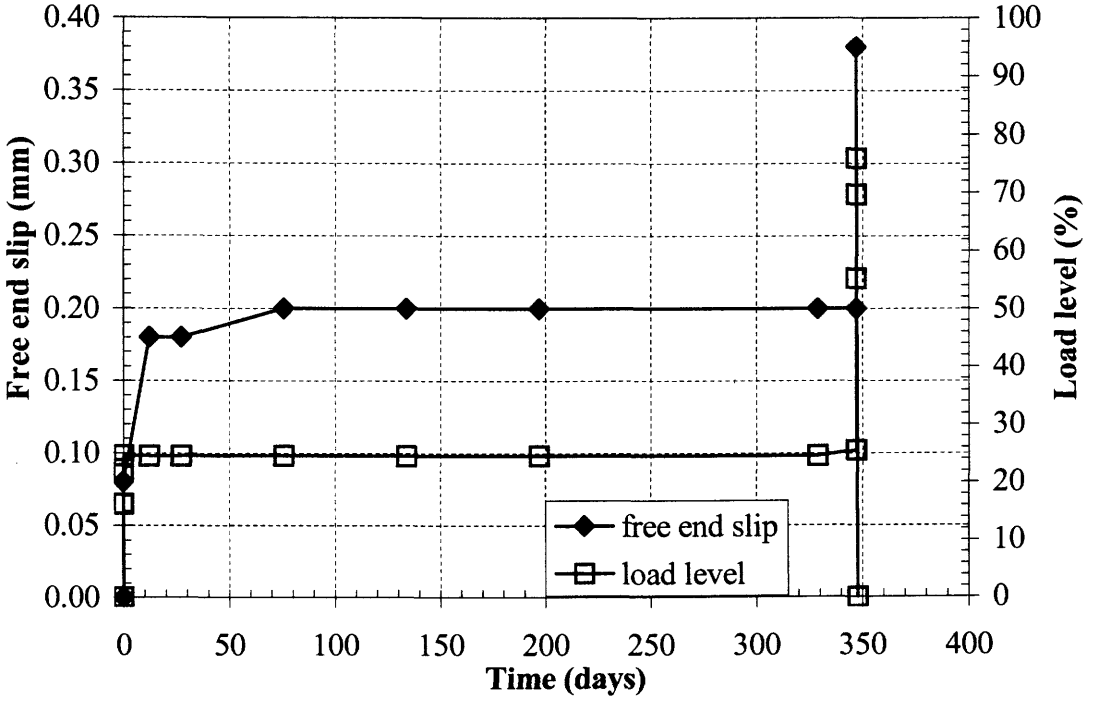

Figure C.28. Free end slip vs. time and load vs. time curves for Specimen Isorod 25-75% Water #2.

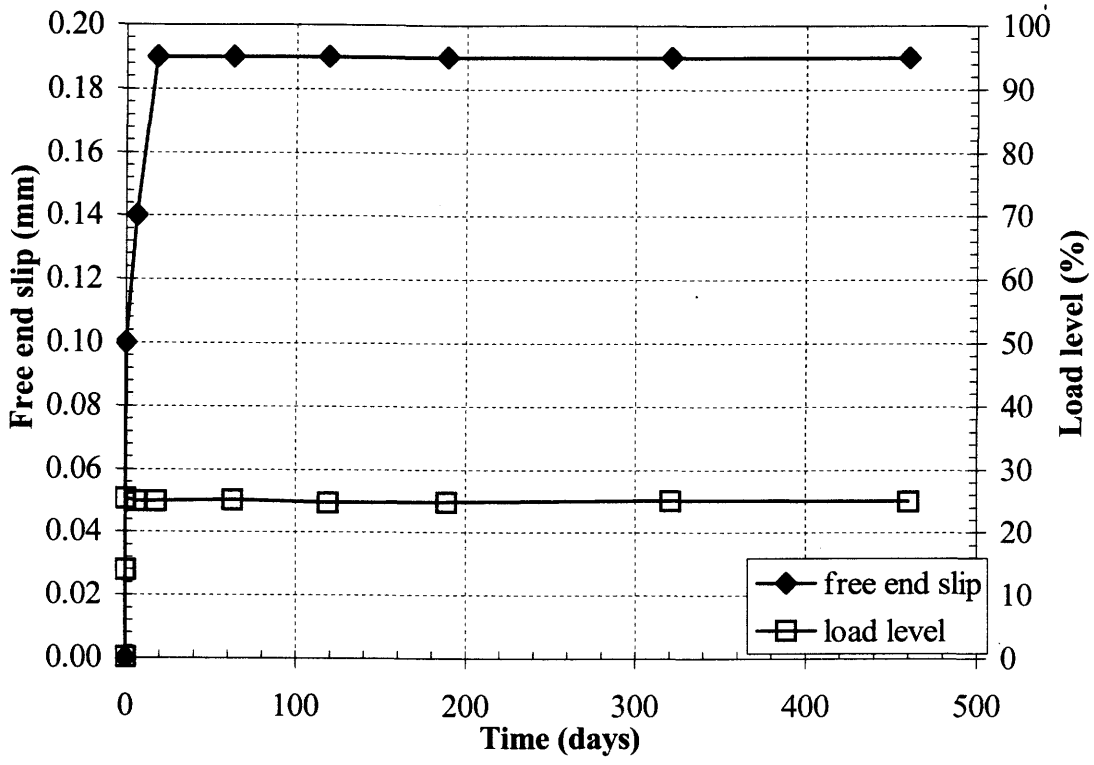

Figure C.29. Free end slip vs. time and load vs. time curves for Specimen Isorod 25% Alkaline #1.

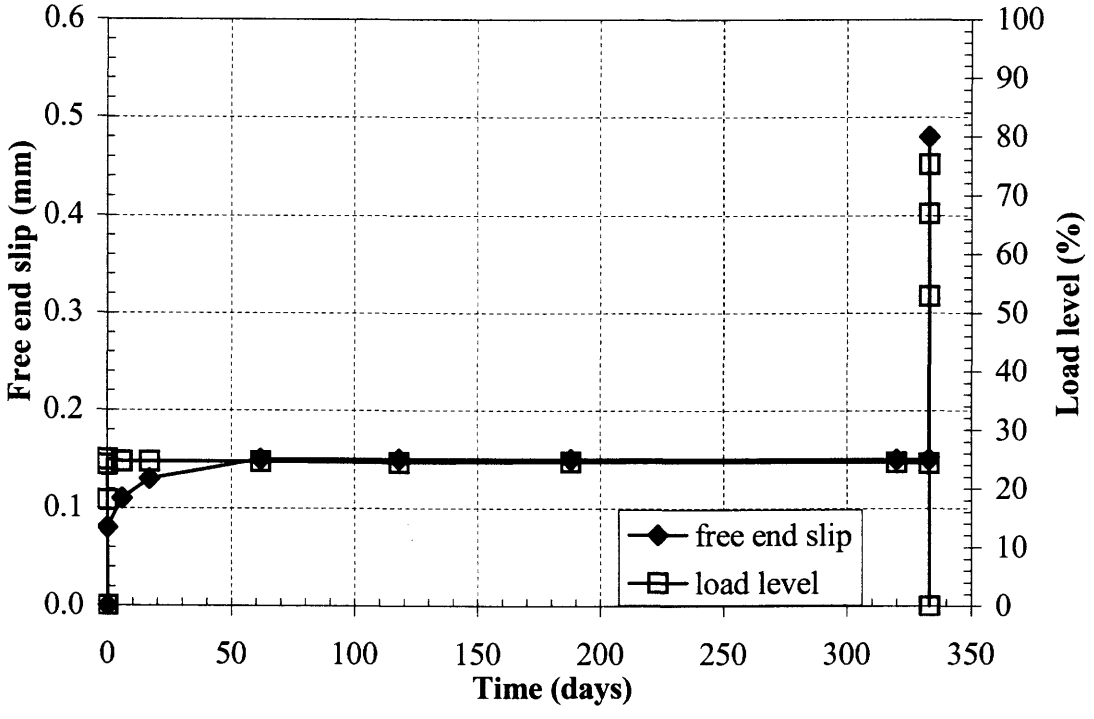

Figure C.30. Free end slip vs. time and load vs. time curves for Specimen Isorod 25-75% Alkaline #2.

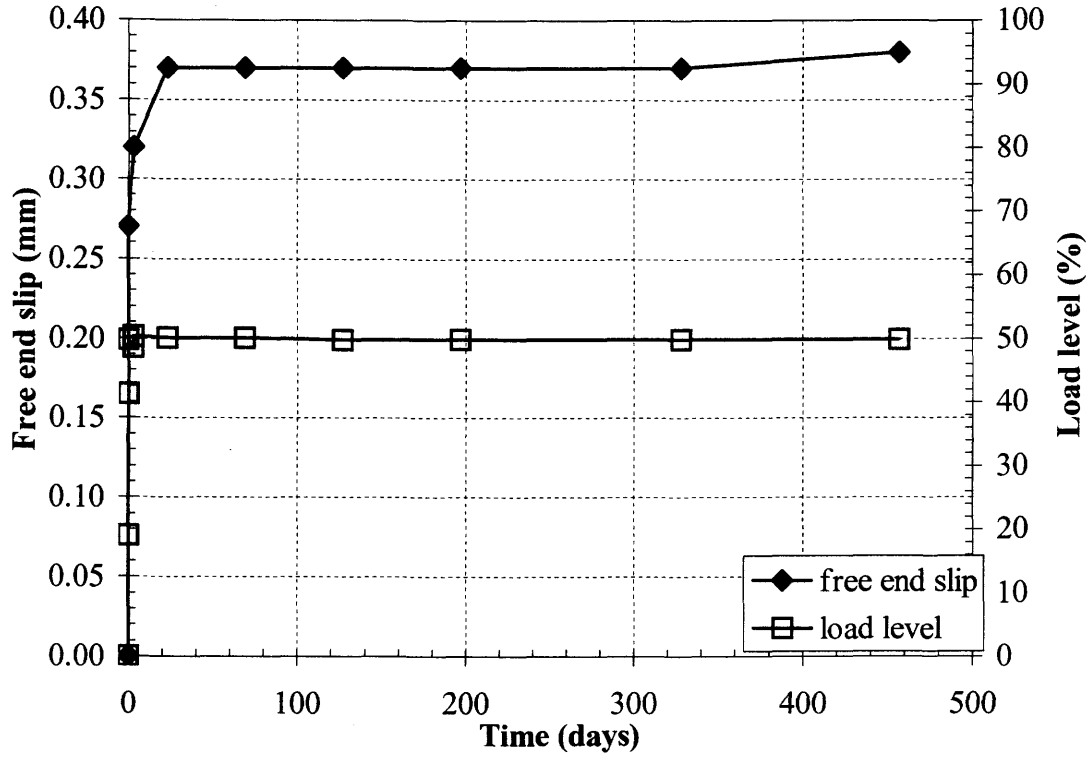

Figure C.31. Free end slip vs. time and load vs. time curves for Specimen Isorod 50% Air #1.

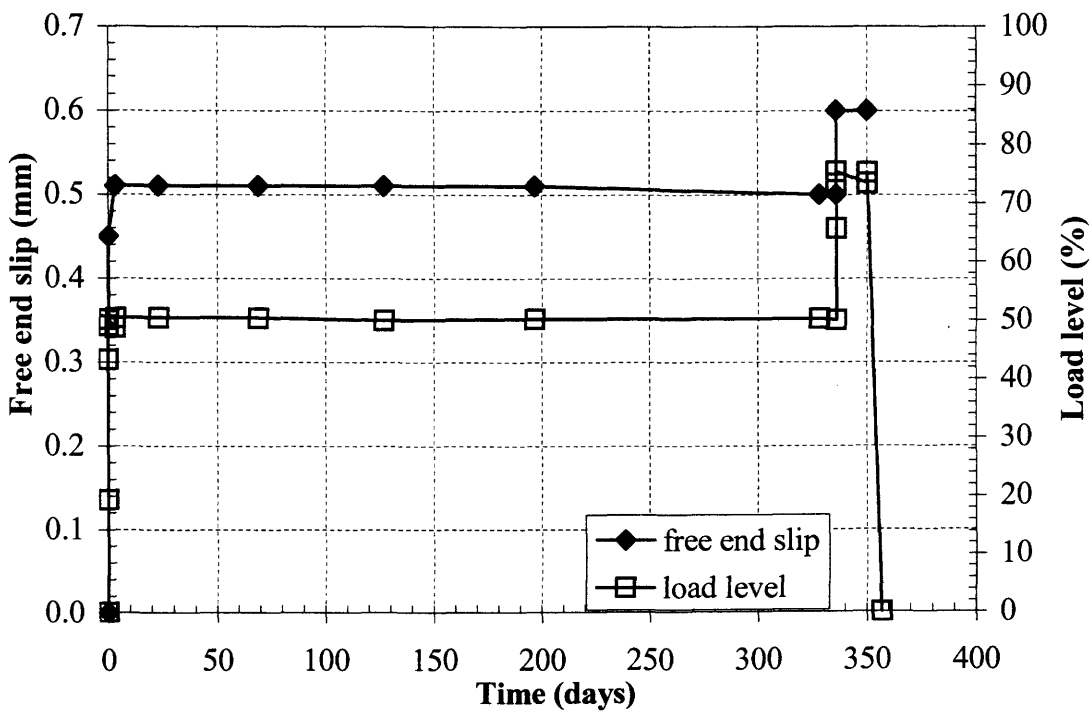

Figure C.32. Free end slip vs. time and load vs. time curves for Specimen Isorod 50-75% Air #2.

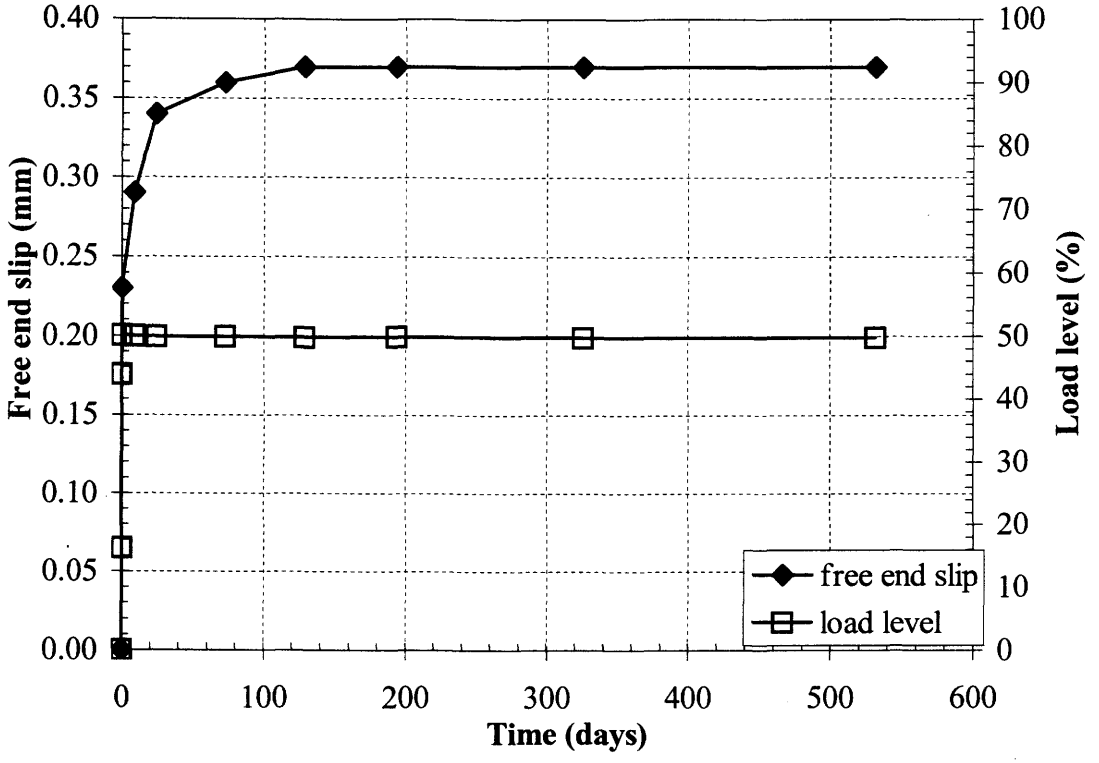

Figure C.33. Free end slip vs. time and load vs. time curves for Specimen Isorod 50% Water #1.

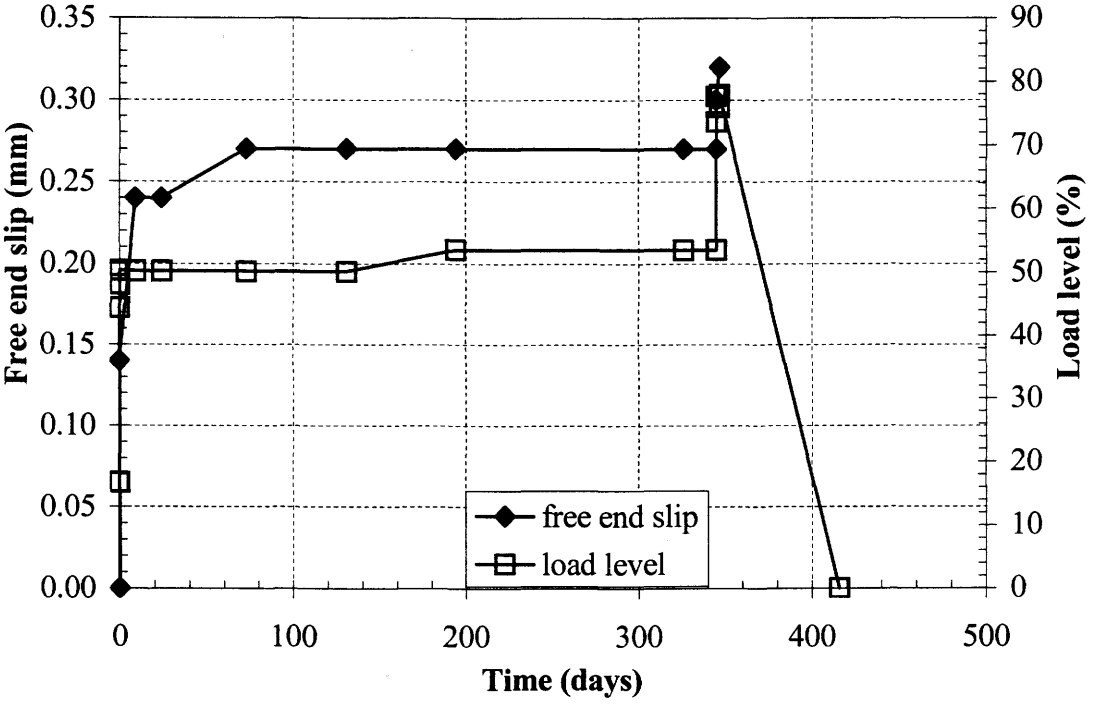

Figure C.34. Free end slip vs. time and load vs. time curves for Specimen Isorod 50-75% Water #2.

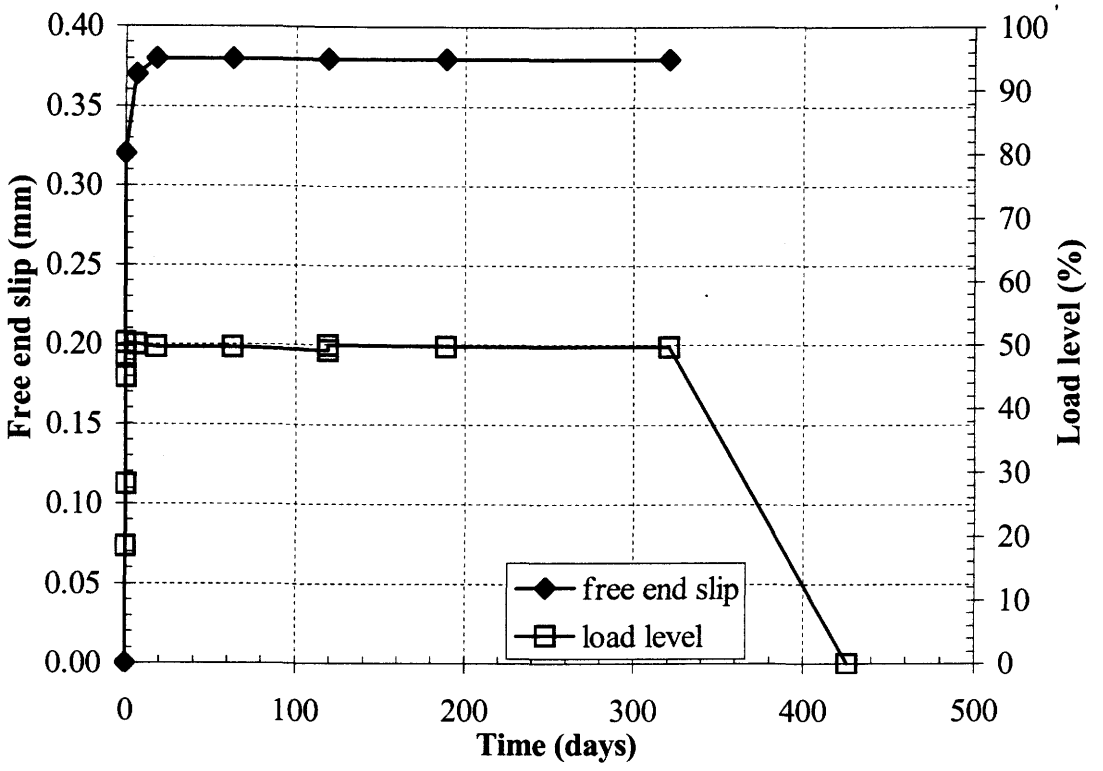

Figure C.35. Free end slip vs. time and load vs. time curves for Specimen Isorod 50% Alkaline #1.

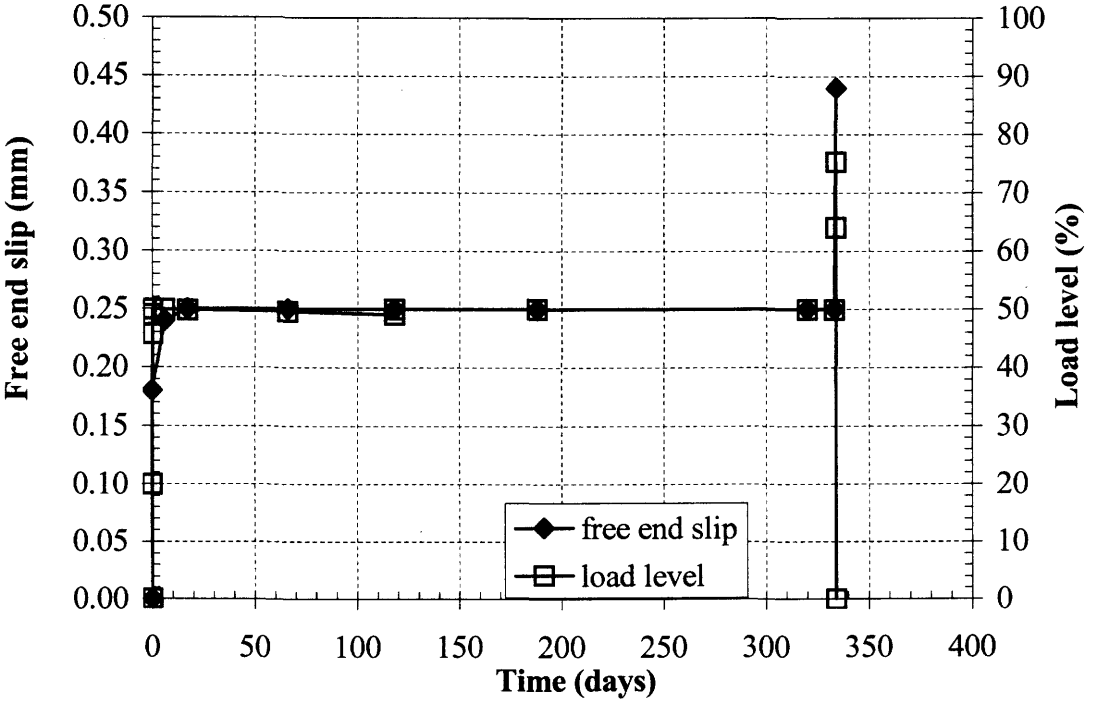

Figure C.36. Free end slip vs. time and load vs. time curves for Specimen 50-75% Alkaline #2.